

**Grenzflächeneigenschaften niedermolekularer π -
konjugierter Moleküle: Wechselwirkung von
Übergangsmetallphthalocyaninen und BN-
Substitution von Nanographenmolekülen**

Dissertation

der Mathematisch-Naturwissenschaftlichen Fakultät
der Eberhard Karls Universität Tübingen
zur Erlangung des Grades eines
Doktors der Naturwissenschaften
(Dr. rer. nat.)

vorgelegt von
Axel Belser
aus Tübingen

Tübingen
2021

Gedruckt mit Genehmigung der Mathematisch-Naturwissenschaftlichen Fakultät der
Eberhard Karls Universität Tübingen.

Tag der mündlichen Qualifikation:

30.09.2021

Dekan:

Prof. Dr. Thilo Stehle

1. Berichterstatter:

Prof. Dr. Thomas Chassé

2. Berichterstatter:

Prof. Dr. Reinhold Fink

Jennifer

In Liebe und Dankbarkeit gewidmet

Inhaltsverzeichnis

| | |
|---|------|
| Abkürzungsverzeichnis | VII |
| Zusammenfassung | IX |
| Abstract..... | XI |
| Publikationen | XII |
| a) Akzeptierte Publikationen | XII |
| b) Noch nicht eingereichte Manuskripte | XII |
| c) Akzeptierte Publikationen mit Koautorschaft | XIII |
| Einleitung | 1 |
| Ergebnisse und Diskussion..... | 11 |
| 1. Elektronische Eigenschaften und Orientierung von perfluoriertem FePc in dünnen Filmen..... | 11 |
| 2. Grenzflächeneigenschaften von perfluoriertem FePc | 17 |
| 3. Möglichkeiten zur Verhinderung der Grenzflächenwechselwirkung an der Grenzfläche von TMPcs und Metallen | 22 |
| 3.1 Verhinderung der Wechselwirkung zwischen TMPcF ₁₆ (M = Fe,Co) und Cu-Oberflächen durch O-Terminierung | 22 |
| 3.2 Verhinderung der Wechselwirkung zwischen CoPc und Au(111) durch eine geordnete Monolage Hexabenzocoronene..... | 28 |
| 4. Molekularer Austausch von Hexabenzocoronene und CoPc an der Grenzfläche zu Au(111)..... | 30 |
| 5. Wachstum und Orientierung des nanographenartigen Moleküls Hexabenzocoronene und verwandter BN-Derivate | 33 |
| 6. Elektronische Struktur des nanographenartigen Moleküls Hexabenzocoronene und verwandter BN-Derivate | 39 |
| 6.1 Elektronische Struktur in dünnen Filmen | 39 |
| 6.2 Elektronische Struktur an der Grenzfläche zu Au(111) und Ni(111) | 42 |
| Literaturverzeichnis..... | 46 |
| Anhang | 63 |
| a) Zusätzliche Abbildungen und Tabellen..... | 63 |
| b) Akzeptierte Publikationen | 67 |
| c) Noch nicht eingereichte Manuskripte..... | 117 |

Abkürzungsverzeichnis

| | |
|---------------------|---|
| Δ | Differenz |
| AEY | Auger Electron Yield (engl. für Auger-Elektronenausbeute) |
| AFM | Atomic Force Microscope (engl. für Rasterkraftmikroskop) |
| BE | Bindungsenergie |
| BN-HBC | B ₃ N ₃ -hexa- <i>peri</i> -hexabenzocoronen |
| BN-HBP | B ₃ N ₃ -hexa-benzotriphenylen |
| BN-HBP-2H | B ₃ N ₃ -hexa-benzotriphenylen-2H |
| CoPc | Cobalt(II)-Phthalocyanin |
| CoPcF ₁₆ | Cobalt(II)-Hexadecafluoro-Phthalocyanin |
| CuPc | Kupfer(II)-Phthalocyanin |
| E _F | Fermienergie |
| et al. | et alii (lateinisch für und andere) |
| E _{Vac} | Vakuumenergie |
| FePc | Eisen(II)-Phthalocyanin |
| FePcF ₁₆ | Eisen(II)-Hexadecafluoro-Phthalocyanin |
| GF | Grenzfläche |
| HBC | Hexa- <i>peri</i> -hexabenzocoronen |
| h-BN | Hexagonales Bornitrid |
| HOMO | Highest Occupied Molecular Orbital (engl. für Höchstes besetztes Orbital) |
| h ν | Anregungsenergie mit der Frequenz ν |
| LEED | Low-Energy Electron Diffraction (engl. für Beugung niederenergetischer Elektronen an Oberflächen) |
| LUMO | Lowest Unoccupied Molecular Orbital (engl. für Niedrigstes unbesetztes Orbital) |
| ML | Monolage |
| MnPc | Mangan(II)-Phthalocyanin |
| NEXAFS | Near-Edge X-ray Absorption Fine Structure (engl. für Röntgen-Nahkanten-Absorptions-Spektroskopie) |
| NPA | Natural Population Analysis (engl. für Natürliche Populationsanalyse) |
| PAH | Polycyclic Aromatic Hydrocarbons (engl. für Polyzyklische Aromatische Kohlenwasserstoffe) |

| | |
|----------------|--|
| PES | Photoelektronenspektroskopie |
| PTCDA | 3,4,9,10-Perylentetracarbonsäuredianhydrid |
| RMS | Root Mean Square (engl. für Quadratisches Mittel) |
| STM | Scanning Tunneling Microscope (Rastertunnelmikroskop) |
| TDDFT | Time-Dependent Density Functional Theory (engl. für Zeitabhängige Dichtefunktionaltheorie) |
| TEY | Total Electron Yield (engl. für Gesamtelektronenausbeute) |
| TMPc | Transition Metal Phthalocyanine (engl. für Übergangsmetall-Phthalocyanin) |
| UPS | Ultraviolettphotoelektronenspektroskopie |
| willk. Einheit | Willkürliche Einheit |
| XAES | Röntgen-Augerelektronenspektroskopie |
| XAS | Röntgenabsorptionsspektroskopie |
| XPS | Röntgenphotoelektronenspektroskopie |

Zusammenfassung

In der vorliegenden Arbeit wurden die Wechselwirkungseigenschaften, das Wachstumsverhalten und die Orientierung von Übergangsmetallphthalocyaninen (TMPcs), insbesondere von perfluoriertem FePc (FePcF_{16}) und (BN-) Nanographenmolekülen in dünnen Schichten sowie an verschiedenen Grenzflächen ausführlich untersucht. Das Besondere an dieser Arbeit ist die Kombination aus verschiedenen Methoden, um die Wechselwirkung jeder im Molekül vorkommenden Atomsorte zu untersuchen. So konnte gezeigt werden, dass die Wechselwirkung an der Grenzfläche zu Metallkontakten sehr vielfältig ist und alle Elemente der Moleküle an dieser beteiligt sind. Bei Untersuchungen des perfluorierten CoPc (CoPcF_{16}) wurde beispielweise die Kombination aus Photoelektronenspektroskopie (PES), Röntgenabsorptionsspektroskopie (XAS) und Augerspektroskopie (XAES) genutzt, um einen komplexen wechselseitigen Ladungstransfer zu Cu-Oberflächen festzustellen. Des Weiteren konnte durch die Kombination von XAS und PES anhand des FePcF_{16} gezeigt werden, dass eine qualitative Bestimmung der Orientierung über eine C1s Peakfitanalyse mit einer oberflächensensitiven Anregungsenergie möglich ist.

Ein sehr wichtiger Schritt zur Aufklärung der elektronischen Struktur der (BN-) Nanographenmoleküle war eine ausführliche Peakfitanalyse der Rumpfniveaus, sowie die Kombination aus experimentellen und gerechneten XAS-Spektren. Zudem konnte für die (BN-) Nanographenmoleküle gezeigt werden, dass sowohl die BN-Dotierung als auch der Grad der Planarität und damit die Größe des konjugierten π -Systems sowohl die elektronischen Eigenschaften, die Morphologie als auch das Wachstum bzw. die Orientierung der Moleküle in dünnen Filmen sowie an der Grenzfläche stark beeinflusst. Die BN-Dotierung beeinflusst dabei hauptsächlich die elektronischen Eigenschaften und die Morphologie dünner Filme, wahrscheinlich bedingt durch unterschiedlich starke Molekül-Molekül Wechselwirkung. Dahingegen wirkt sich der Grad an Planarität am stärksten auf die Orientierung dünner Filme und die Wechselwirkung an der Grenzfläche zu den Metallkontakten aus. Dabei wurde festgestellt, dass das größere planare π -System des B_3N_3 -hexa-*peri*-hexabenzocoronon (BN-HBC) im Vergleich zu den kleinen Biphenyleinheiten des B_3N_3 -hexabenzotriphenylen (BN-HBP) stabilisierend wirkt.

Abstract

In the present work, the interaction properties, the growth mode and the orientation of transition metal phthalocyanines (TMPcs), in particular of perfluorinated FePc (FePcF_{16}), and (BN-) nanographene molecules in thin layers and at different interfaces were investigated in detail. The special thing about this work is the combination of different methods to investigate the interaction of every type of atom in the molecule. It could be shown that the interaction at the interface with metal contacts is very diverse and that all types of atoms of the molecules are involved in it. In investigations of the perfluorinated CoPc (CoPcF_{16}) for example, the combination of photoelectron spectroscopy (PES), X-ray absorption spectroscopy (XAS) and Auger spectroscopy (XAES) was used to determine a complex reciprocal charge transfer to Cu surfaces. Furthermore, the combination of XAS and PES based on FePcF_{16} showed that a qualitative determination of the orientation via a C1s peak fit analysis with a surface-sensitive excitation energy is possible.

A very important step towards elucidating the electronic structure of the BN-nanographene molecules was a detailed peak fit analysis of the core levels, as well as the combination of experimental and calculated XAS spectra. In addition, it was possible to show for the (BN-) nanographene molecules that both the BN doping and the degree of planarity and thus the size of the conjugated π -system affect both the electronic properties, morphology and growth or the orientation of the molecules in thin films as well as at the interface is strongly influenced. The BN doping mainly influences the electronic properties and the morphology of thin films, probably due to different strengths of molecule-molecule interaction. In contrast, the degree of planarity has the greatest impact on the orientation of thin films and the interaction at the interface with the metal contacts. It was found that the larger planar π system of B_3N_3 -hexa-peri-hexabenzocoronene (BN-HBC) has a stabilizing effect compared to the small biphenyl units of B_3N_3 -hexabenzotriphenylene (BN-HBP).

Publikationen

a) Akzeptierte Publikationen

[1] Belser A., Karstens R., Grüninger P., Nagel P., Merz M., Schuppler S., Suturina E.A., Chassé A., Chassé T., Peisert H., Spin State in Perfluorinated FePc Films on Cu(111) and Ag(111) in Dependence on Film Thickness. *Journal of Physical Chemistry C* **2018**, 122, 15390-15394.

[2] Belser A., Karstens R., Nagel P., Merz M., Schuppler S., Chassé T., Peisert H., Interaction Channels Between Perfluorinated Iron Phthalocyanine and Cu(111). *Physica Status Solidi B* **2019**, 256, 1800292.

[3] Belser A.*, Greulich K.*, Grüninger P., Bettinger H.F., Peisert H., Chassé T., Visualization of the Borazine Core of B₃N₃-Doped Nanographene by STM. *ACS Applied Materials & Interfaces* **2020**, 12, 19218-19225.

[4] Greulich K.*, Belser A.*, Bischof D., Widdascheck F., Sättele M.S., Grüninger P., Bettinger H.F., Witte G., Chassé T., Peisert H., B₃N₃-Substituted Nanographene Molecules: Influence of Planarity on the Electronic Structure and Molecular Orientation in Thin Films. *ACS Applied Electronic Materials* **2021**, 3, 825-837.

[5] Belser A., Greulich K., Grüninger P., Karstens R., Ovsyannikov R., Giangrisostomi E., Nagel P., Merz M., Schuppler S., Chassé T., Peisert H., Perfluorinated Phthalocyanines on Cu(110) and Cu(110)-(2x1)O: The Special Role of the Central Cobalt Atom. *Journal of Physical Chemistry C* **2021**, 125, 16, 8803–8814.

*Autoren teilen sich die Erstautorschaft

b) Noch nicht eingereichte Manuskripte

[6] Belser A., Greulich K., Nagel P., Merz M., Schuppler S., Chassé T., Peisert H., Comparison of Interface Properties of Perfluorinated FePc on Au(111) and Ag(111).

[7] Belser A., Greulich K., Grüninger P., Sättele M.S., Fingerle M., Bettinger H.F., Chassé T., Peisert H., Influence of BN-doping of Nanographene Molecules on the Interaction at Different Metal Interfaces.

[8] Belser A., Greulich K., Sättele M.S., Fingerle M., Ovsyannikov R., Giangrisostomi E., Chassé T., Peisert H., Molecular exchange of Hexabenzocoronene and Cobalt Phthalocyanine on Au(111).

c) Akzeptierte Publikationen mit Koautorschaft

Karstens R., Glaser M., Belser A., Balle D., Polek M., Ovsyannikov R., Giangrisostomi E., Chassé T., Peisert H., FePc and FePcF₁₆ on Rutile TiO₂(110) and (100): Influence of the Substrate Preparation on the Interaction Strength. *Molecules* **2019**, *24*, 4579.

Grüninger P., Greulich K., Karstens R., Belser A., Ovsyannikov R., Giangrisostomi E., Bettinger H.F., Batchelor D., Peisert H., Chassé T., Highly Oriented Hexacene Molecules Grown in Thin Films on Cu(110)-(2x1)O. *Journal of Physical Chemistry C* **2019**, *123*, 27672-27680.

Greulich K., Belser A., Bölke S., Grüninger P., Karstens R., Sättele M.S., Ovsyannikov R., Giangrisostomi E., Basova T.V., Klyamer D., Chassé T., Peisert H., Charge Transfer from Organic Molecules to Molybdenum Disulfide: Influence of the Fluorination of Iron Phthalocyanine. *Journal of Physical Chemistry C* **2020**, *124*, 16990-16999.

Greulich K., Trautmann M., Belser A., Bölke S., Karstens R., Nagel P., Merz M., Schuppler S., Chassé A., Chassé T., Peisert H., Influence of the Fluorination of Iron Phthalocyanine on the Electronic Structure of the Central Metal Atom. *Journal of Physical Chemistry C* **2021**, *125*, 6851-6861

Einleitung

Wir leben in einem Zeitalter, welches von der Halbleitertechnologie geprägt und getrieben wird. Immer mehr Transistoren sollen auf immer weniger Raum Platz finden, um Halbleiterchips für die Elektronikindustrie leistungsfähiger, kleiner sowie kosten- und energieeffizienter zu machen. Nur so ist es möglich Projekte wie die künstliche Intelligenz, autonomes Fahren oder auch 5G-Technologie voranzutreiben. Triebkraft für diese Entwicklung ist das bekannte „Moore’sche Gesetz“, welches viel mehr als Prophezeiung denn als Gesetz gesehen werden kann. Gordon Moore, Mitbegründer von Intel, formulierte im Jahr 1965, dass sich die Dichte elektronischer Schaltkreise innerhalb eines Jahres immer weiter verdoppelt.¹ Im Jahr 1975 korrigierte Gordon Moore seine Aussage auf eine Verdoppelung alle zwei Jahre.

Die Halbleitertechnologie basiert auf einer Entdeckung der Wissenschaftler Bardeen, Brattain und Shockley, die im Jahr 1947 den regelbaren Widerstand anhand eines Germanium-Einkristalls und somit den Transistor entdeckten.² Seit es Jack Kilby gelang einen Transistor auf Basis von Silizium, dem zweithäufigsten Element auf unserer Erde, herzustellen,³ ist Silizium das Standardmaterial für die heutigen Hochleistungsbauelemente. Durch gezielte Dotierung und daher eingehend die gezielte Einstellung der elektronischen Eigenschaften kann die Siliziumhalbleitertechnologie in verschiedenen Bereichen wie Sensorik, Photovoltaik, Computertechnik und Unterhaltungs- sowie Kommunikationselektronik eingesetzt werden. Obwohl die auf Silizium basierende Halbleitertechnologie in unserem Leben eine wichtige Rolle spielt, gibt es auch einige Schwachstellen, weshalb alternative Halbleitertechnologien erforscht und zur Serienreife gebracht werden. So ist die Gewinnung von Silizium energetisch sehr aufwendig und somit ineffizient. Das Silizium für die hochwertigen Wafer wird durch Reduktion von Quarzsand gewonnen, ein Verfahren, welches nur unter hohem energetischem Aufwand durchgeführt werden kann. Zudem muss das Silizium für mikroelektronische Anwendungen hochrein sein, da Verunreinigungen den elektrischen Leitungsprozess stark beeinflussen. Dies bedeutet einen hohen Aufwand bei der Aufreinigung, was sich wiederum auch im Preis niederschlägt.

Neben Perowskit-Systemen⁴⁻⁸ wurde die Forschung vor allem im Bereich der organischen Halbleiter vorangetrieben, um eine Alternative zu Silizium basierter

Halbleitertechnologie zu bieten und diese nach und nach abzulösen. Organische Halbleiter bieten einige wichtige Vorteile gegenüber anorganischen Halbleitern: eine hohe thermische Stabilität, einfache und damit kostengünstige Produktion, geringes Gewicht, Flexibilität und damit die Möglichkeit sie via Druckverfahren auf biegsame Oberflächen aufzubringen. Hierfür können sowohl leitende Polymere als auch kleine leitende organische Moleküle eingesetzt werden, wodurch die gewünschten Eigenschaften durch gezielte Auswahl des Materials erzielt werden können.⁹⁻¹⁹

Eine interessante Stoffgruppe organischer Moleküle für die Anwendung in der Halbleitertechnologie stellen die Phthalocyanine dar. Bei den Phthalocyaninen handelt es sich um heterozyklische Kohlenwasserstoffe mit 42 π -Elektronen, wodurch sie laut der Hückel-Regel ($4n+2$) zu den Aromaten zählen. Mittlerweile konnten schon über 70 verschiedene Phthalocyanine mit unterschiedlichen Zentralatomen und Liganden synthetisiert werden.²⁰ Von großem Interesse in der Anwendung sind vor allem die Übergangsmetall-Phthalocyanine (TMPcs, engl. transition metal phthalocyanines) (**Abbildung 1**). Durch ihre hohe chemische und thermische Stabilität, sowie einfache und flexible Handhabung sind sie interessant für verschiedene Anwendungen wie Leuchtdioden, Solarzellen, organische Feldefekt-Transistoren und aufgrund ihrer magnetischen Eigenschaften auch für Spintronik.²¹⁻³⁶ Neben der organischen Elektronik werden Phthalocyanine aufgrund ihrer starken Färbung im sichtbaren Bereich auch als Farbstoffe verwendet.²² Eine aktuelle Forschung zeigt zudem, dass Phthalocyanine in der photodynamischen Therapie eingesetzt werden können.³⁷

Um diese Moleküle in Bauteilen als Halbleiter anwenden zu können, müssen sie mit Elektroden kontaktiert werden um Ladungszufuhr und -abfuhr zu ermöglichen. Die entscheidende Rolle spielt dabei die Grenzfläche zwischen den Molekülen und dem Elektrodenmaterial. Zu den möglichen Effekten, welche an der Grenzfläche auftreten können, zählen Ladungstransfer, chemische Reaktionen, Metallierung bzw. der Austausch des Zentralatoms oder auch Deformation.³⁸⁻⁴⁴ Neben diesen elektronischen Eigenschaften gilt es ebenfalls die Orientierung und Morphologie der Phthalocyanine zu beachten. Weitere Informationen über die Struktur der Phthalocyanine und die für das Verständnis der Grenzflächen-Wechselwirkung wichtige d-Orbitalanordnung der metallischen Zentralatome können in der Literatur eingesehen werden.⁴⁵⁻⁵⁸

Die elektronische Wechselwirkung zwischen den Molekülen und dem Substrat kann durch gezielt hergestellte Pufferschichten unterbunden bzw. manipuliert werden, je nachdem, welche Eigenschaften für die Anwendung benötigt werden. Dies kann beispielweise durch Sauerstoffterminierung, Moleküllagen oder 2D-Netzwerke wie Graphen und hexagonales Bornitrid geschehen.⁵⁹⁻⁶⁴

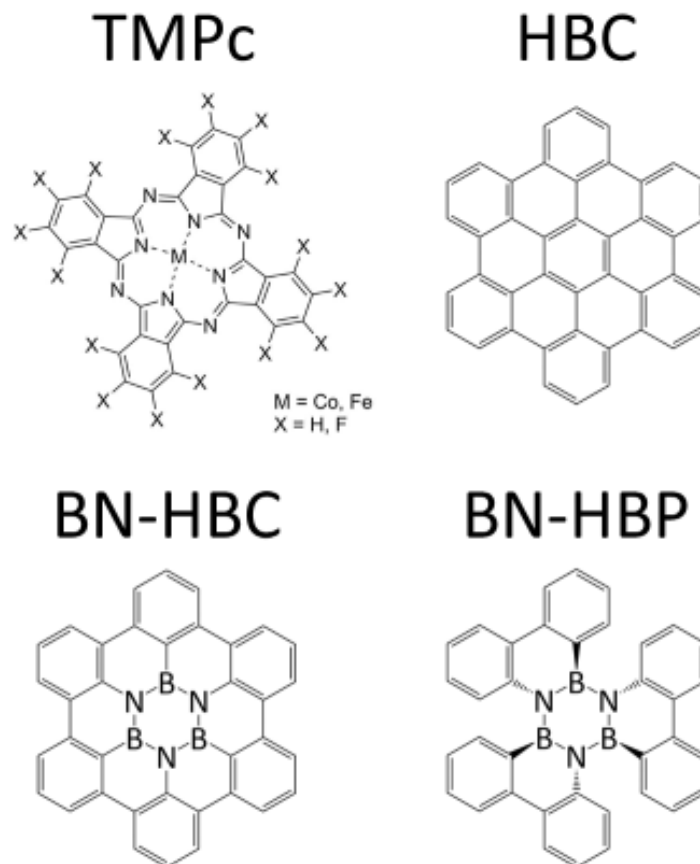


Abbildung 1. Molekülstruktur der TMPCs, des HBCs, des BN-HBCs und des BN-HBPs. Das M im Zentrum des TMPC steht für das zentrale Metallatom, hier Cobalt (Co) und Eisen (Fe). Das X außenherum steht für die Liganden Fluor (F) und Wasserstoff (H). Die in dieser Arbeit verwendeten TMPCs bestehen aus Kombinationen dieser Elemente.

Neben der Stoffgruppe der Phthalocyanine sind in den letzten Jahren auch sogenannte nanographenartige Moleküle in das Blickfeld der anwendungsbezogenen Forschung gelangt.⁶⁵⁻⁶⁹ Das wohl bekannteste nanographenartige Molekül ist der planare und als „Superbenzol“ bezeichnete polyzyklische aromatische Kohlenwasserstoff (PAH, engl. polycyclic aromatic hydrocarbon) Hexa-*peri*-hexabenzocoronene (HBC) (**Abbildung 1**).⁶⁸ Mit Blick auf den Einsatz in Solarzellen und Feldefekttransistoren wurden mit HBC schon vielversprechende Ergebnisse erzielt.^{67, 70-72} Durch das Ersetzen von C-C durch isosterische und isoelektronische B-N Ein-

heiten in den Nanographen-Molekülen können intrinsische elektronische Eigenschaften gezielt verändert werden, wodurch sich neue Einsatzmöglichkeiten ergeben.⁷³⁻⁷⁹ Ein sehr aufwendig herzustellendes BN-Nanographenmolekül stellt das planare B₃N₃-Hexa-*peri*-hexabenzocoronen (BN-HBC) dar (**Abbildung 1**). Im Vergleich zu HBC wurde der innere Benzolring durch einen Borazinring gezielt ersetzt.⁸⁰ Durch die Substitution eines Benzolrings durch einen Borazinring kann die Bandlücke vergrößert werden,⁸¹⁻⁸² ohne die Größe des Moleküls zu verändern.⁸³ Dies führt dazu, dass beispielweise Benzol ein Aromat, Borazin jedoch ein Nichtaromat ist.⁸⁴ Graphen ist elektrisch leitend, h-BN jedoch ein Halbleiter mit großer Bandlücke⁸⁴ bzw. Isolator.⁸⁵ Kohlenstoffnanoröhren sind in Abhängigkeit ihrer Chiralität ebenfalls metallisch oder halbleitend, während BN-Nanoröhren immer halbleitend sind.⁸⁴ Die Erweiterung des HOMO-LUMO-Abstands ist von besonderem Interesse.⁸⁶⁻⁹⁰ Unter anderem deshalb sind Borazinmaterialien mittlerweile auch für elektronische Anwendungen von Bedeutung.^{86, 91-94}

Neben dem direkten Einsatz in elektronischen Bauteilen können PAHs außerdem als Ausgangsmaterial für die *bottom-up* Synthese von Graphen verwendet werden.⁹⁵⁻⁹⁸ Dieses hat mittlerweile in verschiedenen elektronischen Bauteilen Verwendung gefunden, so beispielweise in Energiespeicherelementen, Feldeffekt-Transistoren und Sensoren.⁹⁹⁻¹⁰¹ Gerade gezielt dotiertes Graphen, welches durch die Verknüpfung BN-dotierter Moleküle wie BN-HBC synthetisiert werden kann, erweitert die Einsatzmöglichkeiten des Graphens nochmals deutlich. In ersten Versuchen wurde schon gezeigt, dass es möglich ist BN-HBC Derivate oberflächenkatalysiert zu verknüpfen.¹⁰² Neben BN-HBC könnte auch die Vorstufe B₃N₃-Hexabenzotriphenylen (BN-HBP) (**Abbildung 1**) in Zukunft eine wichtige Rolle als Ausgangsmaterial für die *bottom-up* Synthese von BN-dotiertem Graphen einnehmen. BN-HBP zählt zu den nanographenartigen Molekülen mit nichtplanaren π -konjugierten Kohlenstoffsystemen. Diese Moleküle spielen ebenfalls eine wichtige Rolle für verschiedene Anwendungen. So zeigen beispielweise nichtplanare Porphyrine und andere Tetrapyrrole wichtige biochemische Funktionen und technologische sowie wissenschaftliche Anwendungen.^{40, 103-106} Neben BN-HBP ist auch das B₃N₃-Hexabenzotriphenylen-2H (BN-HBP-2H, nicht gezeigt), welches statt drei nur zwei gebrochene CC-Bindungen aufweist, für diese Anwendungen interessant. Durch die zwei gebrochenen CC-Bindungen ist dieses Molekül ein Hybrid aus BN-HBC und BN-HBP.

Für einen möglichen Einsatz der beschriebenen Moleküle in elektronischen Bauteilen ist es von großer Bedeutung über die elektronischen und wachstumsbezogenen *bulk*- und Grenzflächeneigenschaften Bescheid zu wissen. Dabei spielt die erste Lage an Molekülen (Monolage (ML)) eine entscheidende Rolle, denn sie bestimmt maßgeblich das Wachstum in den weiteren Lagen¹⁰⁷⁻¹⁰⁸ und vor allem können elektronische Eigenschaften an der Grenzfläche zu verschiedenen Metallen in diesem Schichtbereich festgestellt werden. Die Kenntnis über die Wechselwirkung an der Grenzfläche von Substraten und Molekülen spielt bei vielen technologischen Prozessen eine wichtige Rolle, beispielsweise bei der Herstellung von Katalysatoren, Halbleiterbauelementen und chemischen Sensoren. Bei diesen Prozessen wird die Wechselwirkung gezielt zur Kontrolle der Grenzflächen eingesetzt.¹⁰⁹ Grundsätzlich kann zwischen zwei Arten von Wechselwirkung unterschieden werden: Physi- und Chemisorption.

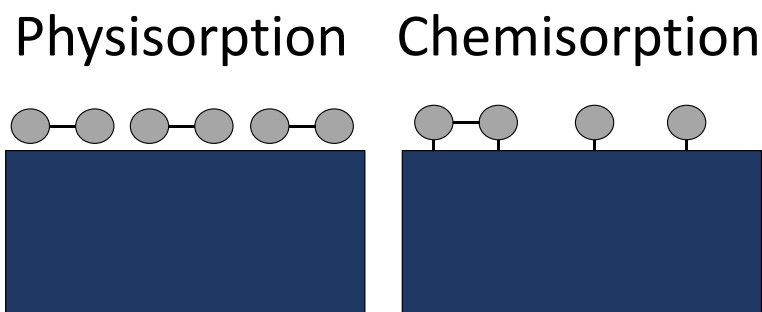


Abbildung 2. Exemplarische Darstellung der beiden Adsorptionsarten Physisorption (links) und Chemisorption (rechts). Zur Verdeutlichung des Unterschieds ist ein zweiatomiges Molekül dargestellt, welches bei der Physisorption keine feste Bindung ausbildet. Dahingegen entsteht bei der Chemisorption eine feste Bindung zum Substrat und durch die starke Wechselwirkung kann das Molekül sogar gespalten werden.

Die Physisorption (**Abbildung 2**) ist eine Art der Adsorption mit einer schwachen Wechselwirkung zwischen den Molekülen in der Gasphase und dem Substrat. Typischerweise entstehen nur schwache Bindungen mit einer Wechselwirkungsenergie von unter 50 kJ/mol.¹⁰⁹ Die Wechselwirkung beruht auf elektrostatischen Kräften zwischen induzierten und/ oder permanenten Dipolen, welche als van-der-Waals-Kräfte bezeichnet werden. Neben der Wechselwirkungsenergie ist die Reversibilität der Wechselwirkung ein entscheidendes Kriterium zur Einstufung der Art der Adsorption. So sind die Bindungen durch die schwache Wechselwirkung bei der Physisorption zumeist reversibel. Die Chemisorption (**Abbildung 2**) stellt

die zweite Adsorptionsweise dar. Bei diesem Prozess ist die Wechselwirkungsenergie größer als 50 kJ/mol und es entstehen chemische Bindungen in Form von ionischen als auch kovalenten Bindungen.¹⁰⁹ Die Wechselwirkung ist somit meist irreversibel oder nur durch extreme Bedingungen wie beispielweise hohe Temperaturen wieder rückgängig zu machen.¹¹⁰

Um das Wachstum und die elektronischen Eigenschaften der Moleküle zu untersuchen bieten sich verschiedene Analysemethoden an. Im Zuge dieser Arbeit wurden dafür hauptsächlich die Photoelektronenspektroskopie (PES), Rastertunnelmikroskopie (STM, engl. scanning tunneling microscopy) und bei Experimenten an den Elektronenspeicherringen Röntgenabsorptionsspektroskopie (XAS, engl. X-ray absorption spectroscopy) angewendet. Weiterhin wurden für zusätzliche Informationen auch Messungen mit der Oberflächenbeugungsmethode LEED (engl. low-energy electron diffraction) und Rasterkraftmikroskopie (AFM, engl. atomic force microscopy) durchgeführt.

Die PES ist eine oberflächensensitive Analysemethode, die in der Oberflächenphysik und -chemie sowie in der Materialforschung eine zentrale Rolle spielt. Sie beruht auf dem äußeren photoelektrischen Effekt, der von Heinrich Hertz und Wilhelm Hallwachs 1887 bzw. 1888 entdeckt¹¹¹⁻¹¹² und von Albert Einstein 1905 schlussendlich theoretisch beschrieben wurde.¹¹³ Er hat den äußeren photoelektrischen Effekt durch die Quantelung der elektromagnetischen Strahlung erklärt und 1921 dafür den Nobelpreis für Physik erhalten. Der Prozess der Photoemission kann nach Berglund und Spicer in die drei separaten Schritte Photoionisation der Probe, Transport des angeregten Elektrons an die Oberfläche und Durchtritt des Elektrons durch die Festkörperoberfläche unterteilt werden.¹¹⁴ PES wird verwendet, um Informationen über chemische und physikalische Eigenschaften der untersuchten Probe zu gewinnen. So kann beispielweise auf das Element, dessen Oxidationszustand und chemische Umgebung geschlossen werden. So können beispielweise Ladungstransfers an Grenzflächen analysiert werden. Zudem kann die gemessene Intensität mit den jeweiligen Empfindlichkeitsfaktoren verrechnet und so eine Aussage über die Probenzusammensetzung gemacht werden.

Eine weitere wichtige Eigenschaft von PES ist die Möglichkeit nominelle Schichtdicken d anhand von **Gleichung 1** zu berechnen:

$$d = \lambda_{IMFP} \cdot \cos(\theta) \cdot \ln \left(1 + \frac{I_D \cdot x_S \cdot \sigma_S \cdot \left(\frac{\rho}{M}\right)_S}{I_S \cdot x_D \cdot \sigma_D \cdot \left(\frac{\rho}{M}\right)_D} \right) \quad (1)$$

- x_D und x_S : Stöchiometrische Faktoren für Deckschicht und Substrat
- σ_D und σ_S : Empfindlichkeitsfaktoren der Rumpfniveaus von Deckschicht und Substrat
- ρ : Dichte
- M : Molare Masse
- I_D : Intensität des Deckschichtsignals
- I_S : Intensität des Substratsignals nach dem Aufdampfen
- λ_{IMFP} : inelastische mittlere freie Weglänge
- θ : Kippwinkel der Probe

Je nach Anregungsenergie wird zwischen Röntgenphotoelektronenspektroskopie (XPS) und Ultravioletter Photoelektronenspektroskopie (UPS) unterschieden. Mit Hilfe von XPS können Informationen über die Rumpfniveaus erhalten werden, mit UPS über das Valenzband (VB) (**Abbildung 3**). Weiterführende Informationen zur PES und (alternativer) Berechnung der Schichtdicke ist der Literatur zu entnehmen.^{109-110, 115-122}

Während mit PES Informationen über besetzte Zustände gewonnen werden, können durch XAS Informationen über unbesetzte Zustände erhalten werden. Sie liefert Informationen über die chemische Umgebung, die molekulare Orientierung und Bindungseigenschaften der jeweiligen im Molekül enthaltenen Elemente.¹²³ Für XAS ist eine durchstimmbare monochromatische Anregungsquelle, wie man sie am Synchrotron vorfindet, nötig, da die Anregungsenergie im Bereich der Ionisationsschwelle des jeweiligen Elements variiert werden muss. Eine Absorption findet statt, wenn sich die Anregungsenergie genau in Resonanz zu einem energetischen Übergang befindet (**Abbildung 3**). Dies wird im Spektrum als sogenannte Absorptionskante sichtbar. Üblicherweise erhalten die Absorptionskanten Bezeichnungen entsprechend der Schale der Rumpfniveaus, aus denen die absorbierten Elektronen stammen. So werden Absorptionskanten beispielweise als K-Kanten bezeichnet, wenn die absorbierten Elektronen aus einem s-Niveau stam-

men. Eine genaue Beschreibung des Absorptionsprozesses anhand Fermis Goldener Regel ist der Literatur zu entnehmen.¹¹⁴ XAS wurde in dieser Arbeit für die Aufklärung von grundsätzlich drei Punkten angewendet: elektronische Strukturaufklärung dünner Schichten, elektronische Struktur an der Grenzfläche zu Metallsubstraten und die Orientierung der Moleküle bei unterschiedlichen Schichtdicken.

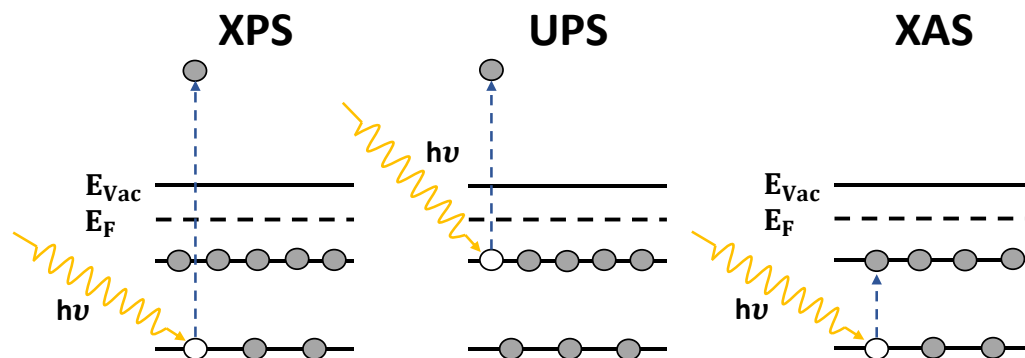


Abbildung 3. Schematische Darstellung des Photoionisationsprozesses aus einem Rumpfniveau (links) und aus dem Valenzband (mittig). Auf der rechten Seite ist der Röntgenabsorptionsprozess dargestellt. E_{vac} (Energie des Vakuumniveaus) steht für die Energie, die das Elektron erreichen muss, um ins Vakuum zu gelangen. E_F entspricht der Fermi-Energie.

Es gibt verschiedene Möglichkeiten die Absorptionsprozesse zu detektieren. In dieser Arbeit wurde meist der Probenstrom gemessen. Der Probenstrom entspricht dem Strom der nachfließenden Elektronen, die die Löcher füllen, die durch den Absorptionsprozess entstanden sind. Die Anzahl der Elektronen ist also proportional zu der Anzahl der Übergänge (engl. Total Electron Yield, TEY). Des Weiteren wurde zur Detektion auch der Auger Electron Yield (AEY) verwendet, wobei die während des molekularen Relaxationsprozesses emittierten Augerelektronen detektiert werden.¹²⁴ Somit ist der AEY oberflächensensitiver. Die mittlere freie Weglänge ist dabei abhängig von der kinetischen Energie der Elektronen.¹¹⁵ Weitere Informationen über XAS sind der vorgeschlagenen Literatur zu entnehmen.^{109, 123, 125}

Neben diesen spektroskopischen Methoden wurde auch STM verwendet, um die Orientierung und Wechselwirkung der Moleküle im Monolagenbereich zu untersuchen. Die Grundlage für STM ist der quantenmechanische Tunneleffekt. Die theoretischen Grundlagen wurden im Jahr 1929 von R. W. Gurney und E. U. Condon veröffentlicht.¹²⁶ Daraufhin vergingen 52 Jahre, bis G. Binnig und H. Rohrer 1981

das Rastertunnelmikroskop entwickelten,¹²⁷ wofür sie schon kurz darauf den Nobelpreis erhielten.¹²⁸

Eine scharfe, leitende Metallspitze, welche meist aus Platin und Iridium oder Wolfram besteht, wird mithilfe von Piezo-Stellelementen bis auf unter einen Nanometer an die zu untersuchende Probe herangefahren. Dann wird eine Spannung, entweder an die Spitze oder die Probe, angelegt und es fließt ein Tunnelstrom, welcher registriert wird. Voraussetzung dafür ist eine gute Leitfähigkeit der Spitze und der Probe. Sobald ein Tunnelstrom fließt, wird die Spitze rasterförmig über den zu messenden Bereich bewegt. Da der Abstand zwischen Probe und Spitze so gering ist, ist es wichtig eine möglichst glatte Probe zu vermessen, damit die Spitze nicht durch den Kontakt mit der Probe zerstört wird. Des Weiteren kann die Bildqualität durch eine ungeeignete Spitzenform (bspw. Mehrfachspitzen), thermische Störungen und Vibrationen stark beeinflusst werden. Weiterführende Literatur zur Methode STM, dem piezoelektrischen Effekt und Tunneleffekt ist der vorgeschlagenen Literatur zu entnehmen.¹²⁶⁻¹³⁸

Ergebnisse und Diskussion

1. Elektronische Eigenschaften und Orientierung von perfluoriertem FePc in dünnen Filmen

Um die Wechselwirkung an Grenzflächen zwischen organischen Molekülen und möglichen metallischen Elektrodenmaterialien zu verstehen ist es unerlässlich zuerst eine detaillierte Untersuchung der Moleküle in dünnen Filmen durchzuführen. So können die Spektren ohne den Einfluss der Grenzfläche auf elektronische Eigenschaften der Moleküle hin untersucht werden. Ein Hauptaugenmerk in dieser Arbeit liegt auf dem erst in jüngerer Vergangenheit in den Fokus gerückten perfluorierten FePc (FePcF_{16}). In den Publikationen [1], [2] und [6] wurden dünne Schichten dieses Moleküls auf den metallischen Oberflächen Au(111), Ag(111) und Cu(111) ausführlich mit XPS und XAS charakterisiert und die Rumpfniveaus mithilfe von detaillierten Peakfits analysiert. Aber auch auf Van-der-Waals Substraten (bspw. MoS_2)¹³⁹ und verschieden präparierten Oxidoberflächen (bspw. TiO_2)¹⁴⁰ wurden schon ausführliche Charakterisierungen durchgeführt.

Das Wachstum und die Orientierung der Moleküle sind für die intermolekularen Wechselwirkungen in den Filmen und somit für die elektronische Struktur der Filme von entscheidender Bedeutung. Eine Untersuchung der Orientierung von planaren π -konjugierten Molekülen kann mit winkelabhängigen XAS-Messungen und linear polarisiertem Licht durchgeführt werden.^{123, 125} Dabei werden die relativen Intensitäten der Anregungen von besetzten in unbesetzte Zustände (π^* oder σ^*) detektiert. Im Falle der TMPcs bietet sich hierfür die N-K Absorptionskante an.¹⁴¹ Absorptionsübergänge vom N1s in π^* -Orbitale sind dabei am intensivsten, wenn \vec{E} vertikal zur Molekülebene ist, während Absorptionsübergänge in σ^* -Orbitale für \vec{E} parallel zur Molekülebene maximal sind. Intensität unterhalb von 404 eV dominieren Absorptionsübergänge vom N1s in π^* -Orbitale, während oberhalb von 404 eV nur Absorptionsübergänge in σ^* -Orbitale detektiert werden.¹⁴¹⁻¹⁴³

In **Abbildung 4** werden die N-K XAS-Spektren dünner Filme auf den verschiedenen Metallsubstraten verglichen und eine Verknüpfung zu den zugehörigen C1s Spektren bei verschiedenen Anregungsenergien hergestellt. Vorab ist anzumerken, dass sich die Schichtdicken sehr stark unterscheiden und somit kein Vergleich der Substrate untereinander in Bezug auf die Eignung zur Herstellung flach liegender Schichten gemacht werden kann. Es ist bekannt, dass die Orientierung der

TMPcs in dünnen Filmen stark vom Substrat abhängt,^{140-141, 144-145} wobei sie auf in-situ präparierten Einkristallen und aufgedampften Metallschichten bevorzugt flach liegen.^{38, 144, 146-149}

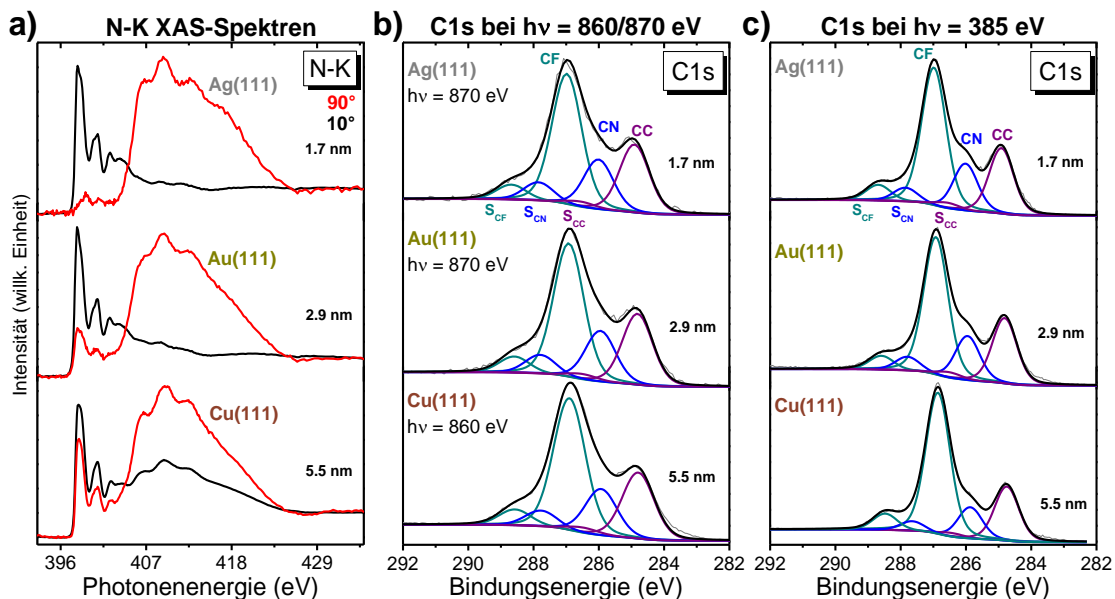


Abbildung 4. Zusammenhang zwischen N-K XAS-Spektren und C1s-Spektren bezüglich der Orientierung dünner Filme FePcF_{16} . a) N-K XAS-Spektren, b) C1s bei $h\nu = 860/870$ eV und c) C1s bei $h\nu = 385$ eV. V.o.n.u.: 1,7 nm auf Ag(111), 2,9 nm auf Au(111) und 5,5 nm auf Cu(111). Die Peakfitparameter der Spektren bei $h\nu = 860/870$ eV sind in **Tabelle A1** zusammengefasst. Die Peakfitparameter der Spektren bei $h\nu = 385$ eV können den zugrundeliegenden Publikationen [2] und [6] entnommen werden.

Auf allen drei Substraten ist die Intensität der π^* -Übergänge bei streifendem Einfall (10°) maximal, während die Intensität der σ^* -Übergänge bei senkrechtem Einfall (90°) des auftreffenden Lichts maximal ist (**Abbildung 4a**). Dies bedeutet, dass die Moleküle jeweils bevorzugt liegen. Jedoch fällt sofort auf, dass der Dichroismus unterschiedlich stark ausgeprägt ist. Am besten liegen die Moleküle der 1,7 nm Schicht auf Ag(111), dann der 2,9 nm Schicht auf Au(111) und am wenigsten in der 5,5 nm Schicht auf Cu(111). Derselbe Trend ist ebenfalls aus den zugehörigen C1s-Spektren zu entnehmen (**Abbildung 4b+c**). Im Molekül FePcF_{16} sind drei verschiedene Sorten von Kohlenstoffatomen mit unterschiedlicher chemischer Umgebung zu unterscheiden: CF, CN und CC im Verhältnis 4-2-2. Innerhalb der C-Atome eines Moleküls befinden sich die CF-Atome am weitesten außen, während sich die CN-Atome am weitesten innen befinden. Bei einer Anregungsenergie von 860 bzw 870 eV (**Abbildung 4b**) entsprechen die aus den Fits erhaltenen stöchiometrischen Verhältnisse sehr gut dem erwarteten Verhältnis von 4-2-2, allerdings sind leichte Abweichungen zu erkennen (**Tabelle 1**). Die geringste Varianz zeigt

die 1,7 nm Schicht auf Ag(111), während die 5,5 nm Schicht auf Cu(111) am stärksten abweicht. Bei einer Anregungsenergie von 385 eV wird die mittlere freie Weglänge der Elektronen aufgrund der geringen kinetischen Energie von etwa 100 eV um einiges geringer als bei 860 bzw 870 eV, wodurch oberflächensensitiver gemessen werden kann. Hier werden die Abweichungen der aus den Peakfits erhaltenen Stöchiometrien deutlich größer als bei der Anregungsenergie 860 bzw. 870 eV (**Abbildung 4c, Tabelle 1**). Die Abweichungen der Schichten auf Ag(111) und Au(111) sind noch gering, auf Cu(111) weicht der Anteil CF+S_{CF} mit 5,5 statt 4 und der Anteil des CN+S_{CN} mit 1,4 statt 2 aber schon deutlich von der erwarteten Stöchiometrie ab. Durch die höhere Oberflächensensitivität bei 385 eV kann darauf geschlossen werden, dass die Moleküle in den höheren Schichten anfangen aufzustehen, während sie in den tieferen Schichten noch flacher liegen. Anhand dieses Vergleichs zwischen N-K XAS-Spektren und C1s Rumpfniveaus kann die Komplementarität eindrucksvoll gezeigt werden. Zudem wird gezeigt, dass man durch geeignete Wahl der Anregungsenergie auch eine Art Tiefenprofil erstellen kann.

Tabelle 1. Stöchiometrische Verhältnisse der C1s-Peakfitkomponenten aus *Abbildung 4* in der Reihenfolge: CF+S_{CF} – CN+S_{CN} – CC+S_{CC}.

| hv (eV) | Ag(111) | Au(111) | Cu(111) |
|---------|-------------|-------------|-------------|
| 860/870 | 4,0-1,9-2,0 | 3,9-1,8-2,0 | 4,2-1,7-2,0 |
| 385 | 4,3-1,7-2,0 | 4,3-1,6-2,0 | 5,5-1,4-2,0 |

Die Rumpfniveaus der nichtmetallischen im Molekül vorkommenden Elemente Fluor (F), Stickstoff (N) und Kohlenstoff (C) der dünnen Filme zeigen auf den verschiedenen Metallsubstraten sehr ähnliche Bindungsenergien: 687,22 ± 0,08 eV (F1s), 398,82 ± 0,12 eV (N1s) und 284,83 ± 0,08 eV (C1s). Im selben Bereich liegen auch die Bindungsenergien der verschiedenen Rumpfniveaus auf dem Halbleiter MoS₂ und defektreichem TiO₂.¹³⁹⁻¹⁴⁰ Dies unterstreicht die Tatsache, dass das Substrat, wenn es eine genügend hohe Leitfähigkeit aufweist, ab einer gewissen Schichtdicke keinen Einfluss mehr auf die elektronische Struktur (der Rumpfniveaus) des Moleküls hat. Jedoch kann durch die Fluorierung des FePcs ein deutlicher Unterschied in den relativen Bindungsenergien von N1s und C1s Rumpfniveaus ausgemacht werden. Um dies zu verdeutlichen ist in **Abbildung 5** die Differenz der Bindungsenergie der N1s und C1s (anhand der CC-Komponente)

Rumpfniveaus und innerhalb des C1s (anhand der CN- und CC-Komponente) dünner Filme FePc und FePcF₁₆ auf verschiedenen Substraten dargestellt. Aus dieser Auftragung ist ein klarer Trend erkennbar: der relative Bindungsenergieabstand zwischen N1s und C1s ist für FePc durchschnittlich um 0,4 eV größer als für FePcF₁₆ (**Abbildung 5a**). Dahingegen ist der relative Bindungsenergieabstand zwischen der CN- und CC-Komponente nur um 0,16 eV größer (**Abbildung 5b**).

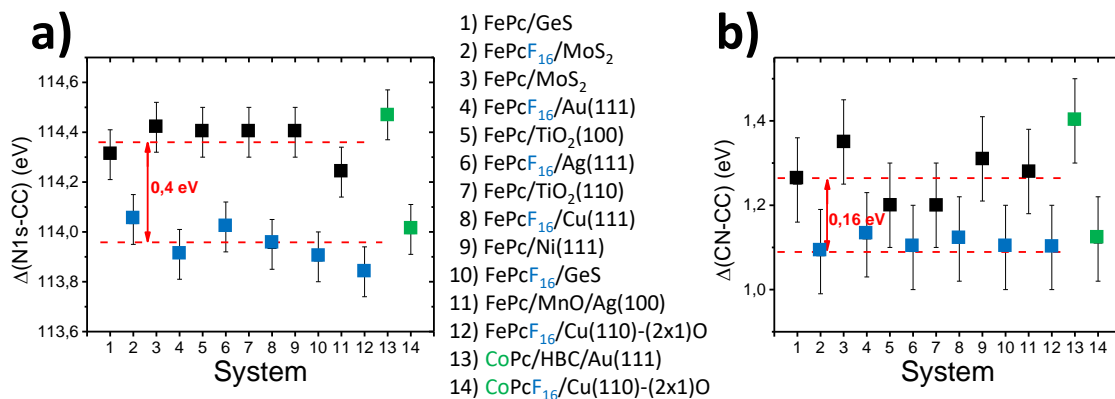


Abbildung 5. Vergleich der Bindungsenergieabstände des a) N1s und C1s (N1s-CC) und b) innerhalb des C1s (CN-CC) dünner Filme FePcF₁₆ (blau) und FePc (schwarz) auf verschiedenen Substraten. Die gestrichelte rote Linie stellt den jeweiligen Mittelwert der Bindungsenergieabstände der dünnen Schichten FePc und FePcF₁₆ dar. Zum Vergleich wurde je ein CoPcF₁₆ und CoPc Experiment hinzugefügt (grün). Als Fehler wurden $\pm 0,1$ eV angenommen. Die Daten stammen teilweise aus Experimenten, die von ehemaligen und aktuellen Kollegen des AK Chassé gemessen, jedoch teilweise nicht veröffentlicht wurden.^{139-140, 150-151}

Um zu überprüfen, ob neben der Fluorierung auch das zentrale Metallatom einen Einfluss auf diesen Abstand hat, wurde jeweils eine Schicht mit CoPcF₁₆ und CoPc hinzugefügt (grün). Die beiden Schichten folgen dem Trend des FePcF_x. Dieser Unterschied scheint also auf die Fluorierung zurückzuführen zu sein. Dies könnte mit dem starken elektronenziehenden induktiven Effekt der Fluoratome erklärt werden, der sich stärker auf die Atome auswirkt, die näher an den Fluoratomen positioniert sind (CC > CN > N). Folglich sorgt die Fluorierung für eine relative chemische Verschiebung und somit für eine Umverteilung der Ladungsdichte in den verschiedenen Kohlenstoffkomponenten und dem Stickstoff. Dieser Effekt beruht auf Untersuchungen Linus Paulings über die Eigenschaften chemischer Bindungen,¹⁵² woraus sich das Konzept der Elektronegativitäten entwickelte und wurde schon für verschiedene fluorierte organische Moleküle und Gruppen untersucht.¹⁵³⁻¹⁵⁸ Vor

allem im medizinischen und pharmazeutischen Bereich werden Fluorsubstituenten aufgrund ihrer Wirkung auf das Restmolekül, gezielt in der Entwicklung neuer Arzneimittel eingesetzt.^{155, 158}

Mit dem Wissen über die Orientierung der Moleküle kann eine ausführliche Analyse der elektronischen Eigenschaften der dünnen Schicht, wie in den erwähnten Publikationen gemacht, erfolgen. An dieser Stelle wird dabei auf die unterschiedlichen Fe-L₃ XAS-Spektren und Fe2p_{3/2} Rumpfniveaus der dünnen Schichten auf Ag(111) und Au(111) im Vergleich zu Cu(111) eingegangen. Eine Möglichkeit die in der Publikation [1] ausführlich diskutiert wird, ist eine Änderung des Spinzustandes des Fe-Atoms. Der Spinzustand von FePc wird in der Literatur kontrovers diskutiert.^{50-52, 55-57, 159-168} Mittlerweile wurde durch Kalkulationen gezeigt, dass der experimentell nachgewiesene Spinzustand von S=1 von FePc nur geringen Änderungen der Ligandenfeldparameter unterliegen muss, um einen anderen Spinzustand anzunehmen.^{163, 169-170} Der Spinzustand und somit die Form der XAS-Spektren hängt folglich stark von der Umgebung und somit der Anordnung der Moleküle in den Filmen ab. Durch eine genaue Untersuchung der Aufdampfparameter war festzustellen, dass sich die verschiedenen Spektren durch eine unterschiedliche Wahl der Aufdampfparameter erzeugen lassen (**Abbildung 6**). Zur Veranschaulichung wurden zwei Proben FePcF₁₆ auf Au(111) bei niedriger Temperatur (Probe 1) und hoher Temperatur (Probe 2) aufgedampft und mit XPS und XAS untersucht. Aus den N-K XAS-Spektren ist ersichtlich, dass die Moleküle in beiden Proben bevorzugt liegen (**Abbildung 6a**). Die Winkelabhängigkeit hängt mit dem Einfluss des linear polarisierten Lichts auf die Intensität für Absorptionsübergänge in verschiedene Orbitale zusammen.¹⁷¹ Dabei sind Übergänge in 3d-Orbitale des Fe-Atoms mit out-of-plane Komponenten (d_{xz}, d_{yz}, d_{z2}) bei streifend einfallendem Licht (10°) am intensivsten, während Übergänge in Orbitale mit in-plane Komponenten (d_{x2-y2}, d_{xy}) bei senkrecht einfallendem Licht am intensivsten sind. Eine genauere Diskussion über die spektrale Form des unfluorierten FePc ist in der Literatur nachzulesen.¹⁷¹ Die dominanten Strukturen bei streifend einfallendem Licht sind mit „A“ gekennzeichnet und repräsentieren out-of-plane Übergänge in a_{1g} und e_g Orbitale, während die mit „B“ gekennzeichneten Strukturen bei senkrechtem Einfall detektiert werden. Diese kommen von in-plane Übergängen, die von Anregungen in b_{1g} und b_{2g} Orbitalen dominiert werden, jedoch auch von Übergängen anderer Symmetrie beeinflusst werden.

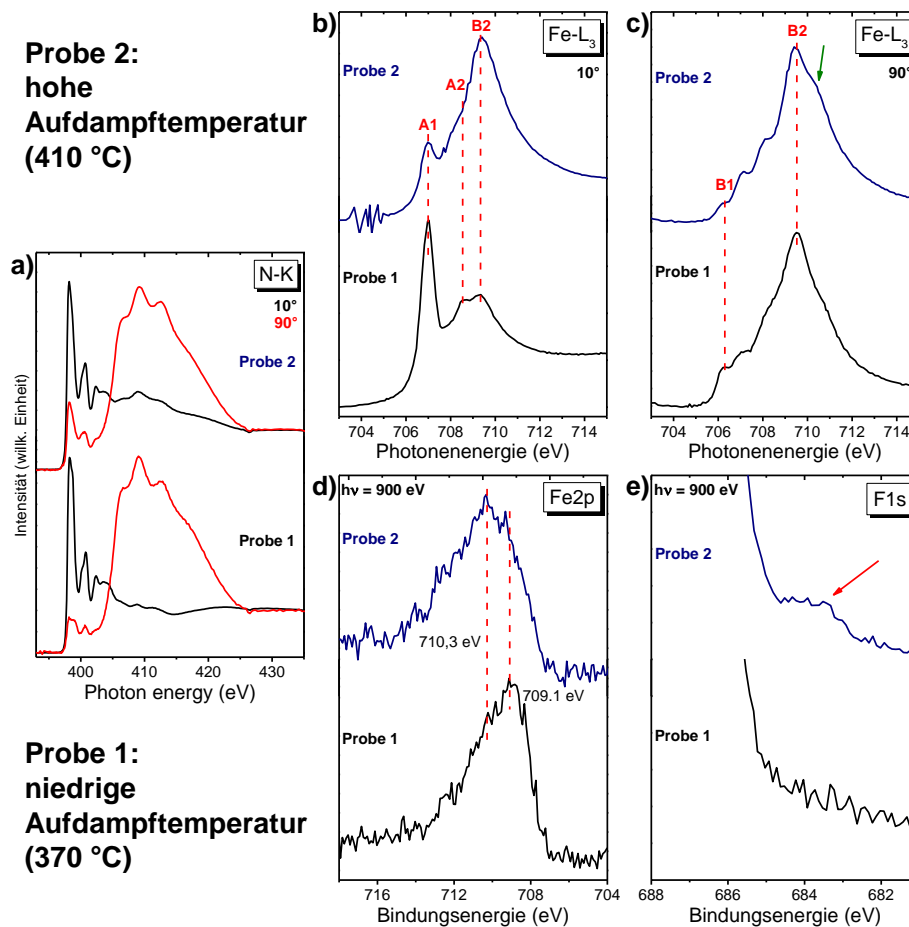


Abbildung 6. Vergleich zweier verschieden präparierter dünner Filme FePcF_{16} . Probe 1 wurde bei niedriger Temperatur aufgedampft (370 °C), während Probe 2 bei hoher Temperatur (410 °C) aufgedampft wurde. a) N-K XAS-Spektren bei 10 und 90°, b) Fe-L_3 XAS-Spektren bei 10°, c) Fe-L_3 XAS-Spektren bei 90°, d) $\text{Fe}2p$ Rumpfniveaus bei $h\nu = 900$ eV und e) Vergrößerung des Bereichs direkt vor dem F1s bei $h\nu = 900$ eV.

Die Fe-L_3 XAS-Spektren sehen deutlich verschieden aus, sowohl bei 10° als auch bei 90° des einfallenden Lichts (**Abbildung 6b+c**). Während Probe 1 die von FePc bekannten Strukturen aufweist und zu den in Publikation [6] diskutierten Spektren passt,^{139, 148, 164} sind bei Probe 2 andere relative Verhältnisse der Strukturen vorhanden (Publikation [1] und [2]). Die elektronische Besetzung der 3d-Orbitale der beiden Proben scheint sich deutlich zu unterscheiden. Am deutlichsten wird dies anhand der A1 Komponente, dem Absorptionsübergang bei niedrigster Photonenenergie. Die zu A1 gehörigen Orbitale sind im Falle von Probe 2 vor der Anregung schon deutlich mehr gefüllt als bei Probe 1, wodurch weniger Absorptionsübergänge stattfinden können und die Intensität dieser Komponente folglich geringer ist. Auffällig ist zudem die im 90°-Spektrum gekennzeichnete Schulter zu höheren

Photonenenergien (grüner Pfeil) (**Abbildung 6c**). Um weitere Hinweise zu erhalten wurden auch die zugehörigen Fe2p_{3/2} und F1s Spektren untersucht (**Abbildung 6d+e**). In den Fe2p_{3/2} Spektren sind auch deutliche Unterschiede erkennbar (**Abbildung 6d**). Neben dem markant breiteren Fe2p_{3/2} Signal von Probe 2, ist auch das Peakmaximum verschoben. Während es bei Probe 1 bei 709,1 eV ist, befindet es sich bei Probe 2 bei 710,3 eV. Der Unterschied von 1,2 eV entspricht in etwa einer Oxidationsstufe, weshalb vermutet werden kann, dass sich die Elektronenbesetzung der Orbitale des zentralen Fe-Atoms bei Probe 2 geändert hat. Die Lage und Form des Fe2p Signals von Probe 1 ist hingegen literaturbekannt und wurde für verschieden fluorierte FePcs diskutiert.^{139-140, 148, 172-173} Ein Blick auf den Bindungsenergiebereich direkt vor dem F1s Rumpfniveau zeigt zudem zusätzliche Intensität bei etwa 684 eV von Probe 2, während bei Probe 1 nichts zu erkennen ist (roter Pfeil, **Abbildung 6e**). Eine mögliche Erklärung ist eine neuformierte Metall-Fluor Bindung, wie auf TiO₂ diskutiert.¹⁴⁰

Zusammenfassend kann festgehalten werden, dass die diskutierten Unterschiede sowohl auf unterschiedliche Wechselwirkung innerhalb der dünnen Filme (siehe Publikation [1]), jedoch ebenfalls auf eine Änderung der Bindungsverhältnisse in den Molekülen beruhen können. So könnte ein Fluoratom zusätzlich an dem zentralen Eisenatom gebunden sein und so die Oxidationsstufe und damit verbunden die elektronische Struktur des Eisenatoms verändert haben.

2. Grenzflächeneigenschaften von perfluoriertem FePc

Nach der ausführlichen Charakterisierung der dünnen Filme FePcF₁₆ auf den verschiedenen Metallsubstraten ist es nun möglich die elektronischen Grenzflächeneigenschaften zu analysieren und diskutieren. Dabei kann das Molekül grob in zwei Teile aufgeteilt werden: der Makrozyklus, bestehend aus Fluor, Stickstoff und Kohlenstoff und das zentrale Eisenatom. Die Beteiligung des Fluors kann beispielsweise anhand einer ausführlichen Augerspektrenanalyse und der daraus resultierenden Berechnung von Augerparametern nachgewiesen werden (siehe Publikation [5]).

Berechnungen ergaben, dass das LUMO von Phthalocyaninen stark am Stickstoff lokalisiert ist,¹⁷⁴⁻¹⁷⁵ weshalb es naheliegend ist, dass die Stickstoffatome und die benachbarten Kohlenstoffatome (CN) bei stark wechselwirkenden Systemen auch

häufig beteiligt sind.^{38, 140, 148, 176} Dies konnte für FePcF₁₆ in den Publikationen [2] und [6] anhand der N-K XAS-Spektren gezeigt werden. In **Abbildung 7a** ist ein Vergleich der N-K XAS-Spektren an der Grenzfläche (1-2 ML) zu verschiedenen stark wechselwirkenden Substraten bei streifend einfallendem Licht (10°) gezeigt: GeS, Au(111), Ag(111) und Cu(111). GeS ist ein sehr schwach wechselwirkendes Substrat und dient für den Vergleich als Referenz für die stärker wechselwirkenden Metallsubstrate. Die N-K XAS-Spektren auf GeS und Au(111) weisen keine strukturellen Unterschiede zu Spektren dicker Schichten auf (Publikationen [2] und [6], Ref.¹³⁹), weshalb man ausschließen kann, dass die Stickstoffatome an der Grenzfläche mit dem Substrat wechselwirken. Folglich kann kein Hinweis auf eine Beteiligung der Stickstoffatome an der Wechselwirkung an der Grenzfläche festgestellt werden. Dahingegen sehen die Spektren an der Grenzfläche zu Ag(111) und Cu(111) deutlich anders aus. Die beiden Strukturen A und B bei 398,2 bzw. 400,7 eV sind deutlich schwächer ausgeprägt als auf GeS und Au(111). Die beteiligten Orbitale scheinen an der Grenzfläche schon partiell gefüllt zu sein, wodurch weniger Absorptionsübergänge möglich sind. Struktur A wird durch Absorptionsübergänge in das LUMO des Moleküls bestimmt, während Struktur B überwiegend durch Absorptionsübergänge in LUMO+n (n>0) Molekülorbitale zustande kommt.^{164, 177} Durch bislang unveröffentlichte XAS-Rechnungen des AK Chassé konnte gezeigt werden, dass Struktur A Absorptionsübergängen aus den verbrückenden Stickstoffatomen und Struktur B den Pyrrol-Stickstoffatomen zugeordnet werden kann. In früheren Arbeiten wurde zudem gezeigt, dass es eine Hybridisierung von Wellenfunktionen der p-Orbitale des Stickstoffs mit d-Orbitalen des zentralen Metallatoms gibt, was zu Struktur A führt.^{162, 164-165, 174, 176, 178-179} Die beteiligten Orbitale scheinen an der Grenzfläche schon partiell gefüllt zu sein, so dass weniger Absorptionsübergänge möglich sind. Dies deutet auf eine Beteiligung der Stickstoffatome an der Wechselwirkung an der Grenzfläche hin, wie beispielweise auch für FePc auf Ag(111) gezeigt wurde.¹⁴⁸

Die Beteiligung der Kohlenstoffatome an der Grenzflächenwechselwirkung wurde am deutlichsten anhand der CN-Kohlenstoffe in den Publikationen [2] und [6] nachgewiesen. Die Wechselwirkung kann anhand einer relativen Verschiebung der CN-Kohlenstoffe im Vergleich zu CC-Kohlenstoffen an der Grenzfläche im Vergleich zu dickeren Schichten verdeutlicht werden (**Abbildung 7b**).

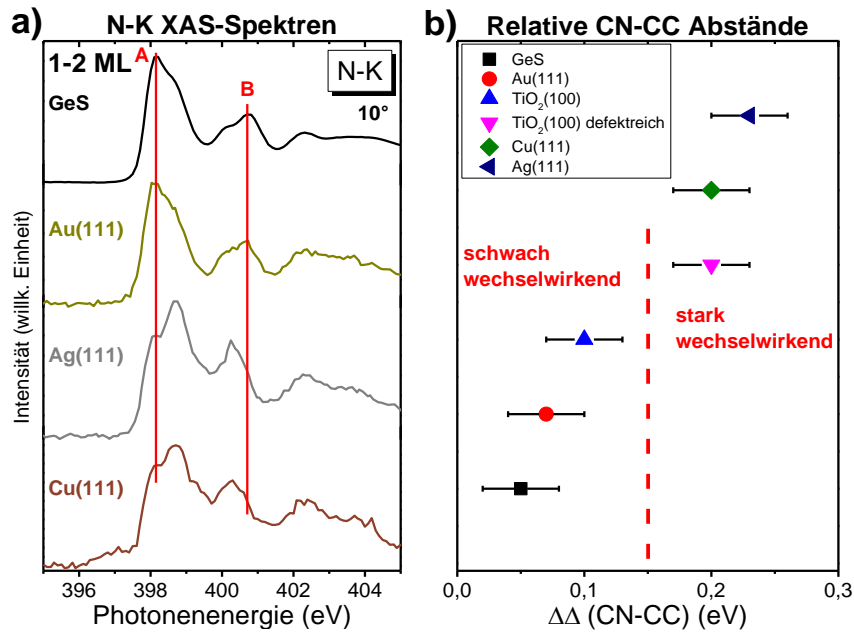


Abbildung 7. Grenzflächenwechselwirkung der Stickstoff- und CN-Atome von $FePcF_{16}$ auf verschiedenen Substraten im 1-2 ML Bereich: a) N-K XAS-Spektren und b) relative CN-CC Abstände im Vergleich dünner Film zu 1-2 ML mit Fehlerbalken (absolute Breite 0,06 eV). Der senkrechte gestrichelte Strich ist nur zur visuellen Abgrenzung der beiden Bereiche gedacht. Der absolute Energiewert ist irrelevant. Die Daten stammen teilweise aus Experimenten, die von aktuellen Kollegen des AK Chassé gemessen, jedoch teilweise nicht veröffentlicht wurden.¹⁴⁰

Auf stark wechselwirkenden Substraten (Ag(111), Cu(111) und defektreiches (TiO₂)) beträgt dieser Bindungsenergieunterschied in etwa 0,2 eV, während er auf schwächer wechselwirkenden Substraten (TiO₂, Au(111) und GeS) unter 0,1 eV beträgt. Hier kann also deutlich zwischen stärker und schwächer wechselwirkenden Substraten und deren Einfluss auf die Kohlenstoffatome unterschieden werden. Grundsätzlich kann diese Verschiebung durch eine elektronische Umverteilung an der Grenzfläche erklärt werden. Die Umverteilung findet für die verschiedenen Kohlenstoffe in unterschiedlichem Ausmaß statt. Neben den relativen Verschiebungen einzelner Komponenten ist auch eine absolute Verschiebung der Rumpfniveaus von den dünnen Filmen hin zur Grenzfläche zu beobachten. Dieser Effekt wird durch zusätzliche Endzustandsabschirmungseffekte des Photolochs hervorgerufen und beträgt meist 0,3-0,6 eV.¹⁸⁰⁻¹⁸³

Neben dem Makrozyklus kann auch das zentrale Metallatom mit dem Substrat wechselwirken (Publikationen [2] und [6]). Ein Vergleich der Fe2p und Fe-L₃ Spektren auf Au(111), Ag(111) und Cu(111) ist in **Abbildung 8** dargestellt. Die Fe2p

Spektren der 1-2 ML Schichten an den verschiedenen Grenzflächen (**Abbildung 8a**) sehen zum Teil deutlich anders aus als die Spektren der dicken Schichten (s. stellvertretend **Abbildung 6d**, Probe 1). In allen drei Spektren ist eine Komponente bei $707 \pm 0,1$ eV zu sehen, die von der Bindungsenergie her zu metallischem Eisen passt. Während diese Komponente die Spektren auf Ag(111) und Cu(111) dominiert, ist sie auf Au(111) schwächer ausgeprägt (rote Komponente).

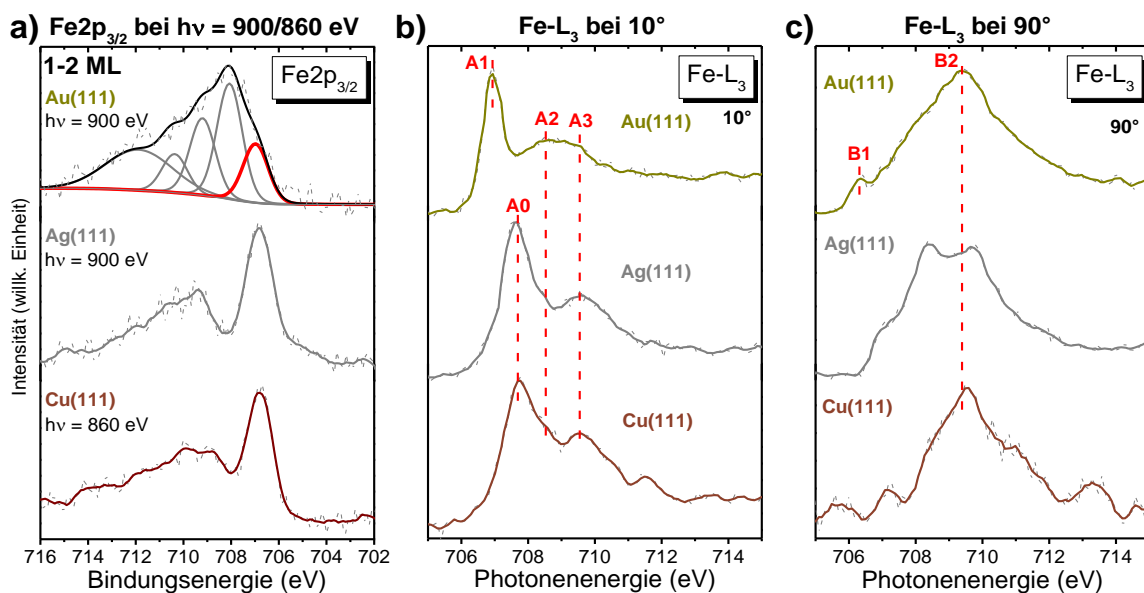


Abbildung 8. Identifizierung der Wechselwirkung des zentralen Fe-Atoms und dem jeweiligen Substrat im 1-2 ML Bereich: a) Fe_{2p_{3/2}}, b) Fe-L₃ (10°) und c) Fe-L₃ (90°).

Diese Komponente besitzt eine tiefere Bindungsenergie als die Hauptkomponente dünner Filme, weshalb es möglich ist, dass an der Grenzfläche eine Reduktion und somit ein Elektronentransfer vom Substrat zum Fe-Atom hin stattgefunden hat. Ein Ladungstransfer ist als Ausgangszustandseffekt zu verstehen. Alternativ könnte die Verschiebung zu niedrigerer Bindungsenergie auch von Endzustandseffekten des PES-Prozesses, wie Abschirmungseffekte durch einen Ladungstransfer, stammen.¹⁸⁴ Dies wurde für FePc auf Ag(111) und den darin zitierten Werken diskutiert.¹⁴⁸ Die schwache zusätzliche Grenzflächen-Komponente auf Au-Oberflächen war ebenfalls für das verwandte FePc feststellbar.¹⁸⁵⁻¹⁸⁶ Die nur teilweise stattfindende Wechselwirkung auf Au(111) kann durch unterschiedlich stark wechselwirkende Adsorptionsplätze erklärt werden.¹⁸⁷ Für den Peakfit des Fe2p Rumpfniveaus auf Au(111) wurde das Modell von Schmid et al.,¹⁸⁵ welches auf den Überlegungen Nefedovs beruht, angewendet.¹⁸⁸

Um weitere Informationen über die Wechselwirkung des zentralen Eisenatoms an der Grenzfläche zu erhalten, wurden mit XAS auch die unbesetzten Zustände untersucht. Um die elektronische Situation an der Grenzfläche richtig interpretieren zu können, ist es nötig die Orientierung der Moleküle auf der Oberfläche zu kennen. In allen drei Fällen (auf Au(111), Ag(111) und Cu(111)) liegen die Moleküle an der Grenzfläche flach auf dem jeweiligen Substrat (Publikationen [2] und [6]). Die Fe-L₃ XAS-Spektren beider Einfallwinkel des Lichts auf Au(111) im 1-2 ML Bereich (**Abbildung 8b+c**) ähneln den dünnen Filmen auf Ag(111) aus (Publikation [6]). Bei 10° einfallendem Licht dominiert die A1 Komponente das Spektrum deutlich, während B2 bei 90° dominant ist. Die weiteren Strukturen A2, A3 und B1 sind auch wie von dünnen Filmen bekannt ausgeprägt (Publikation [6] und Ref.¹³⁹). Es sind keine deutlichen Anzeichen für eine starke Wechselwirkung wie bspw. Ladungstransfer zu erkennen. Dahingegen unterscheiden sich die Spektren an der Grenzfläche zu Ag(111) und Cu(111) deutlich. Die Spektren bei 10° einfallendem Licht werden von der im Spektrum auf Au(111) nicht auftretenden A0 Komponente dominiert. Wie in den Publikationen [2] und [6] und verwandten Systemen diskutiert, kann diese Struktur durch eine Hybridisierung von Orbitalen des zentralen Metallatom und Orbitalen des Substrats als Folge einer Chemisorption von FePcF₁₆ auf der Substratoberfläche verstanden werden.³⁸ Bei 90° einfallendem Licht sind die Strukturen B1 und B2 auf Ag(111) deutlich schwächer als auf dem schwachwechselwirkenden Au(111) (**Abbildung 8c**) und zwei andere Strukturen bei 708,4 und 709,8 eV dominieren das Spektrum. Das schlechte Signal-Rausch-Verhältnis des 1-2 ML XAS-Spektrums bei 90° einfallendem Licht auf Cu(111) lässt keine detaillierte Analyse der Übergänge zu, jedoch sieht es auch in diesem Fall so aus, als wäre die B1 Komponente an der Grenzfläche stark abgeschwächt und auch die B2 Komponente bzw. der komplette Bereich zwischen 708 und 712 eV hat eine deutlich andere Form als auf Au(111). Das zentrale Eisenatom scheint an der Grenzfläche auf Ag(111) und Cu(111) eine deutlich andere elektronische Konfiguration zu besitzen als auf Au(111). Dies kann durch eine Umverteilung der Elektronen der 3d-Orbitale als Folge von Wechselwirkung an der Grenzfläche und/oder durch eine zusätzliche Besetzung von 3d-Orbitalen mit Elektronen als Folge eines Ladungstransfers verstanden werden. Folglich ist das zentrale Fe-Atom stark an der Wechselwirkung auf Ag(111) und Cu(111) beteiligt. Eine starke

Beteiligung des zentralen Metallatoms an der Wechselwirkung wurde auch für verwandte TMPc/Metallsubstrat Systeme festgestellt.^{38, 164, 189}

Zusammenfassend kann an dieser Stelle festgehalten werden, dass sowohl die besetzten als auch die unbesetzten Zustände eine enorme Rolle bei der Wechselwirkung von FePcF₁₆ auf den verschiedenen Substraten einnehmen. Während die Wechselwirkung auf Au(111) eher als schwach einzuordnen ist und hauptsächlich im Fe2p Spektrum sichtbar wird, ist die Wechselwirkung auf Ag(111) und Cu(111) sehr stark und kann sowohl im Fe2p_{3/2} als auch des Fe-L₃ XAS-Spektrums und für Ag(111) auch im VB (Publikation [6]) nachgewiesen werden.

3. Möglichkeiten zur Verhinderung der Grenzflächenwechselwirkung an der Grenzfläche von TMPcs und Metallen

3.1 Verhinderung der Wechselwirkung zwischen TMPcF₁₆ (M = Fe,Co) und Cu-Oberflächen durch O-Terminierung

Es gibt verschiedene Möglichkeiten zur Verhinderung der Wechselwirkung zwischen organischen Molekülen und Metallsubstraten. Kupferoberflächen gehören zu den reaktiveren Oberflächen auf denen häufig starke chemische Reaktionen beobachtet werden können.^{60, 190-196} Eine der vielen Möglichkeiten chemischen Reaktionen zu unterbinden ist die gezielte Bildung einer Lage Sauerstoff auf der Kupferoberfläche.^{60, 107} Ein bekanntes und gut untersuchtes Beispiel ist die Sauerstoffterminierung von Cu(110) wodurch eine Cu(110)-(2x1)O Oberfläche entsteht.¹⁹⁷⁻¹⁹⁹ In Publikation [5] wird diese Variante für die Moleküle FePcF₁₆ und CoPcF₁₆ ausführlich analysiert und diskutiert. In diesem Kapitel sollen die beiden Moleküle mit Blick auf die Verhinderung der Wechselwirkung an der Grenzfläche durch eine O-Terminierung der Cu(110) Oberfläche diskutiert werden. Um eine Aussage über die Verhinderung treffen zu können ist es notwendig die Moleküle auch auf der reinen Cu(110) Oberfläche zu untersuchen. FePcF₁₆ wurde ausführlich auf Cu(111) analysiert (s. Kapitel 1-2). Da Cu(110) im Vergleich zu Cu(111) aufgrund der verschieden dicht gepackten Atome eine höhere Reaktivität aufweist, ist eine Verhinderung der Wechselwirkung auf dieser Oberfläche noch eindrucksvoller.²⁰⁰ Deshalb wurde darauf verzichtet FePcF₁₆ noch zusätzlich auf Cu(110) zu untersuchen.

Zuerst wird diskutiert, inwiefern die Stickstoff- und Kohlenstoffatome und somit Atome des Makrozyklus an der Wechselwirkung an der Grenzfläche beteiligt sind

und ob es durch die O-Terminierung gelungen ist, die Wechselwirkung zu verhindern.

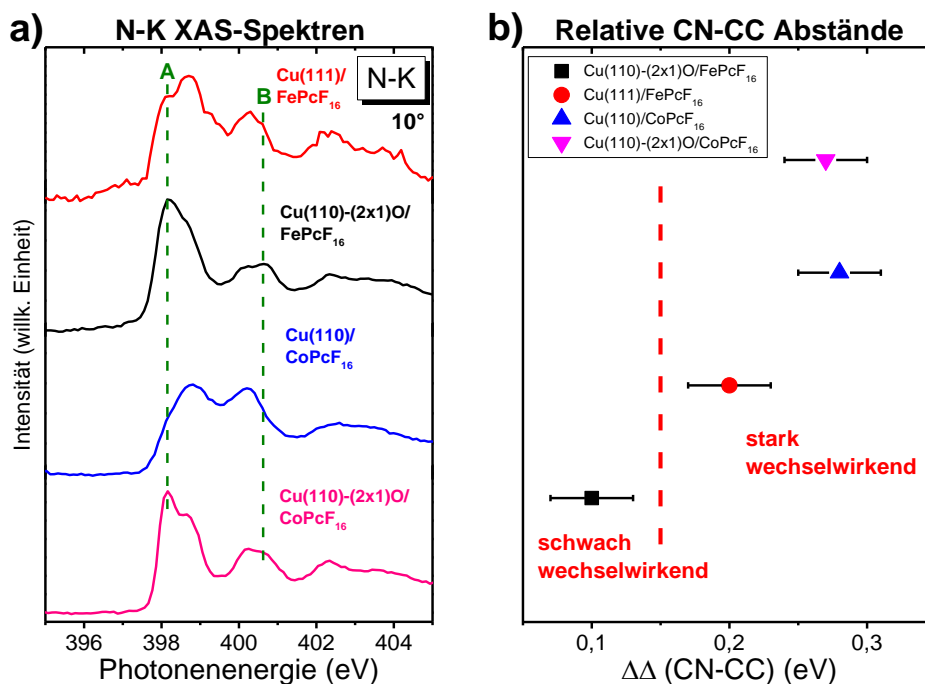


Abbildung 9. Grenzflächenwechselwirkung der N- und CN-Atome von TMPcF_{16} ($M = \text{Fe}, \text{Co}$) auf verschiedenen Substraten im 1-2 ML Bereich: a) N-K XAS-Spektren und b) relative CN-CC Abstände im Vergleich dünner Film zu 1-2 ML ($(\Delta\Delta(\text{CN-CC}) = \Delta(\text{CN-CC})(\text{dünner Film}) - \Delta(\text{CN-CC})(1-2 \text{ ML})) / (\Delta(\text{CN-CC})(1-2 \text{ ML}))$) mit Fehlerbalken (absolute Breite 0,06 eV). Eine Zusammenstellung der relativen CN-CC Abstände aus den **Abbildungen 7 und 9** ist im Anhang als **Abbildung A2** zu finden.

Wie in Kapitel 2 schon diskutiert, kann anhand des N-K XAS-Spektrums von FePcF₁₆ auf Cu(111) eine Beteiligung der Stickstoffatome an der Grenzflächenwechselwirkung nachgewiesen werden (**Abbildung 9a**). Für CoPcF₁₆ auf Cu(110) ist der Effekt noch stärker ausgeprägt als für das FePcF₁₆. Die Beteiligung der Kohlenstoffatome an der Grenzflächenwechselwirkung wurde am deutlichsten anhand der relativen Verschiebung der CN-Kohlenstoffe im Vergleich zu CC-Kohlenstoffen an der Grenzfläche im Vergleich zu dickeren Schichten gezeigt und in den Publikationen [2] und [5] auch ausführlich diskutiert. Auf den nichtterminierten Kupferoberflächen beträgt die relative CN-CC Verschiebung beider perfluorierter Phthalocyanine mindestens 0,2 eV (**Abbildung 9b**).

Betrachtet man die Auswirkung der O-Terminierung auf die Beteiligung der Stickstoff- und Kohlenstoffatome an der Wechselwirkung an der Grenzfläche so erkennt man deutlich Unterschiede zwischen den N-K XAS-Spektren beider TMPcF₁₆ auf

Cu(110)-(2x1)O und den Spektren der Systeme ohne O-Terminierung (**Abbildung 9a**). Die Strukturen A und B sind intensiver und die Spektren weisen insgesamt eine hohe Übereinstimmung mit N-K XAS-Spektren dünner Filme bzw. unreaktiver Oberflächen auf, wie in den vorherigen Kapiteln diskutiert und literaturbekannt.^{64, 139} Dagegen ist dies bei den Kohlenstoffatomen weniger eindeutig. Der relative CN-CC Abstand ist durch die O-Terminierung für FePcF₁₆ geringer geworden und befindet sich mit 0,1 eV im Bereich der schwach wechselwirkenden Systeme (**Abbildung 9b**). Für CoPcF₁₆ wird dieser Effekt jedoch nicht festgestellt. Der relative CN-CC Abstand befindet sich mit 0,27 eV weiterhin im Bereich stark wechselwirkender Systeme und ist nahezu identisch zu dem relativen CN-CC Abstand ohne O-Terminierung der Cu(110) Oberfläche. Für beide Fälle findet jedoch im Vergleich zur jeweiligen dicken Schicht eine Umverteilung der Elektronendichte innerhalb der verschiedenen Kohlenstoffatome statt.

Festzuhalten ist, dass sich die O-Terminierung unterschiedlich stark auf die Stickstoff- und Kohlenstoffatome beider Systeme auswirkt. Während die Stickstoffatome durch die O-Terminierung nicht mehr an der Grenzflächenwechselwirkung beteiligt zu sein scheinen, findet in den Kohlenstoffatomen für beide Fälle offenbar eine Umverteilung der Elektronendichte statt. Dieser Effekt ist bei CoPcF₁₆ jedoch deutlich stärker ausgeprägt als bei FePcF₁₆. Es wurde schon gezeigt, dass Phthalocyanine mit einem zentralen Cobaltatom stärkere Wechselwirkung an Grenzflächen aufweisen als mit einem zentralen Eisenatom.³⁸ Dies hat Auswirkungen auf den jeweiligen Makrozyklus.

Um die Auswirkungen der O-Terminierung auf die Grenzflächenwechselwirkung des zentralen Metallatoms zu untersuchen, wurden die Rumpfniveauspektren Fe2p_{3/2} bzw. Co2p_{3/2} gemessen und als Vergleich jeweils Spektren eines dünnen Films dargestellt (**Abbildung 10**). Für FePcF₁₆ ergibt sich ein eindeutiges Bild (**Abbildung 10a**). Das Fe2p_{3/2} Spektrum des dünnen Films sieht aus wie für dünne Filme aus der Literatur für FePc und FePcF₁₆ bekannt.^{139-140, 148} Verglichen mit dem dünnen Film, wird das Fe2p_{3/2} Spektrum der 1-2 ML FePcF₁₆ auf Cu(111) von einer Struktur bei deutlich niedrigerer Bindungsenergie, in etwa 707 eV, dominiert (Diskussion s. Kapitel 2). Dahingegen ist im Fe2p_{3/2} Spektrum der ~ML FePcF₁₆ auf der Sauerstoff terminierten Cu(110)-(2x1)O Oberfläche keine neue Struktur in diesem Bindungsenergiebereich erkennbar. Die spektrale Form sieht zudem sehr ähnlich zu dem Fe2p_{3/2} Spektrum des dünnen Films aus.

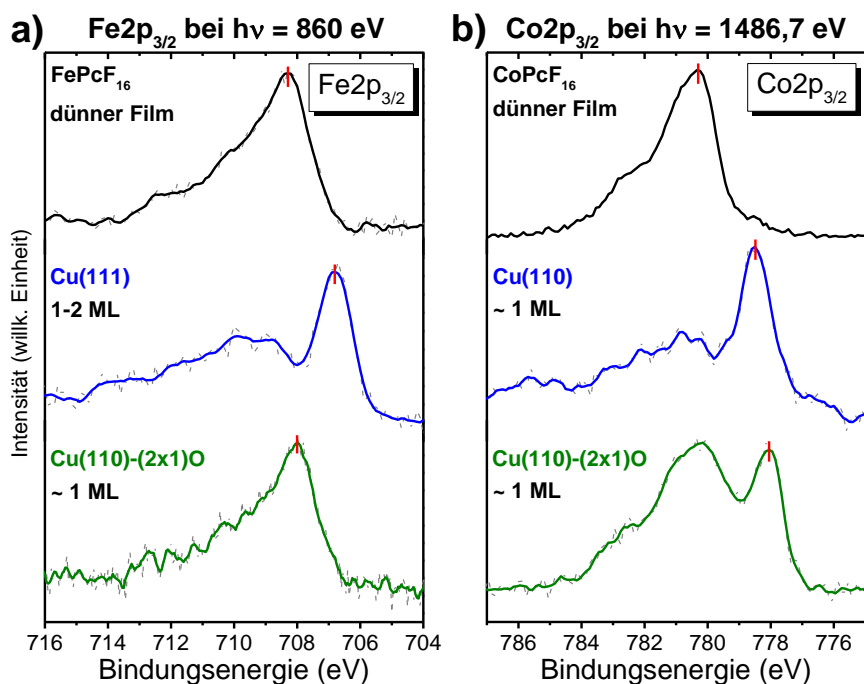


Abbildung 10. Verhinderung der Grenzflächenwechselwirkung der zentralen Metallatome von TMPcF_{16} ($M = \text{Fe}, \text{Co}$) auf $\text{Cu}(110)$ und $\text{Cu}(110)-(2 \times 1)\text{O}$ im Vergleich zu einem dünnen Film. a) $\text{Fe}2p_{3/2}$ Rumpfniveauspektren von FePcF_{16} und b) $\text{Co}2p_{3/2}$ Rumpfniveauspektren von CoPcF_{16} .

Für CoPcF_{16} stellt sich die Situation dahingegen anders dar (**Abbildung 10b**). Wie beim FePcF_{16} , sieht auch das $\text{Co}2p_{3/2}$ Spektrum des dünnen Films wie aus der Literatur für Cobaltphthalocyanine bekannt aus.^{166, 201-203} Das $\text{Co}2p_{3/2}$ Spektrum der ~ 1 ML auf $\text{Cu}(110)$ wird von einer Struktur bei 778,4 eV dominiert: einer typischen Bindungsenergie für reduziertes Cobalt, wie von verschiedenen CoPcF_x auf stark wechselwirkenden Metallsubstraten bekannt (alternative Erklärung s. Kapitel 2 anhand des Fe).^{201, 203-205} Die Intensität oberhalb von 780 eV kann dabei der komplexen Satellitenstruktur des Cobalts zugeschrieben werden.²⁰² Im Gegensatz zum FePcF_{16} ist die Reduktion des zentralen Metallatoms für CoPcF_{16} durch die O-Terminierung nicht komplett zu verhindern. Im $\text{Co}2p_{3/2}$ Spektrum ist bei vergleichbarer Schichtdicke bei 778,1 eV noch eine intensive Struktur erkennbar. Verglichen mit dem $\text{Co}2p_{3/2}$ Spektrum der ~ 1 ML auf $\text{Cu}(110)$ ist die Intensität oberhalb von 780 eV jedoch deutlich höher. Folglich ist neben dem reduzierten Cobalt auch noch Co^{2+} vorhanden, wie es bspw. auch für CoPcF_{16} auf Kupfer interkaliertem Graphen/ $\text{Ni}(111)$ gefunden wurde.⁶⁴ Es findet also nicht zu allen Molekülen der ersten ML auf $\text{Cu}(110)-(2 \times 1)\text{O}$ ein Ladungstransfer statt. Der Ladungstransfer könnte vom Adsorptionsplatz der Moleküle abhängen. Durch die O-Terminierung

verändert sich die Reaktivität der Kupferoberfläche und es gibt deutlich unterschiedliche Adsorptionsplätze für die Moleküle aufgrund der (2x1)-Rekonstruktion.²⁰⁶ Die Auswirkung unterschiedlicher Adsorptionsplätze auf die Stärke der Wechselwirkung zeigte sich schon in einer sehr detaillierten Studie von 4'-(4-tolyl)-2,2':6',2''-terpyridine auf Au(111).¹⁸⁷

Der Erfolg der O-Terminierung zur Verhinderung der Wechselwirkung vom Zentralatom der TMPcs an der Grenzfläche zu Kupferoberflächen hängt folglich stark von der Wahl des metallischen Zentralatoms ab. Während die Wechselwirkung von FePcF₁₆ durch die O-Terminierung größtenteils verhindert werden kann, gibt es für CoPcF₁₆ auch nach der O-Terminierung noch deutliche Hinweise auf einen Ladungstransfer. In Publikation [5] konnte der Unterschied zwischen diesen beiden Molekülen auch über die unbesetzten Zustände via XAS eindrucksvoll und ausführlich gezeigt werden. Aus den schichtdicken- und winkelabhängigen XAS-Messungen wird ersichtlich, dass sich die Besetzung der 3d-Orbitale an der Grenzfläche für FePcF₁₆ auf Cu(110)-(2x1)O nicht zum dünnen Film unterscheidet, währenddessen bei CoPcF₁₆ auf beiden Substraten (mit und ohne O-Terminierung) deutliche Unterschiede zum dünnen Film festzustellen sind. Da die O-Terminierung dazu führt, dass Cu-O Reihen auf dem Cu(110) Einkristall entstehen und diese dabei die halbe Kristalloberfläche besetzen (**Abbildung 10a**), könnte man darauf schließen, dass die Wechselwirkung des CoPcF₁₆ auf Cu(110)-(2x1)O mit Atomen dieser Cu-O Reihen stattfindet. Für andere organische Moleküle wie Hexacen wurde dahingegen dargelegt, dass die O-Terminierung eine nahezu komplette elektronische Entkopplung bewirkt.¹⁰⁷ Das deutlich andere Verhalten des CoPcF₁₆, verglichen zu anderen organischen Molekülen, könnte auf das halbgefüllte 3d_{z²}-Orbital, welches für flach liegende Moleküle in Richtung des Substrats orientiert ist, zurückzuführen sein. Sowohl experimentelle als auch theoretische Arbeiten haben gezeigt, dass der Ladungstransfer durch eine Hybridisierung des 3d_{z²}-Orbitals des Cobalts und Orbitalen des Metallsubstrats und einer daraus resultierenden Bindung entsteht.^{56, 203, 205, 207-208} Der komplexe Ladungstransfer zwischen Cu(110) bzw. Cu(110)-(2x1)O und CoPcF₁₆ konnte in Publikation [5] darüber hinaus auch mit VB-Messungen nachgewiesen werden. In Verbindung mit den in diesem Kapitel diskutierten Ergebnissen konnte sogar eine Prognose über die Herkunft der verschiedenen Grenzflächenzustände in der Bandlücke gemacht werden. So konnten die verschiedenen neuen Grenzflächenzustände teilweise

dem Makrozyklus zugeschrieben werden, da dieser auf Cu(110) deutlich stärker an der Wechselwirkung beteiligt ist als auf Cu(110)-(2x1)O.

Durch diese Ergebnisse kommt die Frage auf, ob der Ladungstransfer nur von den Substraten auf die Moleküle oder auch von den Molekülen auf die Substrate stattfindet. Um diese Frage zu beantworten wurden auch Augerparameter der Fluoratome berechnet und in Publikation [5] ausführlich diskutiert. Durch die Kombination aus XPS und Augerelektronenspektroskopie (XAES, engl. X-ray-excited Auger Electron Spectroscopy) können Ausgangs- und Endzustandseffekte unterschieden werden.²⁰⁹⁻²¹⁴ Aus den schichtdickenabhängigen Spektren des F1s und F KLL wurde der modifizierte Augerparameter und die dynamische Relaxationsenergie berechnet. Vergleicht man die dynamische Relaxationsenergie von 0,7 bzw. 0,4 eV für Cu(110) und Cu(110)-(2x1)O mit den Rumpfniveaushiftungen von dünnem Film verglichen zur ML, so sollten sich die Rumpfniveaus in etwa um den Betrag der dynamischen Relaxationsenergie verschieben. Jedoch konnte für die C1s und N1s Rumpfniveaus auf Cu(110)-(2x1)O nur eine Verschiebung um 0,2-0,3 eV und auf Cu(110) nahezu keine Verschiebung ermittelt werden (Publikation [5]). Daraus lässt sich schließen, dass es einen starken gegensätzlichen Effekt geben muss, der die Verschiebung zu niedrigerer Bindungsenergie an der Grenzfläche kompensiert: ein Ladungstransfer vom Makrozyklus zum Substrat an der direkten Grenzfläche. Diese Art von Analyse geht über viele Analysen zu Grenzflächenwechselwirkungen hinaus. Anhand dieser konnte eindrucksvoll gezeigt werden, dass alle verschiedenen Atomsorten des Moleküls an der Grenzflächenwechselwirkung beteiligt sind. Auf stark wechselwirkenden Substraten wie Ag(111) oder defektreichem TiO₂ wurde für FePcF₁₆ zudem eine neue Komponente an der Grenzfläche entdeckt, die auf einer Fluor-Metall Bindung basieren könnte (Publikation [6]+Ref. ¹⁴⁰). Dies wurde bereits beim Erhitzen von Perfluoro-Pentacen auf Cu(111) beobachtet und durch eine substratinduzierte Dekomposition erklärt.²¹⁵ Durch diese ausführliche Analyse und Kombination verschiedener Methoden konnte der komplexe wechselseitige Ladungstransfer durch Publikation [5] sehr ausführlich dargestellt werden.

3.2 Verhinderung der Wechselwirkung zwischen CoPc und Au(111) durch eine geordnete Monolage Hexabenzocoronen

Neben der O-Terminierung kann auch eine Monolage von Molekülen zur Verhinderung der Wechselwirkung an Grenzflächen eingesetzt werden.⁶¹ Als Pufferschicht stellt Graphen eine Alternative dar, jedoch sind extreme Präparationsbedingungen nötig um Graphen auf Au(111) herzustellen.²¹⁶⁻²¹⁷ Eine sanftere und einfachere Methode ist jedoch die Präparation einer gut orientierten ML HBC via Aufdampfen mehrerer Lagen und darauf folgendem Heizen bis nur noch eine ML über bleibt.²¹⁸⁻²²⁰ Publikation [8] beschreibt die Möglichkeit eine gut orientierte ML HBC als Pufferschicht zwischen das stark wechselwirkende System CoPc/Au(111) einzubringen. Dabei liegt der Fokus der Diskussion auf der Eigenschaft der ML HBC die Wechselwirkung des Systems CoPc/Au(111) zu unterbinden. Die gut orientierte ML HBC wird in Kapitel 5 in einem anderen Kontext genauer diskutiert. Analog zu den Orientierungsdiskussionen aus den vorherigen Kapiteln ist ersichtlich, dass die CoPc Moleküle sehr flach auf dem HBC/Au(111) Substrat liegen: nahezu keine Intensität von Absorptionsübergängen in π^* -Orbitale ist in den XAS-90°-Spektren zu erkennen und umgekehrt ebenfalls nur geringe Intensität von Absorptionsübergängen in σ^* -Orbitale in den 10° Spektren (**Abbildung 11a**).

Wie in Publikation [8] anhand von STM- und LEED-Messungen ausführlich gezeigt und diskutiert, agiert die HBC-Pufferschicht als Templat für das Wachstum der CoPc Moleküle. Zumindest in dünnen Schichten des CoPcs war eine hexagonale Anordnung festzustellen, wohingegen CoPc und andere TMPcs für gewöhnlich eine quadratische Adsorptionsgeometrie aufweisen.²²¹⁻²²⁷

Um die Frage zu klären, ob die HBC-Pufferschicht die Wechselwirkung zwischen CoPc und Au(111) verhindern kann, werden die XAS-Spektren der N-K Absorptionsskante bei 10° und Co-L₃ Absorptionsskante bei 10° und 90° im Vergleich von dünnem Film zur Grenzfläche (1-2 ML) näher betrachtet (**Abbildung 11b-d**). Um die Auswirkungen der HBC-Pufferschicht zu verstehen, ist es unerlässlich zu wissen, dass CoPc auf Goldoberflächen eine sehr starke Wechselwirkung zeigt.^{164,}

186, 201, 203, 227-232

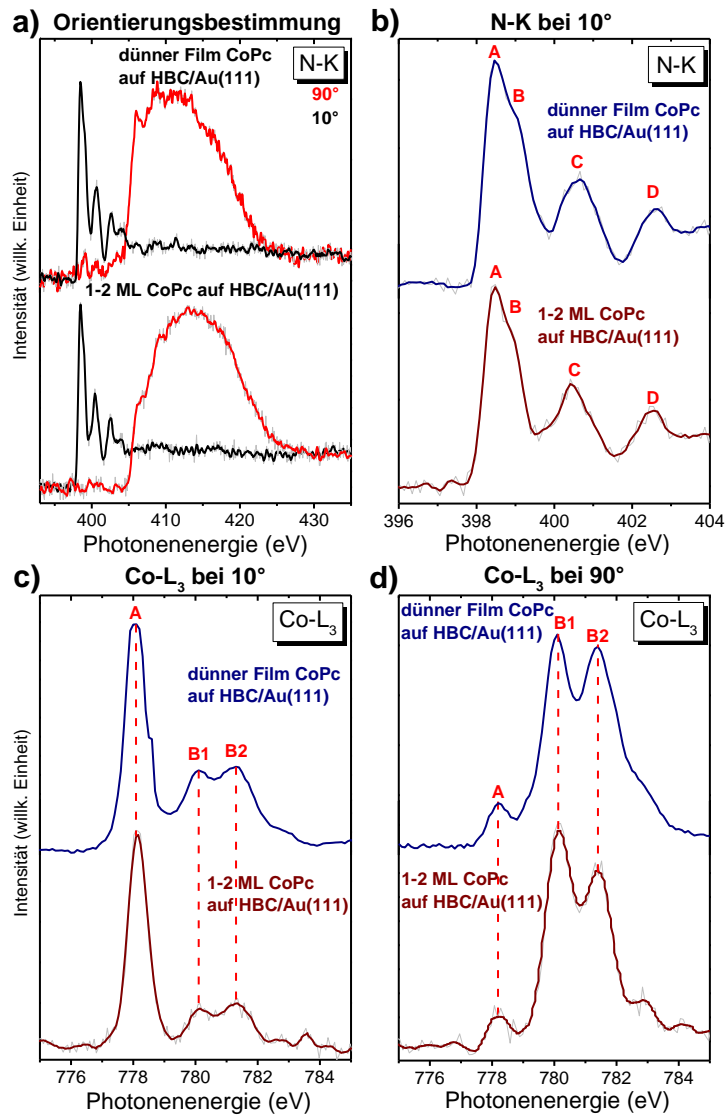


Abbildung 11. N-K und Co-L₃ XAS-Spektren von CoPc auf HBC/Au(111). a) Schichtdicken- und winkelabhängige N-K XAS-Spektren, b) Schichtdickenabhängige N-K XAS-Spektren bei 10° einfallendem Licht, c) Schichtdickenabhängige Co-L₃ XAS-Spektren bei 10° einfallendem Licht und d) Schichtdickenabhängige Co-L₃ XAS-Spektren bei 90° einfallendem Licht.

Die N-K und Co-L₃ XAS-Spektren des dünnen Films weisen alle Strukturen (A-D bzw. A, B1 und B2) auf, wie sie in der Literatur für dünne Filme CoPc beschrieben werden.^{38, 142, 164, 232-233}

Die Form der Co-L₃ Spektren zeigt eine komplexe Multiplettstruktur, welche aufgrund von 16 möglichen Übergängen des Absorptionsprozesses $2p^63d^7 \rightarrow 2p^53d^8$ entsteht. Beide Absorptionskanten der 1-2 ML CoPc auf HBC/Au(111) weisen alle aus dem dünnen Film bekannten Strukturen auf, es sind nur geringfügige Änderungen der spektralen Form erkennbar (**Abbildung 11b-d**). Dies zeigt, dass ein

Ladungstransfer an der Grenzfläche ausgeschlossen werden kann, wie für das ähnliche System CoPc auf goldinterkaliertem Graphen/Ni(111).²³⁴

Durch die HBC-Pufferschicht ist es folglich gelungen die starke Wechselwirkung zwischen CoPc und Au(111) nahezu komplett zu verhindern. Um diesen Effekt zu verdeutlichen, wurden ebenfalls XPS- und UPS-Messungen durchgeführt, durch diese ebenso gezeigt werden konnte, dass die Wechselwirkung zwischen CoPc und Au(111) nahezu komplett verhindert wird (Publikation [8]).

4. Molekularer Austausch von Hexabenzocoronen und CoPc an der Grenzfläche zu Au(111)

Um die Stabilität der HBC-Pufferschicht zu untersuchen, wurde die Probe mit einem dünnen Film CoPc auf HBC/Au(111) bei verschiedenen Temperaturen geheizt. Die gewählte Temperatur muss hoch genug gewählt werden, um eine Desorption der oberen Lagen CoPc zu bewirken. In diesem Fall wurde die Probe auf 630 K geheizt. Bei tieferen Temperaturen sind nicht genug CoPc Schichten desorbiert, um die Grenzfläche gezielt untersuchen zu können. Es gibt viele Beispiele von Bischichtsystemen zweier π -konjugierter organischer Moleküle, bei denen schon bei tieferen Temperaturen eine Diffusion der oberen Moleküle an die Metalloberfläche stattfindet.²³⁵⁻²³⁹ Ob die Diffusion an die Grenzfläche stattfindet, hängt hauptsächlich von der Wechselwirkungsstärke der beiden Moleküle mit dem Substrat ab. Die Wechselwirkung ist sehr komplex und resultiert aus mehreren konkurrierenden Prozessen wie Ladungstransfer, Van-der-Waals Wechselwirkung und Abstoßungseffekte (Pauli). Verschiedene Szenarien wurden in detaillierten Untersuchungen diskutiert und dargelegt.^{38, 139, 240-247} Diffusion kann hauptsächlich stattfinden, wenn die Molekül-Substrat Wechselwirkung der oberen Moleküle deutlich stärker ist als die der unteren Moleküle.^{235-238, 248} Dies kann sogar schon nahe dem absoluten Nullpunkt bei 1,1 K, wie anhand des Beispiels PTCDa/CuPc/Ag(111) eindrucksvoll gezeigt, vorkommen.²³⁸ Ob eine solche Diffusion stattfindet ist eine fundamentale Frage, die schon anhand vieler verschiedener Bischichtsysteme adressiert wurde.^{219, 237-238, 248-252} Pufferschichten zwischen dem aktiven Material und dem Metallkontakt sind ein effizienter Weg um die Grenzflächen-Energetik zu verändern und Energiebarrieren für Ladungstransfers durch eine Reduktion der Austrittsarbeit zu überwinden.²⁵³⁻²⁵⁴ Eine Diffusion der oberen

Moleküle zum Metallkontakt würde die gewünschten Eigenschaften der Grenzfläche verändern und die Pufferschicht wäre obsolet.

Die auf 630 K geheizte Probe wurde mit VB- und XAS-Messungen untersucht (Publikation [8]). Dabei wurden eindeutige Hinweise auf eine Diffusion von CoPc an die Grenzfläche gefunden. In den VB-Spektren erscheinen nach dem Heizen neue Zustände im Bereich der Bandlücke, wie es für CoPc auf Goldoberflächen bekannt ist.^{164, 166, 168, 203, 230, 255} Dies deutet auf eine starke Wechselwirkung der CoPc Moleküle mit dem Substrat hin. Es kann jedoch nicht ausgeschlossen werden, dass die HBC Moleküle auch an dieser Wechselwirkung beteiligt sind.

Durch XAS-Messungen finden sich weitere Hinweise auf eine Diffusion der CoPc Moleküle an die Au(111)-Oberfläche. Die winkelabhängigen Co-L₃ der geheizten Probe unterscheiden sich deutlich von den Spektren der ML CoPc auf HBC/Au(111). Ähnliche Veränderungen in den XAS-Spektren wurden auch für CoPc auf reaktiven Metallsubstraten ausgemacht^{38, 63, 164, 228, 232, 256} und deuten auf einen direkten Kontakt der CoPc Moleküle und der Au(111)-Oberfläche hin. Folglich verdichten sich die Hinweise, dass eine Diffusion der CoPc Moleküle durch die ML HBC stattgefunden hat. Eine ausführliche Diskussion der VB- sowie der zugehörigen XAS-Spektren kann in Publikation [8] nachgelesen werden.

Um einen eindeutigen Beweis für die Diffusion zu erhalten, wurden STM-Messungen der geheizten Probe durchgeführt (**Abbildung 12**). Auf der geheizten Probe können zwei verschiedene Strukturen im Verhältnis von ungefähr 3:2 ermittelt werden: die bekannte vierblättrige Struktur des CoPcs und die bekannte hexagonale Struktur des HBCs (**Abbildung 12a**). Die dunklen Bereiche zwischen den Molekülen kennzeichnen freie Bereiche. Folglich ist keine dicht gepackte Lage mehr vorhanden, wodurch die Moleküle mobiler sind und deshalb auch leicht verschwommen wahrgenommen werden. Die Moleküle einer Sorte (CoPc oder HBC) scheinen geballt aufzutreten, jedoch gibt es auch einzelne Moleküle zwischen den jeweils anderen Sorten. Häufig bilden bimolekulare Schichten geordnete Strukturen aufgrund von Molekül-Molekül Wechselwirkung, Dipol-Dipol Wechselwirkung oder Metallkoordinierung aus.^{240, 257-260} Dieses Verhalten kann für CoPc/HBC nicht festgestellt werden.

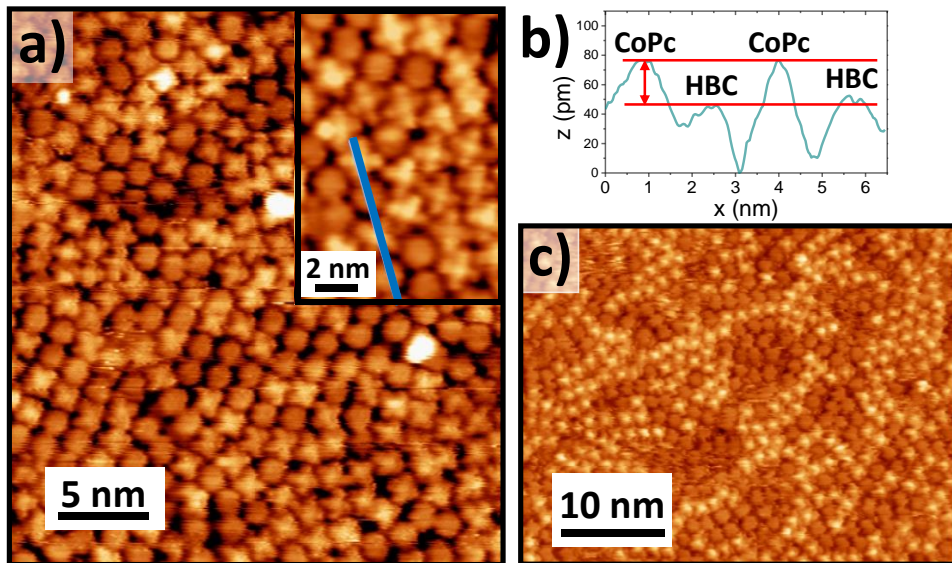


Abbildung 12. STM-Aufnahmen der geheizten CoPc/HBC auf Au(111) Probe bei Raumtemperatur. a) STM-Aufnahme mit $U = 1,5 \text{ V}$ und $I = 950 \text{ pA}$, der Einschub ist ein vergrößerter Bereich aus Aufnahme a ($U = 1,5 \text{ V}$, $I = 950 \text{ pA}$), b) Linienprofil aus dem Einschub aus Aufnahme a und c) STM-Aufnahme mit $U = 1,0 \text{ V}$ und $I = 800 \text{ pA}$. Eine positive Spannung bedeutet, dass Elektronen von der Spitze zur Probe fließen.

In dem Einschub in **Abbildung 12a** ist ein vergrößerter Bereich der Aufnahme dargestellt. Aus dem Linienprofil dieses Ausschnitts wird deutlich, dass die CoPc und HBC Moleküle in einer Ebene auftreten und einen Höhenunterschied von etwa 30 pm aufweisen (**Abbildung 12b**). Der Höhenunterschied lässt sich durch die scheinbare Höhe des zentralen Cobaltatoms aufgrund der Besetzung der d-Orbitale (der TMPcs allgemein) und der damit verbundenen hohen lokalen Elektronendichte erklären.²⁶¹⁻²⁶² Bei einem Vergleich der **Abbildung 12a** und **12c** ist zudem ein deutlicher Unterschied in der Helligkeit der CoPc Moleküle festzustellen. Dieser Effekt erklärt sich durch die starke Abhängigkeit des zentralen Cobaltatoms von der angelegten Spannung aufgrund der Besetzung der d-Orbitale.^{261, 263} So können die scheinbaren Höhen der Moleküle je nach angelegter Spannung variieren. Anhand dieser eingehenden Studie konnte durch Kombination verschiedener Messmethoden eindrucksvoll gezeigt werden, dass die HBC-Pufferschicht die Diffusion der CoPc-Moleküle an die Au(111)-Oberfläche bei einer Temperatur von 630 K nicht mehr verhindern kann und eine gemischte Monolage der beiden Moleküle entsteht.

5. Wachstum und Orientierung des nanographenartigen Moleküls Hexabenzocoronen und verwandter BN-Derivate

Für die geeignete Wahl als Pufferschicht, jedoch ebenso direkt als Material für mögliche elektronische Anwendungen und als Ausgangsmaterial für Graphen bzw. BN-dotiertes Graphen, kommen die nanographenartigen Moleküle HBC, BN-HBC, BN-HBP und B_3N_3 -Hexabenzotriphenylen-2H (BN-HBP-2H) in Frage (**Abbildung 13**). Dafür ist es unerlässlich, das Wachstumsverhalten und die elektronischen Eigenschaften dieser Moleküle in dünnen Filmen und an verschiedenen Grenzflächen ausführlich zu betrachten. In den Publikationen [3], [4] und [7] sind sehr detaillierte und umfangreiche Studien zur elektronischen Struktur und zum Wachstumsverhalten und Orientierung dieser Moleküle in dünnen Filmen und an der Grenzfläche dargelegt. Dabei liegt der Fokus auf den Unterschieden durch die BN-Dotierung und dem unterschiedlichen Grad der Planarität der BN-Moleküle.

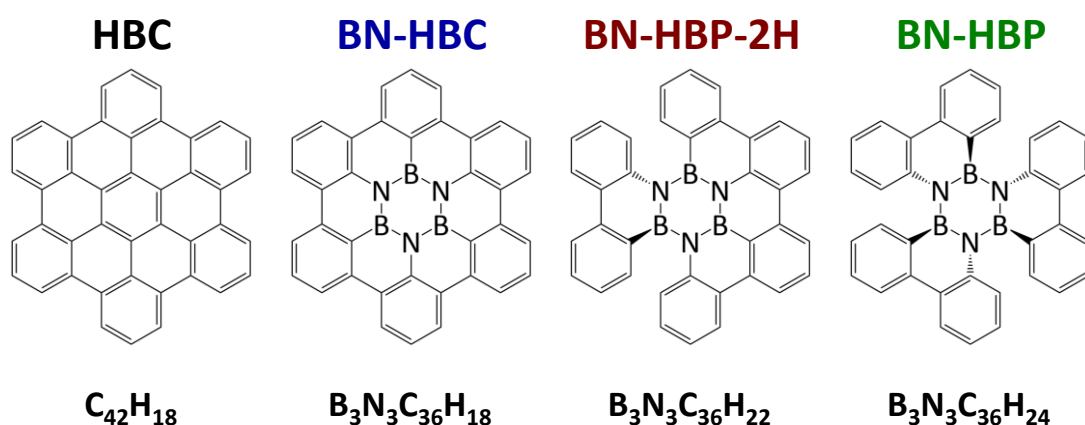


Abbildung 13. Darstellung der untersuchten nanographenartigen Moleküle (v.l.n.r.): HBC, BN-HBC, BN-HBP-2H und BN-HBP.

Für eine mögliche Anwendung ist die Adsorptionsgeometrie und Orientierung in dünnen Filmen relativ zur Substratoberfläche von entscheidender Bedeutung.²⁶⁴⁻²⁷⁰ Für das Wachstumsverhalten und die Orientierung der Moleküle in dünnen Schichten spielt die erste Lage an Molekülen eine entscheidende Rolle, da sie das Wachstum in den weiteren Lagen maßgeblich bestimmt.¹⁰⁷⁻¹⁰⁸

In **Abbildung 14** sind STM-Aufnahmen hochgeordneter Monolagen von HBC, BN-HBC und BN-HBP-2H auf Au(111) dargestellt. Die Monolagen wurden durch Aufdampfen von 2-3 Lagen und nachfolgendes Erhitzen auf 610 K hergestellt. Dieses Vorgehen stellt eine einfache Möglichkeit zur Herstellung exakt einer ML organischer Moleküle dar, da die erste Lage von organischen Molekülen auf Metallen bei

einer höheren Temperatur desorbiert als darauffolgende Lagen.²⁷¹⁻²⁷² Dies lässt sich darauf zurückzuführen, dass in vielen Fällen die Wechselwirkung zwischen Metalloberfläche und Molekül stärker ausgeprägt ist als diejenige zwischen den Molekülen. Leider war es nicht möglich bei Raumtemperatur von BN-HBP auf Au(111) STM-Bilder zu erhalten. Es ist anzunehmen, dass die Nichtplanarität und der damit verbundene geringere Kontakt zum Substrat der Grund hierfür ist. So ist die Molekül-Substrat Wechselwirkung geringer und die Moleküle sind mobiler.

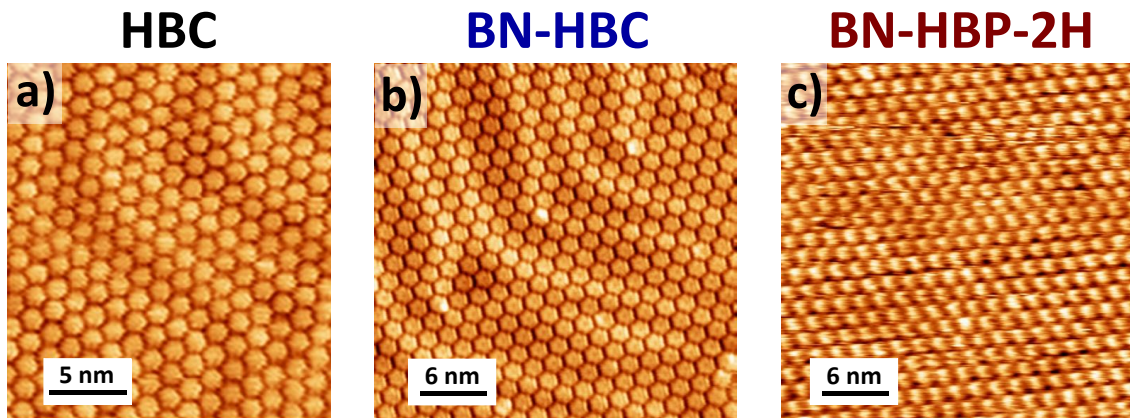


Abbildung 14. Raumtemperatur-STM-Aufnahmen der nanographenartigen Moleküle auf Au(111): a) HBC ($U = 1,1 \text{ V}$, $I = 700 \text{ pA}$), b) BN-HBC ($U = -1,3 \text{ V}$, $I = 630 \text{ pA}$) und c) BN-HBP-2H ($U = -1,3 \text{ V}$, $I = 350 \text{ pA}$).

Anhand der unter den Molekülen liegenden *herringbone* Rekonstruktion des Au(111) Substrats ist die Orientierung der Moleküle einfach bestimmbar. Die HBC Moleküle sind entlang der *herringbone* Rekonstruktion, folglich entlang der $[11\bar{2}]$ -Richtung orientiert (**Abbildung 14a**), während sich BN-HBC und BN-HBP-2H um 30° verdreht anordnen ($[\bar{1}10]$ -Richtung) (**Abbildung 14b+c**). Noch deutlicher wird dies durch die zugehörigen LEED-Aufnahmen (**Abbildung A3**). Für HBC und BN-HBC wurden jeweils auch Domänen, die um 30° verdreht angeordnet sind, gefunden. Die häufigere ist jedoch die jeweils in **Abbildung 14** gezeigte Domäne. Diese Beobachtung passt zur Literatur, in der auch von zwei um 30° verdrehten Domänen des HBCs berichtet wird.^{218-220, 273-274} Daraus lässt sich schließen, dass jeweils eine bestimmte Domäne energetisch bevorzugt wird, der energetische Unterschied jedoch nicht so groß ist, dass sich ausschließlich diese Domäne ausbildet. Die Bestimmung des Winkels zwischen den Gittervektoren $\Gamma = 60^\circ$ und der Gitterparameter $a_1 = a_2 = 1,45 \text{ nm}$ liefert übereinstimmende Ergebnisse mit STM als auch LEED für alle drei geordneten Monolagen. Das HBC orientiert sich also in

einer $(\sqrt{27} \times \sqrt{27})R30^\circ$ -Überstruktur, während BN-HBC und BN-HBP-2H eine (5×5) -Überstruktur bilden.

Für BN-HBC konnte dargelegt werden, dass die bevorzugte Adsorption an Stufenkanten und den Ellenbogen der *herringbone* stattfinden (Publikation [3]). An diesen Stellen ist die Molekül-Substrat Wechselwirkung am stärksten, wodurch die Moleküle dort gut aufgenommen werden können. Abseits dieser Stellen ist die Molekül-Substrat Wechselwirkung schlicht zu schwach, um die Moleküle an diesen Stellen zu fixieren. Die präferierte Adsorption an den Ellbogen der *herringbone* Struktur wurde für weitere organische Moleküle, u.a. aber auch BN-HBC, schon aufgezeigt.^{80, 275-278}

HBC wurde schon häufig bezüglich seiner Orientierung auf verschiedenen Substraten analysiert, wobei festgestellt wurde, dass das Substrat, sowohl im Monolagenbereich als auch in dünnen Filmen, enorme Auswirkungen auf die Orientierung der Moleküle hat,^{220, 279-280} wobei die HBC Moleküle auf gut präparierten Einkristallen flach liegen.^{219-220, 279-281} Deshalb wird an dieser Stelle nur ein Vergleich der drei BN-dotierten nanographenartigen Moleküle mit unterschiedlichem Planaritätsgrad diskutiert. Um die Auswirkung des unterschiedlichen Grades der Planarität auf das Wachstumsverhalten und die Orientierung der drei Moleküle zu untersuchen, wurden sehr ausführliche winkel- und schichtdickenabhängige XAS-Messungen aller drei Absorptionskanten (B-K, C-K und N-K) auf Au(111) durchgeführt (Publikation [4]) (**Abbildung 15**). Die XAS-Spektren wurden im Augerelektronen-Modus (AEY, engl. Auger electron yield) aufgenommen. Somit unterscheiden sich die mittleren freien Weglängen der Elektronen der drei vorhandenen Elemente mit 1,7, 1,4 und 1,1 für die N-K, C-K bzw. B-K Absorptionskante deutlich.¹¹⁵ So ist es möglich bei dickeren Schichten gezielt die Oberfläche des organischen Films zu analysieren.

Die XAS-Spektren aller drei Absorptionskanten des BN-HBCs zeigen einen schichtdickenunabhängigen Dichroismus (**Abbildung 15a+d+g**): bei streifendem Einfall des Lichts (20°) sind die Intensitäten der Übergänge in π^* -Orbitale maximal, während sie bei senkrechtem Einfall des Lichts (90°) nahezu verschwinden. Dies lässt auf eine flach liegende Orientierung schließen. Im ML-Bereich ist die Winkelabhängigkeit aller drei Absorptionskanten von BN-HBP-2H (**Abbildung 15b+e+h**) und BN-HBP (**Abbildung 15c+f+i**) ähnlich zu BN-HBC.

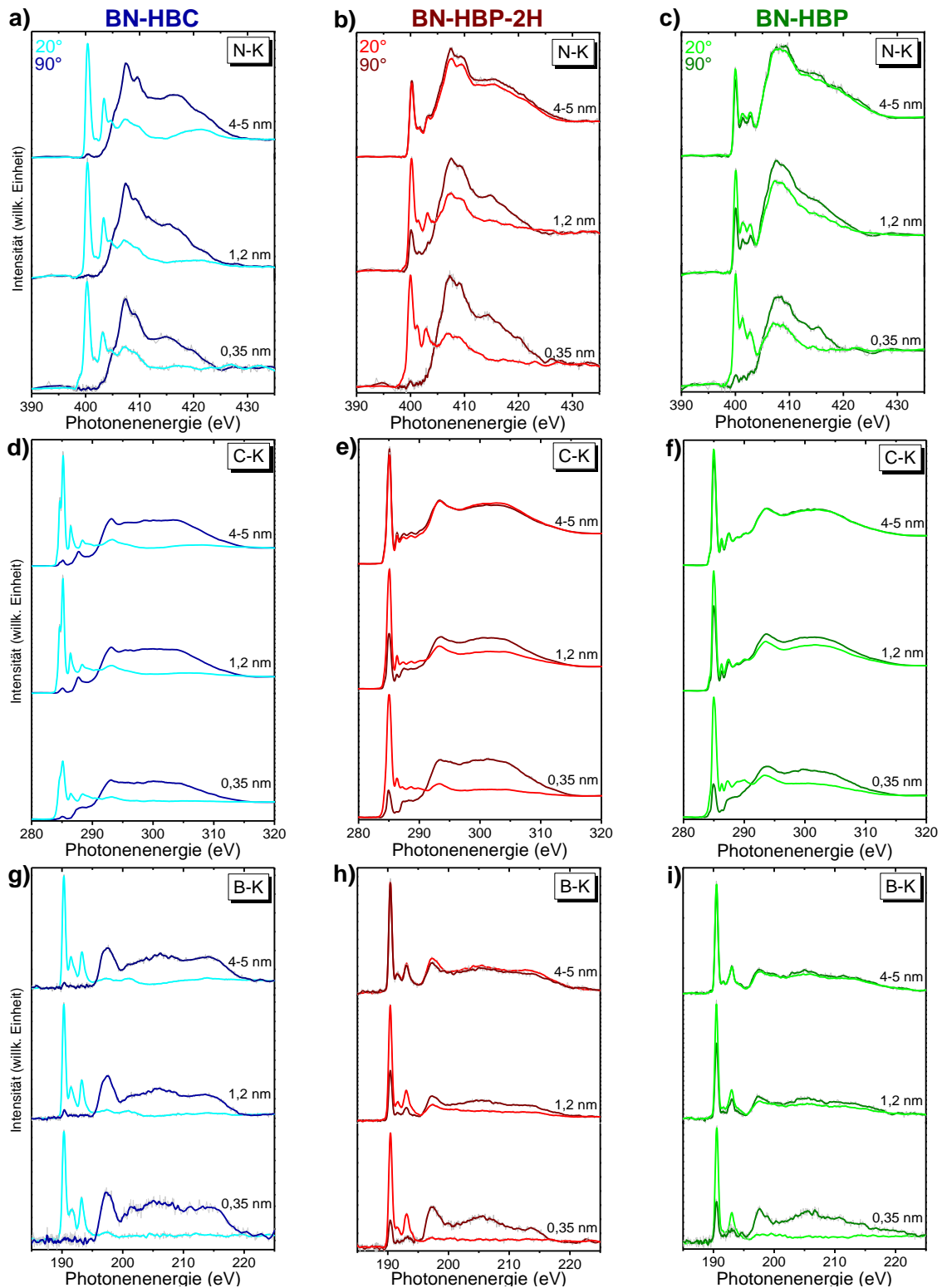


Abbildung 15. Schichtdickenabhängige XAS-Spektren aller drei K-Kanten (N-K, C-K, B-K) der drei BN-dotierten Moleküle: a), d), g) BN-HBC, b), e), h) BN-HBP-2H und c), f), i) BN-HBP.

Die Moleküle liegen präferiert flach, wobei deutliche Intensität im π^* -Bereich der 90° Spektren beider Moleküle und in allen drei Absorptionskanten vorhanden ist.

Dies deutet darauf hin, dass die Moleküle schon im ML-Bereich einen höheren Kippwinkel aufweisen als BN-HBC.

Anhand der Intensität im Bereich der π^* - Übergänge lässt sich außerdem feststellen, dass der Dichroismus der N-K Absorptionskanten deutlich stärker ausgeprägt ist als bei den B-K und C-K Absorptionskanten. Beides kann eine Auswirkung der verdrehten (nichtplanaren) Molekülform sein. Die lateral vorstehenden „Flügel“ des BN-HBPs bestehen aus reinen Biphenyleinheiten und somit nur aus Kohlenstoffatomen, während der Borazinkern aus Bor- und Stickstoffatomen besteht. Die verdrehten Biphenyleinheiten sorgen auch für eine Verdrehung des Borazinkerns. Obwohl alle drei Moleküle in der ML flach liegen (bzw., der BN-Kern ist parallel zum Substrat orientiert), entwickelt sich die Orientierung mit zunehmender Schichtdicke indes unterschiedlich. Während die BN-HBC Moleküle bis zu einer Schichtdicke von nominell 4-5 nm noch sehr flach liegen, sind die BN-HBP-2H und BN-HBP Moleküle an der Oberfläche dieser dünnen Filme nahezu zufällig, oder alle mit einem Kippwinkel nahe dem magischen Winkel, orientiert. Dies lässt sich mit XAS nicht unterscheiden. Dabei behalten die BN-HBP-2H Moleküle die flach liegende Orientierung noch länger bei als die BN-HBP Moleküle. Folglich hat die Nichtplanarität enorme Auswirkungen auf die Orientierung der Moleküle in dünnen Schichten und an der Grenzfläche, jedoch ebenso auf die Molekül-Molekül Wechselwirkung, wodurch die Moleküle ihre hohe flach liegende Orientierung im Monolagenbereich in dickeren Schichten durch schwächere Molekül-Molekül Wechselwirkung verlieren. Im Vergleich zu HBC scheint die BN-Dotierung des BN-HBCs nur geringe Auswirkung auf die Adsorptionsgeometrie und Orientierung der Moleküle zu haben.

Um die Auswirkungen der BN-Dotierung (HBC \rightarrow BN-HBC) und des unterschiedlichen Grades der Planarität (BN-HBC \rightarrow BN-HBP-2H \rightarrow BN-HBP) auf die Morphologie zu prüfen, wurden AFM-Aufnahmen dünner Filme von nominell 4-5 nm Dicke angefertigt (**Abbildung 16**). Schon auf den ersten Blick erkennt man deutliche Unterschiede in der Filmbeschaffenheit von HBC und BN-HBC in den gezeigten Ausschnitten: HBC wächst in Inseln mit einer Höhe von bis zu 20 nm, dahingegen erreichen die Inseln des BN-HBCs nur eine Höhe von bis zu 5 nm. Die Inseln des HBCs wachsen separiert von den anderen Inseln (**Abbildung 16a**), während die Inseln des BN-HBCs nahe beieinander wachsen und teilweise mehrere

kleine Inseln zu größeren Inseln aggregieren (**Abbildung 16b**). Neben der unterschiedlichen Höhe ist auch der Durchmesser der einzelnen Inseln des HBCs um einiges größer als des BN-HBCs. Die HBC-Inseln haben einen durchschnittlichen Radius von 0,07 bis zu 0,1 μm . Beim BN-HBC ist dies nicht eindeutig bestimmbar, da die Inseln sehr nahe beieinander wachsen und teilweise auch „verschmelzen“. Allerdings lässt sich aus dem Profil erahnen, dass die Inseln einen durchschnittlichen Radius von 0,02 – 0,03 μm besitzen.

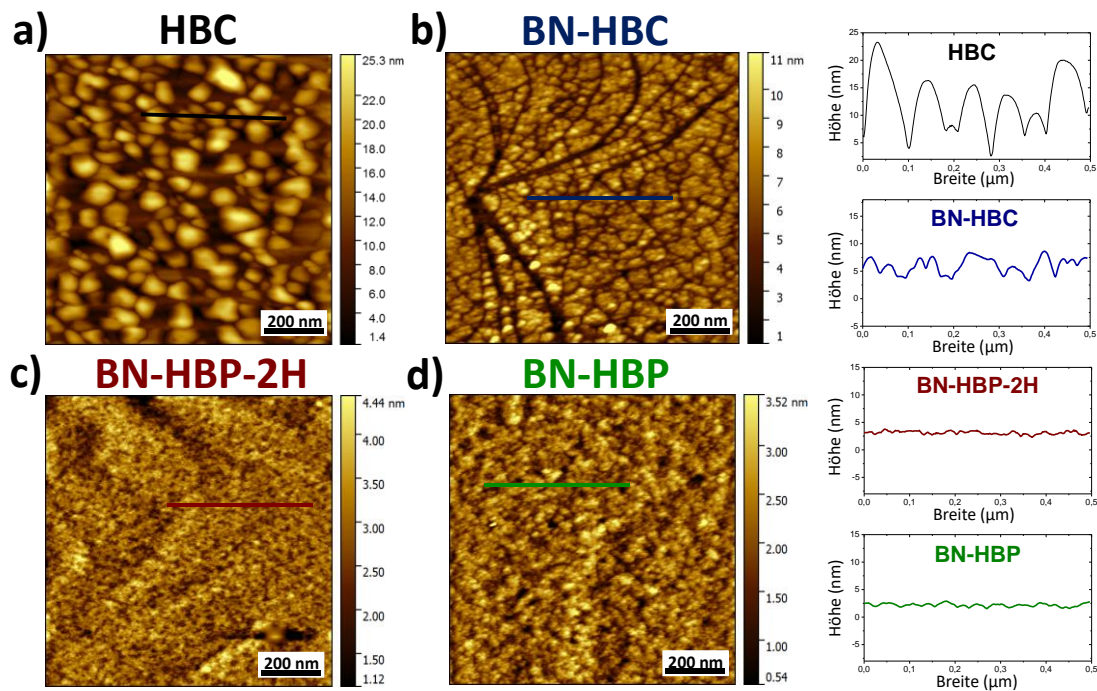


Abbildung 16. AFM-Aufnahmen von nominell 4-5 nm dicken Schichten von a) HBC, b) BN-HBC c) BN-HBP-2H und d) BN-HBP auf Au(111) und die zugehörigen Höhenprofile.

Beide Moleküle zeigen deutliche Korngrenzen auf. Dies macht sich auch in der Rauigkeit deutlich bemerkbar: das quadratische Mittel der Rauigkeit (RMS-Rauigkeit, engl. root-mean-squared roughness) des HBCs beträgt 4,7 nm, während die RMS-Rauigkeit des BN-HBCs 1,7 nm ergibt. Die deutlichen Korngrenzen beider dünner Schichten lassen einen hohen Grad an Kristallinität vermuten. Das bevorzugte Inselwachstum beider Moleküle spricht für ein Volmer-Weber oder Stranski-Krastanov Wachstum. Die STM-Aufnahmen (**Abbildung 14**) deuten eher auf ein Stranski-Krastanov Wachstum hin. Dahingegen zeigen die Schichten von BN-HBP-2H und BN-HBP keine deutlichen Korngrenzen auf (**Abbildung 16c+d**). Die Schichten sehen gleichmäßiger aus. Dies wird auch durch die Höhenprofile sehr deutlich: im Vergleich zu den 20 bzw. 5 nm hohen Inseln des HBCs und BN-HBCs, gibt es bei BN-HBP-2H und BN-HBP nur Höhenunterschiede von bis zu einem

Nanometer. Deshalb ist die RMS-Rauigkeit mit ungefähr 0,52 nm beider Moleküle auch deutlich geringer als die von HBC und BN-HBC. Verglichen zu BN-HBP ist die Körnung von BN-HBP-2H feiner, wodurch die Schicht gleichmäßiger wirkt.

Es können zwei wichtige Beobachtungen festgehalten werden:

- 1) Durch die BN-Dotierung des HBCs entstehen deutliche Unterschiede in der Morphologie der beiden Moleküle. Ein möglicher Grund ist die unterschiedlich starke Wechselwirkung der Moleküle untereinander.
- 2) Wird die Planarität durch das Brechen der CC-Bindungen aufgelöst, so wachsen die Moleküle nicht mehr in Inseln, sondern in gleichmäßigen Schichten mit geringer Rauigkeit.

Dies zeigt auch weshalb häufig von nominellen Schichtdicken gesprochen wird. Bei einer starken Ausbildung von Inseln sind die Schichtdicken lokal deutlich verschieden.

6. Elektronische Struktur des nanographenartigen Moleküls Hexabenzocoronen und verwandter BN-Derivate

6.1 Elektronische Struktur in dünnen Filmen

Um die Auswirkungen der BN-Dotierung und des unterschiedlichen Grades der Planarität auf die elektronische Struktur in dünnen Filmen zu untersuchen, wurden XPS-Messungen dünner Filme HBC, BN-HBC und BN-HBP auf Au(111) durchgeführt (**Abbildung 17**). HBC besteht aus zwei Arten von Kohlenstoffatomen, welche sich in unterschiedlicher chemischer Umgebung befinden: Kohlenstoffatome im Inneren des Moleküls, welche nur zu anderen Kohlenstoffatomen gebunden sind (CC) und Kohlenstoffatome außen am Molekül, die auch zu Wasserstoffatomen gebunden sind (CH). Diese Einteilung führt zu einem stöchiometrischen Verhältnis von 24:18 (CC:CH), welches für den Peakfit angenommen wurde. Die beiden Komponenten sind 0,27 eV auseinander, wobei der CH in Übereinstimmung mit der Literatur zu Graphennanobändern und Acenen bei niedrigerer Bindungsenergie erscheint als der CC (**Abbildung 17a**, oben).²⁸²⁻²⁸⁴ Durch den Austausch des inneren Benzolrings (C_6) mit einem Borazinring (B_3N_3) (BN-HBC), sind zwei weitere Kohlenstoffkomponenten für den Peakfit zu berücksichtigen: Kohlenstoffatome, die auch an Stickstoffatome gebunden sind (CN) und Kohlenstoffatome, die auch an Boratome gebunden sind (CB).

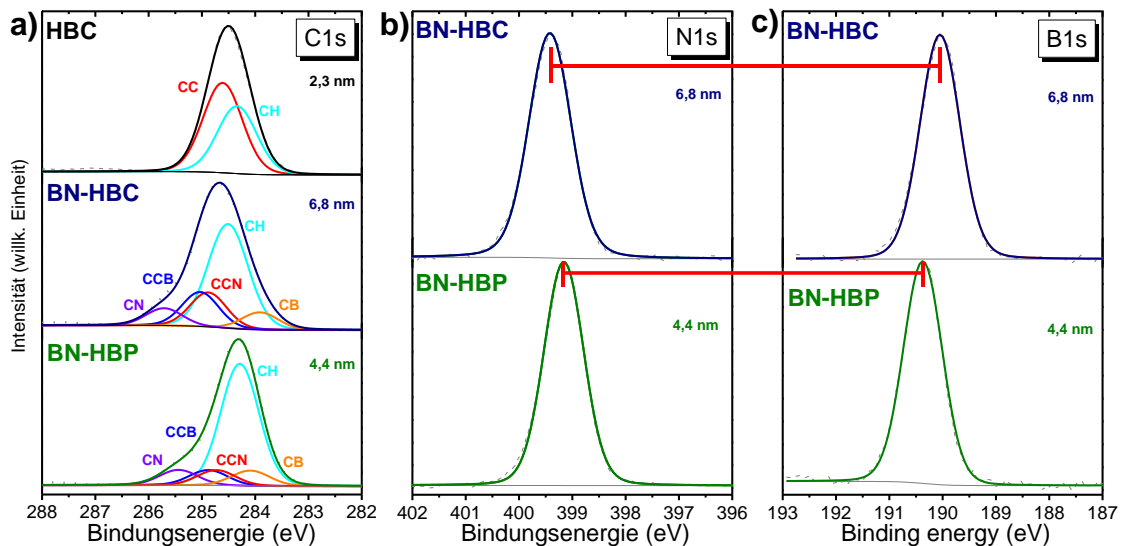


Abbildung 17. Rumpfniveauspektren dünner Filme HBC, BN-HBC und BN-HBP auf Au(111): a) C1s, b) N1s und c) B1s. Die Spektren wurden mit $h\nu = 1487,7$ eV gemessen.

Darüber hinaus konnte durch die Berechnung via Natürlicher Populationsanalyse (NPA, engl. natural population analysis), die von K. Greulich (AK Chassé) durchgeführt wurde, herausgefunden werden, dass CC-Kohlenstoffatome in der Nähe zu Stickstoffatomen (CCN) eine geringere Bindungsenergie aufweisen als CC-Kohlenstoffatome in der Nähe zu Boratomen (CCB). Diese verschiedenen Kohlenstoffkomponenten führen zu einem stöchiometrischen Verhältnis CH:CCB:CCN:CB:CN von 18:6:6:3:3 für BN-HBC und 24:3:3:3:3 für BN-HBP, welches für den jeweiligen Peakfit verwendet wurde (**Abbildung 17a**, mittig und unten). Dies stellt eine Weiterentwicklung des Peakfits, welcher für BN-HBC in früheren Publikationen verwendet wurde, dar (Publikation [3] und Ref.²⁸⁵). Ein Vergleich des früher verwendeten und des weiterentwickelten Peakfits ist in **Abbildung A4** dargestellt.

Durch die BN-Dotierung des HBCs zu BN-HBC wird der energetische Unterschied zwischen den CH- und CC-Komponenten um 0,18 eV von 0,27 auf 0,45 eV erhöht. Ein Vergleich des planaren BN-HBCs mit dem nichtplanaren BN-HBP zeigt interessante Trends: die Distanz zwischen N1s und B1s ist für BN-HBC größer als für BN-HBP, ebenso verhält es sich für die CN- und CB-Komponenten des C1s Peakfits. Zudem ist die Polarität der B-N Bindung des Borazinkerns des BN-HBPs höher als für BN-HBC. Dies zeigt deutlich, dass neben der BN-Dotierung auch der Grad der Planarität Auswirkungen auf die Elektronendichte an den verschiedenen Atomen der Moleküle hat. Diese Beobachtungen werden durch das BN-HBP-2H,

welches sich bei allen Trends zwischen BN-HBC und BN-HBP befindet, bestätigt (Publikation [4]).

Zur Interpretation absoluter Bindungsenergien ist es bei Halbleitern vorteilhaft die Bindungsenergien der Rumpfniveaus auf die HOMO-onsets zu beziehen, um verschiedene Energieniveaueinsparungen vernachlässigen zu können. Dafür wird die Bindungsenergie des HOMO-onsets von der Bindungsenergie der CH-Komponente abgezogen (**Tabelle A2**). Aus den erhaltenen Werten ist ersichtlich, dass die Bindungsenergie durch die BN-Dotierung um 0,23 eV abnimmt. Ein noch größerer Unterschied ergibt sich durch die Veränderung des Grades der Planarität. Die Bindungsenergie des BN-HBPs ist um 0,42 eV geringer als die des BN-HBCs. Der Grad der Planarität beeinflusst die Bindungsenergie des C1s Rumpfniveaus nahezu doppelt so stark wie die BN-Dotierung. Folglich nimmt die Elektronendichte in den CH (und CC) Kohlenstoffatomen in der Reihe BN-HBP > BN-HBC > HBC ab.

Zur Aufklärung der elektronischen Struktur der drei BN-dotierten Moleküle in Abhängigkeit des Grades der Planarität wurden Messungen und Rechnungen mit ORCA²⁸⁶ und StoBe²⁸⁷ der VB- und XAS-Spektren in Kooperation mit K. Greulich (AK Chassé) und D. Bischof (AG Witte, Marburg) vorgenommen (Publikation [4]). Details zu den Rechenmethoden können Publikation [4] entnommen werden.

Hervorzuheben ist vor allem die Kombination aus experimentellen und berechneten XAS-Spektren. Durch einen Vergleich der experimentellen und berechneten B-K und N-K XAS-Spektren der BN-dotierten Moleküle konnten verschiedene Trends bezüglich der Intensität verschiedener Strukturen in Abhängigkeit der Planarität festgestellt werden (Publikation [4]). Analog zu den N1s und B1s Rumpfniveaus ist die Photonenenergie des dominanten Absorptionsübergangs von BN-HBC im N-K XAS-Spektrum am höchsten und im B-K Absorptionsspektrum am geringsten. Für BN-HBP verhält es sich genau umgekehrt und BN-HBP-2H liegt jeweils dazwischen. Darüber hinaus ist es möglich Strukturen in den C-K XAS-Spektren Übergängen bestimmter Kohlenstoffatome zuzuordnen. Beispielweise befindet sich der Absorptionsübergang aus der CB-Komponente bei niedrigster Photonenenergie, während für einen Absorptionsübergang aus der CN-Komponente die höchste Photonenenergie vonnöten ist. Die am Absorptionsprozess der CN-Komponente beteiligten Orbitale sind folglich energetisch am weitesten auseinander, während die der CB-Komponente energetisch am dichtesten zusammen liegen. Analog zu

den C1s Rumpfniveaus sind die Absorptionsübergänge der CB- und CN-Komponenten bei BN-HBC energetisch weiter auseinander als bei BN-HBP. Folglich bewirken die Unterschiede der Ausgangszustände (Rumpfniveaus) auch Unterschiede in den Endzuständen (Röntgenabsorption). Des Weiteren ist bei BN-HBP-2H und BN-HBP nur eine dominante Hauptstruktur bei etwa 285 eV zu sehen, da die Absorptionsübergänge der beteiligten Kohlenstoffatome energetisch sehr nahe zusammenliegen. Bei BN-HBC kommt es aufgrund größerer energetischer Unterschiede in den Absorptionsprozessen der beteiligten Kohlenstoffatome zu einer Aufspaltung der Hauptkomponente. Grund dafür sind dieselben Kohlenstoffatome (in Publikation [4] als C2 und C5 bezeichnet), die auch bei HBC für eine Aufspaltung der dominanten Struktur sorgen.²⁸⁸ Die beiden durch die CB und CN Kohlenstoffatome hervorgerufenen Strukturen sind folgerichtig bei HBC nicht zu sehen.

6.2 Elektronische Struktur an der Grenzfläche zu Au(111) und Ni(111)

In Kapitel 5 wurde anhand der STM-Aufnahmen schon dargelegt, dass es Unterschiede in der Wechselwirkung der Moleküle an der Grenzfläche zu Au(111) gibt. Dies wird durch XAS-Spektren aus Publikation [4] gestützt. Eine weitere sehr eindrucksvolle Möglichkeit, um Informationen über Wechselwirkung an Grenzflächen zu erhalten stellt XPS dar. In der folgend diskutierten detaillierten XPS-Studie liegt der Fokus auf dem Vergleich der Wechselwirkung an der Grenzfläche zu einem schwachwechselwirkenden Metallsubstrat (Au(111)) und einem starkwechselwirkenden Metallsubstrat (Ni(111)). Der Einfluss der BN-Dotierung und des Grades der Planarität wird durch einen Vergleich der Moleküle HBC, BN-HBC und BN-HBP verdeutlicht. Wird der Adsorptionsprozess hauptsächlich durch Physisorption bestimmt, so sind in der Signalform an der Grenzfläche im Vergleich zum dünnen Film keine oder kaum Unterschiede auszumachen.^{107, 139, 289-291} Dominiert jedoch Chemisorption den Adsorptionsprozess, so findet eine drastische Änderung der Signalform bis hin zu neuen Komponenten und/oder starke Verschiebungen der Bindungsenergie statt.^{166, 192, 207, 292} Das C1s Spektrum des HBCs auf Au(111) kann im Grunde mit demselben Modell beschrieben werden wie der zugehörige dünne Film (**Abbildung 18a**, oben). Es sind nur die zwei bekannten Komponenten nötig. Dahingegen muss für BN-HBC und BN-HBP jeweils eine zusätzliche Komponente zu höherer Bindungsenergie hinzugefügt werden, um die experimentellen

Daten zu beschreiben (**Abbildung 18a**, mittig und unten). Die N1s und B1s Rumpfniveaus der beiden Moleküle können dahingegen mit nur einer Struktur gefittet werden (**Abbildung 18b+c**). Dies deutet darauf hin, dass zwischen den beiden BN-dotierten Molekülen und der Au(111) Oberfläche nur eine schwache Wechselwirkung stattfindet.

1-2 ML auf Au(111)

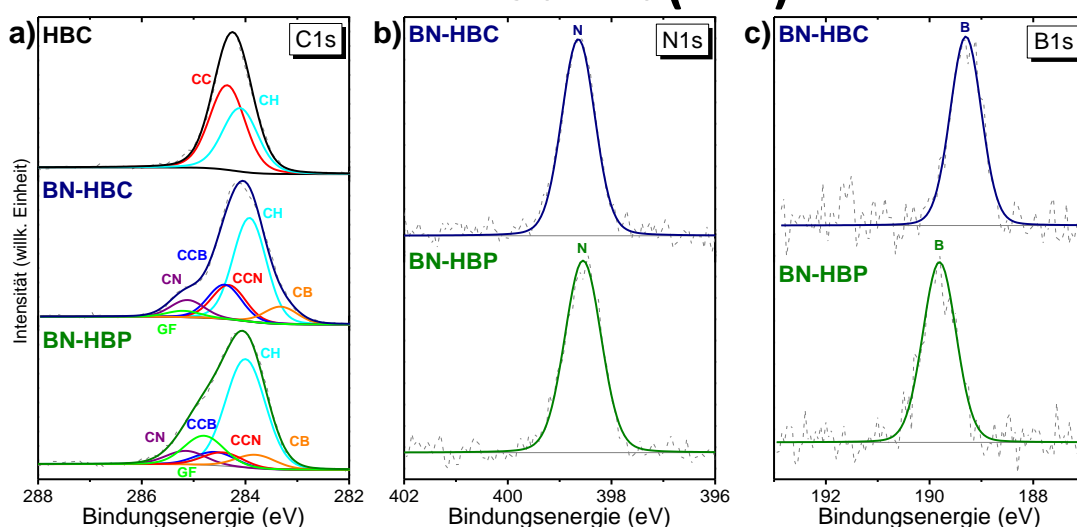


Abbildung 18. Rumpfniveaus von 1-2 ML HBC, BN-HBC und BN-HBP auf Au(111): a) C1s, b) N1s und c) B1s. Die Spektren wurden mit $h\nu = 1486,7$ eV gemessen.

Die zusätzliche Komponente im C1s der beiden BN-dotierten Moleküle könnte von Molekülen, welche auf reaktiven Plätzen wie beispielweise an der *herringbone* Struktur der Au(111) Oberfläche adsorbiert sind, stammen.¹⁸⁷ Im Falle des BN-HBPs ist noch eine andere Tatsache in die Interpretation miteinzubeziehen: wie in den vorherigen Kapiteln gezeigt, adsorbiert BN-HBP aufgrund seiner verdrehten Struktur nicht komplett flach auf der Au(111) Oberfläche. Folglich haben chemisch gleiche Kohlenstoffatome unterschiedliche Abstände zur Substratoberfläche, wodurch sie einer unterschiedlich starken Wechselwirkung aufgrund des Abstands unterliegen.

Um einiges komplexer ist die elektronische Situation an der Grenzfläche zu Ni(111) (**Abbildung 19**), einem sehr reaktiven Metallsubstrat. Es wurde schon in vielen Experimenten eine starke Wechselwirkung zwischen organischen Molekülen und Ni(111)-Oberflächen festgestellt und diskutiert,^{38, 64, 293-294} weshalb Ni(111) Oberflächen auch als Katalysator für Oberflächenreaktionen Verwendung finden.²⁹⁵⁻³⁰²

Die Signalformen aller Rumpfniveaus der drei Moleküle verändern sich an der Grenzfläche enorm.

1-2 ML auf Ni(111)

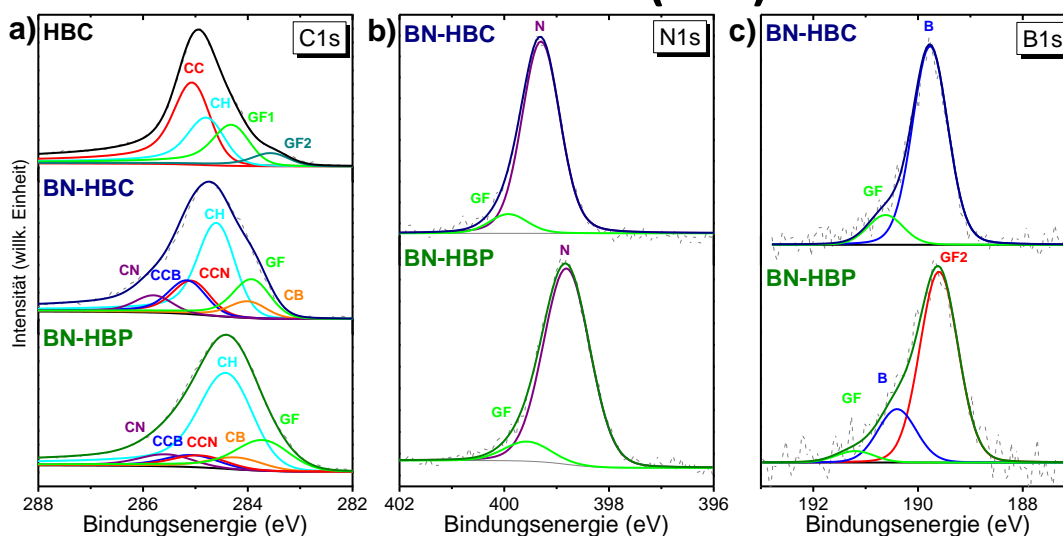


Abbildung 19. Rumpfniveaus von 1-2 ML HBC, BN-HBC und BN-HBP auf Au(111): a) C1s, b) N1s und c) B1s. Die Spektren wurden mit $h\nu = 1486,7$ eV gemessen.

Für den Peakfit des C1s aller drei Moleküle mussten eine Asymmetrie und zusätzliche Komponenten verwendet werden, um die experimentellen Daten widerzugeben (**Abbildung 19a**). Der verwendete Asymmetrie Parameter von 0,16 für HBC und 0,1 für die beiden BN-dotierten Moleküle ist in guter Übereinstimmung mit verwendeten Asymmetrie Parametern für den Peakfit von Graphen auf Ni(111).³⁰³⁻³⁰⁴ Die Bindungsenergien der zusätzlichen Grenzflächenkomponenten GF bzw. GF1 des C1s könnte durch eine Fragmentierung und die der GF2-Komponente des HBCs durch Nickelcarbid-Bildung erklärt werden.³⁰⁵ Im Falle des HBCs ändert sich dadurch das Intensitätsverhältnis von CC:CH von 24:18 auf 24:13,9. Neben dem C1s ändert sich auch die Form der Rumpfniveaus der beiden Heteroatome Stickstoff und Bor. Für Stickstoff ist die elektronische Situation für die beiden BN-dotierten Moleküle BN-HBC und BN-HBP sehr ähnlich: es ist jeweils eine Grenzflächenkomponente bei höherer Bindungsenergie vorhanden (**Abbildung 19b**). Der B1s ist jedoch komplexer und es gibt deutliche Unterschiede zwischen den beiden Molekülen (**Abbildung 19c**). Analog zum N1s Rumpfniveau ist bei BN-HBC eine zusätzliche Komponente zu höherer Bindungsenergie hinzuzufügen. Für BN-HBP reicht eine zusätzliche Komponente zu höherer Bindungsenergie jedoch nicht aus. Das Grenzflächenspektrum wird von einer neuen zu niedrigerer Bindungsenergie

vorhandenen Komponente GF2 klar dominiert und die kleine GF1-Komponente, die für BN-HBC viel intensiver ist, spielt nur eine untergeordnete Rolle für die Interpretation des Spektrums. Die GF2-Komponente wird mit größer werdender Schichtdicke kleiner und im dünnen Film wird der B1s schlussendlich von der B-Komponente dominiert (Publikation [7]). Darüber hinaus mussten die Gaussbreiten der Rumpfniveaus des BN-HBPs stark erhöht werden, was durch Moleküle, die unterschiedlich stark mit der Ni(111) Oberfläche wechselwirken, wie anhand des B1s festgestellt wurde, interpretiert werden kann. So kann es zu energetischen Verschiebungen kommen, wodurch eine Komponente leicht unterschiedliche Bindungsenergien aufweisen kann. Aus diesen Beobachtungen wird deutlich, dass eine Fragmentierung der Moleküle an der Grenzfläche zu Ni(111) in unterschiedlich starkem Ausmaß in Betracht gezogen werden muss, während die Wechselwirkung an der Grenzfläche zu Au(111) sehr schwach ist. Eine Fragmentierung organischer Moleküle auf reaktiven Oberflächen ist keine Seltenheit. Dies wurde beispielweise für MnPc auf Ni(111) und Methylamin auf Pd(111) gefunden.^{292, 306}

Die BN-Dotierung scheint kaum Einfluss auf die Wechselwirkung zu haben. Jedoch spielt die Molekülsymmetrie eine große Rolle: anhand des B1s auf Ni(111) ist ersichtlich, dass die Wechselwirkung des BN-HBPs viel komplexer ist als die des BN-HBCs. Das planare π -konjugierte Kohlenstoffsystem könnte hierbei eine entscheidende Rolle für die Stabilisierung des Moleküls an der Grenzfläche darstellen. Eine ausführlichere Diskussion der Grenzflächenwechselwirkung der verschiedenen Moleküle unter Einbezug einer weiteren Metalloberfläche (Cu(111)) kann in Publikation [7] nachgelesen werden.

Zusammenfassend kann für die (BN-)Nanographenmoleküle festgehalten werden, dass sowohl die BN-Dotierung als auch der Grad der Planarität und damit die Größe des konjugierten π -Systems sowohl die elektronischen Eigenschaften, Morphologie als auch das Wachstum bzw. die Orientierung der Moleküle in dünnen Filmen sowie an der Grenzfläche stark beeinflusst. Die BN-Dotierung beeinflusst dabei hauptsächlich die elektronischen Eigenschaften und Morphologie dünner Filme, während sich der Grad an Planarität am stärksten auf die Orientierung dünner Filme und die Wechselwirkung an der Grenzfläche auswirkt.

Literaturverzeichnis

1. Moore, G. E., *Cramming More Components onto Integrated Circuits*; McGraw-Hill New York, NY, USA, 1965.
2. Vardalas, J., Twists and Turns in the Development of the Transistor. *IEEE-USA Today's Engineer Online* **2003**, *6*.
3. Kilby, J. S., Invention of the Integrated Circuit. *IEEE Trans. Electron Devices* **1976**, *23*, 648-654.
4. Stanbery, B. J., Copper Indium Selenides and Related Materials for Photovoltaic Devices. *Crit. Rev. Solid State Mater. Sci.* **2002**, *27*, 73-117.
5. Jung, H. S.; Park, N.-G., Perovskite Solar Cells: From Materials to Devices. *Small* **2015**, *11*, 10-25.
6. Green, M. A.; Ho-Baillie, A.; Snaith, H. J., The Emergence of Perovskite Solar Cells. *Nature Photonics* **2014**, *8*, 506-514.
7. Wang, D.; Wright, M.; Elumalai, N. K.; Uddin, A., Stability of Perovskite Solar Cells. *Sol. Energy Mater. Sol. Cells* **2016**, *147*, 255-275.
8. Zhou, H.; Chen, Q.; Li, G.; Luo, S.; Song, T.-b.; Duan, H.-S.; Hong, Z.; You, J.; Liu, Y.; Yang, Y., Interface Engineering of Highly Efficient Perovskite Solar Cells. *Science* **2014**, *345*, 542.
9. Qian, Y.; Zhang, X.; Xie, L.; Qi, D.; Chandran, B. K.; Chen, X.; Huang, W., Stretchable Organic Semiconductor Devices. *Adv. Mater.* **2016**, *28*, 9243-9265.
10. Parthasarathy, G.; Burrows, P. E.; Khalfin, V.; Kozlov, V. G.; Forrest, S. R., A Metal-Free Cathode for Organic Semiconductor Devices. *Appl. Phys. Lett.* **1998**, *72*, 2138-2140.
11. Gao, Y., Surface Analytical Studies of Interfaces in Organic Semiconductor Devices. *Mater. Sci. Eng. R Rep.* **2010**, *68*, 39-87.
12. Greiner, M. T.; Lu, Z.-H., Thin-Film Metal Oxides in Organic Semiconductor Devices: Their Electronic Structures, Work Functions and Interfaces. *NPG Asia Mater.* **2013**, *5*, e55.
13. Jiang, C.; Choi, H. W.; Cheng, X.; Ma, H.; Hasko, D.; Nathan, A., Printed Subthreshold Organic Transistors Operating at High Gain and Ultralow Power. *Science* **2019**, *363*, 719.
14. Feng, L.; Jiang, C.; Ma, H.; Guo, X.; Nathan, A., All Ink-Jet Printed Low-Voltage Organic Field-Effect Transistors on Flexible Substrate. *Org. Electron.* **2016**, *38*, 186-192.
15. Forrest, S. R., The Path to Ubiquitous and Low-Cost Organic Electronic Appliances on Plastic. *Nature* **2004**, *428*, 911-918.
16. Cao, Y.; Uhrich, K. E., Biodegradable and Biocompatible Polymers for Electronic Applications: A Review. *J. Bioact. Compat. Polym.* **2019**, *34*, 3-15.
17. Koizumi, Y.; Ide, M.; Saeki, A.; Vijayakumar, C.; Balan, B.; Kawamoto, M.; Seki, S., Thienoisindigo-Based Low-Band Gap Polymers for Organic Electronic Devices. *Polym. Chem.* **2013**, *4*, 484-494.
18. Bao, Z. N.; Rogers, J. A.; Dodabalapur, A.; Raju, V. R.; Katz, H. E.; Peng, Z.; Galvin, M. E.; Lovinger, A. J., Novel Materials and Devices for Polymer Light Emitting Diodes. *Abstr. Pap. Am. Chem. S.* **1998**, *216*, U88-U88.
19. Dimitrakopoulos, C. D.; Mascaro, D. J., Organic Thin-Film Transistors: A Review of Recent Advances. *IBM J. Res. Dev.* **2001**, *45*, 11-27.
20. de la Torre, G.; Claessens, C. G.; Torres, T., Phthalocyanines: The Need for Selective Synthetic Approaches. *Eur. J. Org. Chem.* **2000**, *2000*, 2821-2830.
21. Wöhrle, D.; Schnurpfeil, G.; Makarov, S. G.; Kazarin, A.; Suvorova, O. N., Practical Applications of Phthalocyanines—from Dyes and Pigments to Materials for Optical, Electronic and Photo-Electronic Devices. *Macroheterocycles* **2012**, *5*, 191-202.
22. Wöhrle, D.; Schnurpfeil, G.; Makarov, S.; Suvora, O., Phthalocyanine. *Chem. unserer Zeit* **2012**, *1*, 12-24.
23. Walzer, K.; Maennig, B.; Pfeiffer, M.; Leo, K., Highly Efficient Organic Devices Based on Electrically Doped Transport Layers. *Chem. Rev.* **2007**, *107*, 1233-1271.

24. Cinchetti, M.; Heimer, K.; Wustenberg, J. P.; Andreyev, O.; Bauer, M.; Lach, S.; Ziegler, C.; Gao, Y. L.; Aeschlimann, M., Determination of Spin Injection and Transport in a Ferromagnet/Organic Semiconductor Heterojunction by Two-Photon Photoemission. *Nat. Mater.* **2009**, *8*, 115-119.
25. Claessens, C. G.; Hahn, U.; Torres, T., Phthalocyanines: From Outstanding Electronic Properties to Emerging Applications. *Chem. Rec.* **2008**, *8*, 75-97.
26. Crone, B.; Dodabalapur, A.; Lin, Y. Y.; Filas, R. W.; Bao, Z.; LaDuca, A.; Sarpeshkar, R.; Katz, H. E.; Li, W., Large-Scale Complementary Integrated Circuits Based on Organic Transistors. *Nature* **2000**, *403*, 521-523.
27. Bao, Z.; Lovinger, A. J.; Brown, J., New Air-Stable N-Channel Organic Thin Film Transistors. *J. Am. Chem. Soc.* **1998**, *120*, 207-208.
28. Ling, M. M.; Bao, Z. N., Copper Hexafluorophthalocyanine Field-Effect Transistors with Enhanced Mobility by Soft Contact Lamination. *Org. Electron.* **2006**, *7*, 568-575.
29. Brinkmann, H.; Kelting, C.; Makarov, S.; Tsaryova, O.; Schnurpfeil, G.; Wohrle, D.; Schlettwein, D., Fluorinated Phthalocyanines as Molecular Semiconductor Thin Films. *Phys. Status Solidi A* **2008**, *205*, 409-420.
30. Michaelis, W.; Wöhrle, D.; Schlettwein, D., Organic N-Channels of Substituted Phthalocyanine Thin Films Grown on Smooth Insulator Surfaces for Organic Field Effect Transistors Applications. *J. Mater. Res.* **2004**, *19*, 2040-2048.
31. Urbani, M.; Ragoussi, M.-E.; Nazeeruddin, M. K.; Torres, T., Phthalocyanines for Dye-Sensitized Solar Cells. *Coord. Chem. Rev.* **2019**, *381*, 1-64.
32. Lessard, B. H.; Mohammad, A.-A.; Grant, T. M.; White, R.; Lu, Z.-H.; Bender, T. P., From Chloro to Fluoro, Expanding the Role of Aluminum Phthalocyanine in Organic Photovoltaic Devices. *J. Mater. Chem. A* **2015**, *3*, 5047-5053.
33. Deng, Z.; Lü, Z.; Chen, Y.; Yin, Y.; Zou, Y.; Xiao, J.; Wang, Y., Aluminum Phthalocyanine Chloride as a Hole Injection Enhancer in Organic Light-Emitting Diodes. *Solid-State Electron.* **2013**, *89*, 22-25.
34. Sheats, J. R.; Antoniadis, H.; Hueschen, M.; Leonard, W.; Miller, J.; Moon, R.; Roitman, D.; Stocking, A., Organic Electroluminescent Devices. *Science* **1996**, *273*, 884-888.
35. Tsymbal, E. Y.; Žutić, I., *Spin Transport and Magnetism: Semiconductor Spintronics*; CRC press, 2019; Vol. 2.
36. Naber, W.; Faez, S.; van der Wiel, W. G., Organic Spintronics. *J. Phys. D: Appl. Phys.* **2007**, *40*, R205.
37. Halaskova, M.; Rahali, A.; Almeida-Marrero, V.; Machacek, M.; Kucera, R.; Jamoussi, B.; Torres, T.; Novakova, V.; de la Escosura, A.; Zimcik, P., Peripherally Crowded Cationic Phthalocyanines as Efficient Photosensitizers for Photodynamic Therapy. *ACS Med. Chem. Lett.* **2021**, *12*, 502-507.
38. Peisert, H.; Uihlein, J.; Petraki, F.; Chassé, T., Charge Transfer between Transition Metal Phthalocyanines and Metal Substrates: The Role of the Transition Metal. *J. Electron. Spectrosc. Relat. Phenom.* **2015**, *204*, 49-60.
39. Belser, A.; Karstens, R.; Nagel, P.; Merz, M.; Schuppler, S.; Chassé, T.; Peisert, H., Interaction Channels between Perfluorinated Iron Phthalocyanine and Cu(111). *Phys. Status Solidi B* **2019**, *256*, 1800292.
40. Gottfried, J. M., Surface Chemistry of Porphyrins and Phthalocyanines. *Surf. Sci. Rep.* **2015**, *70*, 259-379.
41. Qasrawi, A. F.; Zyoud, H. M., Dielectric Dispersion at the Mn/ZnPc Interfaces. *Phys. Status Solidi A* **2020**, *257*, 2000089.
42. Kahn, A.; Koch, N.; Gao, W., Electronic Structure and Electrical Properties of Interfaces between Metals and π -Conjugated Molecular Films. *J. Polym. Sci., Part B: Polym. Phys.* **2003**, *41*, 2529-2548.

43. Lei, S.-B.; Deng, K.; Yang, D.-L.; Zeng, Q.-D.; Wang, C., Charge-Transfer Effect at the Interface of Phthalocyanine– Electrode Contact Studied by Scanning Tunneling Spectroscopy. *J. Phys. Chem. B* **2006**, *110*, 1256-1260.
44. Romaner, L.; Heimel, G.; Bredas, J. L.; Gerlach, A.; Schreiber, F.; Johnson, R. L.; Zegenhagen, J.; Duhm, S.; Koch, N.; Zojer, E., Impact of Bidirectional Charge Transfer and Molecular Distortions on the Electronic Structure of a Metal-Organic Interface. *Phys. Rev. Lett.* **2007**, *99*.
45. Gould, R. D., Structure and Electrical Conduction Properties of Phthalocyanine Thin Films. *Coord. Chem. Rev.* **1996**, *156*, 237-274.
46. McKeown, N. B., *Phthalocyanine Materials: Synthesis, Structure and Function*; Cambridge University Press, 1998.
47. Ballirano, P.; Caminiti, R.; Ercolani, C.; Maras, A.; Orru, M. A., X-Ray Powder Diffraction Structure Reinvestigation of the A and B Forms of Cobalt Phthalocyanine and Kinetics of the A→ B Phase Transition. *J. Am. Chem. Soc.* **1998**, *120*, 12798-12807.
48. Evangelisti, M.; Bartolomé, J.; de Jongh, L. J.; Filoti, G., Magnetic Properties of α -Iron(II) Phthalocyanine. *Phys. Rev. B* **2002**, *66*, 144410.
49. Ashida, M.; Uyeda, N.; Suito, E., Thermal Transformation of Vacuum-Condensed Thin Films of Copper-Phthalocyanine. *J. Cryst. Growth* **1971**, *8*, 45-56.
50. Brumboiu, I. E.; Prokopiou, G.; Kronik, L.; Brena, B., Valence Electronic Structure of Cobalt Phthalocyanine from an Optimally Tuned Range-Separated Hybrid Functional. *J. Chem. Phys.* **2017**, *147*, 11.
51. Kroll, T.; Aristov, V. Y.; Molodtsova, O. V.; Ossipyan, Y. A.; Vyalikh, D. V.; Buchner, B.; Knupfer, M., Spin and Orbital Ground State of Co in Cobalt Phthalocyanine. *J. Phys. Chem. A* **2009**, *113*, 8917-8922.
52. Kroll, T.; Kraus, R.; Schönfelder, R.; Aristov, V. Y.; Molodtsova, O.; Hoffmann, P.; Knupfer, M., Transition Metal Phthalocyanines: Insight into the Electronic Structure from Soft X-Ray Spectroscopy. *J. Chem. Phys.* **2012**, *137*, 054306.
53. Marom, N.; Kronik, L., Density Functional Theory of Transition Metal Phthalocyanines, I: Electronic Structure of Nipc and CoPc-Self-Interaction Effects. *Appl. Phys. A* **2009**, *95*, 159-163.
54. Marom, N.; Kronik, L., Density Functional Theory of Transition Metal Phthalocyanines, II: Electronic Structure of MnPc and FePc-Symmetry and Symmetry Breaking. *Appl. Phys. A* **2009**, *95*, 165-172.
55. Liao, M. S.; Scheiner, S., Electronic Structure and Bonding in Metal Phthalocyanines, Metal=Fe, Co, Ni, Cu, Zn, Mg. *J. Chem. Phys.* **2001**, *114*, 9780-9791.
56. Stepanow, S.; Miedema, P. S.; Mugarza, A.; Ceballos, G.; Moras, P.; Cezar, J. C.; Carbone, C.; de Groot, F. M. F.; Gambardella, P., Mixed-Valence Behavior and Strong Correlation Effects of Metal Phthalocyanines Adsorbed on Metals. *Phys. Rev. B* **2011**, *83*, 220401.
57. Stepanow, S., et al., Spin Tuning of Electron-Doped Metal–Phthalocyanine Layers. *J. Am. Chem. Soc.* **2014**, *136*, 5451-5459.
58. Johnson, P. S.; Garcia-Lastra, J. M.; Kennedy, C. K.; Jersett, N. J.; Boukahil, I.; Himpsel, F. J.; Cook, P. L., Crystal Fields of Porphyrins and Phthalocyanines from Polarization-Dependent 2p-to-3d Multiplets. *J. Chem. Phys.* **2014**, *140*, 8.
59. Bernien, M., et al., Tailoring the Nature of Magnetic Coupling of Fe-Porphyrin Molecules to Ferromagnetic Substrates. *Phys. Rev. Lett.* **2009**, *102*, 4.
60. Tsukahara, N., et al., Adsorption-Induced Switching of Magnetic Anisotropy in a Single Iron(II) Phthalocyanine Molecule on an Oxidized Cu(110) Surface. *Phys. Rev. Lett.* **2009**, *102*, 167203.
61. Wang, N.; Yu, J.; Zang, Y.; Huang, J.; Jiang, Y., Effect of Buffer Layers on the Performance of Organic Photovoltaic Cells Based on Copper Phthalocyanine and C60. *Sol. Energy Mater. Sol. Cells* **2010**, *94*, 263-266.

62. Joshi, S.; Bischoff, F.; Koitz, R.; Ecija, D.; Seufert, K.; Seitsonen, A. P.; Hutter, J. r.; Diller, K.; Urgel, J. I.; Sachdev, H., Control of Molecular Organization and Energy Level Alignment by an Electronically Nanopatterned Boron Nitride Template. *ACS Nano* **2014**, *8*, 430-442.
63. Uihlein, J.; Peisert, H.; Glaser, M.; Polek, M.; Adler, H.; Petraki, F.; Ovsyannikov, R.; Bauer, M.; Chassé, T., Communication: Influence of Graphene Interlayers on the Interaction between Cobalt Phthalocyanine and Ni(111). *J. Chem. Phys.* **2013**, *138*, 081101.
64. Balle, D.; Adler, H.; Grüniger, P.; Karstens, R.; Ovsyannikov, R.; Giangrisostomi, E.; Chassé, T.; Peisert, H., Influence of the Fluorination of CoPc on the Interfacial Electronic Structure of the Coordinated Metal Ion. *J. Phys. Chem. C* **2017**, *121*, 18564-18574.
65. Wu, J.; Pisula, W.; Müllen, K., Graphenes as Potential Material for Electronics. *Chem. Rev.* **2007**, *107*, 718-747.
66. Grimsdale, A. C.; Wu, J.; Müllen, K., New Carbon-Rich Materials for Electronics, Lithium Battery, and Hydrogen Storage Applications. *Chem. Commun.* **2005**, 2197-2204.
67. Schmidt-Mende, L.; Fechtenkötter, A.; Müllen, K.; Moons, E.; Friend, R. H.; MacKenzie, J. D., Self-Organized Discotic Liquid Crystals for High-Efficiency Organic Photovoltaics. *Science* **2001**, *293*, 1119.
68. Watson, M. D.; Fechtenkötter, A.; Müllen, K., Big Is Beautiful—"Aromaticity" Revisited from the Viewpoint of Macromolecular and Supramolecular Benzene Chemistry. *Chem. Rev.* **2001**, *101*, 1267-1300.
69. Peyghan, A. A.; Beheshtian, J., Application of Hexa-Peri-Hexabenzocoronene Nanographene and Its B, N, and BN Doped Forms in Na-Ion Batteries: A Density Functional Theory Study. *Thin Solid Films* **2020**, *704*, 137979.
70. Dam, H. H.; Sun, K.; Hanssen, E.; White, J. M.; Marszalek, T.; Pisula, W.; Czolk, J.; Ludwig, J.; Colmann, A.; Pfaff, M., Morphology Change and Improved Efficiency in Organic Photovoltaics Via Hexa-Peri-Hexabenzocoronene Templates. *ACS Appl. Mater. Interfaces* **2014**, *6*, 8824-8835.
71. Wong, W. W.; Singh, T. B.; Vak, D.; Pisula, W.; Yan, C.; Feng, X.; Williams, E. L.; Chan, K. L.; Mao, Q.; Jones, D. J., Solution Processable Fluorenyl Hexa-Peri-Hexabenzocoronenes in Organic Field-Effect Transistors and Solar Cells. *Adv. Funct. Mater.* **2010**, *20*, 927-938.
72. van de Craats, A. M.; Stutzmann, N.; Bunk, O.; Nielsen, M. M.; Watson, M.; Müllen, K.; Chanzy, H. D.; Sirringhaus, H.; Friend, R. H., Meso-Epitaxial Solution-Growth of Self-Organizing Discotic Liquid-Crystalline Semiconductors. *Adv. Mater.* **2003**, *15*, 495-499.
73. Bosdet, M. J. D.; Piers, W. E., B-N as a C-C Substitute in Aromatic Systems. *Can. J. Chem.* **2009**, *87*, 8-29.
74. Campbell, P. G.; Marwitz, A. J. V.; Liu, S.-Y., Recent Advances in Azaborine Chemistry. *Angew. Chem. Int. Ed.* **2012**, *51*, 6074-6092.
75. Giustra, Z. X.; Liu, S.-Y., The State of the Art in Azaborine Chemistry: New Synthetic Methods and Applications. *J. Am. Chem. Soc.* **2018**, *140*, 1184-1194.
76. Helten, H., B=N Units as Part of Extended π -Conjugated Oligomers and Polymers. *Chem. Eur. J.* **2016**, *22*, 12972-12982.
77. Morgan, M. M.; Piers, W. E., Efficient Synthetic Methods for the Installation of Boron-Nitrogen Bonds in Conjugated Organic Molecules. *Dalton Trans.* **2016**, *45*, 5920-5924.
78. Wang, X.-Y.; Wang, J.-Y.; Pei, J., BN Heterosuperbenzenes: Synthesis and Properties. *Chem. Eur. J.* **2015**, *21*, 3528-3539.
79. Helten, H., Doping the Backbone of π -Conjugated Polymers with Tricoordinate Boron: Synthetic Strategies and Emerging Applications. *Chem. Asian J.* **2019**, *14*, 919-935.
80. Krieg, M.; Reicherter, F.; Haiss, P.; Ströbele, M.; Eichele, K.; Treanor, M.-J.; Schaub, R.; Bettinger, H. F., Construction of an Internally B₃N₃-Doped Nanographene Molecule. *Angew. Chem. Int. Ed.* **2015**, *54*, 8284-8286.
81. Otero, N.; El-Kelany, K. E.; Pouchan, C.; Rérat, M.; Karamanis, P., Establishing the Pivotal Role of Local Aromaticity in the Electronic Properties of Boron-Nitride Graphene Lateral Hybrids. *Phys. Chem. Chem. Phys.* **2016**, *18*, 25315-25328.

82. Otero, N. s.; Karamanis, P.; El-Kelany, K. E.; Rérat, M.; Maschio, L.; Civalleri, B.; Kirtman, B., Exploring the Linear Optical Properties of Borazine (B_3N_3) Doped Graphenes. 0D Flakes vs 2D Sheets. *J. Phys. Chem. C* **2017**, *121*, 709-722.
83. Belser, A.; Greulich, K.; Grüninger, P.; Bettinger, H. F.; Peisert, H.; Chassé, T., Visualization of the Borazine Core of B_3N_3 -Doped Nanographene by STM. *ACS Appl. Mater. Interfaces* **2020**, *12*, 19218-19225.
84. Kan, M.; Li, Y.; Sun, Q., Recent Advances in Hybrid Graphene-BN Planar Structures. *WIREs Computational Molecular Science* **2016**, *6*, 65-82.
85. Nagashima, A.; Tejima, N.; Gamou, Y.; Kawai, T.; Oshima, C., Electronic Dispersion Relations of Monolayer Hexagonal Boron Nitride Formed on the Ni(111) Surface. *Phys. Rev. B* **1995**, *51*, 4606-4613.
86. Bonifazi, D.; Fasano, F.; Lorenzo-Garcia, M. M.; Marinelli, D.; Oubaha, H.; Tasseroul, J., Boron–Nitrogen Doped Carbon Scaffolding: Organic Chemistry, Self-Assembly and Materials Applications of Borazine and Its Derivatives. *Chem. Commun.* **2015**, *51*, 15222-15236.
87. Lorenz, T.; Lik, A.; Plamper, F. A.; Helten, H., Dehydrocoupling and Silazane Cleavage Routes to Organic–Inorganic Hybrid Polymers with NBN Units in the Main Chain. *Angew. Chem. Int. Ed.* **2016**, *55*, 7236-7241.
88. Baggett, A. W.; Guo, F.; Li, B.; Liu, S. Y.; Jäkle, F., Regioregular Synthesis of Azaborine Oligomers and a Polymer with a Syn Conformation Stabilized by N H \cdots π Interactions. *Angew. Chem.* **2015**, *127*, 11343-11347.
89. Otero, N.; Karamanis, P.; El-Kelany, K. E.; Rérat, M.; Maschio, L.; Civalleri, B.; Kirtman, B., Exploring the Linear Optical Properties of Borazine (B_3N_3) Doped Graphenes. 0D Flakes vs 2D Sheets. *J. Phys. Chem. C* **2017**, *121*, 709-722.
90. Côté, M.; Haynes, P. D.; Molteni, C., Boron Nitride Polymers: Building Blocks for Organic Electronic Devices. *Phys. Rev. B* **2001**, *63*, 125207.
91. Sham, I. H. T.; Kwok, C.-C.; Che, C.-M.; Zhu, N., Borazine Materials for Organic Optoelectronic Applications. *Chem. Commun.* **2005**, 3547-3549.
92. Kervyn, S.; Fenwick, O.; Di Stasio, F.; Shin, Y. S.; Wouters, J.; Accorsi, G.; Osella, S.; Beljonne, D.; Cacialli, F.; Bonifazi, D., Polymorphism, Fluorescence, and Optoelectronic Properties of a Borazine Derivative. *Chem. Eur. J.* **2013**, *19*, 7771-7779.
93. Urgel, J. I.; Schwarz, M.; Garnica, M.; Stassen, D.; Bonifazi, D.; Ecija, D.; Barth, J. V.; Auwärter, W., Controlling Coordination Reactions and Assembly on a Cu(111) Supported Boron Nitride Monolayer. *J. Am. Chem. Soc.* **2015**, *137*, 2420-2423.
94. Dosso, J.; Tasseroul, J.; Fasano, F.; Marinelli, D.; Biot, N.; Fermi, A.; Bonifazi, D., Synthesis and Optoelectronic Properties of Hexa-Peri-Hexabenzoborazinocoronene. *Angew. Chem. Int. Ed.* **2017**, *56*, 4483-4487.
95. Chen, L.; Hernandez, Y.; Feng, X. L.; Müllen, K., From Nanographene and Graphene Nanoribbons to Graphene Sheets: Chemical Synthesis. *Angew. Chem. Int. Ed.* **2012**, *51*, 7640-7654.
96. Angelova, P., et al., A Universal Scheme to Convert Aromatic Molecular Monolayers into Functional Carbon Nanomembranes. *ACS Nano* **2013**, *7*, 6489-6497.
97. Müller, M.; Kübel, C.; Müllen, K., Giant Polycyclic Aromatic Hydrocarbons. *Chem. Eur. J.* **1998**, *4*, 2099-2109.
98. Ruffieux, P., et al., On-Surface Synthesis of Graphene Nanoribbons with Zigzag Edge Topology. *Nature* **2016**, *531*, 489-492.
99. Lin, Y.-M.; Dimitrakopoulos, C.; Jenkins, K. A.; Farmer, D. B.; Chiu, H.-Y.; Grill, A.; Avouris, P., 100-GHz Transistors from Wafer-Scale Epitaxial Graphene. *Science* **2010**, *327*, 662-662.
100. Wang, Y.; Shao, Y. Y.; Matson, D. W.; Li, J. H.; Lin, Y. H., Nitrogen-Doped Graphene and Its Application in Electrochemical Biosensing. *ACS Nano* **2010**, *4*, 1790-1798.
101. Lv, R.; Terrones, M., Towards New Graphene Materials: Doped Graphene Sheets and Nanoribbons. *Mater. Lett.* **2012**, *78*, 209-218.

102. Sánchez-Sánchez, C., et al., On-Surface Synthesis of BN-Substituted Heteroaromatic Networks. *ACS Nano* **2015**, *9*, 9228-9235.
103. Fajer, J.; Barkigia, K.; Smith, K.; Goff, D., *Consequences of Electron Transfer in Chlorophylls, Chlorins, and Porphyrins: Structural and Theoretical Considerations*; ACS Publications, 1986.
104. Geno, M. K.; Halpern, J., Why Does Nature Not Use the Porphyrin Ligand in Vitamin B12? *J. Am. Chem. Soc.* **1987**, *109*, 1238-1240.
105. Loew, G. H.; Harris, D. L., Role of the Heme Active Site and Protein Environment in Structure, Spectra, and Function of the Cytochrome P450s. *Chem. Rev.* **2000**, *100*, 407-420.
106. Alden, R. G.; Crawford, B. A.; Doolen, R.; Ondrias, M. R.; Shelnutz, J. A., Ruffling of Nickel(II) Octaethylporphyrin in Solution. *J. Am. Chem. Soc.* **1989**, *111*, 2070-2072.
107. Grüninger, P.; Greulich, K.; Karstens, R.; Belser, A.; Ovsyannikov, R.; Giangrisostomi, E.; Bettinger, H. F.; Batchelor, D.; Peisert, H.; Chassé, T., Highly Oriented Hexacene Molecules Grown in Thin Films on Cu(110)-(2 X 1)O. *J. Phys. Chem. C* **2019**, *123*, 27672-27680.
108. Novák, J.; Oehzelt, M.; Berkebile, S.; Koini, M.; Ules, T.; Koller, G.; Haber, T.; Resel, R.; Ramsey, M. G., Crystal Growth of Para-Sexiphenyl on Clean and Oxygen Reconstructed Cu (110) Surfaces. *Phys. Chem. Chem. Phys.* **2011**, *13*, 14675-14684.
109. M. Henzler; Göpel, W., *Oberflächenphysik des Festkörpers*; Teubner Stuttgart, 1994.
110. Göpel, W.; Ziegler, C., *Struktur der Materie*; Teubner Stuttgart Leipzig, 1994.
111. Hertz, H., Ueber Einen Einfluss des Ultravioletten Lichtes Auf Die Electriche Entladung. *Ann. Phys.* **1887**, *267*, 983-1000.
112. Hallwachs, W., Ueber Den Einfluss des Lichtes Auf Electrostaticch Geladene Körper. *Ann. Phys.* **1888**, *269*, 301-312.
113. Einstein, A., Über Einen Die Erzeugung Und Verwandlung des Lichtes Betreffenden Heuristischen Gesichtspunkt. *Ann. Phys.* **1905**, *322*, 132-148.
114. Fermi, E.; Orear, J., *Nuclear Physics*, 1950.
115. Seah, M. P.; Dench, W. A., Quantitative Electron Spectroscopy of Surfaces: A Standard Data Base for Electron Inelastic Mean Free Paths in Solids. *Surf. Interface Anal.* **1979**, *1*, 2-11.
116. Jablonski, A., Evaluation of Procedures for Overlayer Thickness Determination from XPS Intensities. *Surf. Sci.* **2019**, *688*, 14-24.
117. Seah, M. P., et al., Critical Review of the Current Status of Thickness Measurements for Ultrathin SiO₂ on Si Part V: Results of a CcqM Pilot Study. *Surf. Interface Anal.* **2004**, *36*, 1269-1303.
118. Seah, M., The Quantitative Analysis of Surfaces by XPS: A Review. *Surf. Interface Anal.* **1980**, *2*, 222-239.
119. Chastain, J.; King Jr, R. C., Handbook of X-Ray Photoelectron Spectroscopy. *Perkin-Elmer Corporation* **1992**, *40*, 221.
120. Hüfner, S., *Very High Resolution Photoelectron Spectroscopy*; Springer, 2007; Vol. 715.
121. Hüfner, S., *Photoelectron Spectroscopy: Principles and Applications*; Springer Science & Business Media, 2013.
122. Koch, E.-E., Photoemission from Organic Molecular Solids and Organometallic Compounds. *Phys. Scr.* **1987**, *1987*, 120.
123. Stöhr, J., *NEXAFS Spectroscopy*; Springer, 1992.
124. Breuer, T.; Klues, M.; Witte, G., Characterization of Orientational Order in pi-Conjugated Molecular Thin Films by NEXAFS. *J. Electron. Spectrosc. Relat. Phenom.* **2015**, *204*, 102-115.
125. Stöhr, J.; Outka, D. A., Determination of Molecular Orientations on Surfaces from the Angular Dependence of Near-Edge X-Ray Absorption Fine-Structure Spectra. *Phys. Rev. B* **1987**, *36*, 7891-7905.
126. Gurney, R. W.; Condon, E. U., Quantum Mechanics and Radioactive Disintegration. *Phys. Rev.* **1929**, *33*, 127-140.
127. Binnig, G.; Rohrer, H.; Gerber, C.; Weibel, E., Surface Studies by Scanning Tunneling Microscopy. *Phys. Rev. Lett.* **1982**, *49*, 57-61.

128. Binnig, G.; Rohrer, H., Scanning Tunneling Microscopy—from Birth to Adolescence (Nobel Lecture). *Angew. Chem.* **1987**, *26*, 606-614.
129. Katzir, S., *The Discovery of the Piezoelectric Effect*; Springer, 2006, p 15-64.
130. Courjon, D., *Scanning Tunneling Optical Microscopy*; Springer, 1990, p 497-505.
131. Bonča, J.; Trugman, S., Effect of Inelastic Processes on Tunneling. *Phys. Rev. Lett.* **1995**, *75*, 2566.
132. Gol'danskii, V. I.; Trakhtenberg, L. I.; Fleurov, V. N., *Tunneling Phenomena in Chemical Physics*; CRC Press, 1988.
133. Duck, F., 'The Electrical Expansion of Quartz' by Jacques and Pierre Curie. *Ultrasound* **2009**, *17*, 197-203.
134. Tersoff, J.; Lang, N. D., *1. Theory of Scanning Tunneling Microscopy*; Academic Press, 1993; Vol. 27, p 1-29.
135. Chen, C. J., Theory of Scanning Tunneling Spectroscopy. *J. Vac. Sci. Technol. A* **1988**, *6*, 319-322.
136. Tersoff, J.; Hamann, D. R., Theory and Application for the Scanning Tunneling Microscope. *Phys. Rev. Lett.* **1983**, *50*, 1998-2001.
137. Bardeen, J., Tunneling from a Many-Particle Point of View. *Phys. Rev. Lett.* **1961**, *6*, 57.
138. Tersoff, J.; Hamann, D. R., Theory of the Scanning Tunneling Microscope. *Phys. Rev. B* **1985**, *31*, 805.
139. Greulich, K., et al., Charge Transfer from Organic Molecules to Molybdenum Disulfide: Influence of the Fluorination of Iron Phthalocyanine. *J. Phys. Chem. C* **2020**, *124*, 16990–16999.
140. Karstens, R.; Glaser, M.; Belsler, A.; Balle, D.; Polek, M.; Ovsyannikov, R.; Giangrisostomi, E.; Chassé, T.; Peisert, H., FePc and FePcF₁₆ on Rutile TiO₂(110) and (100): Influence of the Substrate Preparation on the Interaction Strength. *Molecules* **2019**, *24*, 4579.
141. Peisert, H.; Biswas, I.; Knupfer, M.; Chassé, T., Orientation and Electronic Properties of Phthalocyanines on Polycrystalline Substrates. *Phys. Status Solidi B* **2009**, *246*, 1529-1545.
142. Rocco, M. L. M.; Frank, K. H.; Yannoulis, P.; Koch, E. E., Unoccupied Electronic Structure of Phthalocyanine Films. *J. Chem. Phys.* **1990**, *93*, 6859-6864.
143. Floreano, L.; Cossaro, A.; Gotter, R.; Verdini, A.; Bavdek, G.; Evangelista, F.; Ruocco, A.; Morgante, A.; Cvetko, D., Periodic Arrays of Cu-Phthalocyanine Chains on Au(110). *J. Phys. Chem. C* **2008**, *112*, 10794-10802.
144. Kothe, M.; Witte, G., Orientational and Crystalline Order of Copper–Phthalocyanine Films on Gold: The Role of Substrate Roughness and Cleanliness. *Langmuir* **2019**, *35*, 13570-13577.
145. Biswas, I.; Peisert, H.; Casu, M. B.; Schuster, B. E.; Nagel, P.; Merz, M.; Schuppler, S.; Chassé, T., Initial Molecular Orientation of Phthalocyanines on Oxide Substrates. *Phys. Status Solidi A* **2009**, *206*, 2524-2528.
146. Forrest, S. R., Ultrathin Organic Films Grown by Organic Molecular Beam Deposition and Related Techniques. *Chem. Rev.* **1997**, *97*, 1793-1896.
147. Okudaira, K. K.; Setoyama, H.; Yagi, H.; Mase, K.; Kera, S.; Kahn, A.; Ueno, N., Study of Excited States of Fluorinated Copper Phthalocyanine by Inner Shell Excitation. *J. Electron. Spectrosc. Relat. Phenom.* **2004**, *137*, 137-140.
148. Petraki, F.; Peisert, H.; Aygul, U.; Latteyer, F.; Uihlein, J.; Vollmer, A.; Chassé, T., Electronic Structure of FePc and Interface Properties on Ag(111) and Au(100). *J. Phys. Chem. C* **2012**, *116*, 11110-11116.
149. Kera, S.; Casu, M. B.; Bauchspiess, K. R.; Batchelor, D.; Schmidt, T.; Umbach, E., Growth Mode and Molecular Orientation of Phthalocyanine Molecules on Metal Single Crystal Substrates: A NEXAFS and XPS Study. *Surf. Sci.* **2006**, *600*, 1077-1084.
150. Glaser, M.; Peisert, H.; Adler, H.; Polek, M.; Uihlein, J.; Nagel, P.; Merz, M.; Schuppler, S.; Chassé, T., Transition-Metal Phthalocyanines on Transition-Metal Oxides: Iron and Cobalt Phthalocyanine on Epitaxial MnO and TiO_x Films. *J. Phys. Chem. C* **2015**, *119*, 27569-27579.

151. Uihlein, J. Einfluss von Graphen Auf Die Wechselwirkung Zwischen Phthalocyaninen Und Substrat. PhD Thesis, Eberhard Karls Universität Tübingen, 2015.
152. Pauling, L., *The Nature of the Chemical Bond*, 1960; Vol. 260.
153. Bralsford, R.; Harris, P. V.; Price, W. C., The Effect of Fluorine on the Electronic Spectra and Ionization Potentials of Molecules. *Proc. R. Soc. A* **1960**, *258*, 459-469.
154. Sheppard, W. A., The Electronic Properties of Fluoroalkyl Groups. Fluorine P- π Interaction. *J. Am. Chem. Soc.* **1965**, *87*, 2410-2420.
155. Müller, K.; Faeh, C.; Diederich, F., Fluorine in Pharmaceuticals: Looking Beyond Intuition. *Science* **2007**, *317*, 1881-1886.
156. Ni, C.; Hu, J., The Unique Fluorine Effects in Organic Reactions: Recent Facts and Insights into Fluoroalkylations. *Chem. Soc. Rev.* **2016**, *45*, 5441-5454.
157. Smart, B. E., Fluorine Substituent Effects (on Bioactivity). *J. Fluorine Chem.* **2001**, *109*, 3-11.
158. Shah, P.; Westwell, A. D., The Role of Fluorine in Medicinal Chemistry. *J. Enzyme Inhib. Med. Chem.* **2007**, *22*, 527-540.
159. Marom, N.; Kronik, L., Density Functional Theory of Transition Metal Phthalocyanines, I: Electronic Structure of NiPc and CoPc—Self-Interaction Effects. *Appl. Phys. A* **2009**, *95*, 159-163.
160. Marom, N.; Ren, X.; Moussa, J. E.; Chelikowsky, J. R.; Kronik, L., Electronic Structure of Copper Phthalocyanine from G(0)W(0) Calculations. *Phys. Rev. B* **2011**, *84*, 195143.
161. Piper, L. F. J.; Cho, S. W.; Zhang, Y.; DeMasi, A.; Smith, K. E.; Matsuura, A. Y.; McGuinness, C., Soft X-Ray Spectroscopy Study of the Element and Orbital Contributions to the Electronic Structure of Copper Hexadecafluoro-Phthalocyanine. *Phys. Rev. B* **2010**, *81*, 045201.
162. Kuz'min, M. D.; Hayn, R.; Oison, V., Ab Initio Calculated XANES and XMCD Spectra of Fe(II) Phthalocyanine. *Phys. Rev. B* **2009**, *79*, 024413.
163. Kuz'min, M. D.; Savoyant, A.; Hayn, R., Ligand Field Parameters and the Ground State of Fe(II) Phthalocyanine. *J. Chem. Phys.* **2013**, *138*, 244308.
164. Betti, M. G.; Gargiani, P.; Frisenda, R.; Biagi, R.; Cossaro, A.; Verdini, A.; Floreano, L.; Mariani, C., Localized and Dispersive Electronic States at Ordered FePc and CoPc Chains on Au(110). *J. Phys. Chem. C* **2010**, *114*, 21638-21644.
165. Bartolomé, J.; Bartolomé, F.; Garcia, L. M.; Filoti, G.; Gredig, T.; Colesniuc, C. N.; Schuller, I. K.; Cezar, J. C., Highly Unquenched Orbital Moment in Textured Fe-Phthalocyanine Thin Films. *Phys. Rev. B* **2010**, *81*.
166. Petraki, F.; Peisert, H.; Biswas, I.; Chassé, T., Electronic Structure of Co-Phthalocyanine on Gold Investigated by Photoexcited Electron Spectroscopies: Indication of Co Ion-Metal Interaction. *J. Phys. Chem. C* **2010**, *114*, 17638-17643.
167. Wallace, A. J.; Williamson, B. E.; Crittenden, D. L., Casscf-Based Explicit Ligand Field Models Clarify the Ground State Electronic Structures of Transition Metal Phthalocyanines (Mpc; M = Mn, Fe, Co, Ni, Cu, Zn). *Can. J. Chem.* **2016**, *94*, 1163-1168.
168. Zhang, T., et al., Conclusively Addressing the CoPc Electronic Structure: A Joint Gas-Phase and Solid-State Photoemission and Absorption Spectroscopy Study. *J. Phys. Chem. C* **2017**, *121*, 26372-26378.
169. Miedema, P. S.; de Groot, F. M. F., The Iron L Edges: Fe 2p X-Ray Absorption and Electron Energy Loss Spectroscopy. *J. Electron. Spectrosc. Relat. Phenom.* **2013**, *187*, 32-48.
170. Miedema, P. S.; Stepanow, S.; Gambardella, P.; de Groot, F. M. F., 2p X-Ray Absorption of Iron-Phthalocyanine. In *14th International Conference on X-Ray Absorption Fine Structure*, DiCicco, A.; Filipponi, A., Eds. Iop Publishing Ltd: Bristol, 2009; Vol. 190.
171. Fernández-Rodríguez, J.; Toby, B.; van Veenendaal, M., Mixed Configuration Ground State in Iron(II) Phthalocyanine. *Phys. Rev. B* **2015**, *91*, 214427.
172. Uihlein, J.; Peisert, H.; Adler, H.; Glaser, M.; Polek, M.; Ovsyannikov, R.; Chassé, T., Interface between FePc and Ni(111): Influence of Graphene Buffer Layers. *J. Phys. Chem. C* **2014**, *118*, 10106-10112.

173. Massimi, L.; Lisi, S.; Pacilè, D.; Mariani, C.; Betti, M. G., Interaction of Iron Phthalocyanine with the Graphene/Ni(111) System. *Beilstein J. Nanotechnol.* **2014**, *5*, 308-312.
174. Willey, T. M.; Bagge-Hansen, M.; Lee, J. R.; Call, R.; Landt, L.; van Buuren, T.; Colesniuc, C.; Monton, C.; Valmianski, I.; Schuller, I. K., Electronic Structure Differences between H₂-, Fe-, Co-, and Cu-Phthalocyanine Highly Oriented Thin Films Observed Using NEXAFS Spectroscopy. *J. Chem. Phys.* **2013**, *139*, 034701.
175. Holland, B. N.; Peltekis, N.; Farrelly, T.; Wilks, R. G.; Gavrilă, G.; Zahn, D. R. T.; McGuinness, C.; McGovern, I. T., NEXAFS Studies of Copper Phthalocyanine on Ge(001)-2 × 1 and Ge(111)-c(2 × 8) Surfaces. *Phys. Status Solidi A* **2009**, *246*, 1546-1551.
176. Petraki, F.; Peisert, H.; Hoffmann, P.; Uihlein, J.; Knupfer, M.; Chassé, T., Modification of the 3d-Electronic Configuration of Manganese Phthalocyanine at the Interface to Gold. *J. Phys. Chem. C* **2012**, *116*, 5121-5127.
177. Calabrese, A.; Floreano, L.; Verdini, A.; Mariani, C.; Betti, M. G., Filling Empty States in a CuPc Single Layer on the Au (110) Surface Via Electron Injection. *Phys. Rev. B* **2009**, *79*, 115446.
178. Åhlund, J.; Nilson, K.; Schiessling, J.; Kjeldgaard, L.; Berner, S.; Mårtensson, N.; Puglia, C.; Brena, B.; Nyberg, M.; Luo, Y., The Electronic Structure of Iron Phthalocyanine Probed by Photoelectron and X-Ray Absorption Spectroscopies and Density Functional Theory Calculations. *J. Chem. Phys.* **2006**, *125*, 034709.
179. Javaid, S., et al., Impact on Interface Spin Polarization of Molecular Bonding to Metallic Surfaces. *Phys. Rev. Lett.* **2010**, *105*, 077201.
180. Peisert, H.; Knupfer, M.; Fink, J., Energy Level Alignment at Organic/Metal Interfaces: Dipole and Ionization Potential. *Appl. Phys. Lett.* **2002**, *81*, 2400-2402.
181. Vazquez, H.; Dappe, Y. J.; Ortega, J.; Flores, F., Energy Level Alignment at Metal/Organic Semiconductor Interfaces: "Pillow" Effect, Induced Density of Interface States, and Charge Neutrality Level. *J. Chem. Phys.* **2007**, *126*, 144703.
182. Betti, M. G.; Kanjilal, A.; Mariani, C.; Vázquez, H.; Dappe, Y. J.; Ortega, J.; Flores, F., Barrier Formation at Organic Interfaces in a Cu(100)-Benzenethiolate-Pentacene Heterostructure. *Phys. Rev. Lett.* **2008**, *100*, 027601.
183. Yamane, H.; Yoshimura, D.; Kawabe, E.; Sumii, R.; Kanai, K.; Ouchi, Y.; Ueno, N.; Seki, K., Electronic Structure at Highly Ordered Organic/Metal Interfaces: Pentacene on Cu(110). *Phys. Rev. B* **2007**, *76*, 165436.
184. Björneholm, O.; Nilsson, A.; Sandell, A.; Hernnäs, B.; Mrtensson, N., Determination of Time Scales for Charge-Transfer Screening in Physisorbed Molecules. *Phys. Rev. Lett.* **1992**, *68*, 1892-1895.
185. Schmid, M.; Zirzmeier, J.; Steinrück, H.-P.; Gottfried, J. M., Interfacial Interactions of Iron(II) Tetrapyrrole Complexes on Au(111). *J. Phys. Chem. C* **2011**, *115*, 17028-17035.
186. Massimi, L.; Angelucci, M.; Gargiani, P.; Betti, M. G.; Montoro, S.; Mariani, C., Metal-Phthalocyanine Ordered Layers on Au(110): Metal-Dependent Adsorption Energy. *J. Chem. Phys.* **2014**, *140*, 244704.
187. Pawlak, R., et al., Design and Characterization of an Electrically Powered Single Molecule on Gold. *ACS Nano* **2017**, *11*, 9930-9940.
188. Nefedov, V. I., *Izv. Nats. Akad. Nauk Resp., Ser. Fiz.* **1964**, *28*, 816.
189. Betti, M. G.; Gargiani, P.; Mariani, C.; Turchini, S.; Zema, N.; Fortuna, S.; Calzolari, A.; Fabris, S., Formation of Hybrid Electronic States in FePc Chains Mediated by the Au(110) Surface. *J. Phys. Chem. C* **2012**, *116*, 8657-8663.
190. Scarfato, A.; Chang, S. H.; Kuck, S.; Brede, J.; Hoffmann, G.; Wiesendanger, R., Scanning Tunneling Microscope Study of Iron(II) Phthalocyanine Growth on Metals and Insulating Surfaces. *Surf. Sci.* **2008**, *602*, 677-683.
191. Ferretti, A.; Baldacchini, C.; Calzolari, A.; Di Felice, R.; Ruini, A.; Molinari, E.; Betti, M. G., Mixing of Electronic States in Pentacene Adsorption on Copper. *Phys. Rev. Lett.* **2007**, *99*.

192. Baldacchini, C.; Allegretti, F.; Gunnella, R.; Betti, M. G., Molecule-Metal Interaction of Pentacene on Copper Vicinal Surfaces. *Surf. Sci.* **2007**, *601*, 2603-2606.
193. Koch, N.; Gerlach, A.; Duhm, S.; Glowatzki, H.; Heimel, G.; Vollmer, A.; Sakamoto, Y.; Suzuki, T.; Zegenhagen, J.; Rabe, J. P., Adsorption-Induced Intramolecular Dipole: Correlating Molecular Conformation and Interface Electronic Structure. *J. Am. Chem. Soc.* **2008**, *130*, 7300-7304.
194. Muller, K.; Seitsonen, A. P.; Brugger, T.; Westover, J.; Greber, T.; Jung, T.; Kara, A., Electronic Structure of an Organic/Metal Interface: Pentacene/Cu(110). *J. Phys. Chem. C* **2012**, *116*, 23465-23471.
195. Ules, T.; Luftner, D.; Reinisch, E. M.; Koller, G.; Puschnig, P.; Ramsey, M. G., Orbital Tomography of Hybridized and Dispersing Molecular Overlayers. *Phys. Rev. B* **2014**, *90*, 8.
196. Shen, K. C., et al., On-Surface Manipulation of Atom Substitution between Cobalt Phthalocyanine and the Cu(111) Substrate. *RSC Adv.* **2017**, *7*, 13827-13835.
197. Coulman, D. J.; Wintterlin, J.; Behm, R.; Ertl, G., Novel Mechanism for the Formation of Chemisorption Phases: The (2×1) O-Cu (110) "Added Row" Reconstruction. *Phys. Rev. Lett.* **1990**, *64*, 1761.
198. Jensen, F.; Besenbacher, F.; Lægsgaard, E.; Stensgaard, I., Surface Reconstruction of Cu (110) Induced by Oxygen Chemisorption. *Phys. Rev. B* **1990**, *41*, 10233.
199. Duan, X.; Warschkow, O.; Soon, A.; Delley, B.; Stampfl, C., Density Functional Study of Oxygen on Cu(100) and Cu(110) Surfaces. *Phys. Rev. B* **2010**, *81*, 15.
200. Nakamura, J.; Campbell, J. M.; Campbell, C. T., Kinetics and Mechanism of the Water-Gas Shift Reaction Catalysed by the Clean and Cs-Promoted Cu(110) Surface: A Comparison with Cu(111). *J. Chem. Soc., Faraday Trans.* **1990**, *86*, 2725-2734.
201. Petraki, F.; Peisert, H.; Uihlein, J.; Aygül, U.; Chassé, T., CoPc and CoPcF₁₆ on Gold: Site-Specific Charge-Transfer Processes. *Beilstein J. Nanotechnol.* **2014**, *5*, 524-531.
202. Schmid, M.; Kaftan, A.; Steinruck, H. P.; Gottfried, J. M., The Electronic Structure of Cobalt(II) Phthalocyanine Adsorbed on Ag(111). *Surf. Sci.* **2012**, *606*, 945-949.
203. Lindner, S.; Treske, U.; Grobosch, M.; Knupfer, M., Charge Transfer at F16CoPc and CoPc Interfaces to Au. *Appl. Phys. A* **2011**, *105*, 921-925.
204. Lindner, S.; Treske, U.; Knupfer, M., The Complex Nature of Phthalocyanine/Gold Interfaces. *Appl. Surf. Sci.* **2013**, *267*, 62-65.
205. Toader, M.; Knupfer, M.; Zahn, D. R. T.; Hietschold, M., Initial Growth at the F16CoPc/Ag(111) Interface. *Surf. Sci.* **2011**, *605*, 1510-1515.
206. Feidenhans'l, R.; Stensgaard, I., Oxygen-Adsorption Induced Reconstruction of Cu(110) Studied by High Energy Ion Scattering. *Surf. Sci.* **1983**, *133*, 453-468.
207. Ruckerl, F.; Waas, D.; Buchner, B.; Knupfer, M., Particular Electronic Properties of F16CoPc: A Decent Electron Acceptor Material. *J. Electron. Spectrosc. Relat. Phenom.* **2017**, *215*, 1-7.
208. Li, Z.; Li, B.; Yang, J.; Hou, J. G., Single-Molecule Chemistry of Metal Phthalocyanine on Noble Metal Surfaces. *Acc. Chem. Res.* **2010**, *43*, 954-962.
209. Peisert, H.; Kolacyak, D.; Chassé, T., Site-Specific Charge-Transfer Screening at Organic/Metal Interfaces. *J. Phys. Chem. C* **2009**, *113*, 19244-19250.
210. Kaindl, G.; Chiang, T. C.; Eastman, D. E.; Himpsel, F. J., Distance-Dependent Relaxation Shifts of Photoemission and Auger Energies for Xe on Pd(001). *Phys. Rev. Lett.* **1980**, *45*, 1808-1811.
211. Moretti, G., The Wagner Plot and the Auger Parameter as Tools to Separate Initial- and Final-State Contributions in X-Ray Photoemission Spectroscopy. *Surf. Sci.* **2013**, *618*, 3-11.
212. Kolacyak, D.; Peisert, H.; Chasse, T., Charge Transfer and Polarization Screening in Organic Thin Films: Phthalocyanines on Au(100). *Appl. Phys. A* **2009**, *95*, 173-178.
213. Chiang, T. C.; Kaindl, G.; Mandel, T., Layer-Resolved Shifts of Photoemission and Auger-Spectra from Physisorbed Rare-Gas Multilayers. *Phys. Rev. B* **1986**, *33*, 695-711.

214. Peisert, H.; Petershans, A.; Chassé, T., Charge Transfer and Polarization Screening at Organic/Metal Interfaces: Distinguishing between the First Layer and Thin Films. *J. Phys. Chem. C* **2008**, *112*, 5703-5706.
215. Schmidt, C.; Breuer, T.; Wippermann, S.; Schmidt, W. G.; Witte, G., Substrate Induced Thermal Decomposition of Perfluoro-Pentacene Thin Films on the Coinage Metals. *J. Phys. Chem. C* **2012**, *116*, 24098-24106.
216. Nie, S.; Bartelt, N. C.; Wofford, J. M.; Dubon, O. D.; McCarty, K. F.; Thürmer, K., Scanning Tunneling Microscopy Study of Graphene on Au (111): Growth Mechanisms and Substrate Interactions. *Phys. Rev. B* **2012**, *85*, 205406.
217. Oznuluer, T.; Pince, E.; Polat, E. O.; Balci, O.; Salihoglu, O.; Kocabas, C., Synthesis of Graphene on Gold. *Appl. Phys. Lett.* **2011**, *98*, 183101.
218. Proehl, H.; Toerker, M.; Sellam, F.; Fritz, T.; Leo, K.; Simpson, C.; Müllen, K., Comparison of Ultraviolet Photoelectron Spectroscopy and Scanning Tunneling Spectroscopy Measurements on Highly Ordered Ultrathin Films of Hexa-Peri-Hexabenzocoronene on Au (111). *Phys. Rev. B* **2001**, *63*, 205409.
219. Sellam, F.; Schmitz-Hübsch, T.; Toerker, M.; Mannsfeld, S.; Proehl, H.; Fritz, T.; Leo, K.; Simpson, C.; Müllen, K., LEED and STM Investigations of Organic–Organic Heterostructures Grown by Molecular Beam Epitaxy. *Surf. Sci.* **2001**, *478*, 113-121.
220. Ruffieux, P.; Gröning, O.; Biemann, M.; Simpson, C.; Müllen, K.; Schlapbach, L.; Gröning, P., Supramolecular Columns of Hexabenzocoronenes on Copper and Gold (111) Surfaces. *Phys. Rev. B* **2002**, *66*, 073409.
221. Gopakumar, T.; Lackinger, M.; Hackert, M.; Müller, F.; Hietschold, M., Adsorption of Palladium Phthalocyanine on Graphite: STM and LEED Study. *J. Phys. Chem. B* **2004**, *108*, 7839-7843.
222. Hamalainen, S. K.; Stepanova, M.; Drost, R.; Liljeroth, P.; Lahtinen, J.; Sainio, J., Self-Assembly of Cobalt-Phthalocyanine Molecules on Epitaxial Graphene on Ir(111). *J. Phys. Chem. C* **2012**, *116*, 20433-20437.
223. Buchholz, J.; Somorjai, G., The Surface Structures of Phthalocyanine Monolayers and Vapor-Grown Films: A Low-Energy Electron Diffraction Study. *J. Chem. Phys.* **1977**, *66*, 573-580.
224. England, C.; Collins, G.; Schuerlein, T.; Armstrong, N., Epitaxial Thin Films of Large Organic Molecules: Characterization of Phthalocyanine and Coronene Overlayers on the Layered Semiconductors MoS₂ and SnS₂. *Langmuir* **1994**, *10*, 2748-2756.
225. Jarvinen, P.; Hamalainen, S. K.; Ijas, M.; Harju, A.; Liljeroth, P., Self-Assembly and Orbital Imaging of Metal Phthalocyanines on a Graphene Model Surface. *J. Phys. Chem. C* **2014**, *118*, 13320-13325.
226. Barlow, D. E.; Hipps, K. W., A Scanning Tunneling Microscopy and Spectroscopy Study of Vanadyl Phthalocyanine on Au(111): The Effect of Oxygen Binding and Orbital Mediated Tunneling on the Apparent Corrugation. *J. Phys. Chem. B* **2000**, *104*, 5993-6000.
227. Yamane, H.; Kosugi, N., Site-Specific Intermolecular Valence-Band Dispersion in A-Phase Crystalline Films of Cobalt Phthalocyanine Studied by Angle-Resolved Photoemission Spectroscopy. *J. Chem. Phys.* **2014**, *141*, 224701.
228. Petraki, F.; Peisert, H.; Biswas, I.; Aygul, U.; Latteyer, F.; Vollmer, A.; Chassé, T., Interaction between Cobalt Phthalocyanine and Gold Studied by X-Ray Absorption and Resonant Photoemission Spectroscopy. *J. Phys. Chem. Lett.* **2010**, *1*, 3380-3384.
229. Barlow, D. E.; Scudiero, L.; Hipps, K., Scanning Tunneling Microscopy Study of the Structure and Orbital-Mediated Tunneling Spectra of Cobalt (II) Phthalocyanine and Cobalt (II) Tetraphenylporphyrin on Au (111): Mixed Composition Films. *Langmuir* **2004**, *20*, 4413-4421.
230. Gargiani, P.; Angelucci, M.; Mariani, C.; Betti, M. G., Metal-Phthalocyanine Chains on the Au(110) Surface: Interaction States Versus D-Metal States Occupancy. *Phys. Rev. B* **2010**, *81*.

231. Zhang, Y. Y.; Du, S. X.; Gao, H. J., Binding Configuration, Electronic Structure, and Magnetic Properties of Metal Phthalocyanines on a Au(111) Surface Studied with Ab Initio Calculations. *Phys. Rev. B* **2011**, *84*, 125446.
232. Gargiani, P., et al., Spin and Orbital Configuration of Metal Phthalocyanine Chains Assembled on the Au(110) Surface. *Phys. Rev. B* **2013**, *87*, 165407.
233. Koch, E.; Jugnet, Y.; Himpsel, F., High-Resolution Soft X-Ray Excitation Spectra of 3d-Metal Phthalocyanines. *Chem. Phys. Lett.* **1985**, *116*, 7-11.
234. Uihlein, J., et al., Influence of Graphene on Charge Transfer between CoPc and Metals: The Role of Graphene–Substrate Coupling. *J. Phys. Chem. C* **2015**, *119*, 15240-15247.
235. Amsalem, P.; Wilke, A.; Frisch, J.; Niederhausen, J.; Vollmer, A.; Rieger, R.; Müllen, K.; Rabe, J.; Koch, N., Interlayer Molecular Diffusion and Thermodynamic Equilibrium in Organic Heterostructures on a Metal Electrode. *J. Appl. Phys.* **2011**, *110*, 113709.
236. Duhm, S.; Salzmann, I.; Bröker, B.; Glowatzki, H.; Johnson, R. L.; Koch, N., Interdiffusion of Molecular Acceptors through Organic Layers to Metal Substrates Mimics Doping-Related Energy Level Shifts. *Appl. Phys. Lett.* **2009**, *95*, 223.
237. Gallego, J. M.; Ecija, D.; Martín, N.; Otero, R.; Miranda, R., An STM Study of Molecular Exchange Processes in Organic Thin Film Growth. *Chem. Commun.* **2014**, *50*, 9954-9957.
238. Stadtmüller, B.; Gruenewald, M.; Peuker, J.; Forker, R.; Fritz, T.; Kumpf, C., Molecular Exchange in a Heteromolecular PTCDA/CuPc Bilayer Film on Ag (111). *J. Phys. Chem. C* **2014**, *118*, 28592-28602.
239. Wang, Q.; Franco-Cañellas, A.; Ji, P.; Bürker, C.; Wang, R.-B.; Broch, K.; Thakur, P. K.; Lee, T.-L.; Zhang, H.; Gerlach, A., Bilayer Formation vs Molecular Exchange in Organic Heterostructures: Strong Impact of Subtle Changes in Molecular Structure. *J. Phys. Chem. C* **2018**, *122*, 9480-9490.
240. Goiri, E.; Borghetti, P.; El-Sayed, A.; Ortega, J. E.; de Oteyza, D. G., Multi-Component Organic Layers on Metal Substrates. *Adv. Mater.* **2016**, *28*, 1340-1368.
241. Jakobs, S.; Narayan, A.; Stadtmüller, B.; Droghetti, A.; Rungger, I.; Hor, Y. S.; Klyatskaya, S.; Jungkenn, D.; Stöckl, J.; Laux, M., Controlling the Spin Texture of Topological Insulators by Rational Design of Organic Molecules. *Nano Lett.* **2015**, *15*, 6022-6029.
242. Maurer, R. J.; Ruiz, V. G.; Camarillo-Cisneros, J.; Liu, W.; Ferri, N.; Reuter, K.; Tkatchenko, A., Adsorption Structures and Energetics of Molecules on Metal Surfaces: Bridging Experiment and Theory. *Prog. Surf. Sci.* **2016**, *91*, 72-100.
243. Zamborlini, G.; Lüftner, D.; Feng, Z.; Kollmann, B.; Puschnig, P.; Dri, C.; Panighel, M.; Di Santo, G.; Goldoni, A.; Comelli, G., Multi-Orbital Charge Transfer at Highly Oriented Organic/Metal Interfaces. *Nat. Commun.* **2017**, *8*, 1-8.
244. Hofmann, O.; Glowatzki, H.; Bürker, C.; Rangger, G.; Bröker, B.; Niederhausen, J.; Hosokai, T.; Salzmann, I.; Blum, R.-P.; Rieger, R., Orientation-Dependent Work-Function Modification Using Substituted Pyrene-Based Acceptors. *J. Phys. Chem. C* **2017**, *121*, 24657-24668.
245. Riss, A.; Paz, A. P.; Wickenburg, S.; Tsai, H.-Z.; De Oteyza, D. G.; Bradley, A. J.; Ugeda, M. M.; Gorman, P.; Jung, H. S.; Crommie, M. F., Imaging Single-Molecule Reaction Intermediates Stabilized by Surface Dissipation and Entropy. *Nat. Chem.* **2016**, *8*, 678-683.
246. Jiang, L.; Papageorgiou, A. C.; Oh, S. C.; Sağlam, O. z.; Reichert, J.; Duncan, D. A.; Zhang, Y.-Q.; Klappenberger, F.; Guo, Y.; Allegretti, F., Synthesis of Pyrene-Fused Pyrazaacenes on Metal Surfaces: Toward One-Dimensional Conjugated Nanostructures. *ACS Nano* **2016**, *10*, 1033-1041.
247. Ugolotti, A.; Harivyasi, S. S.; Baby, A.; Dominguez, M.; Pinardi, A. L.; López, M. F.; Martín-Gago, J. Á.; Fratesi, G.; Floreano, L.; Brivio, G. P., Chemisorption of Pentacene on Pt (111) with a Little Molecular Distortion. *J. Phys. Chem. C* **2017**, *121*, 22797-22805.
248. Sun, L.; Liu, C.; Queteschner, D.; Weidinger, G.; Zeppenfeld, P., Layer Inversion in Organic Heterostructures. *Phys. Chem. Chem. Phys.* **2011**, *13*, 13382-13386.
249. Gruenewald, M.; Sauer, C.; Peuker, J.; Meissner, M.; Sojka, F.; Schöll, A.; Reinert, F.; Forker, R.; Fritz, T., Commensurism at Electronically Weakly Interacting Phthalocyanine/PTCDA Heterointerfaces. *Phys. Rev. B* **2015**, *91*, 155432.

250. Kleimann, C.; Stadtmüller, B.; Schröder, S.; Kumpf, C., Electrostatic Interaction and Commensurate Registry at the Heteromolecular F16cupc–CuPc Interface. *J. Phys. Chem. C* **2014**, *118*, 1652-1660.
251. Häming, M.; Greif, M.; Sauer, C.; Schöll, A.; Reinert, F., Electronic Structure of Ultrathin Heteromolecular Organic-Metal Interfaces: SnPc/PTCDA/Ag (111) and SnPc/Ag (111). *Phys. Rev. B* **2010**, *82*, 235432.
252. Borghetti, P.; De Oteyza, D.; Rogero, C.; Goiri, E.; Verdini, A.; Cossaro, A.; Floreano, L.; Ortega, J. E., Molecular-Level Realignment in Donor–Acceptor Bilayer Blends on Metals. *J. Phys. Chem. C* **2016**, *120*, 5997-6005.
253. Zhang, X.; Shao, Z.; Zhang, X.; He, Y.; Jie, J., Surface Charge Transfer Doping of Low-Dimensional Nanostructures toward High-Performance Nanodevices. *Adv. Mater.* **2016**, *28*, 10409-10442.
254. Akaike, K.; Nardi, M. V.; Oehzelt, M.; Frisch, J.; Opitz, A.; Christodoulou, C.; Ligorio, G.; Beyer, P.; Timpel, M.; Pis, I., Effective Work Function Reduction of Practical Electrodes Using an Organometallic Dimer. *Adv. Funct. Mater.* **2016**, *26*, 2493-2502.
255. Yamane, H.; Kosugi, N., Site-Specific Organic/Metal Interaction Revealed from Shockley-Type Interface State. *J. Phys. Chem. C* **2016**, *120*, 24307-24313.
256. Petraki, F.; Peisert, H.; Latteyer, F.; Aygul, U.; Vollmer, A.; Chassé, T., Impact of the 3d Electronic States of Cobalt and Manganese Phthalocyanines on the Electronic Structure at the Interface to Ag(111). *J. Phys. Chem. C* **2011**, *115*, 21334-21340.
257. Bouju, X.; Mattioli, C.; Franc, G.; Pujol, A.; Gourdon, A., Bicomponent Supramolecular Architectures at the Vacuum–Solid Interface. *Chem. Rev.* **2017**, *117*, 1407-1444.
258. El-Sayed, A.; Borghetti, P.; Goiri, E.; Rogero, C.; Floreano, L.; Lovat, G.; Mowbray, D. J.; Cabellos, J. L.; Wakayama, Y.; Rubio, A., Understanding Energy-Level Alignment in Donor–Acceptor/Metal Interfaces from Core-Level Shifts. *ACS Nano* **2013**, *7*, 6914-6920.
259. Wakayama, Y., On-Surface Molecular Nanoarchitectonics: From Self-Assembly to Directed Assembly. *Jpn. J. Appl. Phys.* **2016**, *55*, 1102AA.
260. Henneke, C.; Felter, J.; Schwarz, D.; Tautz, F. S.; Kumpf, C., Controlling the Growth of Multiple Ordered Heteromolecular Phases by Utilizing Intermolecular Repulsion. *Nat. Mater.* **2017**, *16*, 628-633.
261. Lu, X.; Hipps, K.; Wang, X.; Mazur, U., Scanning Tunneling Microscopy of Metal Phthalocyanines: d⁷ and d⁹ Cases. *J. Am. Chem. Soc.* **1996**, *118*, 7197-7202.
262. Lu, X.; Hipps, K., Scanning Tunneling Microscopy of Metal Phthalocyanines: d⁶ and d⁸ Cases. *J. Phys. Chem. B* **1997**, *101*, 5391-5396.
263. Takada, M.; Tada, H., Low Temperature Scanning Tunneling Microscopy of Phthalocyanine Multilayers on Au(111) Surfaces. *Chem. Phys. Lett.* **2004**, *392*, 265-269.
264. Tracz, A.; Jeszka, J. K.; Watson, M. D.; Pisula, W.; Müllen, K.; Pakula, T., Uniaxial Alignment of the Columnar Super-Structure of a Hexa (Alkyl) Hexa-Peri-Hexabenzocoronene on Untreated Glass by Simple Solution Processing. *J. Am. Chem. Soc.* **2003**, *125*, 1682-1683.
265. Wang, Q.; Setlur, A.; Lauerhaas, J.; Dai, J.; Seelig, E.; Chang, R. P., A Nanotube-Based Field-Emission Flat Panel Display. *Appl. Phys. Lett.* **1998**, *72*, 2912-2913.
266. Liu, C.-y.; Fechtenkötter, A.; Watson, M. D.; Müllen, K.; Bard, A. J., Room Temperature Discotic Liquid Crystalline Thin Films of Hexa-Peri-Hexabenzocoronene: Synthesis and Optoelectronic Properties. *Chem. Mater.* **2003**, *15*, 124-130.
267. Jung, H.-T.; Kim, S. O.; Ko, Y.; Yoon, D. K.; Hudson, S.; Percec, V.; Holerca, M.; Cho, W.-D.; Mosier, P., Surface Order in Thin Films of Self-Assembled Columnar Liquid Crystals. *Macromolecules* **2002**, *35*, 3717-3721.
268. Friedlein, R.; Crispin, X.; Simpson, C.; Watson, M. D.; Jäckel, F.; Osikowicz, W.; Marciniak, S.; de Jong, M. P.; Samori, P.; Jönsson, S., Electronic Structure of Highly Ordered Films of Self-Assembled Graphitic Nanocolumns. *Phys. Rev. B* **2003**, *68*, 195414.

269. Smolenyak, P.; Peterson, R.; Nebesny, K.; Törker, M.; O'Brien, D. F.; Armstrong, N. R., Highly Ordered Thin Films of Octasubstituted Phthalocyanines. *J. Am. Chem. Soc.* **1999**, *121*, 8628-8636.
270. Donley, C. L.; Xia, W.; Minch, B. A.; Zangmeister, R. A.; Drager, A. S.; Nebesny, K.; O'Brien, D. F.; Armstrong, N. R., Thin Films of Polymerized Rodlike Phthalocyanine Aggregates. *Langmuir* **2003**, *19*, 6512-6522.
271. Struzzi, C.; Scardamaglia, M.; Angelucci, M.; Massimi, L.; Mariani, C.; Betti, M. G., Adsorption Energy of Iron-Phthalocyanine on Crystal Surfaces. *Il nuovo cimento C* **2013**, *36*, 51-57.
272. Weippert, J.; Hauns, J.; Bachmann, J.; Böttcher, A.; Yao, X.; Yang, B.; Narita, A.; Müllen, K.; Kappes, M. M., A Tpd-Based Determination of the Graphite Interlayer Cohesion Energy. *J. Chem. Phys.* **2018**, *149*, 194701.
273. Gross, L.; Moresco, F.; Ruffieux, P.; Gourdon, A.; Joachim, C.; Rieder, K.-H., Tailoring Molecular Self-Organization by Chemical Synthesis: Hexaphenylbenzene, Hexa-Peri-Hexabenzocoronene, and Derivatives on Cu (111). *Phys. Rev. B* **2005**, *71*, 165428.
274. Wagner, C.; Kasemann, D.; Golnik, C.; Forker, R.; Esslinger, M.; Müllen, K.; Fritz, T., Repulsion between Molecules on a Metal: Monolayers and Submonolayers of Hexa-Peri-Hexabenzocoronene on Au(111). *Phys. Rev. B* **2010**, *81*, 035423.
275. Zhang, X.; Tang, L.; Guo, Q., Low-Temperature Growth of C60 Monolayers on Au(111): Island Orientation Control with Site-Selective Nucleation. *J. Phys. Chem. C* **2010**, *114*, 6433-6439.
276. Yokoyama, T.; Yokoyama, S.; Kamikado, T.; Okuno, Y.; Mashiko, S., Selective Assembly on a Surface of Supramolecular Aggregates with Controlled Size and Shape. *Nature* **2001**, *413*, 619-621.
277. Gao, L., et al., Constructing an Array of Anchored Single-Molecule Rotors on Gold Surfaces. *Phys. Rev. Lett.* **2008**, *101*, 197209.
278. Cheng, Z. H.; Gao, L.; Deng, Z. T.; Jiang, N.; Liu, Q.; Shi, D. X.; Du, S. X.; Guo, H. M.; Gao, H. J., Adsorption Behavior of Iron Phthalocyanine on Au(111) Surface at Submonolayer Coverage. *J. Phys. Chem. C* **2007**, *111*, 9240-9244.
279. Beyer, P.; Breuer, T.; Ndiaye, S.; Zykov, A.; Viertel, A.; Gensler, M.; Rabe, J. P.; Hecht, S.; Witte, G.; Kowarik, S., Lattice Matching as the Determining Factor for Molecular Tilt and Multilayer Growth Mode of the Nanographene Hexa-peri-hexabenzocoronene. *ACS Appl. Mater. Interfaces* **2014**, *6*, 21484-21493.
280. Breuer, T.; Klues, M.; Liesfeld, P.; Viertel, A.; Conrad, M.; Hecht, S.; Witte, G., Self-Assembly of Partially Fluorinated Hexabenzocoronene Derivatives in the Solid State. *Phys. Chem. Chem. Phys.* **2016**, *18*, 33344-33350.
281. Keil, M.; Samorí, P.; dos Santos, D. A.; Kugler, T.; Stafström, S.; Brand, J. D.; Müllen, K.; Brédas, J. L.; Rabe, J. P.; Salaneck, W. R., Influence of the Morphology on the Electronic Structure of Hexa-peri-hexabenzocoronene Thin Films. *J. Phys. Chem. B* **2000**, *104*, 3967-3975.
282. Simonov, K. A.; Vinogradov, N. A.; Vinogradov, A. S.; Generalov, A. V.; Zagrebina, E. M.; Mårtensson, N.; Cafolla, A. A.; Carpy, T.; Cuniffe, J. P.; Preobrajenski, A. B., Effect of Substrate Chemistry on the Bottom-up Fabrication of Graphene Nanoribbons: Combined Core-Level Spectroscopy and STM Study. *J. Phys. Chem. C* **2014**, *118*, 12532-12540.
283. Grüninger, P., et al., Electronic Structure of Hexacene and Interface Properties on Au(110). *J. Phys. Chem. C* **2018**, *122*, 19491-19498.
284. Alagia, M.; Baldacchini, C.; Betti, M. G.; Bussolotti, F.; Carravetta, V.; Ekstrom, U.; Mariani, C.; Stranges, S., Core-Shell Photoabsorption and Photoelectron Spectra of Gas-Phase Pentacene: Experiment and Theory. *J. Chem. Phys.* **2005**, *122*.
285. Ciccullo, F.; Calzolari, A.; Piš, I.; Savu, S. A.; Krieg, M.; Bettinger, H. F.; Magnano, E.; Chassé, T.; Casu, M. B., A Quasi-Free-Standing Single Layer of a B₃N₃-Doped Nanographene Molecule Deposited on Au(111) Single Crystals. *J. Phys. Chem. C* **2016**, *120*, 17645-17651.
286. Neese, F., The Orca Program System. *Wiley Interdiscip. Rev. Comput.* **2012**, *2*, 73-78.

287. Hermann, K., et al. StoBe-deMon Version 3.3 (2014). <http://www.fhi-berlin.mpg.de/KHsoftware/StoBe>.
288. Luo, Y.; Ågren, H.; Keil, M.; Friedlein, R.; Salaneck, W. R., A Theoretical Investigation of the Near-Edge X-Ray Absorption Spectrum of Hexa-Peri-Hexabenzocoronene. *Chem. Phys. Lett.* **2001**, 337, 176-180.
289. Kang, S.; Yi, Y.; Kim, C.; Cho, S.; Noh, M.; Jeong, K.; Whang, C., Energy Level Diagrams of C60/Pentacene/Au and Pentacene/C60/Au. *Synth. Met.* **2006**, 156, 32-37.
290. Peisert, H.; Knupfer, M.; Fink, J., Electronic Structure of Partially Fluorinated Copper Phthalocyanine (CuPcF₄) and Its Interface to Au(100). *Surf. Sci.* **2002**, 515, 491-498.
291. Peisert, H.; Knupfer, M.; Schwieger, T.; Auerhammer, J. M.; Golden, M. S.; Fink, J., Full Characterization of the Interface between the Organic Semiconductor Copper Phthalocyanine and Gold. *J. Appl. Phys.* **2002**, 91, 4872-4878.
292. Uihlein, J.; Peisert, H.; Adler, H.; Glaser, M.; Polek, M.; Ovsyannikov, R.; Bauer, M.; Chassé, T., Strong Interaction of MnPc on Ni(111): Influence of Graphene Buffer Layer. *J. Phys. Chem. C* **2014**, 118, 28671-28678.
293. Lehwald, S.; Ibach, H., Decomposition of Hydrocarbons on Flat and Stepped Ni(111) Surfaces. *Surf. Sci.* **1979**, 89, 425-445.
294. Umbach, E.; Glöckler, K.; Sokolowski, M., Surface "Architecture" with Large Organic Molecules: Interface Order and Epitaxy. *Surf. Sci.* **1998**, 402-404, 20-31.
295. Demuth, J. E., The Interaction of Acetylene with Ni(111), Chemisorbed Oxygen on Ni(111), and NiO(111); the Formation of C₁ Species on Chemically Modified Ni(111) Surfaces. *Surf. Sci.* **1977**, 69, 365-384.
296. Mittendorfer, F.; Garhofer, A.; Redinger, J.; Klimeš, J.; Harl, J.; Kresse, G., Graphene on Ni (111): Strong Interaction and Weak Adsorption. *Phys. Rev. B* **2011**, 84, 201401.
297. Chorkendorff, I.; Russell Jr, J.; Yates Jr, J., Surface Reaction Pathways of Methylamine on the Ni (111) Surface. *J. Chem. Phys.* **1987**, 86, 4692-4700.
298. Gates, S.; Russell Jr, J.; Yates Jr, J., Bond Activation Sequence Observed in the Chemisorption and Surface Reaction of Ethanol on Ni (111). *Surf. Sci.* **1986**, 171, 111-134.
299. Dinca, L. E.; Fu, C.; MacLeod, J. M.; Lipton-Duffin, J.; Brusso, J. L.; Szakacs, C. E.; Ma, D.; Perepichka, D. F.; Rosei, F., Unprecedented Transformation of Tetrathienoanthracene into Pentacene on Ni (111). *ACS Nano* **2013**, 7, 1652-1657.
300. Dinca, L.; De Marchi, F.; MacLeod, J.; Lipton-Duffin, J.; Gatti, R.; Ma, D.; Perepichka, D.; Rosei, F., Pentacene on Ni (111): Room-Temperature Molecular Packing and Temperature-Activated Conversion to Graphene. *Nanoscale* **2015**, 7, 3263-3269.
301. Auwärter, W.; Suter, H. U.; Sachdev, H.; Greber, T., Synthesis of One Monolayer of Hexagonal Boron Nitride on Ni (111) from B-Trichloroborazine (Cl₃BNH)₃. *Chem. Mater.* **2004**, 16, 343-345.
302. Song, S.; Su, J.; Telychko, M.; Li, J.; Li, G.; Li, Y.; Su, C.; Wu, J.; Lu, J., On-Surface Synthesis of Graphene Nanostructures with π -Magnetism. *Chem. Soc. Rev.* **2021**.
303. Grüneis, A.; Kummer, K.; Vyalikh, D. V., Dynamics of Graphene Growth on a Metal Surface: A Time-Dependent Photoemission Study. *New J. Phys.* **2009**, 11, 073050.
304. Preobrajenski, A. B.; Ng, M. L.; Vinogradov, A. S.; Martensson, N., Controlling Graphene Corrugation on Lattice-Mismatched Substrates. *Phys. Rev. B* **2008**, 78, 073401.
305. Kovacs, G. J.; Bertóti, I.; Radnóczy, G., X-Ray Photoelectron Spectroscopic Study of Magnetron Sputtered Carbon-Nickel Composite Films. *Thin Solid Films* **2008**, 516, 7942-7946.
306. Chen, J. J.; Winograd, N., The Adsorption and Decomposition of Methylamine on Pd{111}. *Surf. Sci.* **1995**, 326, 285-300.

Anhang

a) Zusätzliche Abbildungen und Tabellen

Tabelle A1. Bindungsenergien der Peakfitkomponenten der dünnen Schichten FePcF_{16} auf $\text{Ag}(111)$, $\text{Au}(111)$ und $\text{Cu}(111)$ bei $h\nu = 860/870$ eV aus Abbildung 5 in eV. Die Lorentzbreiten sind jeweils 0,2 eV, Gaussbreiten variieren zwischen 0,96 und 1,04 eV, wobei sie innerhalb eines Spektrums konstant sind.

| Substrat | CF | S _{CF} | CN | S _{CN} | CC | S _{CC} |
|----------|--------|-----------------|--------|-----------------|--------|-----------------|
| Ag(111) | 286,98 | 288,68 | 286,01 | 287,85 | 284,91 | 286,57 |
| Au(111) | 286,92 | 288,59 | 285,95 | 287,79 | 284,82 | 286,51 |
| Cu(111) | 286,86 | 288,53 | 285,89 | 287,73 | 284,76 | 286,45 |

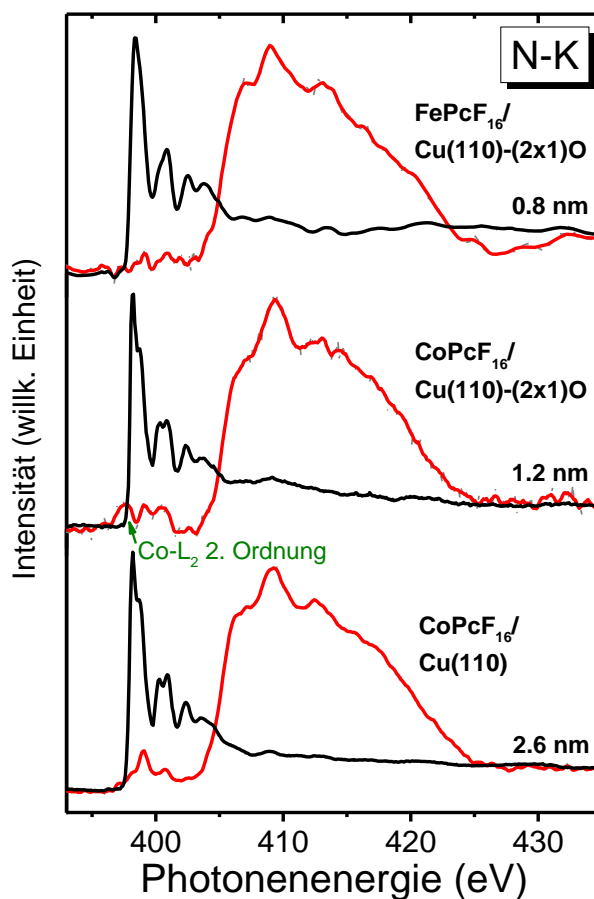


Abbildung A1. N-K XAS-Spektren der dicksten Schichten MPcF_{16} ($M = \text{Fe}, \text{Co}$) auf $\text{Cu}(110)-(2\times 1)\text{O}$ und $\text{Cu}(110)$. Die Moleküle aller drei Proben zeigen eine stark präferierte flachliegende Orientierung.

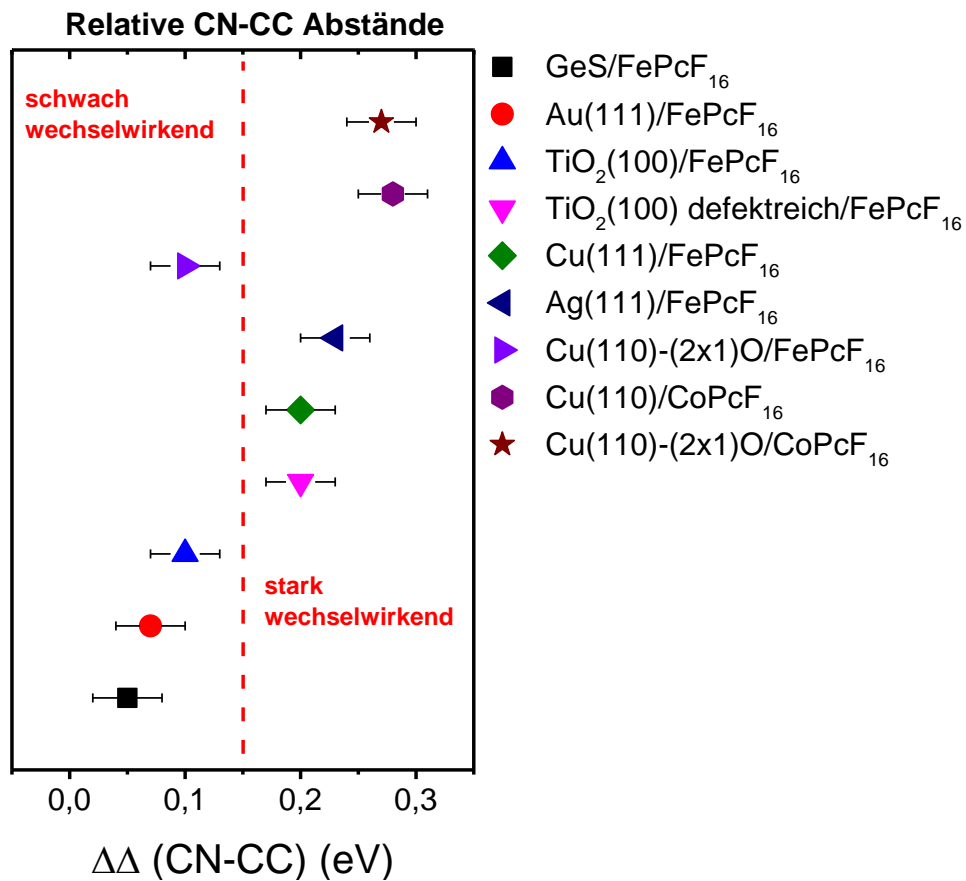


Abbildung A2. Grenzflächenwechselwirkung der CN-Atome von $MPcF_{16}$ ($M = Fe, Co$) auf verschiedenen Substraten im 1-2 ML Bereich: a) N-K Absorptionskanten und b) relative CN-CC Abstände im Vergleich dünner Film zu 1-2 ML mit Fehlerbalken (absolute Breite 0,06 eV).

In **Abbildung A2** kann anhand des relativen CN-CC Abstands gezeigt werden, dass es möglich ist, für verschiedene in dieser Arbeit diskutierte $TMPcF_{16}$ /Substrat-Systeme eine Unterteilung in schwach und stark wechselwirkende Systeme vorzunehmen. Dies scheint unabhängig vom Zentralatom (Fe oder Co) zu sein.

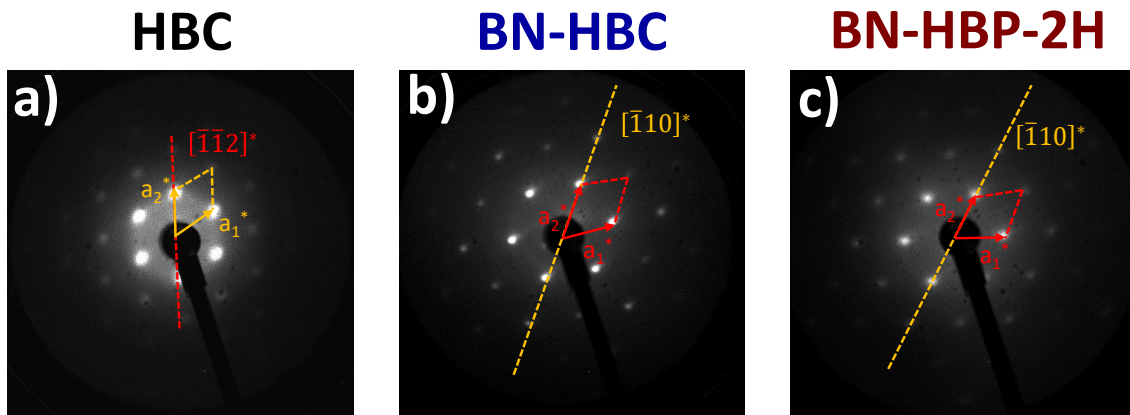


Abbildung A3. LEED-Aufnahmen der hochgeordneten Monolagen: a) HBC, b) BN-HBC und c) BN-HBP-2H bei 24,5 eV gemessen. Die Verdrehung von BN-HBC und BN-HBP-2H um 30° im Vergleich zu HBC wird deutlich ersichtlich. Zur Feststellung der Orientierung wurden Aufnahmen bei 50 eV, bei denen die Au(111)- und Molekülreflexe sichtbar, verwendet.

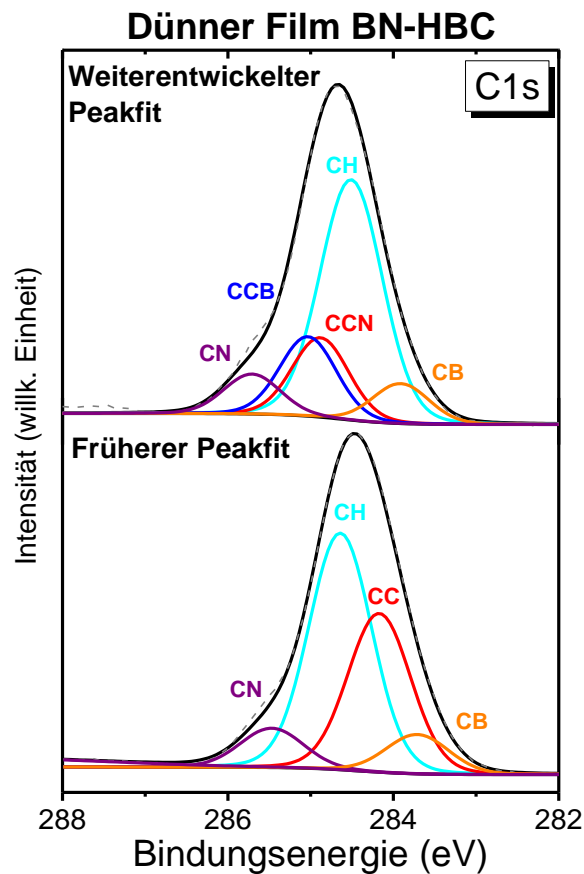


Abbildung A4. Vergleich des früheren (unten) und des weiterentwickelten (oben) C1s-Peakfits von BN-HBC.

Tabelle A2. Bindungsenergien des C1s Rumpfniveaus (anhand der CH-Komponente) bezogen auf den HOMO-onset in eV.

| | BE(E_F) | HOMO-onset | BE (E_F)-(HOMO-onset) |
|--------|--------------------------|-------------------|--|
| HBC | 284,34 | 1,2 | 283,14 |
| BN-HBC | 284,51 | 1,6 | 282,91 |
| BN-HBP | 284,29 | 1,8 | 282,49 |

b) Akzeptierte Publikationen

- Spin State in Perfluorinated FePc Films on Cu(111) and Ag(111) in Dependence on Film Thickness
- Interaction Channels between Perfluorinated Iron Phthalocyanine and Cu(111)
- Visualization of the Borazine Core of B₃N₃ Nanographene by STM
- B₃N₃-Substituted Nanographene Molecules: Influence of Planarity on the Electronic Structure and Molecular Orientation in Thin Films
- Perfluorinated Phthalocyanines on Cu(110) and Cu(110)-(2 × 1)O: The Special Role of the Central Cobalt Atom

Spin State in Perfluorinated FePc Films on Cu(111) and Ag(111) in Dependence on Film Thickness

Axel Belser,[†] Reimer Karstens,[†] Peter Grüninger,[†] Peter Nagel,[§] Michael Merz,[§] Stefan Schuppler,[§] Elizaveta A. Sutura,^{||,‡} Angelika Chassé,[⊥] Thomas Chassé,^{†,‡} and Heiko Peisert^{*,†}

[†]Institute of Physical and Theoretical Chemistry and [‡]Center for Light–Matter Interaction, Sensors & Analytics (LISA+), University of Tübingen, Auf der Morgenstelle 18, 72076 Tübingen, Germany

[§]Institut für Festkörperphysik, Karlsruher Institut für Technologie, 76021 Karlsruhe, Germany

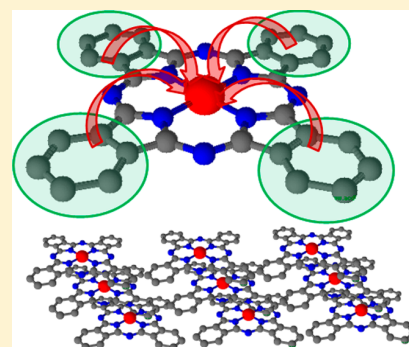
^{||}School of Chemistry, University of Southampton, University Road, Southampton SO1 71BJ, U.K.

[‡]Novosibirsk State University, Pirogova 2, Novosibirsk 630090, Russia

[⊥]Institute of Physics, Martin Luther University Halle–Wittenberg, Von-Danckelmann-Platz 3, 06120 Halle, Germany

Supporting Information

ABSTRACT: The electronic structure of the central iron ion of perfluorinated iron phthalocyanine (FePcF₁₆) in thin films has been studied on Cu(111) and Ag(111) using polarization dependent X-ray absorption spectroscopy (XAS). The data are compared to FePc on Ag(111). Ligand field parameters have been computed, and multiplet calculations (CTM4XAS) were carried out to simulate XAS spectra. The planar molecules are preferentially oriented lying flat on the substrate surface during the growth of the 1–4 nm thick films. A clear polarization dependence of the Fe L edge absorption spectra is observed, arising from transitions into orbitals with in-plane and out-of-plane character. The shape of the spectra for three to four monolayers of FePcF₁₆ on Cu(111) is comparable to that of the thin films of FePc on Ag(111). However, a drastic change of the XAS peak shape is observed for thicker FePcF₁₆ films on both Ag(111) and Cu(111), although the molecular orientation is very similar to coverages consisting of a few monolayers. Since in both cases the film thickness is distinctly beyond the monolayer regime, interface interactions can be ruled out as a possible origin of this behavior. Rather, the different XAS peak shapes seem to indicate that the multiplicity may depend on the detailed arrangement of the FePcF₁₆ molecules. The large flexibility of the ground state of Fe could be of high interest for spintronic applications.



1. INTRODUCTION

The recently increasing research efforts devoted to transition metal phthalocyanines (TMPcs) and porphyrins (TMPors) derive from their unique optical, electronic, and magnetic properties.^{1,2} Fundamental magnetic interactions of TMPcs were found on various types of substrates,^{3–6} which may support their application in molecular quantum devices. On the other hand, the electronic configuration of the central metal atom of some TMPcs is still not completely understood and has been intensely debated in recent years, in particular, at interfaces.^{7–22} An impressive example for their complex electronic structure is iron phthalocyanine (FePc). The electronic structure of Fe in FePc is discussed controversially, and even a mixture of quintet and triplet ground states with excited states energetically very close to the ground state was predicted.²³ More recent calculations have demonstrated that only a small ligand field parameter region fits for FePc with the (experimentally evidenced) spin state of $S = 1$.^{14,24,25} This indicates that the ground state of Fe may have a large flexibility in ground state symmetries depending on the detailed surroundings, described, e.g., by the ligand field. For related

trivalent iron porphyrins, it was shown that even a moderate substitution at the macrocycle may affect the electronic structure of the central metal atom distinctly.²⁶ In Fe-based metal–organic networks, a ligand influence on the electronic structure was predicted,²⁷ and also, Fe-based spin crossover complexes are known from the literature.²⁸

The fluorination of TMPcs offers an ideal tool to modify the ionization potential (IP) of the organic component, whereas further electronic properties, such as the optical gap or the composition of the HOMO and the LUMO, are less affected (see, e.g., refs 29, 30). In addition, it was shown in the example of VOPcF₁₆ and CoPcF₁₆ that the fluorination may affect distinctly the ordering in thin films and the ability to phase transitions upon annealing.^{31,32} While these aspects have been known for a longer time, the impact of the fluorination on the electronic structure of the central metal atom has received less attention. We study experimentally the influence of the

Received: April 11, 2018

Revised: June 1, 2018

Published: June 8, 2018

fluorination of FePc on the electronic structure of the Fe ion in thin films grown on Cu(111) and Ag(111) single crystals using X-ray absorption spectroscopy (XAS).

2. EXPERIMENTAL SECTION

X-ray absorption spectroscopy (XAS) measurements have been performed at the WERA beamline at the Karlsruhe Research Accelerator (KARA, Karlsruhe, Germany). The energy resolutions were set to 220 and 340 meV at photon energies of 400 and 710 eV, respectively. The absorption was monitored indirectly by measuring the total electron yield (sample current). The spectra were normalized to the same step height. The energy was calibrated to reproduce the energy of the Ni L_3 absorption of NiO at 853.0 eV. The substrates were cleaned prior to organic film deposition by repeated cycles of argon ion sputtering and annealing; the cleanliness was checked by XPS. The stoichiometry was checked by monitoring the intensity of C 1s, N 1s, and F 1s core level spectra. FePcF₁₆, purchased from SYNTHON Chemicals GmbH & Co.KG, was evaporated from a temperature-controlled crucible with evaporation rates between 0.5 and 0.8 nm/min. The film thickness was estimated from both a quartz microbalance and the XPS intensity ratios assuming layer-by-layer growth in each step of deposition.

Geometry optimization and harmonic frequency calculations have been carried out using the B3LYP functional and cc-pVDZ basis set in the gas phase. Ligand field parameters have been computed using a complete active space self-consistent field (CASSCF), also accounting for dynamic correlation (NEVPT2) as implemented in ORCA³³ (for details, see Supporting Information). All multiplet calculations were done using the CTM4XAS package.^{34,35}

3. RESULTS AND DISCUSSION

If the molecular orientation of highly ordered films is known, XAS provides comprehensive information about the unoccupied electronic structure. For phthalocyanines, the polarization dependence of N $1s-\pi^*$ excitations can be used for the analysis of the molecular orientation (e.g., ref 36). The intensity of excitations from N $1s$ to a π^* orbital is maximal if the electric field vector of the incoming synchrotron light E is parallel to the $2p_z$ orbitals (i.e., vertical to the molecular plane), whereas the transition to σ^* is allowed for (components of) E parallel to the molecular plane and thus to the chemical bond.

In Figure 1, we show angular dependent N K edge absorption spectra for two film thicknesses of FePcF₁₆ on Cu(111). We select the two prominent angles, normal ($\theta = 90^\circ$) and grazing ($\theta = 10^\circ$) incidence; the measurement geometry is shown as an inset of Figure 1a. Spectral features at photon energies < 402 eV correspond essentially to N $1s-\pi^*$ transitions, although we note that weak in-plane polarized transitions may appear in the same energy range as the π^* resonances.^{36–38}

The shape of the N K XAS spectra in Figure 1 is typical for phthalocyanines.³⁹ The maximal intensity at grazing incidence indicates that the molecules grow with a preferred flat lying adsorption geometry. Most important, the linear dichroism is almost independent of film thickness. Therefore, we expect such a distinct angular dependence also for Fe L edge absorption spectra, as discussed below.

On the other hand, the normal-incidence XAS data of the 1.3 and 3 nm examples show some differences; the N $1s-\pi^*$

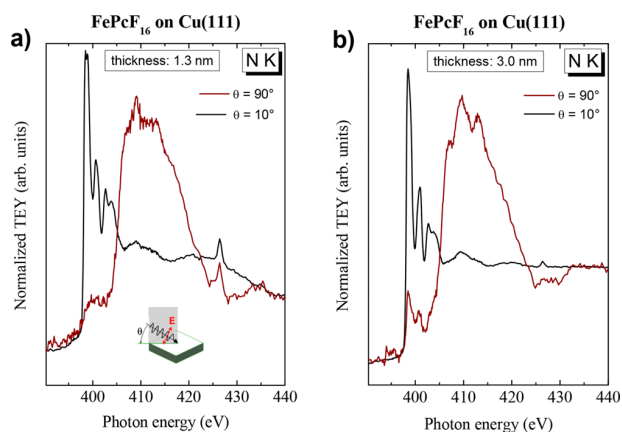


Figure 1. N K edge X-ray absorption spectra for two different film thicknesses of FePcF₁₆ on Cu(111) measured at normal ($\theta = 90^\circ$) and grazing ($\theta = 10^\circ$) incidence of the incoming synchrotron light (see inset of a)). The linear dichroism indicates almost flat lying molecules in both cases.

resonances become well resolved and clearly visible at a film thickness of 3 nm. This can be explained by a slightly increased tilt angle with increasing film thickness, which might be caused by the balance between the molecule–substrate and intermolecular interactions (see, e.g., ref 36). The change in the molecular orientation may introduce the transition of the molecular arrangement.

Knowing that the molecules in thin films are highly ordered and that the adsorption geometry is flat lying with respect to the substrate surface, the angular dependence of L edge absorption spectra of the transition metal of the TMPc can be understood in more detail.³⁹ Using linearly, p-polarized synchrotron radiation, at normal incidence ($\theta = 90^\circ$), we preferentially probe transitions into orbitals lying in the molecular plane ($d_{x^2-y^2}$ and d_{xy}), whereas at grazing incidence ($\theta = 10^\circ$), transitions into orbitals with out-of-plane components (d_{xz} , d_{yz} and d_z^2) determine the spectral shape.

In Figure 2, we compare polarization dependent L edge XAS spectra of a 1.3 nm thick FePcF₁₆ film on Cu(111) (a) with a 3

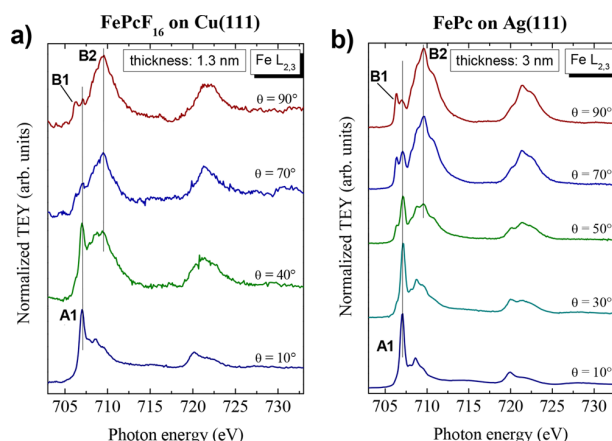


Figure 2. Polarization dependent Fe L edge XAS spectra of a 1.3 nm thick FePcF₁₆ film on Cu(111) (a) compared to FePc on Ag(111) (b). Data for FePc/Ag(111) are taken from refs 39,40. The peak shape is very similar indicating a similar electronic structure of Fe in both cases.

nm thick FePc film on Ag(111) (b). At the probed film thickness of 1.3 nm, possible contributions from interactions of the first monolayer are almost negligible, as can be seen, e.g., for FePc on Ni(111).⁴¹ The 3 nm thick FePc film on Ag(111) was chosen as an example for bulk-like FePc films on single crystalline metal substrates; the XAS spectra on other substrates, such as Au(100), behave very similarly.⁴⁰ Data for FePc/Ag(111) are taken from refs 39, 40. The spectra are very similar in both cases; we will focus on the discussion of $2p_{3/2}$ excitations (L_3 edge). At grazing incidence, a feature A1 with maximal intensity at 707.1 eV dominates the spectrum, polarized perpendicular to the molecular plane (z -polarized). In contrast, features polarized within the molecular plane (xy -polarized), probed at normal incidence, consist obviously of manifold excitations with the maximum of B1 at 706.3 eV and B2 at 709.5 eV. Since multiplet effects determine the shape of XAS spectra of transition metal L edges, the ground state electronic configuration cannot be obtained directly from the spectra but might be discussed qualitatively. Most literature agrees that in particular the $d_{x^2-y^2}$ orbital lies much higher in energy than the rest of the 3d states.¹³ Therefore, two holes can be expected in the $d_{x^2-y^2}$ orbital with the highest energy for all TMPcs. Transitions into this orbital may therefore contribute to the broad bump in the region of B2 (xy -polarized). The interpretation of B1 is more complicated; the lower energy compared to B2 and the polarization dependence within the molecular plane may however point to transitions into a partially empty d_{xy} orbital as suggested in ref 17. In this manner, the z -polarized feature A1 may point to transitions into orbitals with out-of-plane components (d_z^2). However, we note that the electronic structure is indeed more complex, and most likely, mixed valences also have to be considered.¹⁷ Most important, the comparison of the peak shape of FePcF₁₆ and FePc in Figure 2 indicates that the electronic configuration of the central Fe atom is similar in both cases.

Surprisingly, the angular dependence of the XAS spectra is distinctly different for thicker films of FePcF₁₆ on Cu(111), as shown in Figure 3a. Generally, the angular dependence is

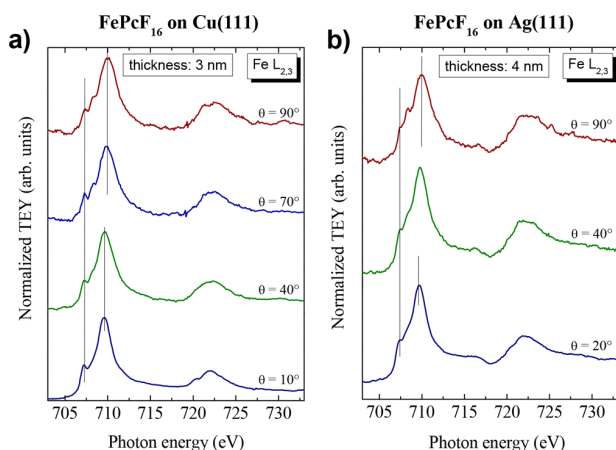


Figure 3. Polarization dependent Fe L edge XAS spectra of thick FePcF₁₆ films: (a) 3.0 nm on Cu(111) and (b) 4 nm on Ag(111). In both cases, a bulk-like behavior is expected. The peak shape is distinctly changed compared to that of the thinner FePcF₁₆ film on Cu(111) and FePc on Ag(111) (Figure 2), indicating a change of the electronic structure most likely due to the detailed molecular arrangement.

hardly visible, and the peak shape seems to be distinctly broadened. Two main features might be identified with maximal intensity at 707.3 and 710.0 eV, indicated by lines in Figure 3a. Since the molecules are still highly ordered (Figure 1b), this points to the presence of manifold empty 3d-orbitals with both in-plane and out-of-plane character. The situation is very similar for a 4 nm thick FePcF₁₆ film on Ag(111); the corresponding polarization dependent Fe L edge XAS spectra are shown in Figure 3b. Also in this case, we conclude from N K edge XAS spectra that the molecules are highly oriented, preferentially lying flat on the substrate surface.

The question arises of what could be the origin for such a drastic change of the shape of the Fe L edge XAS spectra. Generally, a possible explanation is a change of the spin multiplicity as a direct consequence of the fluorination. The overall broadening of the features may point to the presence of more holes in the respective d-orbitals, i.e., to a quintet state. This might be supported by crystal field phase diagrams,²⁴ in which for FePc only a small parameter region fits to the spin state of $S = 1$, depending on the predicted ground state. Therefore, we calculated ligand field parameters with the complete active space self-consistent field (CASSCF) method. The results, summarized in Table S1 (Supporting Information), reveal that the overall influence of the fluorination on the ligand field of an FePc molecule is expected to be minor. The calculated Ballhausen ligand field parameters Dq and Dt agree well with values recently used for the multiplet calculations of XAS spectra,¹⁷ whereas Ds is somewhat less than reported for the FePc film.

Simulated polarization dependent Fe L edge X-ray absorption spectra using ligand field parameters of ref 17 for multiplet calculations (CTM4XAS) are shown in Figure 4

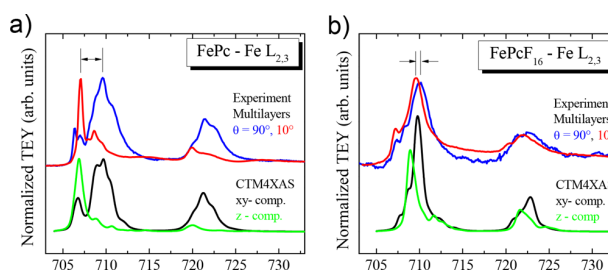


Figure 4. Simulated polarization dependent Fe L edge X-ray absorption spectra (black curves) compared with experimental spectra (blue curves) for about 3 nm thick films of (a) FePc on Ag(111) and (b) FePcF₁₆ on Cu(111). Ligand field parameters Dq , Dt , and Ds of ref 17 are used to simulate spectra of FePc (a). Although calculations predict a minor influence of the fluorination on ligand field parameters, Ds has to be lowered distinctly to obtain reasonable agreement with experimental data for FePcF₁₆ (b).

(black curves). The out-of-plane (z) and in-plane (xy) components are compared to experimental data taken at grazing and normal incidence of the incoming p -polarized synchrotron light, respectively. In Figure 4a, we obtain a good agreement with our data on FePc/Ag(111) (blue curves) and thus also with the 1.3 nm FePcF₁₆ film on Cu(111) (Figure 2). Both the z -component (a) and the xy -component (b) of the calculated spectrum is in reasonable agreement with experimental data taken at grazing (10°) and normal (90°) incidence of the incoming linearly polarized synchrotron light,

respectively. However, to simulate spectra for the thicker FePcF₁₆ films using CTM4XAS, all ligand field parameters have to be varied over a broad range. If we vary Ds only, a value as low as 0.3 eV would be needed to reach only a fair agreement with the experiment. However, in order to simulate the rather small experimental energy splitting between the positions of the *xy*- and *z*-polarized contributions in the Fe-L XAS of the thicker FePcF₁₆ films (see arrows in Figure 4), a substantial reduction in the main ligand field splitting parameter Dq has to be applied. We obtain a reasonable approach to the experimental spectra by such an appropriate reduction of Dq including a variation of the other Ballhausen parameters, too, as shown by the simulated spectra for FePcF₁₆ in Figure 4 (black curves). Parameters are summarized in Table S2. In addition, this Ballhausen parameter set and, in particular, Dq for thicker FePcF₁₆ films now falls in the range predicted for *S* = 2 spin states of Fe(II), while the one obtained for FePc films (and the thinner FePcF₁₆ films) falls in a parameter region ascribed to *S* = 1 for Fe(II).^{24,25} Thus, the observed change of the spectral shapes of the polarized Fe L XAS in FePcF₁₆ films points to a related change in spin state of the Fe(II) from *S* = 1 to *S* = 2.

Since such a drastic change of ligand field parameters is not expected from the ligand field calculations for these molecules in the gas phase (Table S1), we are left with the conclusion that the detailed arrangement of the molecules in the film is crucial for the electronic structure of Fe in FePcF₁₆. The impact of substituents on the spin state in organic molecules including iron as Fe(II) has been discussed for some time and has been related to the influence on intramolecular bonding.²⁸ Also, a change of the spin state due to electron doping and for molecules in direct contact with a solid surface has been reported.^{2,18} Interestingly, the electron doping of FePc films using alkali atoms results in a transition of Fe(II) from triplet to quintet spin states.¹⁸ However, here we report clear evidence of the influence of the molecular packing on spin states, which was hardly recognized so far.

SUMMARY

We studied the electronic structure of the central iron ion of perfluorinated iron phthalocyanine (FePcF₁₆) in thin films using polarization dependent X-ray absorption spectroscopy (XAS). The data are compared to FePc. For all studied films, the molecules are oriented preferentially lying on the substrate surface, enabling a comprehensive analysis of the (unoccupied) electronic structure of Fe as a function of the film thickness. Slightly increased tilt angles were observed with increasing film thickness, which may affect the detailed molecular arrangement.

Whereas the shape of the XAS spectra for three to four monolayers of FePcF₁₆ on Cu(111) is comparable to those of thin films of FePc on Ag(111), a drastic change of the XAS peak shape is observed for thicker FePcF₁₆ films on both Ag(111) and Cu(111). Since in both cases the film thickness is distinctly above the monolayer regime, interface interactions can be ruled out as a possible origin of this behavior. Calculations on molecules in the gas phase reveal that the overall influence of the fluorination on the ligand field of a FePc molecule is expected to be minor. On the other hand, whereas spectra of FePc are well described by known ligand field parameters, they have to be varied over a broader range to simulate spectra for FePcF₁₆ in thicker films. Thus, the different XAS peak shapes seem to indicate that the spin

multiplicity depends on the detailed arrangement of the FePcF₁₆ molecules. To describe the electronic structure more exactly, further theoretical approaches are needed. The large flexibility of the ground state of Fe could be of high interest for spintronic applications.

ASSOCIATED CONTENT

Supporting Information

The Supporting Information is available free of charge on the ACS Publications website at DOI: 10.1021/acs.jpcc.8b03436.

Ligand field parameters extracted from excited state calculations with SOC-CASSCF(6,5)/NEVPT2, obtained from CTM4XAS simulations and N K edge XAS spectra for a 4 nm thick film of FePcF₁₆ on Ag(111) (PDF)

AUTHOR INFORMATION

Corresponding Author

*E-mail: heiko.peisert@uni-tuebingen.de; Tel.: (+49) 07071/29-76931; Fax: (+49) 07071/29-5490.

ORCID

Elizaveta A. Suturina: 0000-0003-4407-1882

Heiko Peisert: 0000-0002-9742-5800

Notes

The authors declare no competing financial interest.

ACKNOWLEDGMENTS

We acknowledge the KARA (former ANKA) synchrotron radiation source and KNMF (both Karlsruhe, Germany) for the provision of beamtime. We thank Hilmar Adler, David Balle, and Sven Bölke (Tübingen) for helpful discussions and technical support. E.A.S. acknowledges Russian Science Foundation for a financial support of the computational part of this work (project 16-13-10155). Support by the Supercomputer Center of Novosibirsk State University is also acknowledged.

REFERENCES

- (1) Gottfried, J. M. Surface chemistry of porphyrins and phthalocyanines. *Surf. Sci. Rep.* **2015**, *70* (3), 259–379.
- (2) Kuch, W. G.; Bernien, M. Controlling the magnetism of adsorbed metal-organic molecules. *J. Phys.: Condens. Matter* **2017**, *29* (2), 023001.
- (3) Girovsky, J.; Nowakowski, J.; Ali, E.; Baljovic, M.; Rossmann, H. R.; Nijs, T.; Aebi, E. A.; Nowakowska, S.; Siewert, D.; Srivastava, G.; et al. Long-range ferrimagnetic order in a two-dimensional supramolecular Kondo lattice. *Nat. Commun.* **2017**, *8*, 15388.
- (4) Hewitt, A. S.; Boltersdorf, J.; Maggard, P. A.; Dougherty, D. B. Recovery of the bulk-like electronic structure of manganese phthalocyanine beyond the first monolayer on Bi₂Te₃. *Surf. Sci.* **2017**, *662*, 87–92.
- (5) Gruber, M.; Ibrahim, F.; Boukari, S.; Joly, L.; Da Costa, V.; Studniarek, M.; Peter, M.; Isshiki, H.; Jabbar, H.; Davesne, V.; et al. Spin-Dependent Hybridization between Molecule and Metal at Room Temperature through Inter layer Exchange Coupling. *Nano Lett.* **2015**, *15* (12), 7921–7926.
- (6) Yamane, H.; Carlier, A.; Kosugi, N. Orbital-specific electronic interaction in crystalline films of iron phthalocyanine grown on Au(111) probed by angle-resolved photoemission spectroscopy. *Materials Chemistry Frontiers* **2018**, *2* (3), 609–614.
- (7) Liao, M. S.; Scheiner, S. Electronic structure and bonding in metal phthalocyanines, Metal = Fe, Co, Ni, Cu, Zn, Mg. *J. Chem. Phys.* **2001**, *114* (22), 9780–9791.

- (8) Marom, N.; Kronik, L. Density functional theory of transition metal phthalocyanines, I: electronic structure of NiPc and CoPc-self-interaction effects. *Appl. Phys. A: Mater. Sci. Process.* **2009**, *95* (1), 159–163.
- (9) Marom, N.; Ren, X.; Moussa, J. E.; Chelikowsky, J. R.; Kronik, L. Electronic structure of copper phthalocyanine from G(0)W(0) calculations. *Phys. Rev. B: Condens. Matter Mater. Phys.* **2011**, *84* (19), 195143.
- (10) Kroll, T.; Aristov, V. Y.; Molodtsova, O. V.; Ossipyan, Y. A.; Vyalikh, D. V.; Buchner, B.; Knupfer, M. Spin and orbital ground state of Co in cobalt phthalocyanine. *J. Phys. Chem. A* **2009**, *113* (31), 8917–8922.
- (11) Kroll, T.; Kraus, R.; Schonfelder, R.; Aristov, V. Y.; Molodtsova, O. V.; Hoffmann, P.; Knupfer, M. Transition metal phthalocyanines: insight into the electronic structure from soft x-ray spectroscopy. *J. Chem. Phys.* **2012**, *137* (5), 054306.
- (12) Piper, L. F. J.; Cho, S. W.; Zhang, Y.; DeMasi, A.; Smith, K. E.; Matsuura, A. Y.; McGuinness, C. Soft x-ray spectroscopy study of the element and orbital contributions to the electronic structure of copper hexadecafluoro-phthalocyanine. *Phys. Rev. B: Condens. Matter Mater. Phys.* **2010**, *81* (4), 045201.
- (13) Kuz'min, M. D.; Hayn, R.; Oison, V. Ab initio calculated XANES and XMCD spectra of Fe(II) phthalocyanine. *Phys. Rev. B: Condens. Matter Mater. Phys.* **2009**, *79* (2), 024413.
- (14) Kuz'min, M. D.; Savoyant, A.; Hayn, R. Ligand field parameters and the ground state of Fe(II) phthalocyanine. *J. Chem. Phys.* **2013**, *138* (24), 244308.
- (15) Betti, M. G.; Gargiani, P.; Frisenda, R.; Biagi, R.; Cossaro, A.; Verdini, A.; Floreano, L.; Mariani, C. Localized and Dispersive Electronic States at Ordered FePc and CoPc Chains on Au(110). *J. Phys. Chem. C* **2010**, *114* (49), 21638–21644.
- (16) Bartolomé, J.; Bartolomé, F.; García, L. M.; Filoti, G.; Gredig, T.; Colesniuc, C. N.; Schuller, I. K.; Cezar, J. C. Highly unquenched orbital moment in textured Fe-phthalocyanine thin films. *Phys. Rev. B: Condens. Matter Mater. Phys.* **2010**, *81* (19), 195405.
- (17) Stepanow, S.; Miedema, P. S.; Mugarza, A.; Ceballos, G.; Moras, P.; Cezar, J. C.; Carbone, C.; de Groot, F. M. F.; Gambardella, P. Mixed-valence behavior and strong correlation effects of metal phthalocyanines adsorbed on metals. *Phys. Rev. B: Condens. Matter Mater. Phys.* **2011**, *83* (22), 220401.
- (18) Stepanow, S.; Lodi Rizzini, A.; Krull, C.; Kavich, J.; Cezar, J. C.; Yakhov-Harris, F.; Sheverdyaeva, P. M.; Moras, P.; Carbone, C.; Ceballos, G.; Mugarza, A.; Gambardella, P. Spin Tuning of Electron-Doped Metal-Phthalocyanine Layers. *J. Am. Chem. Soc.* **2014**, *136* (14), 5451–5459.
- (19) Peisert, H.; Biswas, I.; Aygul, U.; Vollmer, A.; Chasse, T. Electronic structure of cobalt phthalocyanine studied by resonant photoemission: Localization of Co-related valence band states. *Chem. Phys. Lett.* **2010**, *493* (1–3), 126–129.
- (20) Brumboiu, I. E.; Prokopiou, G.; Kronik, L.; Brena, B. Valence electronic structure of cobalt phthalocyanine from an optimally tuned range-separated hybrid functional. *J. Chem. Phys.* **2017**, *147* (4), 11.
- (21) Wallace, A. J.; Williamson, B. E.; Crittenden, D. L. CASSCF-based explicit ligand field models clarify the ground state electronic structures of transition metal phthalocyanines (MPC; M = Mn, Fe, Co, Ni, Cu, Zn). *Can. J. Chem.* **2016**, *94* (12), 1163–1168.
- (22) Zhang, T.; Brumboiu, I. E.; Lanzilotto, V.; Luder, J.; Grazioli, C.; Giangrisostomi, E.; Ovsyannikov, R.; Sassa, Y.; Bidermane, I.; Stupar, M.; et al. Conclusively Addressing the CoPc Electronic Structure: A Joint Gas-Phase and Solid-State Photoemission and Absorption Spectroscopy Study. *J. Phys. Chem. C* **2017**, *121* (47), 26372–26378.
- (23) Thole, B. T.; Van Der Laan, G.; Butler, P. H. Spin-mixed ground state of Fe phthalocyanine and the temperature-dependent branching ratio in X-ray absorption spectroscopy. *Chem. Phys. Lett.* **1988**, *149* (3), 295–299.
- (24) Miedema, P. S.; Stepanow, S.; Gambardella, P.; de Groot, F. M. F. 2p x-ray absorption of iron-phthalocyanine. In *14th International Conference on X-Ray Absorption Fine Structure*, DiCiccio, A.; Filippini, A., Eds; IOP Publishing Ltd: Bristol, UK, 2009; Vol. 190; Abstract 012143.
- (25) Miedema, P. S.; de Groot, F. M. F. The iron L edges: Fe 2p X-ray absorption and electron energy loss spectroscopy. *J. Electron Spectrosc. Relat. Phenom.* **2013**, *187*, 32–48.
- (26) Kaczmarzyk, T.; Jackowski, T.; Dzilinski, K.; Sinyakov, G. N. Asymmetry in Mossbauer spectra of Fe-III-azaporphyrin complexes. *Nukleonika* **2007**, *52*, S93–S98.
- (27) Mabrouk, M.; Savoyant, A.; Giovanelli, L.; Clair, S.; Hayn, R.; Ben Chaabane, R. Ligand Influence on Local Magnetic Moments in Fe-Based Metal–Organic Networks. *J. Phys. Chem. C* **2017**, *121* (8), 4253–4260.
- (28) Halcrow, M. A. The Effect of Ligand Design on Metal Ion Spin State-Lessons from Spin Crossover Complexes. *Crystals* **2016**, *6* (5), 58.
- (29) Peisert, H.; Knupfer, M.; Schwieger, T.; Fuentes, G. G.; Olligs, D.; Fink, J.; Schmidt, T. Fluorination of copper phthalocyanines: Electronic structure and interface properties. *J. Appl. Phys.* **2003**, *93* (12), 9683–9692.
- (30) Toader, M.; Gopakumar, T. G.; Shukryna, P.; Hietschold, M. Exploring the F_{1s}CoPc/Ag(110) Interface Using Scanning Tunneling Microscopy and Spectroscopy. 2. Adsorption-Induced Charge Transfer Effect. *J. Phys. Chem. C* **2010**, *114* (49), 21548–21554.
- (31) Basova, T. V.; Kiselev, V. G.; Dubkov, I. S.; Latteyer, F.; Gromilov, S. A.; Peisert, H.; Chasse, T. Optical Spectroscopy and XRD Study of Molecular Orientation, Polymorphism, and Phase Transitions in Fluorinated Vanadyl Phthalocyanine Thin Films. *J. Phys. Chem. C* **2013**, *117* (14), 7097–7106.
- (32) Schuster, B. E.; Basova, T. V.; Plyashkevich, V. A.; Peisert, H.; Chasse, T. Effects of temperature on structural and morphological features of CoPc and CoPcF16 thin films. *Thin Solid Films* **2010**, *518* (23), 7161–7166.
- (33) Neese, F. The ORCA program system. *Wiley Interdisciplinary Reviews-Computational Molecular Science* **2012**, *2* (1), 73–78.
- (34) Delgado-Jaime, M. U.; Zhang, K. L.; Vura-Weis, J.; de Groot, F. M. F. CTM4DOC: electronic structure analysis from X-ray spectroscopy. *J. Synchrotron Radiat.* **2016**, *23*, 1264–1271.
- (35) Stavitski, E.; de Groot, F. M. F. The CTM4XAS program for EELS and XAS spectral shape analysis of transition metal L edges. *Micron* **2010**, *41* (7), 687–694.
- (36) Peisert, H.; Biswas, I.; Knupfer, M.; Chasse, T. Orientation and electronic properties of phthalocyanines on polycrystalline substrates. *Phys. Status Solidi B* **2009**, *246* (7), 1529–1545.
- (37) Rocco, M. L. M.; Frank, K. H.; Yannoulis, P.; Koch, E. E. Unoccupied electronic structure of phthalocyanine films. *J. Chem. Phys.* **1990**, *93* (9), 6859–6864.
- (38) Floreano, L.; Cossaro, A.; Gotter, R.; Verdini, A.; Bavdek, G.; Evangelista, F.; Ruocco, A.; Morgante, A.; Cvetko, D. Periodic Arrays of Cu-Phthalocyanine Chains on Au(110). *J. Phys. Chem. C* **2008**, *112* (29), 10794–10802.
- (39) Peisert, H.; Uihlein, J.; Petraki, F.; Chasse, T. Charge transfer between transition metal phthalocyanines and metal substrates: The role of the transition metal. *J. Electron Spectrosc. Relat. Phenom.* **2015**, *204*, 49–60.
- (40) Petraki, F.; Peisert, H.; Aygul, U.; Latteyer, F.; Uihlein, J.; Vollmer, A.; Chasse, T. Electronic Structure of FePc and Interface Properties on Ag(111) and Au(100). *J. Phys. Chem. C* **2012**, *116* (20), 11110–11116.
- (41) Uihlein, J.; Peisert, H.; Adler, H.; Glaser, M.; Polek, M.; Ovsyannikov, R.; Chassé, T. Interface between FePc and Ni(111): Influence of Graphene Buffer Layers. *J. Phys. Chem. C* **2014**, *118* (19), 10106–10112.

Interaction Channels Between Perfluorinated Iron Phthalocyanine and Cu(111)

Axel Belser, Reimer Karstens, Peter Nagel, Michael Merz, Stefan Schuppler, Thomas Chassé, and Heiko Peisert*

The initial growth and interfacial electronic structure of perfluorinated iron phthalocyanine (FePcF₁₆) on Cu(111) has been studied using X-ray photoelectron spectroscopy (XPS) and polarization dependent X-ray absorption spectroscopy (XAS). The planar molecules are oriented preferred flat lying on the substrate surface during the growth of the first layers while the tilt angle is increased in thicker films. A clear interaction at the interface is observed, involving both the central metal ion and the macrocycle. At monolayer coverages, the Fe2p spectrum shows an interface signal at 707.1 eV, while the C-N component of the C1s spectrum is distinctly shifted with respect to the thicker films. In addition, the nitrogen atom is involved in the complex interaction (including charge transfer), best visible in the change of the shape in the π^* resonance of N K edge spectra recorded from molecules at the interface.

1. Introduction

Transition metal phthalocyanines (TMPcs) represent a group of molecules with promising magnetic, optical, and electronic properties.^[1,2] They are of common interest for opto-electronic devices such as solar cells, field-effect transistors, light-emitting diodes, and spintronic devices.^[3–8] On many substrates, phthalocyanines form highly ordered thin films, which are of high importance for applications in organic electronics. Depending on the transition metal and the substrate, TMPcs may show distinct interactions at the interface, affecting also the magnetic and electronic properties at the interface to the substrate.^[2,9–13] Different interaction channels are known for phthalocyanines, involving both the central metal atom and the macrocycle – in

many cases the charge transfer is expected to be bidirectional.^[14–18] Due to its flexibility in the spin ground state, iron complexes might be of particular interest in the view of electronic properties.^[19,20] Compared to other metal substrates, less attention was paid to iron phthalocyanines on copper substrates.^[21–23] For FePc on Cu(111), a charge transfer from the substrate to the molecule was reported.^[21,23]

The aim of our study is the investigation of interface properties of perfluorinated FePcF₁₆ on Cu(111). For applications, perfluorinated TMPcs have shown high stability and performance in air and they are used as n-type channels in electronic devices.^[24,25] The fluorination allows a tuning of electronic properties such as the ionization potential of the molecule and may affect interface properties such as dipoles and/or charge transfer distinctly.^[17,26,27]


2. Experimental Section

X-ray absorption spectroscopy (XAS) and X-ray photoelectron spectroscopy (XPS) measurements have been performed at the WERA beamline at the Karlsruhe Research Accelerator (KARA, Karlsruhe, Germany). The base pressure in the preparation and analysis chambers are $<3 \cdot 10^{-10}$ mbar. The energy resolution was set to 220 and 340 meV at a photon energy of 400 and 710 eV for XAS and to 625, 375, and 188 meV at a photon energy of 860, 500, and 385 eV, respectively. The photoemission core level spectra were calibrated with respect to the Cu 3p_{3/2} peak of the substrate at 75.2 eV. Polarization dependent X-ray absorption spectra were acquired at different angles of the incident p-polarized light with respect to the surface plane (with $\theta = 90^\circ$ – normal incidence, 10° – grazing incidence) in both total electron yield (TEY, drain current) mode. For background correction, the photon flux I_0 of the incident synchrotron light was monitored using a gold mesh. The spectra were normalized to the same step height. The energy was calibrated to reproduce the energy of the Ni L₃ absorption edge of NiO at 853.0 eV. The substrate was cleaned prior to organic film deposition by repeated cycles of each 30 min argon ion sputtering with a pressure of $5 \cdot 10^{-5}$ mbar and annealing at 500–540 °C. Typically 5–7 cycles are needed; the cleanliness was checked by XPS. The stoichiometry was checked by monitoring the intensity of C1s, N1s, and F1s core level spectra. FePcF₁₆, purchased from

A. Belser, R. Karstens, Prof. T. Chassé, Prof. H. Peisert
Institute of Physical and Theoretical Chemistry
University of Tübingen
Auf der Morgenstelle 18, 72076 Tübingen, Germany
E-mail: heiko.peisert@uni-tuebingen.de

Dr. P. Nagel, Dr. M. Merz, Dr. S. Schuppler
Karlsruher Institut für Technologie
Institut für Festkörperphysik
76021 Karlsruhe, Germany

Prof. T. Chassé
Center for Light-Matter Interaction, Sensors & Analytics (LISA+)
at the University of Tübingen
Auf der Morgenstelle 18, 72076 Tübingen, Germany

 The ORCID identification number(s) for the author(s) of this article can be found under <https://doi.org/10.1002/pssb.201800292>.

DOI: 10.1002/pssb.201800292

SYNTHON Chemicals GmbH & Co. KG, was resublimed and thoroughly degassed *in vacuo*. The molecules were evaporated from a temperature-controlled crucible with evaporation rates between 0.5 and 0.9 nm min⁻¹. The film thickness was estimated from both a quartz microbalance and the XPS intensity ratios assuming layer-by-layer growth in each step of deposition. Measurements on different sample positions ensure the absence of radiation damaging. Photoemission data were reproduced in the home-lab (Figure S2, Supporting Information) using a multi-chamber UHV system (base pressure of 2 × 10⁻¹⁰ mbar) equipped with a Phoibos 150 Hemispherical Energy Analyzer (SPECS), X-ray source with monochromator (XR 50 M, SPECS), and an Ultraviolet source (UVS 300, SPECS).

Peak fitting of C1s core level spectra was performed using the software Unifit 2018.^[28] A Shirley model background and a Voigt function, that is, a convolution of a Lorentzian and Gaussian line profile, was used. The background simulation is integrated in the fitting procedure. The Lorentzian peak width is related to the (core-hole) lifetime broadening, while the Gaussian width is usually attributed to the experimental resolution of the spectrometer. Further experimental artefacts, such as an unequal environment of the considered atom, different adsorption sites or small layer dependent energy shifts, are assumed to contribute to the Gaussian line width.

3. Results and Discussion

3.1. Growth and Molecular Orientation

For studying the molecular orientation of organic molecules on various substrates polarization dependent XAS is a very useful tool.^[29] For example, in a planar conjugated carbon system the excitation from C1s to a π^* orbital is strongest for E vertical to the molecular plane (parallel to 2p_z), whereas the transition to σ^* is strongest for E parallel to the molecular plane and to the chemical σ bond. For phthalocyanines, besides C1s- π^* in a similar manner also N1s- π^* excitations can be used for the analysis of the molecular orientation,^[30] avoiding problems of the analysis of C1s- π^* spectra arising from common carbon contaminations for example of beam-line components. For studying the growth mode of FePcF₁₆ on Cu(111) we show polarization dependent N K edge XAS spectra of different film thicknesses in Figure 1. The region below 403 eV corresponds almost to π^* -transitions, while the region above 403 eV photon energy belongs to σ^* -transitions, although we note that weak in-plane polarized transitions appear below 403 eV, too.^[30–32]

Generally, a sensitive balance between molecule-substrate interactions and intermolecular forces controls molecular ordering on a surface. The interaction strength at the substrate surface depends not only on the material but also on the local roughness of the substrate at the adsorption site. In former works it was shown, that TMPcs are preferred lying in the first layers on well-defined substrates like single crystals,^[30,33–39] but prefer a standing orientation on weakly interacting and rough substrates like ITO or oxidized silicon.^[30,40]

The N K edge spectra of Figure 1 show strong π^* - and weak σ^* -transitions for grazing incidence up to a thickness of 3 nm indicating a preferred lying orientation of FePcF₁₆ at the

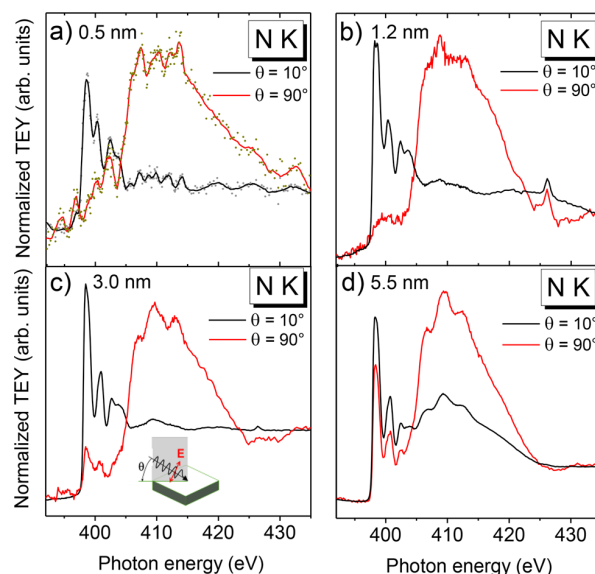


Figure 1. N K edge XAS spectra of four different film thicknesses of FePcF₁₆ on Cu(111) (a–d) at grazing (10°) and normal (90°) incidence of the incoming synchrotron light. The measurement geometry is illustrated in (c).

interface to Cu(111). The comparable noisy spectra for monolayer coverages do not allow a more detailed analysis of the adsorption geometry. However, for the related FePc molecule a flat lying adsorption geometry was observed on copper surfaces using scanning tunneling microscopy, although a bending of the molecule has to be considered in some cases.^[41,42] However, this signature changes for the 5.5 nm thick film. The high π^* -intensities at normal incidence indicate molecules with a distinctly higher tilt angle than in the thin layers. Under the assumption of a uniform molecular tilt in the probed sample area and depth an overall tilt angle can be calculated from the angular dichroism.^[29] Assuming further azimuthal averaging, we obtain tilt angles of 34° and 48° for the 3.0 and 5.5 nm film, respectively. We note that even small systematic errors may result in uncertainties, which are in particular large for small tilt angles.^[30] Examples for systematic errors are weak in-plane polarized transitions in the energy range of the π^* resonances^[30] or the data normalization procedure.

Nevertheless, our data show clearly that the molecular orientation changes with increasing film thickness. The reason could be stronger intermolecular interactions at higher coverages^[18,43] as well as less influence of the substrate. These intermolecular interactions seem to be dominant at higher coverage, while at lower coverage the molecule–substrate interactions play a significant role. We also recognize a change in the form of the π^* -signals, which will be discussed later.

In Figure 2 we show F K edge XAS spectra for three different film thicknesses up to 3 nm, where the molecules are almost flat lying (cf. Figure 1). Generally, the interpretation of the dichroism of F K edges is more complicated, since both F1s- π^* and F1s- σ^* transitions are expected in the same energy range, already shown in calculations and observed in different experiments.^[14,44,45] For 1.2 and 3.0 nm thick films, intense features at about 689 eV are clearly visible, apparently weakly depending on the angle of

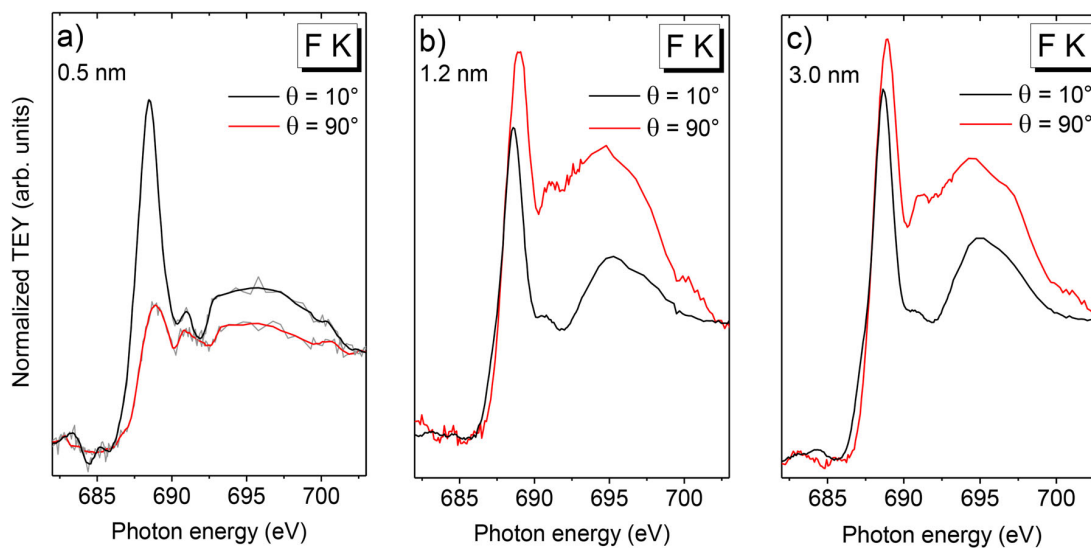


Figure 2. XAS spectra of F K edge: (a) 0.5 nm, (b) 1.2 nm, and (c) 3.0 nm thick layers.

incidence of the synchrotron light. This feature consists of transitions from F1s into both π^* and σ^* orbitals. The slight, but reproducible energetic shift of the maximal intensity from 688.6 (grazing incidence) to 688.9 eV (normal incidence) may indicate different underlying transitions depending on measurement geometry. Obviously the normal incidence spectrum of the 0.5 nm film behaves different compared to all other spectra; the dominant feature at about 689 eV is much weaker. The weak intensity at normal incidence can be understood taking into account the possibly different molecular structure of adsorbed molecules directly at the surface. For perfluorinated CuPc on Cu(111) and Ag(111), it was found that the molecules of the first monolayer could be distorted. The fluorine atoms reside 0.27 Å above the benzene rings, resulting in an angle of

about 101.5° between the C–F bond and the surface, which might be understood by a change from the sp^2 hybridization to a more tetrahedral sp^3 symmetry.^[46] As a consequence, the C–F bonds are not parallel to the substrate surface anymore, the different position of the fluorine atoms will result in particular in weaker F1s σ^* -transitions at normal incidence. A second reason for the weak intensity in the energy range between 687 eV and 690 eV could be the change of the overall electron density distribution at the interface as a result of both the distortion of the molecule and the strong interaction between the molecules and the substrate.

3.2. Interface Properties

In this part, we will discuss different interaction channels of FePcF₁₆ at the interface to Cu(111). In **Figure 3** and **4**, we show core level spectra of atoms of the macrocycle (C, N, F) at surface sensitive excitation energies of 385, 500, and 860 eV for C1s, N1s, and F1s, respectively. **Figure 3a** shows the thickness dependent development of the C1s spectra. Like for related perfluorinated phthalocyanines,^[26] the C1s core level consists of three main peaks, from high to low binding energy: carbon bonded to fluorine (CF), carbon bonded to nitrogen (CN), and carbon bonded to carbon (CC) and respective satellites (S_{CF} , S_{CN} , S_{CC}). It is obvious that there is a change in the peak shape as a function of thickness, mainly indicated by a shift of the CN component with respect to CC by 0.2 eV (see solid line **Figure 3a**).

For a better understanding exemplary peak fits of the thickest and thinnest film were carried out (**Figure 3b**). A Shirley model background and a Voigt profile (convolution of Gaussian and Lorentzian peaks) were used, the energetic position of all components is summarized in **Table 1**. Additional fit parameters are summarized in **Table S1** and **S2** (Supporting Information). For the 0.5 nm thick film the intensity ratio

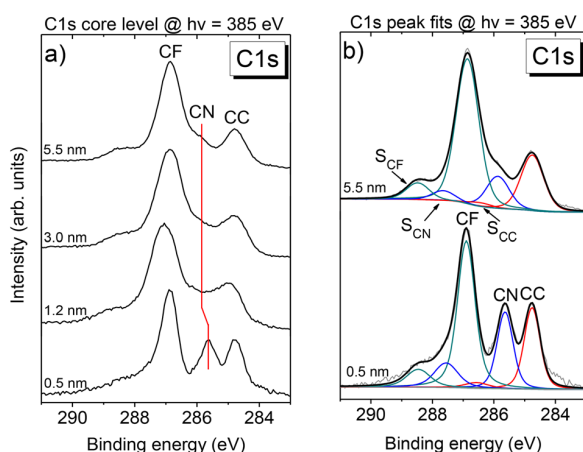


Figure 3. C1s core level spectra of FePcF₁₆ on Cu(111) as a function of the film thickness (a) and exemplary peak fits for a film thickness of 0.5 and 5.5 nm (b).

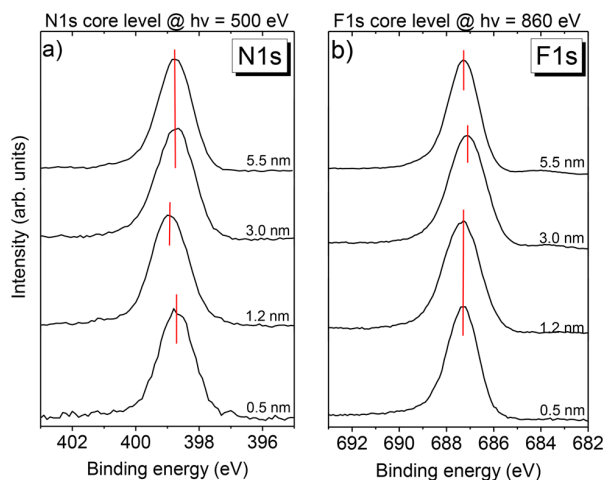


Figure 4. Core level spectra of the FePcF₁₆ macrocycle as a function of the film thickness: (a) N1s and (b) F1s.

CF + S_{CF}/CN + S_{CN}/CC + S_{CC} is 2/2.5/4.3, in reasonable agreement with stoichiometry of carbon atoms in FePcF₁₆. This indicates that the macrocycle is still intact for molecules adsorbed on the Cu(111) surface.

We note that the relative satellite intensity, energetic position, and shape cannot be assumed to be constant for each carbon component. For CuPcF₁₆ it was shown that different values for the satellite intensities are explainable by the atomic orbital composition of the HOMO and the LUMO.^[26] The high contribution of the carbon atom directly bonded to nitrogen (CN) to both the HOMO and to the LUMO, may explain the experimentally determined high intensity of S_{CN} in CuPcF₁₆. Moreover, at interfaces, photoemission satellites might be (differently) quenched, for example, due to an electronic interaction between the molecule and the substrate.^[47,48]

Comparing the two peak fits for the thick and thin layer in Figure 3b, the CN component of the 5.5 nm thick film has much smaller intensity in respect to the CC and especially to CF, the peak fit results in an intensity ratio CF + S_{CF}/CN + S_{CN}/CC + S_{CC} of 2/1.4/5.5. The larger deviation for the 5.5 nm film can be explained by the high surface sensitivity at the chosen excitation energy and the increasing tilt angle of the molecules in thicker films. For CuPc it was shown that in the case of adsorption geometries deviating from flat lying, the relative intensity of components in C1s core level spectra is not stoichiometric.^[30] Rather, the intensity of uppermost atoms is increased for molecules with larger tilt angles with respect to the substrate surface. For tilted FePcF₁₆ molecules, we expect that carbon bonded to fluorine (CF) will be more intense than

Table 1. C1s peak fit data of the 5.5 and 0.5 nm layers in eV.

| Thickness [nm] | CC | S _{CC} | CN | S _{CN} | CF | S _{CF} |
|----------------|--------|-----------------|--------|-----------------|--------|-----------------|
| 5.5 | 284.75 | 286.45 | 285.87 | 287.65 | 286.86 | 288.48 |
| 0.5 | 284.76 | 286.55 | 285.64 | 287.56 | 286.89 | 288.46 |

carbon bonded to nitrogen (CN). Indeed, at higher excitation energies the CC/CN/CF intensity ratio approaches the value expected from stoichiometry (see in Figure S1 and S2, Supporting Information). The peak shape and the fitting results are comparable to CuPcF₁₆.^[26]

In contrast to carbon, no clear hint for the involvement of nitrogen and fluorine in the interaction the interface can be obtained from the corresponding N1s and F1s core level spectra (Figure 4a,b). The main N1s and F1s peaks of the thickest layer are located at 398.7 and 687.3 eV, respectively. The small energy shifts at lower coverages (see lines in Figure 4) can be explained by screening effects of the photohole, often observed for organic molecules at metal surfaces, such as perfluorinated phthalocyanine (ZnPcF₁₆) on Au(100).^[49]

Additional information about the interaction of nitrogen at the interface can be obtained from XAS at the N K edge. In Figure 5, we show the thickness dependent N K edge spectra, zooming into the N1s-π* resonances at grazing incidence. Two features at 398.1 and 400.8 eV exhibit significantly lower intensity for low coverages (solid lines in Figure 4). The peak shape of N1s-π* transitions is affected by the hybridization between wave functions of the d-orbitals of the central metal atom of the phthalocyanine and nitrogen p-orbitals.^[50–55] The decrease of the relative intensity of the two features at 398.1 and 400.8 eV at low coverages may point to a partial filling of the corresponding orbitals and therefore indicates involvement of nitrogen atoms in the interaction at the interface. We note that this behavior is similar to FePc on Ag(111).^[39]

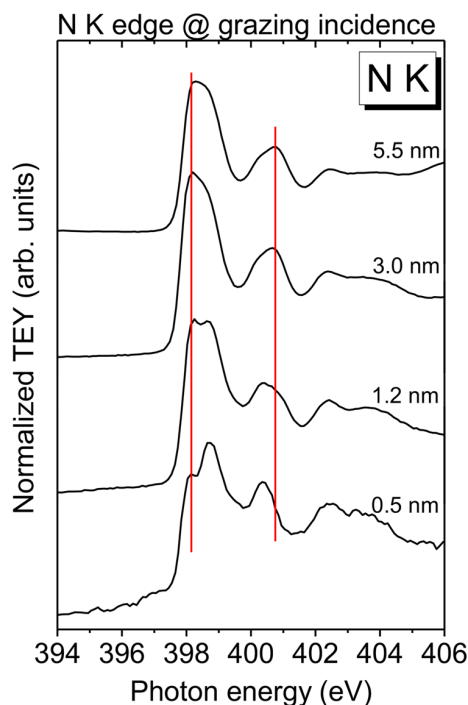


Figure 5. XAS N K edge spectra comparing different film thicknesses at grazing incidence: zoom into the region of N1s-π* transitions. The changes of the peak shape reveal an involvement of N in the interaction at the interface.

The question arises whether only the macrocycle interacts with the Cu(111) substrate. In **Figure 6** thickness dependent core level spectra of Fe2p are shown, measured at an excitation energy of 860 eV. At 0.5 nm (1–2 ML) coverage a feature at 707.1 eV dominates the spectrum (solid line), while at higher coverages a dominant broad feature resides at higher binding energies, resulting from the complex multiplet structure of the Fe ion in the molecule. The complexity of this structure is also expressed in energetic shifts and changes of the shape of the broad multiplet feature comparing 1.2 and 3.0 nm thick films. A possible reason is a change of spin state as discussed in ref. [56]. However, the dominant feature at 0.5 nm coverage results from an interaction between the central iron ion and the copper substrate, as has been discussed for related systems, such as FePc on Ag(111).^[39] We note that for FePc monolayers on Cu(110) a change of the spin state from $S = 1$ to $S = 0$ was proposed as an origin for the change of the XPS peak shape.^[57]

Further information about changes of the electronic structure of the Fe ion in dependence on the film thickness can be obtained from Fe L edge spectra. Fe L edge XAS spectra as a function of the film thickness at grazing (out of plane excitations) and normal incidence (in plane excitations) are shown in **Figure 7**. Especially for grazing incidence (Figure 7a), clear changes going from high to low coverages are visible. Two different aspects have to be discussed: First, comparing 1.2 to 0.5 nm coverages, only the spectra of the 1.2 nm thick film in Figure 7a,b are comparable to Fe L edge spectra of FePc in thin

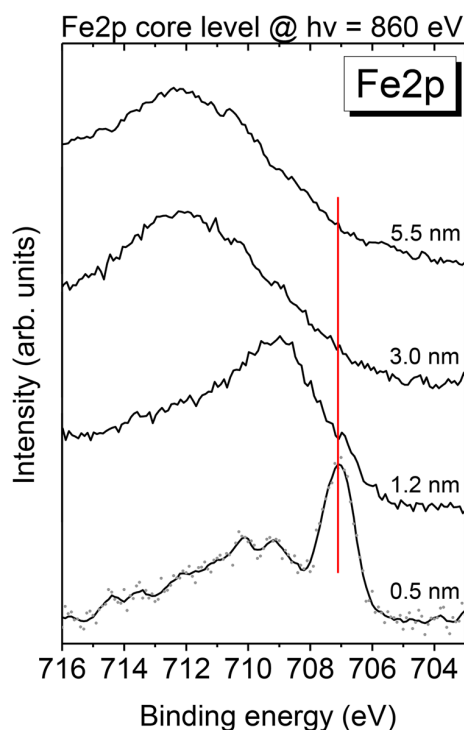


Figure 6. Fe2p core level spectrum of FePcF16 on Cu(111) as a function of the film thickness, measured with $h\nu = 860$ eV. An interface peak is clearly visible at a coverage of 0.5 nm.

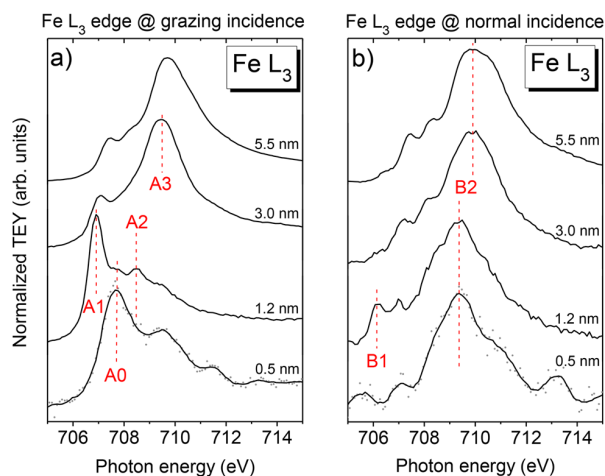


Figure 7. XAS spectra of Fe L edge at (a) grazing and (b) normal incidence. The feature A0 can be understood by a hybridization of Fe and substrate related orbitals, whereas the increasing complexity at higher coverages point to a change of the spin multiplicity.

films. At monolayer coverages, a new feature A0 at higher photon energies compared to A1 appears at grazing incidence which can be understood analogously to related systems^[58] by a hybridization of Fe and substrate related orbitals, formed by the chemisorption of the FePcF16 molecule on the Cu(111) substrate. The second aspect is the drastic change of the whole excitation signal for coverages higher than 1.2 nm. At 3.0 nm, new dominant features A3 (Figure 7a) and B3 appear at higher photon energies, resulting in a drastic change of the shape of the spectra compared to the 1.2 nm film and to FePc in bulk-like films.^[58] This can be explained by a change of the spin multiplicity of the central iron atom, possibly due to a change of the detailed arrangement of molecules as a function of the film thickness.^[56] The discussion of the Fe L edge spectra of the thickest film (5.5 nm) is somewhat hindered by the change of the molecular orientation, but also in this case the broad features hint to a higher spin multiplicity compared to Fe in FePc.

4. Summary

The electronic structure and interface properties of FePcF₁₆ on Cu(111) were analyzed. The molecules are almost flat lying on the substrate surface until a film thickness of 3.0 nm, enabling a detailed analysis of the electronic structure as a function of the film thickness. The interaction at the interface involves both the macrocycle (carbon and nitrogen) and the central metal ion of FePcF₁₆. Interface peaks were identified in photoemission and X-ray absorption spectra, indicating a charge transfer from the substrate to the molecule and a hybridization of molecule and substrate related states. At higher coverages most likely the spin multiplicity of the Fe ion changes.

Supporting Information

Supporting Information is available from the Wiley Online Library or from the author.

Acknowledgements

We acknowledge the KARA (former ANKA) synchrotron radiation source and KNMF (both Karlsruhe, Germany) for the provision of beamtime. We thank Hilmar Adler and Sven Bölke (Tübingen) for technical support.

Conflict of Interest

The authors declare no conflict of interest.

Keywords

charge transfer, fluorinated phthalocyanine, interfaces, photoemission, X-ray absorption spectroscopy

Received: June 20, 2018

Revised: August 15, 2018

Published online: September 9, 2018

- [1] J. M. Gottfried, *Surf. Sci. Rep.* **2015**, *70*, 259.
- [2] W. G. Kuch, M. Bernien, *J. Phys.: Condens. Matter* **2017**, *29*, 14.
- [3] K. Walzer, B. Maennig, M. Pfeiffer, K. Leo, *Chem. Rev.* **2007**, *107*, 1233.
- [4] M. V. Martinez-Diaz, G. de la Torre, T. Torres, *Chem. Commun.* **2010**, *46*, 7090.
- [5] M. Cinchetti, K. Heimer, J.-P. Wüstenberg, O. Andreyev, M. Bauer, S. Lach, C. Ziegler, Y. Gao, M. Aeschlimann, *Nat. Mater.* **2008**, *8*, 115.
- [6] L. Bogani, W. Wernsdorfer, *Nat. Mater.* **2008**, *7*, 179.
- [7] C. G. Claessens, U. Hahn, T. Torres, *Chem. Record* **2008**, *8*, 75.
- [8] S. Sanvito, *Chem. Soc. Rev.* **2011**, *40*, 3336.
- [9] T. S. Ellis, K. T. Park, M. D. Ulrich, S. L. Hulbert, J. E. Rowe, *J. Appl. Phys.* **2006**, *100*, 093515.
- [10] M. Toader, P. Shukryna, M. Knupfer, D. R. T. Zahn, M. Hietschold, *Langmuir* **2012**, *28*, 13325.
- [11] A. Ruocco, F. Evangelista, R. Gotter, A. Attili, G. Stefani, *J. Phys. Chem. C* **2008**, *112*, 2016.
- [12] H. Yamane, A. Carlier, N. Kosugi, *Mater. Chem. Front.* **2018**, *2*, 609.
- [13] A. Candini, V. Bellini, D. Klar, V. Corradini, R. Biagi, V. De Renzi, K. Kummer, N. B. Brookes, U. del Pennino, H. Wende, M. Affronte, *J. Phys. Chem. C* **2014**, *118*, 17670.
- [14] F. Petraki, H. Peisert, J. Uihlein, U. Aygül, T. Chassé, *Beilstein J. Nanotechnol.* **2014**, *5*, 524.
- [15] S. Lindner, U. Treske, M. Knupfer, *Appl. Surf. Sci.* **2013**, *267*, 62.
- [16] Y. Huang, E. Wruss, D. Egger, S. Kera, N. Ueno, W. Saidi, T. Bucko, A. Wee, E. Zojer, *Molecules* **2014**, *19*, 2969.
- [17] D. Balle, H. Adler, P. Grüninger, R. Karstens, R. Ovsyannikov, E. Giangrisostomi, T. Chassé, H. Peisert, *J. Phys. Chem. C* **2017**, *121*, 18564.
- [18] S. Ahmadi, M. N. Shariati, S. Yu, M. Göthelid, *J. Chem. Phys.* **2012**, *137*, 084705.
- [19] P. S. Miedema, F. M. F. de Groot, *J. Electron Spectrosc.* **2013**, *187*, 32.
- [20] M. A. Halcrow, *Crystals* **2016**, *6*, 58.
- [21] F. Hu, H. Y. Mao, H. J. Zhang, K. Wu, Y. L. Cai, P. M. He, *J. Chem. Phys.* **2014**, *140*, 6.
- [22] A. Scarfato, S. H. Chang, S. Kuck, J. Brede, G. Hoffmann, R. Wiesendanger, *Surf. Sci.* **2008**, *602*, 677.
- [23] O. Snezhkova, F. Bischoff, Y. Q. He, A. Wiengarten, S. Chaudhary, N. Johansson, K. Schulte, J. Knudsen, J. V. Barth, K. Seufert, W. Auwärter, J. Schnadt, *J. Chem. Phys.* **2016**, *144*, 9.
- [24] M.-M. Ling, Z. Bao, *Org. Electron.* **2006**, *7*, 568.
- [25] H. Brinkmann, C. Kelting, S. Makarov, O. Tsaryova, G. Schnurpfeil, D. Wohrle, D. Schlettwein, *Phys. Status Solidi A* **2008**, *205*, 409.
- [26] H. Peisert, M. Knupfer, T. Schwieger, G. G. Fuentes, D. Olligs, J. Fink, T. Schmidt, *J. Appl. Phys.* **2003**, *93*, 9683.
- [27] H. Peisert, M. Knupfer, J. Fink, *Appl. Phys. Lett.* **2002**, *81*, 2400.
- [28] R. Hesse, T. Chassé, P. Streubel, R. Szargan, *Surf. Interface Anal.* **2004**, *36*, 1373.
- [29] J. Stöhr, *NEXAFS Spectroscopy*, Springer, Berlin, Heidelberg **1992**.
- [30] H. Peisert, I. Biswas, M. Knupfer, T. Chasse, *Phys. Status Solidi B* **2009**, *246*, 1529.
- [31] M. L. M. Rocco, K. H. Frank, P. Yannoulis, E. E. Koch, *J. Chem. Phys.* **1990**, *93*, 6859.
- [32] L. Floreano, A. Cossaro, R. Gotter, A. Verdini, G. Bavdek, F. Evangelista, A. Ruocco, A. Morgante, D. Cvetko, *J. Phys. Chem. C* **2008**, *112*, 10794.
- [33] S. Kera, M. B. Casu, K. R. Bauchspieß, D. Batchelor, T. Schmidt, E. Umbach, *Surf. Sci.* **2006**, *600*, 1077.
- [34] S. Kera, Y. Yabuuchi, H. Yamane, H. Setoyama, K. K. Okudaira, A. Kahn, N. Ueno, *Phys. Rev. B* **2004**, *70*, 085304.
- [35] S. R. Forrest, *Chem. Rev.* **1997**, *97*, 1793.
- [36] L. Ottaviano, S. Di Nardo, L. Lozzi, M. Passacantando, P. Picozzi, S. Santucci, *Surf. Sci.* **1997**, *373*, 318.
- [37] D. A. Evans, H. J. Steiner, A. R. Vearey-Roberts, A. Bushell, G. Cabailh, S. O'Brien, J. W. Wells, I. T. McGovern, V. R. Dhanak, T. U. Kampen, D. R. T. Zahn, D. Batchelor, *Nucl. Instrum. Methods Phys. Res. B* **2003**, *199*, 475.
- [38] T. S. Ellis, K. T. Park, S. L. Hulbert, M. D. Ulrich, J. E. Rowe, *J. Appl. Phys.* **2004**, *95*, 982.
- [39] F. Petraki, H. Peisert, U. Aygül, F. Latteyer, J. Uihlein, A. Vollmer, T. Chassé, *J. Phys. Chem. C* **2012**, *116*, 11110.
- [40] H. Peisert, T. Schwieger, J. M. Auerhammer, M. Knupfer, M. S. Golden, J. Fink, P. R. Bressler, M. Mast, *J. Appl. Phys.* **2001**, *90*, 466.
- [41] S. H. Chang, S. Kuck, J. Brede, L. Lichtenstein, G. Hoffmann, R. Wiesendanger, *Phys. Rev. B* **2008**, *78*, 233409.
- [42] O. Snezhkova, J. Lüder, A. Wiengarten, S. R. Burema, F. Bischoff, Y. Q. He, J. Ruzs, J. Knudsen, M. L. Bocquet, K. Seufert, J. V. Barth, W. Auwärter, B. Brena, J. Schnadt, *Phys. Rev. B* **2015**, *92*, 075428.
- [43] D. G. de Oteyza, E. Barrena, J. O. Ossó, S. Sellner, H. Dosch, *J. Am. Chem. Soc.* **2006**, *128*, 15052.
- [44] D. G. de Oteyza, A. Sakko, A. El-Sayed, E. Goiri, L. Floreano, A. Cossaro, J. M. Garcia-Lastra, A. Rubio, J. E. Ortega, *Phys. Rev. B* **2012**, *86*, 075469.
- [45] M. Klues, P. Jerabek, T. Breuer, M. Oehzelt, K. Hermann, R. Berger, G. Witte, *J. Phys. Chem. C* **2016**, *120*, 12693.
- [46] A. Gerlach, F. Schreiber, S. Sellner, H. Dosch, I. A. Vartanyants, B. C. C. Cowie, T. L. Lee, J. Zegenhagen, *Phys. Rev. B* **2005**, *71*, 205425.
- [47] A. Schöll, Y. Zou, M. Jung, T. Schmidt, R. Fink, E. Umbach, *J. Chem. Phys.* **2004**, *121*, 10260.
- [48] P. Grüninger, M. Polek, M. Ivanovic, D. Balle, R. Karstens, P. Nagel, M. Merz, S. Schuppler, R. Ovsyannikov, H. F. Bettinger, H. Peisert, T. Chassé, *J. Phys. Chem. C* **2018**, *122*, 19491.
- [49] H. Peisert, D. Kolacyak, T. Chassé, *J. Phys. Chem. C* **2009**, *113*, 19244.
- [50] M. D. Kuz'min, R. Hayn, V. Oison, *Phys. Rev. B* **2009**, *79*, 024413.
- [51] M. G. Betti, P. Gargiani, R. Frisenda, R. Biagi, A. Cossaro, A. Verdini, L. Floreano, C. Mariani, *J. Phys. Chem. C* **2010**, *114*, 21638.
- [52] J. Bartolomé, F. Bartolomé, L. M. García, G. Filoti, T. Gredig, C. N. Colesniuc, I. K. Schuller, J. C. Cezar, *Phys. Rev. B* **2010**, *81*, 195405.

- [53] S. Javid, M. Bowen, S. Boukari, L. Joly, J. B. Beaufrand, X. Chen, Y. J. Dappe, F. Scheurer, J. P. Kappler, J. Arabski, W. Wulfhekel, M. Alouani, E. Beaurepaire, *Phys. Rev. Lett.* **2010**, *105*, 4.
- [54] F. Petraki, H. Peisert, P. Hoffmann, J. Uihlein, M. Knupfer, T. Chassé, *J. Phys. Chem. C* **2012**, *116*, 5121.
- [55] J. Ahlund, K. Nilson, J. Schiessling, L. Kjeldgaard, S. Berner, N. Mårtensson, C. Puglia, B. Brena, M. Nyberg, Y. Luo, *J. Chem. Phys.* **2006**, *125*, 034709.
- [56] A. Belser, R. Karstens, P. Grüniger, P. Nagel, M. Merz, S. Schuppler, E. A. Suturina, A. Chassé, T. Chassé, H. Peisert, *J. Phys. Chem. C* **2018**, *122*, 15390.
- [57] N. Tsukahara, K. I. Noto, M. Ohara, S. Shiraki, N. Takagi, Y. Takata, J. Miyawaki, M. Taguchi, A. Chainani, S. Shin, M. Kawai, *Phys. Rev. Lett.* **2009**, *102*, 167203.
- [58] H. Peisert, J. Uihlein, F. Petraki, T. Chassé, *J. Electron Spectrosc.* **2015**, *204*, 49.

Visualization of the Borazine Core of B₃N₃-Doped Nanographene by STM

Axel Belser, Katharina Greulich, Peter Grüninger, Holger F. Bettinger, Heiko Peisert,* and Thomas Chassé

Cite This: *ACS Appl. Mater. Interfaces* 2020, 12, 19218–19225

Read Online

ACCESS |



Metrics & More



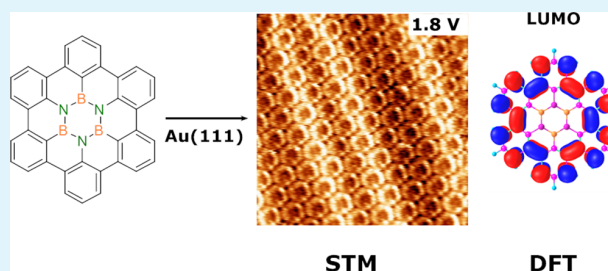
Article Recommendations



Supporting Information

ABSTRACT: Electronic interface properties and the initial growth of hexa-*peri*-hexabenzocoronene with a borazine core (BN-HBC) on Au(111) have been studied by using X-ray photoelectron spectroscopy (XPS), low-energy electron diffraction (LEED), and scanning tunneling microscopy (STM). A weak, but non-negligible, interaction between BN-HBC and Au(111) was found at the interface. Both hexa-*peri*-hexabenzocoronene (HBC) and BN-HBC molecules form well-defined monolayers. The different contrast in STM images of HBC and BN-HBC at different tunneling voltages with submolecular resolution can be ascribed to differences in the local density of states (LDOS). At positive and negative tunneling voltages, STM images reproduce the distribution of the highest occupied and lowest unoccupied molecular orbitals (HOMO and LUMO) as determined by density functional theory (DFT) calculations very well.

KEYWORDS: BN-doped hexa-*peri*-hexabenzocoronene, hexa-*peri*-hexabenzocoronene, interaction, photoemission, low-energy electron diffraction, scanning tunneling microscopy, density functional theory



INTRODUCTION

Extended polycyclic aromatic hydrocarbons (PAHs), also called “nanographenes”, recently attracted broad attention, boosted by the experimental accessibility of graphene and hexagonal boron nitride.^{1,2} Among others, PAHs can be regarded as the starting point for the bottom-up approach for the graphene synthesis.^{3–6} The possibly best-known representative of this class of molecules is hexa-*peri*-hexabenzocoronene (HBC, Figure 1), a material that exhibits noble electronic properties, such as a very high charge carrier mobility.^{7,8} Possible applications of HBC in electronic devices have been studied intensely.^{7,9–11} Through chemical design, it

is possible to tune the properties of nanographene molecules at the molecular level and to achieve nanoscale control over their self-assembly to form multifunctional (nano)materials.¹²

A promising pathway to modify the intrinsic electronic properties of nanographenes is the substitution of C–C units by isoelectronic and isosteric B–N units.^{13–19} This includes extended B/N/C graphene²⁰ and graphene-type nanomeshes.²¹ Even the incorporation of the well-defined borazine (B₃N₃) unit in the center of HBC (BN-HBC, Figure 1) is synthetically feasible in an atom-precise manner.²² It was shown that flat lying BN-HBC layers can be prepared on Au(111) and that borazine doping leads to a tuning of the band gap in the same energy range as of carbon-doped hexagonal boron nitride (h-BN).²³ This observation is in agreement with the conclusion that borazine substitution of an aromatic ring in a nanographene should increase the HOMO–LUMO gap.^{24,25} The reason for this is rooted in the electronegativity difference of boron, carbon, and nitrogen. The borazine occupied π molecular orbitals are lower and the unoccupied π^* orbitals are higher in energy than those of

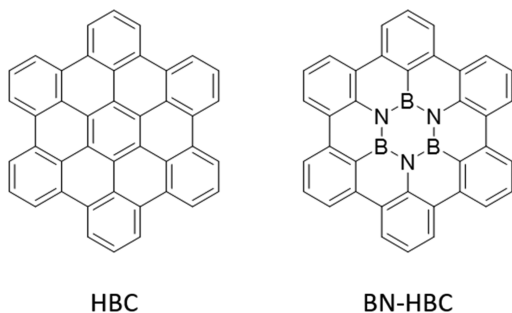
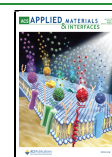


Figure 1. Hexa-*peri*-hexabenzocoronene (HBC) and the B₃N₃-doped hexa-*peri*-hexabenzocoronene (BN-HBC).

Received: February 6, 2020

Accepted: March 30, 2020

Published: March 30, 2020



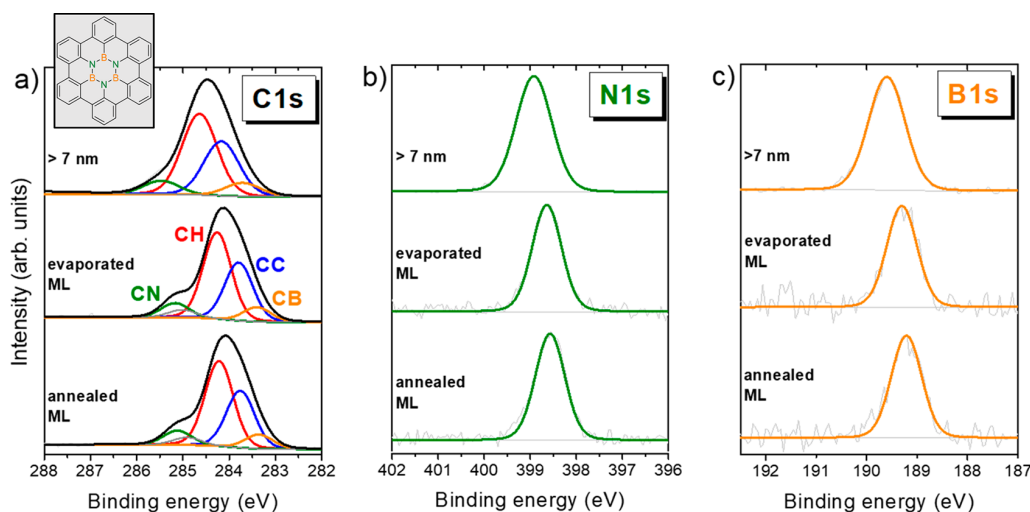


Figure 2. BN-HBC core level spectra: (a) C 1s, (b) N 1s, and (c) B 1s. In the upper panel we show a thick layer (>7 nm), in the middle panel an evaporated ML, and in the lower panel an annealed ML. In the fit of the C 1s ML spectra an additional interface component was used.

Table 1. Peak Fit Data of the C 1s, N 1s, and B 1s Core Levels of the Thick Layer and the Evaporated and Annealed ML (in eV)

| layer | B 1s | | N 1s | | C 1s | | | |
|---------------|--------|--|--------|--|--------|--------|--------|--------|
| | | | | | CN | CH | CC | CB |
| >7 nm | 189.60 | | 398.92 | | 285.47 | 284.64 | 284.17 | 283.71 |
| evaporated ML | 189.30 | | 398.64 | | 285.17 | 284.26 | 283.79 | 283.40 |
| annealed ML | 189.21 | | 398.57 | | 285.12 | 284.22 | 283.76 | 283.36 |

benzene. Consequently, substitution of an aromatic ring that has nonvanishing orbital coefficients by a borazine ring will alter the energy of the corresponding orbitals. In the case of the HBC/BN-HBC pair, the substitution in particular changes the nature of the lowest energy unoccupied molecular orbital (LUMO).²⁶ Therefore, we may expect that the molecular BN-core does not at all contribute to the charge density distribution related to this particular LUMO in the case of BN-HBC. This opens up opportunities for local probes like STM to sample and visualize differences in the internal molecular electronic structure.

In this study, we visualize the change of the electronic structure of HBC upon doping with a borazine core by STM. In particular, we show that borazine substitution causes a significant change in the unoccupied states that allows visualizing the “borazine hole” in BN-HBC. Our study thus directly demonstrates the dramatic effects of borazine doping on the electronic structure that can only be inferred indirectly, e.g., from optical spectroscopy.

METHODS AND EXPERIMENTS

The Au(111) single crystal was cleaned by several cycles of Ar⁺-ion sputtering and subsequent annealing. The sputtering was performed at a voltage of 0.8 kV for typically 30 min at an argon partial pressure of 5×10^{-5} mbar, and the annealing was performed for 30 min at a temperature of 770 K. The cleanliness and orientation of the crystal were checked by STM, XPS, UPS, and LEED.

The molecules were evaporated at rates of about 0.1–0.3 nm/min determined by a quartz microbalance. During deposition, the crystal was held at 293 K at a pressure of about 5×10^{-9} mbar.

All experiments were performed in UHV systems with a base pressure of 2×10^{-10} mbar. The STM and LEED measurements were performed in a two-chamber system equipped with a variable

temperature (VT)-STM from Omicron NanoTechnology GmbH and a LEED/AES spectrometer from OCI Vacuum Microengineering Inc. For the STM measurements, mechanically cut Pt/Ir tips were used. The sample and tip were held at room temperature, and all given tunneling voltages are given with respect to the sample. On the shown STM images, no smoothing or filtering was performed; the WSXM program was used to improve the image contrast.²⁷

The XPS measurements were performed using a multichamber UHV system equipped with a Phoibos 150 hemispherical energy analyzer (SPECS) and an X-ray source with monochromator (XR 50 M, SPECS) and Al K α radiation. The energy scale was calibrated reproducing the binding energies (BE) of Au 4f_{7/2} and Cu 2p_{3/2} at 84.00 and 932.56 eV, respectively. Peak fitting of XP spectra were performed using the program Unifit, version 2018.²⁸ A Shirley model background and a Voigt profile (convolution of Gaussian and Lorentzian peaks) were used for the peak fitting procedure of the core levels. The Lorentzian width for C 1s, N 1s, and B 1s was set to 0.08, 0.10, and 0.07 eV, respectively, according to the literature.^{29–31} The error of absolute binding energies is estimated to be less than ± 0.05 eV.

For density functional theory (DFT) calculations, the ORCA program was used.³² The B3LYP/def2-SVP basis set^{33–35} was used for the geometry optimization and the calculation of electronic states of both HBC and BN-HBC. Chemcraft was used for the visualization of the frontier orbitals calculated by DFT. To produce highly ordered monolayers, multilayers of BN-HBC were evaporated on the Au(111) single crystal, followed by an annealing of the sample to 610 K for about 15 min. The measurements were made at 293 K.

RESULTS AND DISCUSSION

Interface Electronic Properties of BN-HBC on Au(111). For the interpretation of STM images, a thorough characterization of the strength of the interaction between the molecule and the substrate is needed. For such investigations, XPS is a useful tool. As example, for chemisorbed pentacene on

copper surfaces, the presence of an additional, intense carbon component is observed at the interface, attributed to a relatively strong substrate–molecule bond.^{36–38}

In Figure 2, we show XPS core level spectra of differently prepared BN-HBC monolayers and compare them to spectra of a several nanometers thick multilayer film on Au(111). For the more than 7 nm thick film, effects of the interface on the peak shape can be neglected. Whereas N 1s and B 1s spectra can be described by a single component, chemically inequivalent carbon species have to be considered in the C 1s spectra. Similar to ref 23, we distinguish in Figure 2a between carbon bonded to hydrogen (CH), to other carbon (CC), to nitrogen (CN), and to boron (CB). The intensities were fixed as expected from stoichiometry 18:12:3:3. The binding energies of all peaks are summarized in Table 1; the corresponding Gaussian widths are given in Table S1 (Supporting Information). The binding energies of the components of the C 1s spectrum for the thin film are in good agreement with the recently published data,²³ whereas values for monolayer coverages are slightly (about 0.2 eV) lower than reported. We note that due to significantly enhanced accessibility of molecules, the procedures for preparing monolayers exactly have recently been much improved. The observed energetic shifts of the monolayer peaks to about 0.3–0.4 eV lower binding energies with respect to the thick layer for all three core levels can be ascribed to a screening of the photohole at the interface to the metal, intensely studied for interfaces between rare gases and metals.^{39,40} Effects of the same magnitude were observed for many related organic–metal interfaces.^{41,42} Interestingly, the Gaussian widths for all components of the C 1s, N 1s, and B 1s spectra are slightly (0.15–0.18 eV) higher compared to the monolayers (cf. Table S1), possibly due to different electronic environments arising from a lower degree of ordering in thicker films.

We note that for the C 1s peak fit of the monolayer systems an additional component of very low intensity was inserted at a binding energy between the CH and CN components (gray component in Figure 2a). This component might be explained by molecules adsorbed at more reactive sites like steps or vacancies, as observed for rare gas–metal interfaces⁴³ or related organic–metal systems.⁴⁴ Also, in N 1s and B 1s monolayer spectra we note some additional intensity at the high-energy tail of the peak maximum, which is, however, in the range of the noise. Thus, we observe a very weak, but not fully negligible, interaction between BN-HBC and the gold substrate.

Most important, the fitting results for the annealed and the evaporated monolayer are very similar. The peak shape is almost the same, just slightly lower binding energies of all three core levels (less than 0.1 eV) are observed for the annealed monolayer. This indicates that the annealing procedure does not affect the electronic structure of the interface significantly.

Adsorption Geometry and Electronic Structure of BN-HBC on Au(111). Although it is already known that BN-HBC adsorbs in a flat-lying manner on Au(111),²³ the detailed adsorption geometry was not studied so far. On the other hand, the structural ordering of the first monolayer is very important because it determines the interfacial electronic structure and may affect the structure and ordering of subsequent layers.⁴⁵

Submonolayer Coverages. To shed light on the early stages of BN-HBC film growth, STM measurements on samples with different BN-HBC coverages were performed.

First, a submonolayer BN-HBC was deposited at 293 K on Au(111). Two representative STM images are shown in Figure 3, zooming at a step edge and a wide terrace of the Au(111)

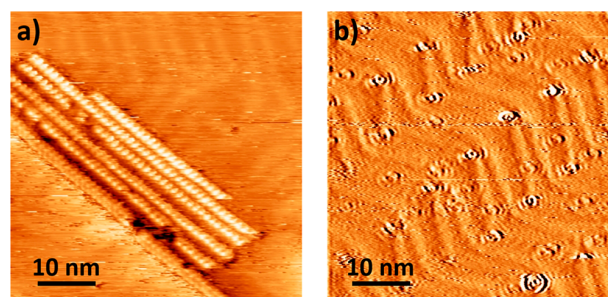


Figure 3. STM images of BN-HBC/Au(111) in submonolayer coverage (nominal coverage 0.2–0.3 monolayers). (a) A BN-HBC island which is found near the step edge after deposition of BN-HBC ($U = 1.3$ V, $I = 330$ pA, measured at room temperature). (b) Constant height image of individual BN-HBC molecules adsorbed on Au(111) ($U = 1.3$ V, $I = 500$ pA).

substrate. The well-known features of the herringbone reconstruction on Au(111) remain present and may be well recognized in both images. Clearly visible in Figure 3a, the molecules are preferably adsorbed at edges of monatomic steps on narrow terraces, which act as nucleation sites for the formation of islands. In these islands, the molecules retain the adsorption geometry of the first row; subsequent rows are aligned along the direction of the step edge. Nucleation along step edges or other substrate inhomogeneities has been observed for many organic molecules on a variety of substrates^{46,47} due to the commonly higher adsorption energies at atomic steps and other coordinatively unsaturated sites.⁴⁵ When increasing the coverage, atoms or molecules adsorbed on these sites can act themselves as nucleation center for the growth of islands or clusters, which results in the formation of 2D islands. Related ordered structures of BN-HBC near the step edge are visible in Figure 3a.

On the other hand, on larger (111) terraces, islands of ordered molecules could not be imaged for submonolayer coverages at room temperature. An ordered BN-HBC layer only forms when the monolayer is closed. Similar growth modes are often observed for polyaromatic hydrocarbons (PAHs), including hexa-*peri*-hexabenzocoronene (HBC).^{48–51} Such observations are often explained by very weak intermolecular interaction or even by repulsive forces between the molecules. If both attractive molecule–molecule and molecule–substrate forces are weak, the molecules might be too mobile for imaging by STM at room temperature.⁵² Therefore, the presence of (isolated) BN-HBC molecules at room temperature for submonolayer coverages in Figure 3b indicates that the interaction between BN-HBC and the Au(111) surface is strong enough to keep the molecules fixed on terrace sites for monitoring by STM.

In Figure 3b, the BN-HBC molecules appear as bright spots surrounded by concentric rings, which are located preferred at the elbows of the herringbone reconstruction. Such preferred adsorption at elbow sites of the Au(111) surface was recently observed for other organic molecules^{53–56} and BN-HBC.²²

Apparently, besides step edges also elbow sites are energetically favored; i.e., at these sites the molecule–substrate interaction is distinctly stronger than the molecule–molecule interaction. However, only by attachment to the step edges may a large number of molecules establish in-plane bonds both to the metal atoms at the edge and in addition to several further molecules at once in this manner, supporting the two-dimensional island growth.

The concentric rings can be explained by oscillations of the electron density, first observed by STM on a Cu(111) surface emerging from steps and charged defects.⁵⁷ These standing waves are also known as Friedel oscillations—a term that has been used first to describe the perturbed charge density of a free electron gas exposed to disorder.⁵⁸ The screening of the perturbing charges happens with oscillations of the charge carrier density having a period of half the Fermi wavelength. We note that the appearance of the concentric rings is almost independent of the measurement parameters; artifacts by the tip are therefore rather unlikely.

In the case of BN-HBC/Au(111), such a perturbation can result from the conjugated π -electron system of the BN-HBC molecule affecting the substrate. The behavior is reminiscent of coronene on Ag(111).⁵⁹ In both cases, for BN-HBC on Au(111) and coronene on Ag(111), the Friedel oscillations can be clearly seen in room temperature STM images, although this phenomenon is more often observed at low temperatures. In this manner, STM provides evidence for a non-negligible electronic interaction between the molecule and the substrate.

BN-HBC Monolayers on Au(111). With increasing coverage, the formation of close-packed layers was observed (see Figure S1). Although ordered monolayers can be generally prepared without annealing, we focus in the following on monolayers prepared by annealing due to its particular high order.

Because attractive forces between BN-HBC and the Au(111) substrate are much higher than the intermolecular forces, layers beyond a monolayer will desorb at lower temperatures, while the first monolayer remains adsorbed on the surface. Therefore, a BN-HBC monolayer can be prepared by annealing of 2–3 layers to 610 K. In addition, the annealing causes a high mobility of the molecules enabling the diffusion to the optimal adsorption sites. This procedure results in the formation of a highly ordered monolayer, denoted “annealed monolayer”.

To monitor the long-range ordering in such layers LEED may be used, providing information about the size and rotational alignment of the adsorbate unit cell with respect to the substrate unit cell. In Figure 4, we show the LEED pattern of an annealed BN-HBC monolayer on Au(111) at different energies (Figure 4a,b) and compare them to the clean Au(111) substrate (Figure 4c).

In Figure 4a, the LEED pattern of the annealed monolayer of BN-HBC on Au(111) taken at 24.5 V beam voltage and normal incidence of the electron beam is shown. At this beam energy the spots represent the ordered molecular layer, exclusively. Hexagonal patterns of sharp LEED spots are clearly visible, indicating the formation of a highly ordered BN-HBC superstructure under the reported conditions. To determine the real space unit cell from the reciprocal lattice observed with LEED, another lattice for reference is helpful. For this comparison the LEED image at 50 eV (Figure 4c) is used because it contains spots from both the substrate (large

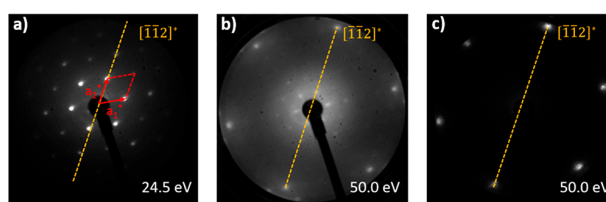


Figure 4. LEED images of an annealed BN-HBC monolayer on Au(111) at (a) 24.5 eV and (b) 50 eV. (c) LEED image of the clean Au(111) substrate at 50 eV for comparison.

reciprocal unit cell) and the adsorbate (small reciprocal unit cell). Hence, the lattice constant and the azimuthal orientation of the unit cell with respect to the Au(111) substrate can be determined for the covering layer. Lattice parameters $a_1 = a_2 = 1.45$ nm and the angle between the lattice vectors $\Gamma = 60^\circ$ are obtained for the ordered monolayer. The BN-HBC lattice vector is oriented along the Au $[\bar{1}10]$ direction. From the LEED data, we conclude that BN-HBC forms a commensurate (5×5)-superstructure on Au(111). This structure will be denoted structure A in the following.

In a next step, the BN-HBC monolayer on Au(111) was investigated by STM. Figure 5a shows an STM image of the

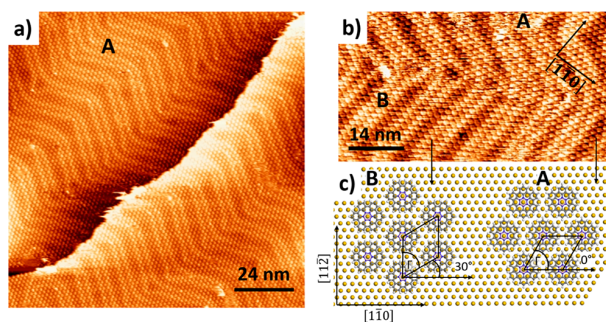


Figure 5. STM images of the annealed BN-HBC monolayer. (a) Large domain with structure A ($U = 1.5$ V, $I = 400$ pA), (b) smaller domains of an additional structure B that is rotated by 30° ($U = 1.2$ V, $I = 600$ pA), and (c) illustration of the proposed structures for A and B with respect to the Au(111) lattice.

BN-HBC monolayer prepared by annealing. The herringbone pattern originating from the $(22 \times \sqrt{3})$ -reconstruction of the underlying Au(111) substrate is still visible. The surface reconstruction is useful to determine the rotational alignment of the BN-HBC structure with respect to the gold substrate directly from the STM image.

Two different domains were observed by STM. The larger domains consist of structure A, where the BN-HBC lattice is rotated by 30° with respect to the long knees of the herringbone reconstruction, i.e., the $[\bar{1}12]$ direction of the Au(111) substrate. This means that the lattice of structure A of BN-HBC is oriented along the $[\bar{1}10]$ direction of the unreconstructed Au(111) (cf. Figure 5c). This orientation is in good agreement with the results of the LEED studies discussed above.

Additionally, a second hexagonal structure B appears, in which the lattice vector direction is oriented along the reconstruction lines of the herringbone structure (Au- $[\bar{1}12]$) (see Figure S2). The related domains are distinctly smaller. This might be the reason why they cannot be observed on the

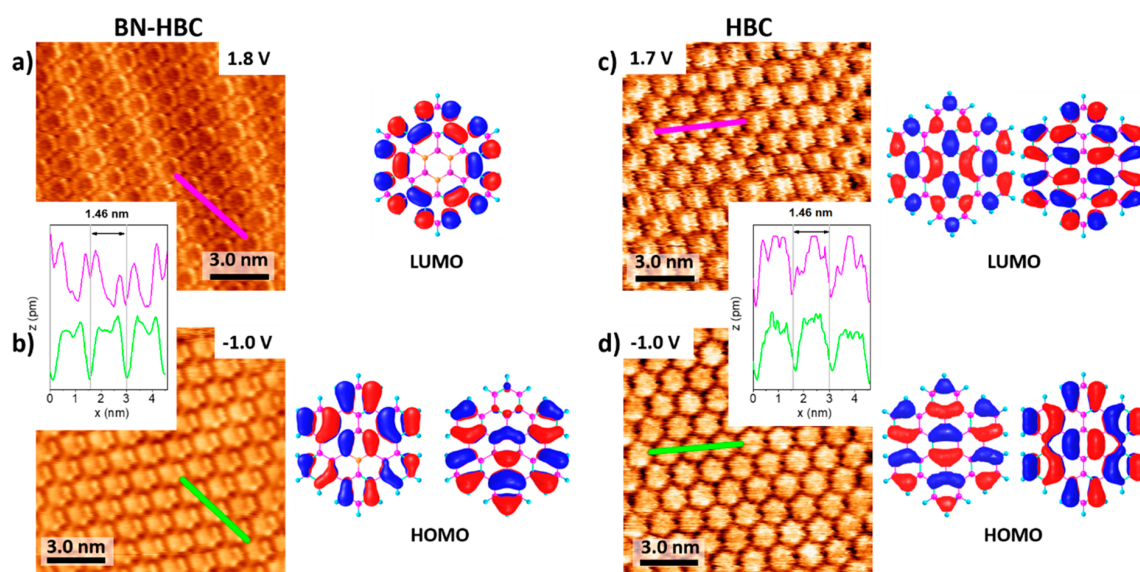


Figure 6. High-resolution STM images of BN-HBC and HBC at different tunneling voltages ($I = 400$ pA) in comparison to the frontier orbitals calculated by DFT. (a) STM image of BN-HBC at 1.8 V sample bias and LUMO. (b) STM image of BN-HBC at -1.0 V sample bias and HOMO. (c) STM image of HBC at 1.7 V sample bias and LUMO. (d) STM image of HBC at -1.0 V sample bias and HOMO. The orbital plots are calculated with B3-LYP/def2-SVP, isosurface at 0.02. Line profiles along the green and magenta lines are shown in the insets.

LEED images. Both domains merge to form a complete monolayer as it can be seen in Figure 5b. The unit cells of both structures (A and B) have the same geometry but are rotated by 30° with respect to each other. In both cases, the BN-HBC molecules are flat lying and the short molecular axes are aligned with the lattice vectors of the BN-HBC lattice. The angle Γ between the two-dimensional lattice vectors is 60° .

The BN-HBC lattice parameter is determined from STM to be 1.46 ± 0.03 nm for structure A, which is in excellent agreement to the value derived from LEED. The lattice parameter of structure B appears to be slightly larger with 1.50 ± 0.03 nm. This could indicate that structure B is a commensurate $(\sqrt{27} \times \sqrt{27})R30^\circ$ superstructure with respect to the unreconstructed Au(111) lattice. Both suggested commensurate superstructures are illustrated in Figure 5c.

We note that the adsorption geometry of BN-HBC is very similar to the related HBC molecule on Au(111).^{48,49,60–62} It was reported that well-ordered HBC monolayers with large domains can be produced by deposition of several layers and subsequent annealing.^{60–62} For comparison, we show an STM image of a HBC monolayer prepared in this manner in Figure S3, which is in excellent agreement to the reported prior results.

Electronic Structure of BN-HBC in Comparison to HBC. STM always probes the topographic and electronic contrast; the latter is a complex interplay between the electronic structure of the molecule, substrate, and the STM tip. Because of its dependence on the electronic structure, STM is also capable to visualize heteroatoms in PAHs.^{63,64} Nevertheless, valuable information about the electronic structure of the molecule can be gained from the tunneling bias dependence of STM images.

In Figure 6, we show high-resolution STM images of BN-HBC and its parent molecule HBC in dependence on the tunneling voltage in comparison to DFT calculations of the frontier orbitals and the dedicated z -profiles. Because of the low mobility of the BN-HBC molecules in the monolayer,

STM images with intramolecular contrast could be obtained at room temperature. In STM, the tunneling current depends exponentially on the distance between the tip and the substrate as well as on the density of states at both sides of the tunneling junction. Thus, for the same tip, at a certain lateral position the current is proportional to the local density of states of the molecule, enabling the visualization of the charge density distribution derived from the frontier orbitals (HOMO and LUMO), if a mixing with the electronic continuum of the substrate can be neglected.⁶⁵ Applying a positive sample bias voltage, electrons will tunnel from filled states of the tip into empty states of the sample. In contrast, at a negative sample bias voltage, electrons will tunnel from filled states of the sample into empty states of the tip. Thus, for molecules adsorbed on a substrate, its frontier orbitals are often used for the interpretation of the intramolecular contrast in an STM image.^{65–67} However, it is important to note that the molecular levels can get broadened, shifted, and mixed because of the interaction with the substrate.⁶⁵ In particular, at higher voltages, many molecular orbitals can contribute to the STM images.⁶⁸

The STM images of both molecules, BN-HBC and HBC, show a clear dependence on the tunneling voltage (see Figure 6). Upon applying a bias voltage of 1.8 V, the STM image of an ordered layer of BN-HBC on Au(111) shows an apparent darker region in the center of the molecule. This region has an even lower apparent height as the space in between the BN-HBC molecules. In STM images taken at lower, positive tunneling voltages, the molecule has uniform apparent height (not shown). Therefore, we conclude that the different contrast in STM images is essentially caused by a different density of states at the molecule/substrate side. We note that also for BN-HBC networks on Ag(111) a weak intramolecular contrast at higher tunneling voltages might be observable.²¹ In contrast, for coronene and HBC such a contrast is hardly visible.^{69,70}

To shed more light on the observed contrast in STM images of HBC and BN-HBC, we performed electronic structure calculations. The results are in good agreement with the literature.²⁶ In HBC, both HOMO and LUMO as computed at the B3-LYP/def2-SVP level of theory are doubly degenerate. Upon substitution of the central benzene ring by a borazine core, the HOMO is shifted to lower energies, whereas the LUMO is shifted to higher energies. This result is in agreement with the observed larger optical gap of 3.1 eV.²³

Interestingly, the BN-HBC LUMO is rather similar to the HBC LUMO+1. The latter has also vanishing coefficients in the central ring. Therefore, this molecular orbital (MO) is possibly not much affected by the central ring exchange, while other unoccupied MOs are influenced in their charge distribution and energy to a much larger extent. The strikingly different appearance of the relevant LUMOs is the reason why the STM images at higher sample bias of HBC and BN-HBC exhibit distinct differences (see below).

At small negative and positive sample bias voltages ($< \pm 0.8$ V, not shown), the intramolecular contrast is generally weak. This might be expected since the electrons tunnel through the gap of BN-HBC, and therefore the topographical contribution determines the contrast of the STM image. For increasing tunneling voltages, resonances to the frontier orbitals might be expected. However, in the HOMO of BN-HBC as well as the HOMO and LUMO of HBC, the electron density is almost homogeneously distributed over the molecule. Consequently, the corresponding STM images in Figure 6b–d exhibit a weak contrast, even if the center of the HBC molecule in Figure 6c appears slightly brighter.

Most important, the fact that the calculated BN-HBC LUMO is located mainly at the outer rings of the molecule is very well reproduced in the contrast of the STM image at positive tunneling voltage (Figure 6a). The contrast obtained from the molecules appears brighter at the outer rings and has a dark spot in the center. This visual impression is clearly supported by looking at the line scans inserted in the figures. The very narrow and deep minima of the tunneling currents observed at the very same positions in all scans for the respective molecular layer along the lines clearly correspond to the pitches between the molecules along the sampled lines. In between and thus in the molecules much higher currents are measured except for the case of Figure 6a. An apparent dip of the tunneling current inside the molecule recorded in the BN-HBC line scans at +1.8 V seems to be even deeper than between the molecules. This is not at all the case for the line scan at -1.0 V. Comparing STM images of BN-HBC and HBC close to the resonance to the LUMO at positive tunneling voltages in Figure 6a and 6c, respectively, the different contrast is obvious. This supports the assumption that the STM contrast is determined to a large extent by the different electronic structure of the molecules caused by the exchange of the inner benzene ring in HBC by a borazine ring in BN-HBC.

CONCLUSIONS

The adsorption of BN-HBC on Au(111) was investigated by XPS, LEED, and STM. We were able to prepare a monolayer of particularly high order. According to STM and LEED, the monolayer structure is dominated by large domains consisting of a commensurate (5×5)-superstructure (A). Additionally, small domains of a $(\sqrt{27} \times \sqrt{27})R30^\circ$ -superstructure (B) were detected.

Weak, but not negligible, interactions between BN-HBC and Au(111) were found, also visible in STM images of submonolayers as perturbations of the electron density (most likely Friedel oscillations).

High-resolution monolayer STM images of BN-HBC in dependence of the tunneling voltage are shown and analyzed in terms of the molecular electronic structure for the first time. At HOMO/LUMO resonance energies, the contrast in STM images with submolecular resolution is distinctly different for BN-HBC and its parent molecule HBC. That is due to the change of the electronic structure as a result of the substitution of the inner benzene ring by a borazine core. The results are in good agreement with DFT calculations of the frontier orbitals of BN-HBC and HBC.

ASSOCIATED CONTENT

Supporting Information

The Supporting Information is available free of charge at <https://pubs.acs.org/doi/10.1021/acsami.0c02324>.

Gaussian widths of the XPS peak fits; STM image of close-packed BN-HBC multilayers; STM image of the minority domain, found in the annealed BN-HBC monolayer; STM image of an annealed HBC monolayer (PDF)

AUTHOR INFORMATION

Corresponding Author

Heiko Peisert – Institute of Physical and Theoretical Chemistry, University of Tübingen, 72076 Tübingen, Germany; orcid.org/0000-0002-9742-5800; Phone: (+49) 07071/29-76931; Email: heiko.peisert@uni-tuebingen.de; Fax: (+49) 07071/29-5490

Authors

Axel Belser – Institute of Physical and Theoretical Chemistry, University of Tübingen, 72076 Tübingen, Germany
Katharina Greulich – Institute of Physical and Theoretical Chemistry, University of Tübingen, 72076 Tübingen, Germany
Peter Grüninger – Institute of Physical and Theoretical Chemistry and Institute of Organic Chemistry, University of Tübingen, 72076 Tübingen, Germany
Holger F. Bettinger – Institute of Organic Chemistry, University of Tübingen, 72076 Tübingen, Germany; Center for Light–Matter Interaction, Sensors & Analytics (LISA+) at the University of Tübingen, 72076 Tübingen, Germany; orcid.org/0000-0001-5223-662X
Thomas Chassé – Institute of Physical and Theoretical Chemistry, University of Tübingen, 72076 Tübingen, Germany; Center for Light–Matter Interaction, Sensors & Analytics (LISA+) at the University of Tübingen, 72076 Tübingen, Germany; orcid.org/0000-0001-6442-8944

Complete contact information is available at: <https://pubs.acs.org/doi/10.1021/acsami.0c02324>

Author Contributions

A.B. and K.G. contributed equally to this work.

Notes

The authors declare no competing financial interest.

ACKNOWLEDGMENTS

The research was funded in part by the Vector Foundation. The authors acknowledge support by the state of Baden-

Württemberg through bwHPC and the German Research Foundation (DFG) through Grant INST 40/467-1 FUGG (JUSTUS cluster). We thank H. Adler (University of Tübingen) for valuable discussions and technical support.

REFERENCES

- (1) Narita, A.; Wang, X.-Y.; Feng, X.; Müllen, K. New Advances in Nanographene Chemistry. *Chem. Soc. Rev.* **2015**, *44* (18), 6616–6643.
- (2) Geim, A. K.; Grigorieva, I. V. Van Der Waals Heterostructures. *Nature* **2013**, *499* (7459), 419–425.
- (3) Chen, L.; Hernandez, Y.; Feng, X. L.; Mullen, K. From Nanographene and Graphene Nanoribbons to Graphene Sheets: Chemical Synthesis. *Angew. Chem., Int. Ed.* **2012**, *51* (31), 7640–7654.
- (4) Angelova, P.; Vieker, H.; Weber, N.-E.; Matei, D.; Reimer, O.; Meier, I.; Kurasch, S.; Biskupek, J.; Lorbach, D.; Wunderlich, K.; Chen, L.; Terfort, A.; Klapper, M.; Müllen, K.; Kaiser, U.; Götzhäuser, A.; Turchanin, A. A Universal Scheme to Convert Aromatic Molecular Monolayers into Functional Carbon Nanomembranes. *ACS Nano* **2013**, *7* (8), 6489–6497.
- (5) Müller, M.; Kübel, C.; Müllen, K. Giant Polycyclic Aromatic Hydrocarbons. *Chem. - Eur. J.* **1998**, *4* (11), 2099–2109.
- (6) Ruffieux, P.; Wang, S.; Yang, B.; Sánchez-Sánchez, C.; Liu, J.; Dienel, T.; Talirz, L.; Shinde, P.; Pignedoli, C. A.; Passerone, D.; Dumslaff, T.; Feng, X.; Müllen, K.; Fasel, R. On-Surface Synthesis of Graphene Nanoribbons with Zigzag Edge Topology. *Nature* **2016**, *531* (7595), 489–492.
- (7) Grimsdale, A. C.; Wu, J.; Mullen, K. New Carbon-Rich Materials for Electronics, Lithium Battery, and Hydrogen Storage Applications. *Chem. Commun.* **2005**, *17*, 2197–2204.
- (8) Seyler, H.; Purushothaman, B.; Jones, D. J.; Holmes, A. B.; Wong, W. W. H. Hexa-peri-Hexabenzocoronene in Organic Electronics. *Pure Appl. Chem.* **2012**, *84*, 1047.
- (9) Watson, M. D.; Fechtenkötter, A.; Müllen, K. Big Is Beautiful—“Aromaticity” Revisited from the Viewpoint of Macromolecular and Supramolecular Benzene Chemistry. *Chem. Rev.* **2001**, *101* (5), 1267–1300.
- (10) Schmidt-Mende, L.; Fechtenkötter, A.; Müllen, K.; Moons, E.; Friend, R. H.; MacKenzie, J. D. Self-Organized Discotic Liquid Crystals for High-Efficiency Organic Photovoltaics. *Science* **2001**, *293* (5532), 1119–1122.
- (11) Wu, J.; Pisula, W.; Müllen, K. Graphenes as Potential Material for Electronics. *Chem. Rev.* **2007**, *107* (3), 718–747.
- (12) Müllen, K. Evolution of Graphene Molecules: Structural and Functional Complexity as Driving Forces Behind Nanoscience. *ACS Nano* **2014**, *8* (7), 6531–6541.
- (13) Bosdet, M. J. D.; Piers, W. E. B-N as a C-C Substitute in Aromatic Systems. *Can. J. Chem.* **2009**, *87* (1), 8–29.
- (14) Campbell, P. G.; Marwitz, A. J. V.; Liu, S.-Y. Recent Advances in Azaborine Chemistry. *Angew. Chem., Int. Ed.* **2012**, *51* (25), 6074–6092.
- (15) Giustra, Z. X.; Liu, S.-Y. The State of the Art in Azaborine Chemistry: New Synthetic Methods and Applications. *J. Am. Chem. Soc.* **2018**, *140* (4), 1184–1194.
- (16) Helten, H. B = N Units as Part of Extended π -Conjugated Oligomers and Polymers. *Chem. - Eur. J.* **2016**, *22* (37), 12972–12982.
- (17) Morgan, M. M.; Piers, W. E. Efficient Synthetic Methods for the Installation of Boron–Nitrogen Bonds in Conjugated Organic Molecules. *Dalton Transactions* **2016**, *45* (14), 5920–5924.
- (18) Wang, X.-Y.; Wang, J.-Y.; Pei, J. BN Heterosuperbenzenes: Synthesis and Properties. *Chem. - Eur. J.* **2015**, *21* (9), 3528–3539.
- (19) Helten, H. Doping the Backbone of π -Conjugated Polymers with Tricoordinate Boron: Synthetic Strategies and Emerging Applications. *Chem. - Asian J.* **2019**, *14* (7), 919–935.
- (20) Beniwal, S.; Hooper, J.; Miller, D. P.; Costa, P. S.; Chen, G.; Liu, S.-Y.; Dowben, P. A.; Sykes, E. C. H.; Zurek, E.; Enders, A. Graphene-Like Boron–Carbon–Nitrogen Monolayers. *ACS Nano* **2017**, *11* (3), 2486–2493.
- (21) Sánchez-Sánchez, C.; Brüller, S.; Sachdev, H.; Müllen, K.; Krieg, M.; Bettinger, H. F.; Nicolai, A.; Meunier, V.; Talirz, L.; Fasel, R.; Ruffieux, P. On-Surface Synthesis of BN-Substituted Heteroaromatic Networks. *ACS Nano* **2015**, *9* (9), 9228–9235.
- (22) Krieg, M.; Reicherter, F.; Haiss, P.; Ströbele, M.; Eichele, K.; Treanor, M.-J.; Schaub, R.; Bettinger, H. F. Construction of an Internally B₃N₃-Doped Nanographene Molecule. *Angew. Chem., Int. Ed.* **2015**, *54* (28), 8284–8286.
- (23) Ciccullo, F.; Calzolari, A.; Piš, I.; Savu, S. A.; Krieg, M.; Bettinger, H. F.; Magnano, E.; Chassé, T.; Casu, M. B. A Quasi-Free-Standing Single Layer of a B₃N₃-Doped Nanographene Molecule Deposited on Au(111) Single Crystals. *J. Phys. Chem. C* **2016**, *120* (31), 17645–17651.
- (24) Otero, N.; El-kelany, K. E.; Pouchan, C.; Rérat, M.; Karamanis, P. Establishing the Pivotal Role of Local Aromaticity in the Electronic Properties of Boron-Nitride Graphene Lateral Hybrids. *Phys. Chem. Chem. Phys.* **2016**, *18* (36), 25315–25328.
- (25) Otero, N.; Karamanis, P.; El-Kelany, K. E.; Rérat, M.; Maschio, L.; Civalleri, B.; Kirtman, B. Exploring the Linear Optical Properties of Borazine (B₃N₃) Doped Graphenes. 0D Flakes vs 2D Sheets. *J. Phys. Chem. C* **2017**, *121* (1), 709–722.
- (26) Tönshoff, C.; Müller, M.; Kar, T.; Latteyer, F.; Chassé, T.; Eichele, K.; Bettinger, H. F. B₃N₃ Borazine Substitution in Hexa-peri-Hexabenzocoronene: Computational Analysis and Scholl Reaction of Hexaphenylborazine. *ChemPhysChem* **2012**, *13* (5), 1173–1181.
- (27) Horcas, I.; Fernández, R.; Gomez-Rodriguez, J.; Colchero, J.; Gómez-Herrero, J.; Baro, A. WSXM: A Software for Scanning Probe Microscopy and a Tool for Nanotechnology. *Rev. Sci. Instrum.* **2007**, *78* (1), No. 013705.
- (28) Hesse, R.; Chasse, T.; Streubel, P.; Szargan, R. Error Estimation in Peak-Shape Analysis of XPS Core-Level Spectra Using Unifit 2003: How Significant Are the Results of Peak Fits? *Surf. Interface Anal.* **2004**, *36* (10), 1373–1383.
- (29) Schöll, A.; Zou, Y.; Jung, M.; Schmidt, T.; Fink, R.; Umbach, E. Line Shapes and Satellites in High-Resolution X-Ray Photoelectron Spectra of Large π -Conjugated Organic Molecules. *J. Chem. Phys.* **2004**, *121* (20), 10260–10267.
- (30) Savu, S.-A.; Biswas, I.; Sorace, L.; Mannini, M.; Rovai, D.; Caneschi, A.; Chassé, T.; Casu, M. B. Nanoscale Assembly of Paramagnetic Organic Radicals on Au(111) Single Crystals. *Chem. - Eur. J.* **2013**, *19* (10), 3445–3450.
- (31) Thomas, T. D.; Püttner, R.; Fukuzawa, H.; Prümper, G.; Ueda, K.; Kuk, E.; Sankari, R.; Harries, J.; Tamenori, Y.; Tanaka, T.; Hoshino, M.; Tanaka, H. Boron 1s Photoelectron Spectrum of ¹¹BF₃: Vibrational Structure and Linewidth. *J. Chem. Phys.* **2007**, *127* (24), 244309.
- (32) Neese, F. The Orca Program System. *Wiley Interdiscip. Rev.: Comput. Mol. Sci.* **2012**, *2* (1), 73–78.
- (33) Becke, A. D. Density-Functional Thermochemistry. I. The Effect of the Exchange-Only Gradient Correction. *J. Chem. Phys.* **1992**, *96* (3), 2155–2160.
- (34) Becke, A. D. A New Mixing of Hartree-Fock and Local Density-Functional Theories. *J. Chem. Phys.* **1993**, *98* (2), 1372–1377.
- (35) Weigend, F.; Ahlrichs, R. Balanced Basis Sets of Split Valence, Triple Zeta Valence and Quadruple Zeta Valence Quality for H to Rn: Design and Assessment of Accuracy. *Phys. Chem. Chem. Phys.* **2005**, *7* (18), 3297–3305.
- (36) Baldacchini, C.; Allegretti, F.; Gunnella, R.; Betti, M. G. Molecule-Metal Interaction of Pentacene on Copper Vicinal Surfaces. *Surf. Sci.* **2007**, *601* (13), 2603–2606.
- (37) Koch, N.; Gerlach, A.; Duhm, S.; Glowatzki, H.; Heimel, G.; Vollmer, A.; Sakamoto, Y.; Suzuki, T.; Zegenhagen, J.; Rabe, J. P.; Schreiber, F. Adsorption-Induced Intramolecular Dipole: Correlating Molecular Conformation and Interface Electronic Structure. *J. Am. Chem. Soc.* **2008**, *130* (23), 7300–7304.

- (38) McDonald, O.; Cafolla, A. A.; Li, Z. S.; Hughes, G. Synchrotron Photoemission Studies of Pentacene Films on Cu(110). *Surf. Sci.* **2006**, *600* (9), 1909–1916.
- (39) Kaindl, G.; Chiang, T. C.; Eastman, D. E.; Himpsel, F. J. Distance-Dependent Relaxation Shifts of Photoemission and Auger Energies for Xe on Pd(001). *Phys. Rev. Lett.* **1980**, *45* (22), 1808–1811.
- (40) Chiang, T. C.; Kaindl, G.; Mandel, T. Layer-Resolved Shifts of Photoemission and Auger-Spectra from Physisorbed Rare-Gas Multilayers. *Phys. Rev. B: Condens. Matter Mater. Phys.* **1986**, *33* (2), 695–711.
- (41) Peisert, H.; Kolacyak, D.; Chasse, T. Site-Specific Charge-Transfer Screening at Organic/Metal Interfaces. *J. Phys. Chem. C* **2009**, *113* (44), 19244–19250.
- (42) Helander, M. G.; Greiner, M. T.; Wang, Z. B.; Lu, Z. H. Effect of Electrostatic Screening on Apparent Shifts in Photoemission Spectra near Metal/Organic Interfaces. *Phys. Rev. B: Condens. Matter Mater. Phys.* **2010**, *81* (15), 153308.
- (43) Wandelt, K. Properties and Influence of Surface Defects. *Surf. Sci.* **1991**, *251–252*, 387–395.
- (44) Balle, D.; Adler, H.; Grüninger, P.; Karstens, R.; Ovsyannikov, R.; Giangrisostomi, E.; Chassé, T.; Peisert, H. Influence of the Fluorination of CoPc on the Interfacial Electronic Structure of the Coordinated Metal Ion. *J. Phys. Chem. C* **2017**, *121* (34), 18564–18574.
- (45) Grüninger, P.; Greulich, K.; Karstens, R.; Belsler, A.; Ovsyannikov, R.; Giangrisostomi, E.; Bettinger, H. F.; Batchelor, D.; Peisert, H.; Chassé, T. Highly Oriented Hexacene Molecules Grown in Thin Films on Cu(110)-(2 × 1)O. *J. Phys. Chem. C* **2019**, *123* (45), 27672–27680.
- (46) Altman, E. I.; Colton, R. J. Nucleation, Growth, and Structure of Fullerene Films on Au(111). *Surf. Sci.* **1992**, *279* (1–2), 49–67.
- (47) Forrest, S. R. Ultrathin Organic Films Grown by Organic Molecular Beam Deposition and Related Techniques. *Chem. Rev.* **1997**, *97* (6), 1793–1896.
- (48) Wagner, C.; Kasemann, D.; Golnik, C.; Forcker, R.; Esslinger, M.; Müllen, K.; Fritz, T. Repulsion between Molecules on a Metal: Monolayers and Submonolayers of Hexa-peri-Hexabenzocoronene on Au(111). *Phys. Rev. B: Condens. Matter Mater. Phys.* **2010**, *81* (3), No. 035423.
- (49) Gross, L.; Moresco, F.; Ruffieux, P.; Gourdon, A.; Joachim, C.; Rieder, K.-H. Tailoring Molecular Self-Organization by Chemical Synthesis: Hexaphenylbenzene, Hexa-peri-Hexabenzocoronene, and Derivatives on Cu (111). *Phys. Rev. B: Condens. Matter Mater. Phys.* **2005**, *71* (16), 165428.
- (50) Seidel, C.; Ellerbrake, R.; Gross, L.; Fuchs, H. Structural Transitions of Perylene and Coronene on Silver and Gold Surfaces: A Molecular-Beam Epitaxy LEED Study. *Phys. Rev. B: Condens. Matter Mater. Phys.* **2001**, *64* (19), 195418.
- (51) Gao, L.; Deng, Z. T.; Ji, W.; Lin, X.; Cheng, Z. H.; He, X. B.; Shi, D. X.; Gao, H. J. Understanding and Controlling the Weakly Interacting Interface in Perylene/Ag(110). *Phys. Rev. B: Condens. Matter Mater. Phys.* **2006**, *73* (7), No. 075424.
- (52) Müller, K.; Kara, A.; Kim, T. K.; Bertschinger, R.; Scheybal, A.; Osterwalder, J.; Jung, T. A. Multimorphism in Molecular Monolayers: Pentacene on Cu(110). *Phys. Rev. B: Condens. Matter Mater. Phys.* **2009**, *79* (24), 245421.
- (53) Cheng, Z. H.; Gao, L.; Deng, Z. T.; Jiang, N.; Liu, Q.; Shi, D. X.; Du, S. X.; Guo, H. M.; Gao, H. J. Adsorption Behavior of Iron Phthalocyanine on Au(111) Surface at Submonolayer Coverage. *J. Phys. Chem. C* **2007**, *111* (26), 9240–9244.
- (54) Gao, L.; Liu, Q.; Zhang, Y. Y.; Jiang, N.; Zhang, H. G.; Cheng, Z. H.; Qiu, W. F.; Du, S. X.; Liu, Y. Q.; Hofer, W. A.; Gao, H. J. Constructing an Array of Anchored Single-Molecule Rotors on Gold Surfaces. *Phys. Rev. Lett.* **2008**, *101* (19), 197209.
- (55) Yokoyama, T.; Yokoyama, S.; Kamikado, T.; Okuno, Y.; Mashiko, S. Selective Assembly on a Surface of Supramolecular Aggregates with Controlled Size and Shape. *Nature* **2001**, *413* (6856), 619–621.
- (56) Zhang, X.; Tang, L.; Guo, Q. M. Low-Temperature Growth of C-60 Monolayers on Au(111): Island Orientation Control with Site-Selective Nucleation. *J. Phys. Chem. C* **2010**, *114* (14), 6433–6439.
- (57) Crommie, M.; Lutz, C.; Eigler, D. Imaging Standing Waves in a Two-Dimensional Electron Gas. *Nature* **1993**, *363* (6429), 524.
- (58) Friedel, J. The Absorption of Light by Noble Metals and Its Relation to the van der Waals Contribution to the Cohesive Energy. *Proc. Phys. Soc., London, Sect. B* **1952**, *65* (10), 769–774.
- (59) Lackinger, M.; Griessl, S.; Heckl, W. M.; Hietschold, M. Coronene on Ag(111) Investigated by LEED and STM in UHV. *J. Phys. Chem. B* **2002**, *106* (17), 4482–4485.
- (60) Ruffieux, P.; Gröning, O.; Biemann, M.; Simpson, C.; Müllen, K.; Schlapbach, L.; Gröning, P. Supramolecular Columns of Hexabenzocoronenes on Copper and Gold (111) Surfaces. *Phys. Rev. B: Condens. Matter Mater. Phys.* **2002**, *66* (7), No. 073409.
- (61) Sellam, F.; Schmitz-Hübsch, T.; Toerker, M.; Mannsfeld, S.; Proehl, H.; Fritz, T.; Leo, K.; Simpson, C.; Müllen, K. LEED and STM Investigations of Organic–Organic Heterostructures Grown by Molecular Beam Epitaxy. *Surf. Sci.* **2001**, *478* (1–2), 113–121.
- (62) Proehl, H.; Toerker, M.; Sellam, F.; Fritz, T.; Leo, K.; Simpson, C.; Müllen, K. Comparison of Ultraviolet Photoelectron Spectroscopy and Scanning Tunneling Spectroscopy Measurements on Highly Ordered Ultrathin Films of Hexa-peri-Hexabenzocoronene on Au (111). *Phys. Rev. B: Condens. Matter Mater. Phys.* **2001**, *63* (20), 205409.
- (63) Xiao, W. D.; Zhang, Y. Y.; Tao, L.; Ait-Mansour, K.; Chernichenko, K. Y.; Nenajdenko, V. G.; Ruffieux, P.; Du, S. X.; Gao, H. J.; Fasel, R. Impact of Heterocirculene Molecular Symmetry Upon Two-Dimensional Crystallization. *Sci. Rep.* **2015**, *4* (1), 5415.
- (64) Kawai, S.; Saito, S.; Osumi, S.; Yamaguchi, S.; Foster, A. S.; Spijker, P.; Meyer, E. Atomically Controlled Substitutional Boron-Doping of Graphene Nanoribbons. *Nat. Commun.* **2015**, *6* (1), 8098.
- (65) Villagomez, C. J.; Zambelli, T.; Gauthier, S.; Gourdon, A.; Stojkovic, S.; Joachim, C. STM Images of a Large Organic Molecule Adsorbed on a Bare Metal Substrate or on a Thin Insulating Layer: Visualization of Homo and Lumo. *Surf. Sci.* **2009**, *603* (10–12), 1526–1532.
- (66) Ohtani, H.; Wilson, R. J.; Chiang, S.; Mate, C. M. Scanning Tunneling Microscopy Observations of Benzene Molecules on the Rh(111)-(3 × 3)(C₆H₆ + 2CO) Surface. *Phys. Rev. Lett.* **1988**, *60* (23), 2398–2401.
- (67) Lippel, P.; Wilson, R.; Miller, M.; Wöll, C.; Chiang, S. High-Resolution Imaging of Copper-Phthalocyanine by Scanning-Tunneling Microscopy. *Phys. Rev. Lett.* **1989**, *62* (2), 171.
- (68) Sautet, P.; Joachim, C. Interpretation of STM Images: Copper-Phthalocyanine on Copper. *Surf. Sci.* **1992**, *271* (3), 387–394.
- (69) Dappe, Y. J.; Andersen, M.; Balog, R.; Hornekær, L.; Bouju, X. Adsorption and STM Imaging of Polycyclic Aromatic Hydrocarbons on Graphene. *Phys. Rev. B: Condens. Matter Mater. Phys.* **2015**, *91* (4), No. 045427.
- (70) Schmitz-Hübsch, T.; Sellam, F.; Staub, R.; Törker, M.; Fritz, T.; Kübel, C.; Müllen, K.; Leo, K. Direct Observation of Organic–Organic Heteroepitaxy: Perylene-Tetracarboxylic-Dianhydride on Hexa-peri-Hexabenzocoronene on Highly Ordered Pyrolytic Graphite. *Surf. Sci.* **2000**, *445* (2), 358–367.

B₃N₃-Substituted Nanographene Molecules: Influence of Planarity on the Electronic Structure and Molecular Orientation in Thin Films

Katharina Greulich,[⊥] Axel Belser,[⊥] Daniel Bischof, Felix Widdascheck, Marie S. Sättele, Peter Grüninger, Holger F. Bettinger, Gregor Witte, Thomas Chassé, and Heiko Peisert*



Cite This: *ACS Appl. Electron. Mater.* 2021, 3, 825–837



Read Online

ACCESS |



Metrics & More



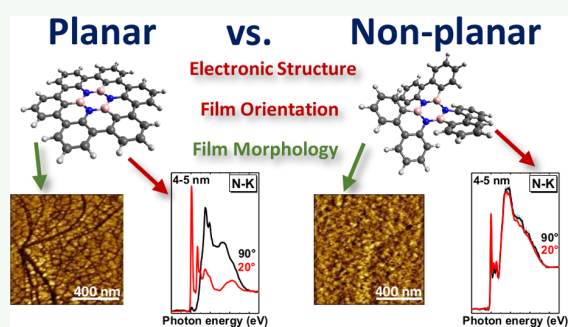
Article Recommendations



Supporting Information

ABSTRACT: BN-substituted nanographene molecules are currently the focus of interest because the substitution of C–C units by isoelectronic and isosteric BN units is a straightforward way of changing the electronic properties of nanographenes. Another parameter influencing the electronic structure, orientation, and growth mode of nanographene molecules is the planarity of the molecules. The electronic structure, orientation, and film growth of the related molecules B₃N₃-hexa-*peri*-hexabenzocoronene (BN-HBC), B₃N₃-hexabenzotriphenylen (BN-HBP), and B₃N₃-hexabenzotriphenylen-2H (BN-HBP-2H) on Au(111) have been studied by photoelectron spectroscopy (PES), X-ray absorption spectroscopy (XAS), atomic force microscopy (AFM), and scanning tunneling microscopy (STM). XA spectra were simulated using time-dependent density functional theory (TDDFT). The calculation of C 1s excitation spectra allows the assignment of individual transitions and the examination of the degree of cross-linking between biphenyl units. It is shown that the planarity of the molecules distinctly affects the electronic structure, interface properties, as well as growth in thin films.

KEYWORDS: BN-doped hexa-*peri*-hexabenzocoronene, interaction, photoemission, X-ray absorption spectroscopy, near-edge X-ray absorption fine structure, scanning tunneling microscopy, density functional theory, atomic force microscopy, valence band, planarity, π -conjugated systems, BN-doped nanographene



1. INTRODUCTION

Nanographene molecules have been studied intensely for possible applications in electronic devices.^{1–4} The probably best-known representative is hexa-*peri*-hexabenzocoronene (HBC), which is a polycyclic aromatic hydrocarbon (PAH) that can readily be synthesized and consists of a central aromatic ring surrounded by six aromatic rings that are interconnected by quasi-single bonds in a planar manner.^{5–8} Such extended PAHs, in turn, can be regarded as the starting point for a bottom-up approach for the graphene synthesis.^{9–12} Band gap opening and engineering of graphene have attracted significant attention in context with the development of graphene electronics and optoelectronics. Various applications have been explored, including energy conversion and storage components, field effect transistors, and sensors.^{13–15} The variation of band gap can be achieved by chemical doping with foreign atoms, and both “top-down” and “bottom-up” approaches are known.¹⁶ A promising pathway to modify the intrinsic electronic properties of nanographenes is the substitution of C–C units by isoelectronic and isosteric B–N units.^{17–23} The investigation of molecules with BN cores is the aim of this study.

The cross-linking of nanographenes can be triggered on surfaces at elevated temperatures, enabling, e.g., the synthesis

of networks of HBC and its derivatives.^{10,24–26} Intrinsic electronic properties can be tuned at the molecular level; a promising way is the substitution of C–C units by isoelectronic and isosteric B–N units.^{17–19,21–23,27}

Generally, the interplay between molecular structure, electronic structure, and ordering determines device efficiency parameters to a large extent.^{28,29} It was shown that HBC as well as B₃N₃-doped hexa-*peri*-hexabenzocoronene (BN-HBC) (Figure 1) adsorb highly ordered, in a flat-lying geometry on single-crystalline substrates such as Au(111) and that this orientation is almost unchanged in thin films.^{30–35} On the other hand, also nonplanar π -conjugated carbon systems are promising materials for a variety of applications. For example, nonplanar macrocyclic conformations of porphyrins and other tetrapyrroles have been studied in detail because of their important biochemical function^{36–39} as well as numerous other technological and scientific applications.⁴⁰

Received: November 3, 2020

Accepted: January 8, 2021

Published: January 21, 2021



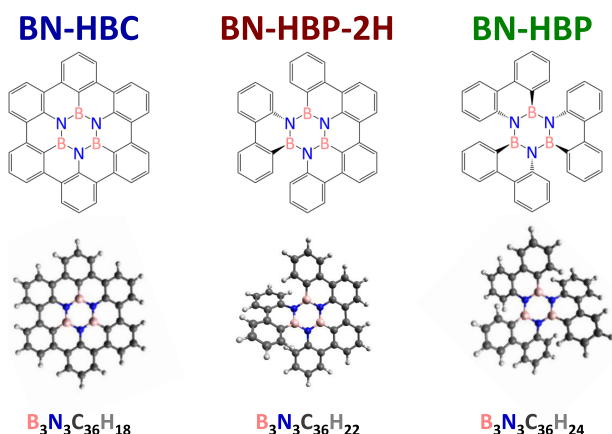


Figure 1. Chemical structure (top) and geometric structure as obtained from density functional theory (DFT, bottom) of B_3N_3 -doped hexa-*peri*-hexabenzocoronene (BN-HBC), B_3N_3 -hexabenzotriphenylen-2H (BN-HBP-2H), and the propeller-like B_3N_3 -hexabenzotriphenylene (BN-HBP) (carbon atoms, dark gray; hydrogen light gray; nitrogen blue and boron, red).

However, the planarity of the molecule may distinctly affect the electronic structure, in particular at interfaces. For example, the interaction strength is expected to increase for planar molecules due to the closer contact, and, vice versa, the substrate–molecule interaction may induce a change of the conformation depending on the type of the ligand.⁴¹

The aim of the present study is the investigation of the interplay between planarity, electronic structure, and film growth using the example of BN-doped nanographenes. Additionally, the characteristic X-ray absorption resonances can be utilized for the identification of BN-doped nanographene molecules as well as for BN-doped graphene sheets in further investigations. We have chosen three closely related molecules consisting of six peripheral aromatic rings and feature an internal borazine core. They differ in the degree of hydrogenation and extension of the aromatic conjugation (Figure 1). 1,2:3,4:5,6-Tris(*o,o'*-biphenylene)borazine (BN-HBP) has a propeller-like structure that results from repulsive interactions of pairs of hydrogen atoms.^{42–44} One-fold cyclodehydrogenation gives dibenzo[fg,ij]-1,3,4a,2,4,12b-triazatriboratriphenyleno[1,2,3,4-rst]-13,13b,13a,14 diazadiborapentaphen (BN-HBP-2H),⁴⁵ while threefold cyclodehydrogenation results in 18d,18f,18h-triaza-18e,18g,18i-triborahexabenzo [bc,ef,hi,kl,no,qr]coronene (BN-HBC).⁴⁶ The number of carbon, boron, and nitrogen atoms is the same for all three molecules, but the number of C–C and C–H bonds, as well as the number of hydrogen atoms in the outer π -conjugated carbon system are varied. The degree of hydrogenation has a profound influence on the degree of distortion of the PAH and thus the planarity and extension of the outer π -conjugated carbon system, which affects the electronic structure, film growth, and molecular orientation in thin films.

2. METHODS AND EXPERIMENTAL SECTION

Samples of BN-HBC, BN-HBP-2H, and BN-HBP were synthesized as described previously.^{42,45,46} The molecules were evaporated from a Knudsen cell at rates of 0.2–0.4 nm/min on a Au(111) single crystal, controlled by a quartz crystal microbalance (QCM). During deposition, the crystal was held at room temperature at a pressure of $<1 \times 10^{-8}$ mbar. Prior to organic film deposition, the Au(111) single crystal was cleaned by repeated cycles of each 30 min Ar^+ -ion

sputtering at a voltage of 0.8 kV at a partial pressure of 5×10^{-5} mbar and subsequent annealing at a temperature of 770 K. The purity and orientation of the crystal were checked by scanning tunneling microscopy (STM), X-ray photoelectron spectroscopy (XPS), ultraviolet photoelectron spectroscopy (UPS), and low-energy electron diffraction (LEED).

X-ray absorption spectroscopy (XAS) measurements were performed at the HE-SGM dipole beamline of the synchrotron storage ring BESSY II (Berlin).⁴⁷ To determine the average molecular orientation relative to the sample surface, polarization-dependent X-ray absorption spectra were acquired at different angles of the incident p-polarized light with respect to the surface plane (with $\theta = 90^\circ$ —normal incidence, 20° —grazing incidence) in Auger electron yield (AEY), where a hemispherical energy analyzer (Scienta R3000) was used to detect electrons within a defined energetic window. This window was set around the kinetic energy of the Auger electrons, which are emitted during the molecular relaxation process, whereas the size of the window was selected in a way that valence electrons as well as substrate core electrons do not contribute to the spectra (for more details, see ref 47). Hence, windows of 174 ± 5 , 260 ± 10 , and 375 ± 5 eV were chosen for B-K, C-K, and N-K edges, respectively. The energy resolution was set at 250 meV at a photon energy of 280 eV, and to 300 meV at photon energies of 190 and 400 eV. The pressure in the chamber was $<3 \times 10^{-9}$ mbar during measurements and $<3 \times 10^{-8}$ mbar while depositing the organic layers. Comparability of the measured XA spectra was facilitated by first subtracting a reference background (zero signal) from the XA spectra, second considering the photon flux by referencing to a clean substrate, and last normalizing the spectra to the same step height. The photoelectron spectroscopy (PES) and scanning tunneling microscopy (STM) measurements were carried out in the home laboratory of AK Chassé; the base pressure of both ultrahigh-vacuum (UHV) systems was $<3 \times 10^{-10}$ mbar. The PES measurements (both X-ray photoelectron spectroscopy (XPS) and ultraviolet photoelectron spectroscopy (UPS)) were realized using a multichamber UHV system equipped with an X-ray source with monochromator (XR 50 M, SPECS) and Al K α radiation ($h\nu = 1486.7$ eV), an ultraviolet source (UVS 300 SPECS), and a Phoibos 150 hemispherical energy analyzer (SPECS). For UPS measurements, the excitation energy of He II (40.8 eV) was used. The photoemission spectra were calibrated to reproduce the binding energies (BE) of Au 4f_{7/2} and Cu 2p_{3/2} at 84.00 and 932.56 eV, respectively. The peak fitting procedure of core-level spectra was realized using Unifit version 2018.⁴⁸ A Shirley model background and a Voigt profile (convolution of Lorentzian and Gaussian profiles) were used. According to the literature, the Lorentzian widths for N 1s, C 1s, and B 1s core levels were set at 0.10, 0.08, and 0.07 eV, respectively.^{49–51} The error of absolute binding energies and thus also for the peakfits is estimated to be less than ± 0.05 eV.

The STM measurements were performed in a two-chamber system equipped with a low-energy electron diffraction (LEED) system from OCI Vacuum Microengineering, Inc. and a variable-temperature (VT)-STM from Omicron GmbH. For the STM measurements, mechanically cut Pt/Ir tips were used. All given tunneling voltages are referenced to the sample. On the shown STM images, no filtering or smoothing was performed. The WSxM program was used to enhance the image contrast.⁵²

The atomic force microscopy (AFM) measurements were carried out on air using a Bruker multimode 8 AFM system with RTESPA-150 tips from Bruker, especially for tapping mode. Filtering and smoothing of the images were performed with the Gwyddion program.⁵³

The quantum chemical calculations were made with the ORCA package.⁵⁴ For the geometry optimizations, the global hybrid B3LYP density functional^{55,56} was used in combination with the def2-TZVP basis set.⁵⁷ The calculation of the Coulomb and exchange terms was accelerated using the resolution of identity (RI) and chain of sphere (COSX)⁵⁸ approximations with the def2/J basis set.⁵⁹ An analytical frequency analysis was made to ensure optimization of the structure

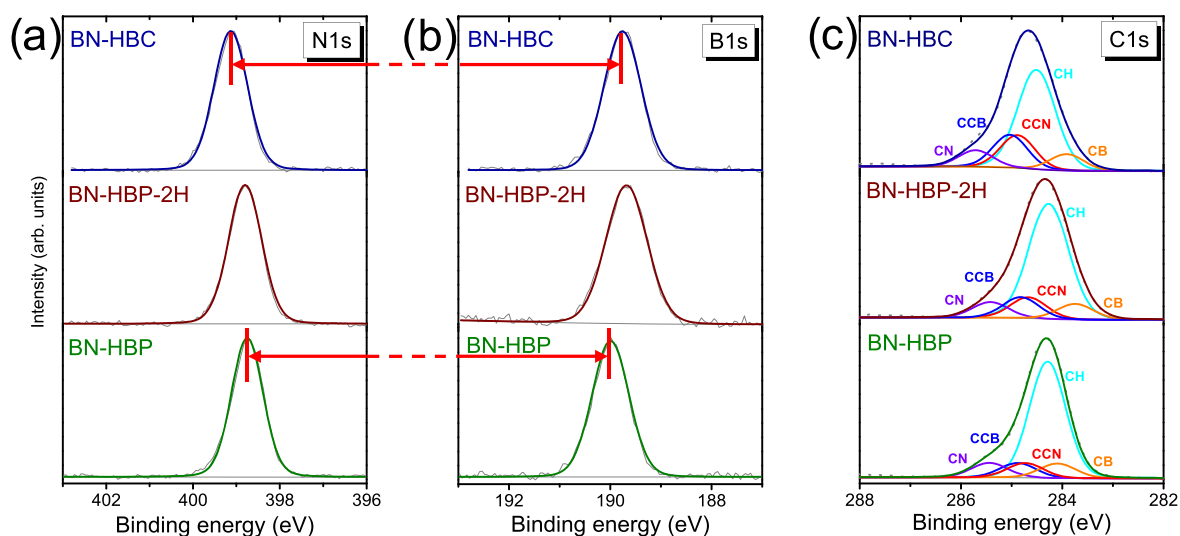


Figure 2. Multilayer core-level spectra (film thickness, 7–8 nm) of BN-HBC (top), BN-HBP-2H (middle), and BN-HBP (bottom): (a) N 1s, (b) B 1s, and (c) C 1s, measured with $h\nu = 1487.7$ eV.

Table 1. Binding Energies of the Multilayer N 1s, C 1s, and B 1s Core Levels for All Three Molecules (in eV)^a

| | N 1s | B 1s | C 1s | | | | |
|-----------|--------|--------|--------|--------|--------|--------|--------|
| | | | CN | CCB | CCN | CH | CB |
| BN-HBC | 399.13 | 189.76 | 285.71 | 285.03 | 284.88 | 284.51 | 283.91 |
| BN-HBP-2H | 398.80 | 189.68 | 285.42 | 284.82 | 284.67 | 284.27 | 283.74 |
| BN-HBP | 398.75 | 190.00 | 285.44 | 284.88 | 284.73 | 284.29 | 284.09 |

^aThe Gaussian widths are in between 0.76 and 0.89 eV for all core levels and components (see Table S1).

to its minimum energy. A natural population analysis (NPA) was performed with the NBO 6.0.18a code.⁶⁰

For a comparison with experimental UP spectra, the B3LYP/def2-TZVP molecular orbitals were convolved with a Gaussian broadening (full width at half-maximum = 0.3 eV). The energy scale of the calculated spectra was adjusted and expanded by a factor of 1.05 to match the experimental features. This procedure is common practice when comparing DFT data to UP spectra and accounts for the well-known fact that DFT often underestimates orbital energies.^{61–63}

The K-edge XA spectra were calculated as described in ref 64 by applying the time-dependent density functional theory (TDDFT) formalism, as implemented in ORCA. Symmetry-equivalent B, N, or C 1s orbitals were localized using the Pipek–Mezey formalism.⁶⁵ TDDFT calculations were carried out by allowing excitations from the localized 1s orbitals only. To allow a comparison with experimental spectra, the calculated discrete excitations were broadened with Gaussian functions of varying width.⁶⁶ Starting from the first transition, a broadening σ of 0.5 eV was used for the first 5 eV. After this, a linear increase of the full width at half-maximum (FWHM) from 2.0 up to 15.0 eV was applied to account for the reduced lifetime of the σ^* resonances.⁶⁷ Furthermore, B 1s NEXAFS spectra were also calculated on the Slater transition-state level using the StoBe package⁶⁸ for comparison purposes by first optimizing the molecular geometry using the gradient-corrected revised Perdew–Burke–Ernzerhof (RPBE) functional and all-electron TZVP basis sets. Afterward, the excited states for each nonsymmetry-equivalent excitation center, i.e., boron atoms, were calculated separately. To avoid B 1s core orbital mixing in this step, the excitation center is modeled using an IGLO-III basis set, while the other boron centers are described by effective core potentials (ECPs). Further details on the computations can be found in previous work.⁶⁹

3. RESULTS AND DISCUSSION

3.1. Electronic Structure and Planarity in Multilayer Films.

Although the chemical structures of the three investigated molecules in Figure 1 appear very similar at first glance, the analysis of XP core-level spectra reveals significant differences. XP core-level spectra of thick layers (7–8 nm) of BN-HBC, BN-HBP-2H, and BN-HBP on Au(111) are compared in Figure 2. At this film thickness, a possible influence of the interface on the peak shape can be neglected because a strong dewetting can be excluded from the AFM micrographs (discussed below). The binding energies of the core levels and the different C 1s components are summarized in Table 1 (additional data (Gaussian widths) can be found in Table S1 (Supporting Information)). The N 1s and B 1s spectra (Figure 2a,b) can be described by a single component for all molecules, as might be expected from the chemical structure, because the N and B atoms exhibit similar chemical environments in all presented molecules.

For the description of the C 1s spectra in Figure 2c, we assume that the binding energy of chemically inequivalent carbon species is determined by the charge density, neglecting photoemission final state effects. Based on the calculated NPA charges, we distinguish in sequence from lower to higher binding energies: carbon bonded to boron (CB), hydrogen (CH), other carbon (CC), and nitrogen (CN). In agreement with the literature on related acenes^{70,71} and graphene nanoribbons,⁷² the CH component appears at a lower binding energy compared to CC. Further, the calculations suggest that the binding energy of CC carbons in proximity to nitrogen (CCN) is somewhat lower compared to CC carbons in proximity to boron (CCB). NPA charges and the exact

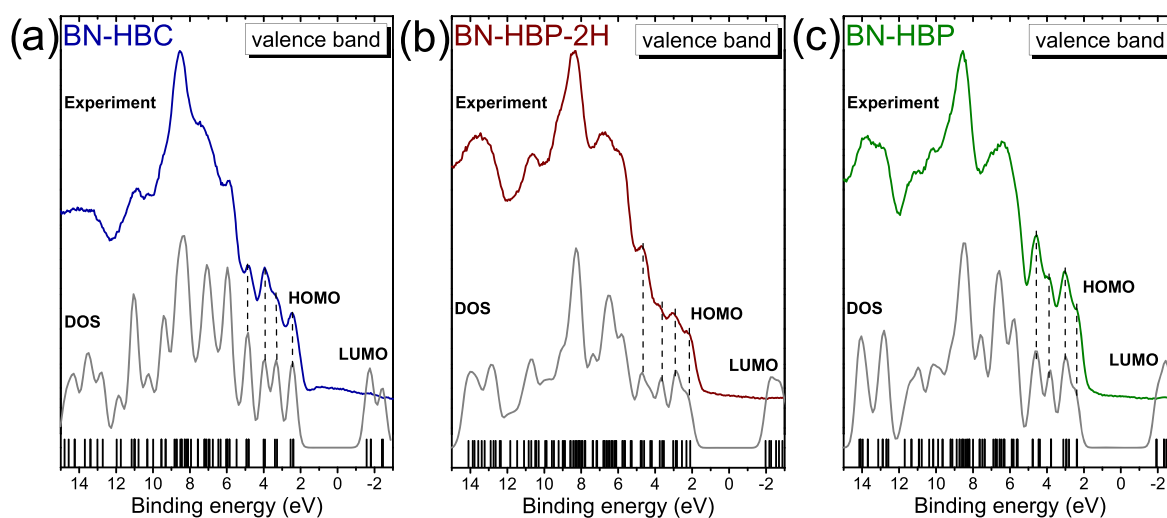


Figure 3. Multilayer valence band spectra (film thickness, 7–8 nm) of (a) BN-HBC, (b) BN-HBP-2H, and (c) BN-HBP: Experimental UP spectra measured with He II radiation ($h\nu = 40.8$ eV) and MO energies with Gaussian broadening. The dashed lines match the first four experimental features to the calculations.

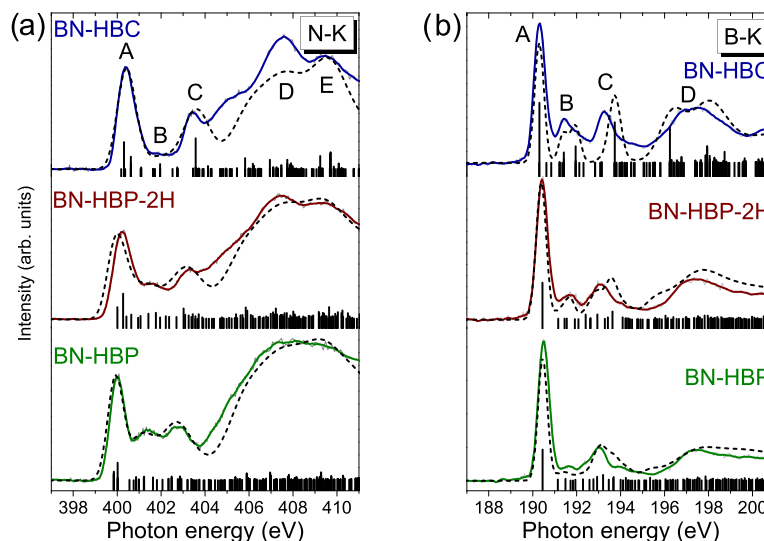


Figure 4. X-ray absorption spectra of the (a) N-K and (b) B-K edge of 4–5 nm thin films of BN-HBC (top), BN-HBP-2H (middle), and BN-HBP (bottom) measured close to the magic angle (55°). The experimental data (solid line) are compared to calculated data (dashed line) and the dedicated absorption transitions (black bars). The calculated spectra were obtained by broadening the discrete transitions with Gaussian functions.

numbering of carbon atoms are summarized in Tables S2–S4 (Supporting Information). For the peak fits, the intensities of the various compounds were fixed according to the stoichiometry CH:CCB:CCN:CB:CN (18:6:6:3:3 for BN-HBC, 22:4:4:3:3 for BN-HBP-2H, and 24:3:3:3:3 for BN-HBP). Slight deviations between the stoichiometric peak fit and experimental data might be caused by the presence of shake-up satellite structures, which were not considered in the model. Often, highest occupied molecular orbital–lowest unoccupied molecular orbital (HOMO–LUMO) shake-up processes dominate the satellite structure, and thus an energy separation with respect to the main line in the order of the size of the optical gap might be expected.⁷³ On the other hand, for other nanographene molecules (acenes), it has been shown that the satellite structure is very complex and the distance between HOMO–LUMO shake-up satellites and the C 1s

main line can be distinctly smaller than the optical gap.⁷⁴ This may be explained by a more efficient screening of the photogenerated core hole, potentially due to an optimized redistribution of charge in the final state of the photoemission.⁷⁴

A comparison of core-level binding energies for the three investigated molecules (Table 1) reveals distinct differences: BN-HBC possesses the highest N 1s and C 1s binding energies (399.13 and 284.51 eV (CH), respectively), while the values for BN-HBP-2H and BN-HBP are 0.2–0.4 eV lower. In contrast, for the B 1s core level, the energetic situation is vice versa: The highest binding energy is observed for BN-HBP (190.00 eV), whereas the binding energies for BN-HBC and BN-HBP-2H are lower (189.76 and 189.68 eV, respectively). This opposite behavior indicates not only a shift of the reference level (e.g., due to a different energy-level alignment)

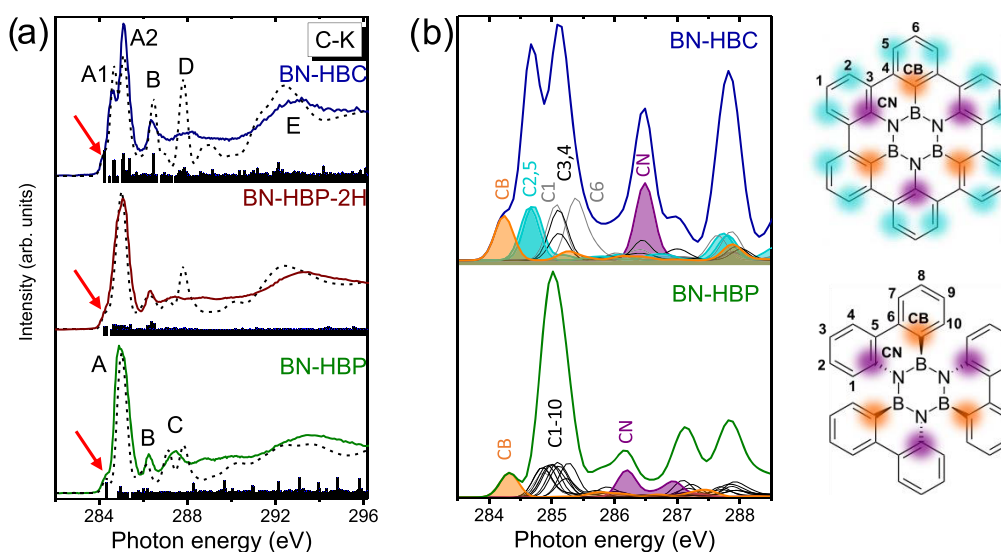


Figure 5. (a) X-ray absorption spectra of the C-K edge of 4–5 nm thin films of BN-HBC (top), BN-HBP-2H (middle), and BN-HBP (bottom) close to the magic angle (55°). The experimental data (solid line) are compared to calculated data (dashed line) and the dedicated absorption transitions (black bars, enlarged by factor 3 for better visibility). (b) Calculated spectra for each inequivalent carbon atom at the example of BN-HBC and BN-HBP. Calculated spectra were obtained by broadening the discrete transitions with Gaussian functions.

but also a different electron density at the respective atom sites. This might be more clearly demonstrated by comparing relative core-level binding energies for each molecule separately: The N 1s–B 1s separation is largest for BN-HBC (209.37 eV) and smallest for BN-HBP (208.75 eV) (highlighted in Figure 2a,b), which could indicate a higher polarity of the B–N bond in the case of BN-HBP. This trend is still visible in the C 1s binding energies for C atoms neighbored to N and B (Figure 2c). The C 1s binding energy difference for CN and CB components is largest in the BN-HBC peak fit and the smallest for BN-HBP. Additionally, energy separations between CC and CH components are not the same for all molecules, indicating different electron densities at these atoms. Consequently, the differences in the relative binding energy of carbon components cause a different broadness of the overall C 1s peak: BN-HBC > BN-HBP-2H > BN-HBP. Thus, the different core-level binding energies for the three studied molecules indicate weak but significant changes in the electron densities. Hence, the number of π -bonds on the surrounding carbon atoms determines not only the planarity of the molecule but also the electronic structure.

The different electronic structure should affect UP valence band spectra. The experimental UP spectra of BN-HBC, BN-HBP-2H, and BN-HBP are compared to the molecular orbital energies obtained from DFT calculations (Figure 3). Although we are aware that our calculations do not consider photoemission cross sections and, in addition, we assume that the photoemission process is nonadiabatic, the calculated spectra are in good agreement with the experimental data and allow an assignment of the features, especially at low binding energies. The calculated HOMO–LUMO gaps (3.8 eV for BN-HBC and 4.1 eV for BN-HBP) are larger than the experimental values for the optical gaps (3.1 eV for BN-HBC³³ and 3.4 eV for BN-HBP (cf. Figure S1)). All three spectra show similarities, for example, a very intense feature at about 8 eV, but the valence band spectrum of BN-HBP-2H is also the most complex, due to the lower symmetry of the molecule. The symmetry of the molecular orbitals (cf. Figure S2) indicates

that all molecular orbitals below 4.5 eV binding energy have predominant π -character.

Further insight into the (unoccupied) electronic structure can be obtained by XAS. Measurements at the N-K, B-K, and C-K edges are shown for 4–5 nm thick BN-HBC, BN-HBP-2H, and BN-HBP films (Figures 4 and 5). The spectra are compared to calculations, illustrated as dashed lines. To omit effects arising from a different molecular orientation (discussed below), the chosen angle between the incident synchrotron light and the sample surface θ was 55° , i.e., close to the “magic angle”, where the intensity of the resonances is independent of the orientation of the transition dipole moment.⁶⁷ Additionally, effects induced by the substrate can be ruled out at film thicknesses of 4–5 nm. Therefore, differences in the shown BN-HBC, BN-HBP-2H, and BN-HBP spectra can be essentially ascribed to differences in the unoccupied valence electronic structure of the molecules. Generally, two different regions can be distinguished: Intensity at lower photon energies (below 404 eV (N-K),^{75–77} 290 eV (C-K),^{31,35} and 195 eV (B-K)⁷⁸) can be mainly ascribed to transitions into π^* orbitals, while transitions at higher photon energies have predominantly σ^* character.

For both the N-K and B-K XA spectra, three features denoted A–C in the sequence of increasing photon energies can be distinguished in the π^* region (Figure 4). In all cases, A is the most intense feature. At first glance, this might imply a similar origin of these features, i.e., transitions from the respective 1s core level into the same unoccupied molecular orbitals. However, from the ground-state molecular orbitals (cf. Figure S2), we conclude that the BN-HBC LUMO is not located in the inner BN core, whereas for BN-HBP, the LUMO is distributed over the whole molecule. Hence, feature A is mainly caused by transitions into the LUMO for BN-HBP, but for BN-HBC, feature A is caused by transitions into higher unoccupied orbitals (i.e., LUMO+1, +2). In contrast to feature A, the intensity of B in Figure 4 varies distinctly. In N-K XA spectra, B is most intense for BN-HBP, weaker for BN-HBP-2H, and barely visible for BN-HBC. The opposite trend is

visible in B-K XA spectra. For a quantitative discussion, the ratio of features A/B and A/C is summarized in Table 2. We

Table 2. Intensity Comparison for Features A, B, and C of the N-K and B-K Edges

| | N-K | | B-K | |
|-----------|-----|-----|-----|-----|
| | A/B | A/C | A/B | A/C |
| BN-HBC | 6.3 | 1.7 | 3.1 | 2.7 |
| BN-HBP-2H | 2.4 | 1.8 | 5.7 | 3.9 |
| BN-HBP | 2.1 | 2.0 | 9.4 | 4.3 |

note that the values depend slightly on the procedure of background correction, but the discussed phenomena are very clear. The ratios A/B and A/C differ distinctly for each molecule, indicating a distinct influence of the planarity on the electronic structure of the considered molecule. The strongest intensity variations are observed for the A/B ratios. In the N-K XA spectra, the A/B ratio is about 3-fold higher for BN-HBC compared to BN-HBP, but the order is reversed for the B-K XA spectra, i.e., the A/B ratio in Table 2 shows opposite trends for the B-K and N-K edges.

Significant differences are also visible in the σ^* region: Two well-resolved features denoted D and E can be distinguished in the BN-HBC N-K spectrum, whereas these structures are less resolved for BN-HBP-2H and indiscernible for BN-HBP. In the σ^* region of B-K XA spectra, just one feature D is visible for all three molecules, but a splitting of D into two features might be suspected for BN-HBC.

We note that also energetic shifts in the N-K and B-K spectra are visible in Figure 4. In the N-K XA spectra, feature A is located at 400.4, 400.2, and 400.0 eV for BN-HBC, BN-HBP-2H, and BN-HBP, respectively. For the B-K edge spectra, an opposite trend is observed for BN-HBC (190.3 eV), BN-HBP-2H (190.4 eV), and BN-HBP (190.5 eV). Such shifts may originate from different energies of the respective initial or final energy level and/or a variation of the energy gap of the molecules. The opposite trend in N-K and B-K XAS spectra rules out a variation of the gap as the only reason for the observed energy shifts. Rather, the initial state, i.e., the N 1s and B 1s binding energies may explain the observed shifts in XAS to a large extent: The lowest N 1s and highest B 1s core-level binding energy is observed for BN-HBP with respect to the other molecules (Table 1), causing also an energy shift of the corresponding XA spectra.

To understand the shapes of B-K and N-K edge XA spectra as a function of the planarity of the molecules more in detail, we performed DFT calculations. For BN-HBP and BN-HBC, all B and N atoms produce the same spectra because of the threefold symmetry of the molecules. In contrast, the B and N atoms in BN-HBP-2H have different contributions: For the atoms located in the planar part of the molecule, the calculated spectra are very similar to the ones of BN-HBC, the atoms on the vertically protruding part of the molecule are similar to the ones of BN-HBP. The calculations indicate that the BN-HBP-2H spectra can be obtained from a combination of the BN-HBC and BN-HBP features (cf. Figure S3). This can explain why in all trends discussed here, BN-HBP-2H lies in between BN-HBC and BN-HBP.

Generally, the calculated spectra (dashed lines in Figure 4) reproduce the main features of experimental spectra very well. Both the intensity and energetic position of features A, B, and C in the π^* region of B-K and N-K edge spectra are in good

agreement with the experimental data. We note that for the simulation of B-K edge absorption spectra, another DFT-based program package was used (StoBe⁶⁸). The similar results (cf. Figure S4) indicate a weak dependence on the computational details such as the calculation of the excited states (TDDFT vs Slater transition-state method) and the treatment of the excitation center (i.e., calculation with localized core orbitals vs calculation with effective core potentials). The experimentally observed intensity variation of feature B is clearly visible in the calculated spectra. The electron density variation between excited state and ground state can be discussed by means of difference density plots, shown for both the B-K and the N-K edge of BN-HBC and BN-HBP as in the Supporting Information (cf. Figures S5–S8). The symmetry of these plots with respect to the molecular plane confirms the predominant π^* character of features A, B, and C. Further, it is visible that the final state for transitions contributing to A is mostly localized in the inner BN-substituted ring. In contrast, the final state of transitions involved in B seems to be more delocalized over the entire molecule, making the intensity dependence of this feature on the planarity plausible. One might speculate that for transitions at the nitrogen atom of the nonplanar BN-HBP molecule, a delocalization of the excited electron is supported by the neighboring B and C atoms with lower electronegativity, resulting in a relatively high intensity of the B feature in the corresponding N-K XA spectrum.

The C-K edge spectra are more complex (Figure 5) because of contributions from several chemically inequivalent carbon atoms. For all molecules, the π^* region is dominated by a strong feature A, accompanied by weaker features denoted B–D. In the σ^* region, a single, broad feature E is visible. Apparently, feature A of the BN-HBC spectrum is split into two features A1 and A2. Looking more in detail in the C-K edge spectra, a distinct shoulder at the low-energy side of feature A can be detected for all three molecules (see red arrow in Figure 5a).

As for N-K and B-K XA spectra (cf. Figure 4), also the calculated C-K spectra (dashed lines in Figure 5a) reproduce the experimental data well. To understand the nature of the C 1s excitations in more detail, we have carried out sophisticated TDDFT calculations for each symmetry inequivalent carbon atom, which are shown for BN-HBC and BN-HBP in Figure 5b. For BN-HBP-2H, these spectra exhibit a higher complexity and contain essentially individual carbon spectra of both BN-HBC and BN-HBP. The individual spectra for BN-HBC and BN-HBP in Figure 5 reveal that the shoulder of feature A at the low-photon-energy side (indicated by the red arrow in Figure 5a at 284.2 and 284.3 eV for BN-HBC and BN-HBP, respectively) in the experimental C-K XA spectra arises from transitions localized at the three carbon atoms directly bonded to boron (orange curve in Figure 5b). The spectra of the three carbon atoms that are directly bonded to nitrogen are observed at much higher photon energies and have their lowest-lying feature at 286.4 and 286.2 eV for BN-HBC and BN-HBP, respectively (purple curve in Figure 5b).

It is worth mentioning that the C-K edge spectrum of BN-HBC is nevertheless comparable to HBC (i.e., the “parent molecule” without BN core).³⁵ The similarity indicates that the electronic structure of the outer carbon atoms is only weakly affected by the BN core. The differences can be mainly attributed to the carbon atoms directly bonded to the BN core. As can be seen from Figure 5b, the splitting of feature A in the C-K edge of BN-HBC is mainly caused by a lower energy of

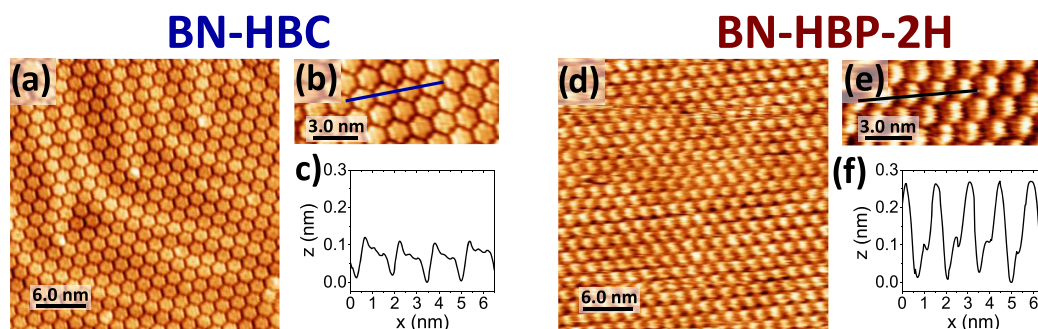


Figure 6. Room-temperature STM images of about a monolayer of BN-HBC: (a) $U = -1.3$ V, $I = 630$ pA; (b) $U = -0.4$ V, $I = 490$ pA and BN-HBP-2H (d) $U = -1.3$ V, $I = 350$ pA; (e) $U = 1.2$ V, $I = 400$ pA. (c, f) Apparent height profiles along the blue lines.

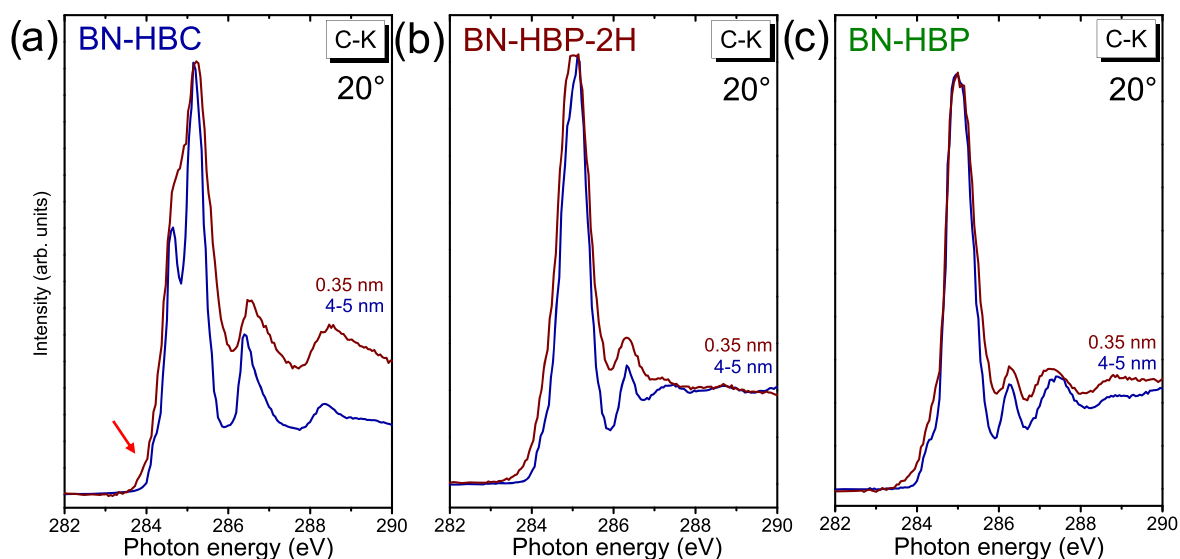


Figure 7. Comparison of C-K XA spectra for a monolayer and multilayers (multilayer film thickness, 4–5 nm) at grazing incidence (20°): (a) BN-HBC, (b) BN-HBP-2H, and (c) BN-HBP.

the main transitions from the CH atoms denoted C2 and C5, contributing to A1, similar to HBC.³⁵ A general explanation of the shape of the C-K edge is possible taking into account the ground-state electronic structure considering the Clar and Hückel models of aromaticity: A large split of $1s \pi^*$ transitions (about 2 eV, not observed here) is predicted for molecules rich in isolated double bonds, whereas nearly degenerate π^* orbitals lead to a small split of $1s \pi^*$ transitions.⁷⁹ For HBC and related molecules, the smaller but distinct split of the most intense A feature was ascribed to the so-called core-hole effect, caused by the interaction between the core hole and the excited electron.^{35,80}

3.2. Orientation and Film Growth. It can be expected that the planarity of the molecules affects distinctly the molecular orientation and growth of thin films. The structural ordering of the first layer in organic thin films may affect the growth of subsequent layers and determines the interfacial electronic structure. The detailed adsorption geometry of BN-HBC and BN-HBP-2H monolayers was studied by STM (Figure 6). Unfortunately, it was not possible to obtain STM images of BN-HBP on Au(111) at room temperature. A reason for this could be the higher mobility of BN-HBP compared to the other two molecules, probably because of its nonplanar molecular structure preventing close contact to the substrate.

As a result, comparably weak molecule–substrate interactions might be expected. Both BN-HBC and BN-HBP-2H molecules form well-ordered structures (Figure 6). The images were taken after annealing films of two to three layers to 610 K. Due to the commonly weaker intermolecular interaction strength compared to the molecule–substrate interaction, the annealing provokes a desorption of molecules exceeding monolayer coverage. Further, the increased mobility at elevated temperatures enables the formation of large domains with fewer defects compared to the deposition at room temperature. However, in principle, the same arrangement of BN-HBC and BN-HBP-2H molecules on Au(111) is obtained for monolayers prepared without any annealing.

In Figure 6a large, hexagonal BN-HBC domains are visible. A commensurate (5×5) superstructure is determined from the corresponding LEED image of Figure S9a, in agreement with a recent study.³⁴ The line profile (Figure 6c) emphasizes the regularity and the low apparent height differences. Similarly, BN-HBP-2H adsorbs in a hexagonally ordered lattice (Figure 6d), which can be reproduced also for the monolayers prepared without annealing. The corresponding LEED image is comparable to BN-HBC (cf. Figure S9b), indicating the same superstructure. However, in the enlarged section of the BN-HBP-2H monolayer STM image (Figure 6e), the

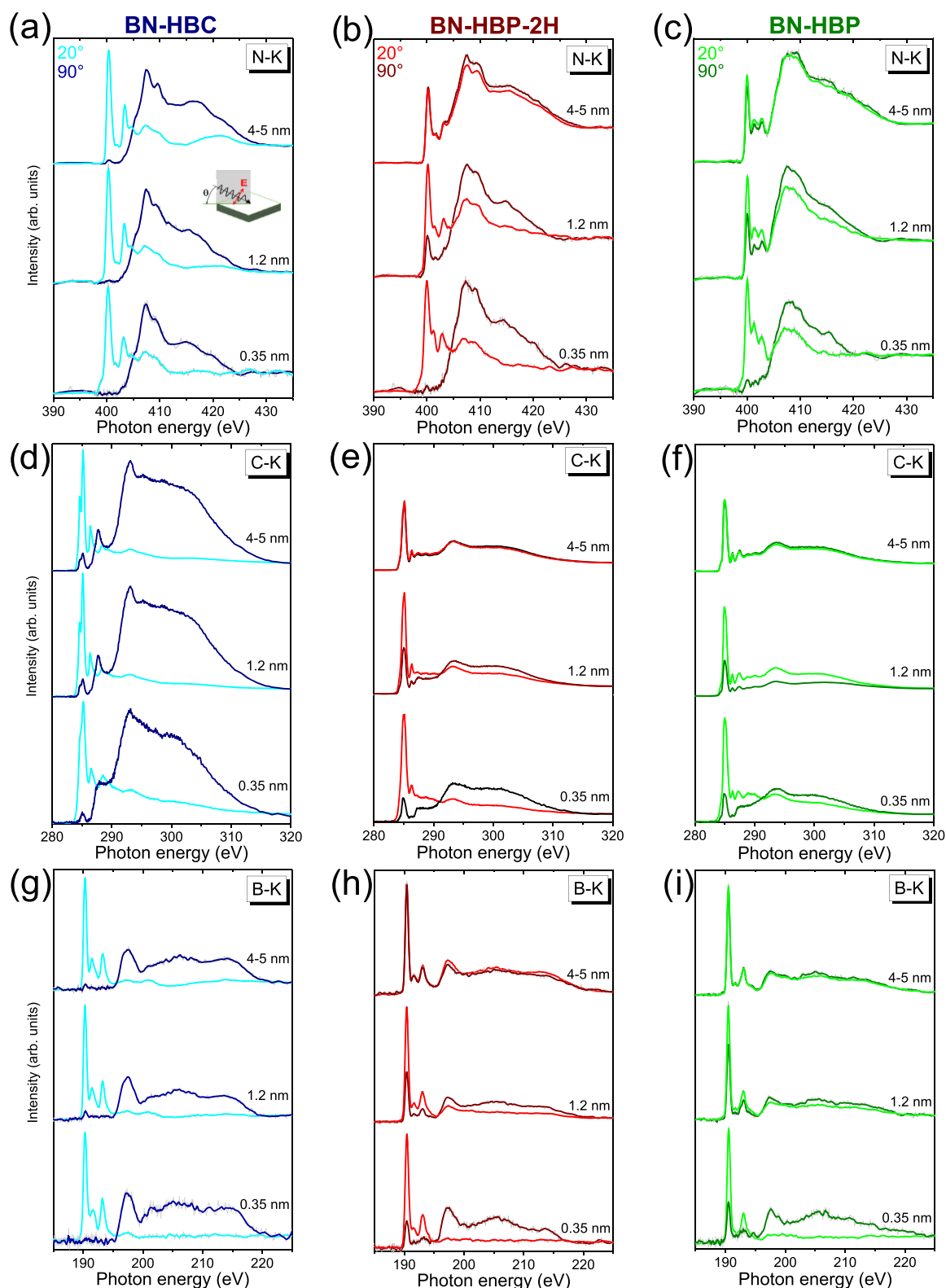


Figure 8. Thickness-dependent XA spectra of the three K edges of the three BN molecules. (Left) BN-HBC (a, d, g), (middle) BN-HBP-2H (b, e, h), and (right) BN-HBP (c, f, i).

molecules do not appear homogeneous: While the BN-HBC molecules appear as flat hexagons (Figure 6b), one side of the BN-HBP-2H molecule appears brighter than the other and the

height profiles along the blue lines in the enlarged section of the STM images show a much larger apparent height difference for BN-HBP-2H than for BN-HBC.

Generally, the STM image contrast is caused by a complex interplay between sample topography and electronic structure of sample and tip. Since the STM images in Figure 6 were taken at low bias voltages (located within the HOMO–LUMO gap of the molecules), we suspect that the topographic contrast determines the apparent height. This suggests that, in contrast to BN-HBC, the adsorption geometry of BN-HBP-2H is not completely flat. This observation is in good agreement with tilt angles in the monolayer range, calculated from polarization-dependent XAS spectra (see below). Apparently, a flat adsorption geometry is hindered by the nonplanar structure of BN-HBP-2H, preventing stronger molecule–substrate interactions. In other words, a planarization of BN-HBP-2H at the interface is not observed.

The comparably strong molecule–substrate interaction for BN-HBC on Au(111) might also affect electronic interface properties. Indeed, the comparison of the shape of K-edge XA spectra for monolayer coverages to thicker films reveals small, but distinct differences, in particular for the C-K edge. In Figure 7, we compare C-K edge XA spectra for all three molecules at grazing incidence. Most visibly, the XA spectra for BN-HBC show a clear broadening of feature A at coverages in the monolayer range, and also small, but distinct relative energy shifts (0.1–0.2 eV) with respect to the main component (feature B and transitions from carbon bonded to boron; see red arrow). A distinct broadening is also visible for BN-HBP-2H at low coverages, whereas thickness-dependent changes of the peak shape are hardly visible for BN-HBP. We note that for submonolayers of BN-HBC on Au(111), perturbations of the electron density (Friedel oscillations) were observed in STM images, indicating weak, but non-negligible electronic interactions.³⁴ It seems that the loss of the planarity for the series BN-HBC → BN-HBP-2H → BN-HBP is accompanied with a weaker contact causing a decrease of the electronic coupling between the molecule and the substrate.

Besides the information on the (interfacial) electronic structure, valuable information on the molecular orientation in thin films can be extracted from polarization-dependent XA spectra.⁶⁷ In planar carbon systems, transitions from C 1s states to a π^* orbital are strongest for \vec{E} vertical to the molecular plane, whereas transitions to σ^* are strongest for \vec{E} parallel to the molecular plane. Commonly, a vector model is utilized to determine the tilt angle of the molecular plane with respect to the substrate surface.⁸¹ Since the exact determination of resonance intensities depends, among others, on the background treatment and normalization,^{47,81} in some cases, an accurate determination of the tilt angle is hindered. Most commonly, C 1s π^* excitations are used for the analysis of the adsorption geometry. In addition, for molecules possessing heteroatoms, the corresponding transitions into π^* can be utilized in a similar manner. For example, N 1s π^* excitations are often analyzed to determine the orientation of phthalocyanines.^{75,82–84} Analogously, for the studied molecules, N 1s π^* and B 1s π^* excitations are available for an analysis of the adsorption geometry. For planar molecules, such as BN-HBC, the information obtained from N 1s π^* and B 1s π^* excitations is expected to be comparable to the analysis of C 1s π^* transitions.

In contrast, the BN-HBP molecule is nonplanar.⁴⁴ The laterally protruding “wings” consisting of unsubstituted biphenyl units are tilted by a considerable amount with respect to the BN-substituted core. Due to the localized nature

of core-level excitations, the C-K edge probes the orientation of the (tilted) wings, B-K and N-K edges probing the orientation of the (distorted) BN core. Thus, it is expected that the analysis of B-K and N-K edges yields a different tilt angle compared to the analysis of the C-K edge. The distortion of the BN core and the complicated background correction procedure only allow a qualitative discussion of relative changes of the orientation of biphenyl units with respect to the BN core. Further, the surface sensitivity of XA spectra recorded in Auger electron yield (AEY) is slightly different: The mean free path depends on the kinetic energy of the electrons and is estimated to be about 1.7, 1.4, and 1.1 nm for the N-K, C-K, and B-K edges, respectively (according to ref⁸⁵ for organic molecules assuming a density of BN-HBC of about 1.3 g/cm³). Thus, at least for thicker films, the molecular orientation is preferentially probed at the surface of the organic film.

Polarization-dependent B-K, N-K, and C-K XA spectra for two prominent angles (grazing and normal incidence) are shown for the three investigated molecules in Figure 8 as a function of the thickness. The measurement geometry is shown as an inset in Figure 8a. All XA spectra of BN-HBC (Figure 8a,d,g) show a very clear, uniform trend for all thicknesses: At grazing incidence ($\theta = 20^\circ$), the intensity for transitions into π^* orbitals is maximal, whereas these transitions are almost disappeared at normal incidence ($\theta = 90^\circ$). From the intensity of π^* transitions in N-K spectra (<402 eV) at normal and grazing incidence of the incoming synchrotron light, we estimated the average molecular tilt angle with respect to the substrate surface according to (ref⁶⁷)

$$I \sim P(\sin^2 \alpha \sin^2 \theta + 2 \cos^2 \alpha \cos^2 \theta) + (1 - P)\sin^2 \alpha \quad (1)$$

where P is the polarization degree, θ is the angle of incidence of the p-polarized synchrotron radiation, and α denotes the average tilt angle of the molecules with respect to the substrate surface. With $P = 0.91$ (91%), we arrive at 13, 7, and 1° for film thicknesses of 4–5, 1.2, and 0.35 nm of BN-HBC, respectively. The experimental error is estimated to be about $\pm 5^\circ$. Tilt angles calculated via the C-K and B-K π^* intensities (Figure 8d,f) yield similar results within the given error. This proves that BN-HBC monolayers adsorb in a flat-lying geometry, in good agreement with above-discussed STM data and recent studies.^{33,34,46} This orientation is almost maintained up to a film thickness of 4–5 nm. We note that the related, planar HBC molecule grows in a similar manner on metal substrates.^{30–32,35,86} At coverages in the monolayer range, the angular dependence of all three K edge XA spectra in Figure 8 is comparable to BN-HBC: For both molecules, BN-HBP-2H and BN-HBP, features in the π^* region are most intense at grazing incidence and weak at normal incidence pointing to a preferred flat-lying adsorption geometry. However, the remaining intensity for 1s π^* transitions at normal incidence is clearly visible and may point to distinct tilt angles. The calculated tilt angles from N-K π^* intensities of the monolayers are 10 ± 5 and $22 \pm 5^\circ$ for BN-HBP-2H and BN-HBP, respectively. We note that from B-K and C-K edges even larger tilt angles were obtained (up to $40 \pm 5^\circ$), which may be due to the distortion of the BN core and a different orientation of the biphenyl units for the first monolayer adsorbed on Au(111) (see above).

With increasing film thicknesses of BN-HBP-2H and BN-HBP (1.2 and 4–5 nm, respectively), the dichroism of K edge

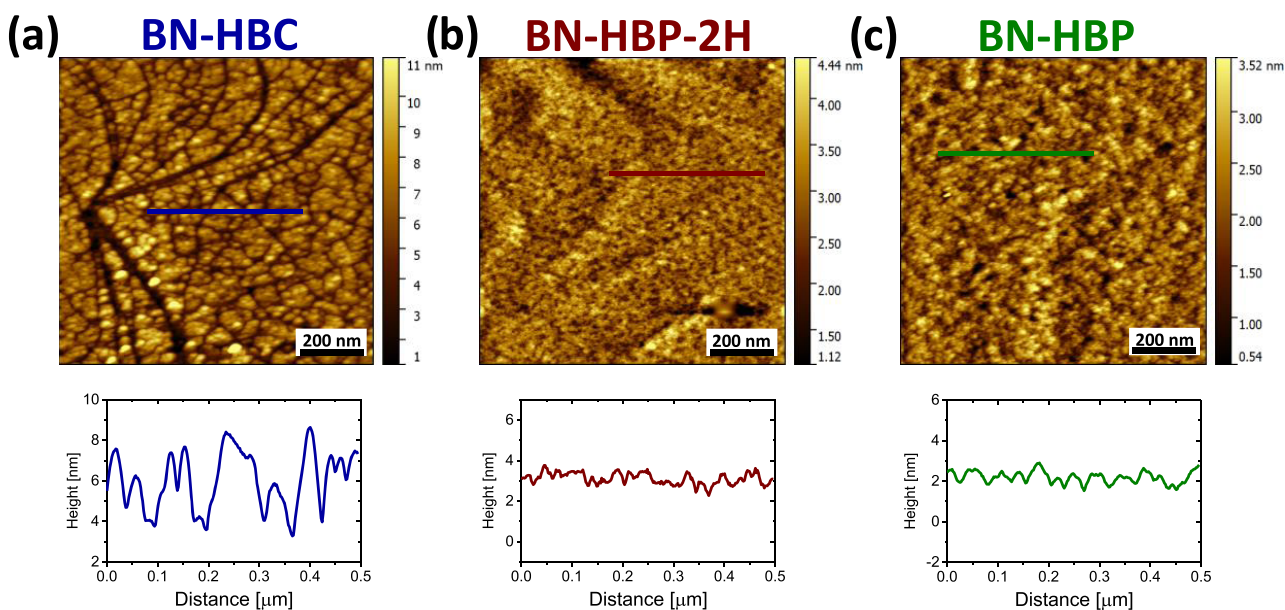


Figure 9. AFM micrographs of 4–5 nm thin films of (a) BN-HBC, (b) BN-HBP-2H, and (c) BN-HBP on Au(111) and their respective line profiles. To prevent measurement artifacts from influencing the mapping too much, a heuristically determined subinterval (5–95%) of the full value range was mapped onto the full color range. Values outside this subrange are displayed with the edge colors.

XA spectra decreases distinctly. At the intermediate thickness (1.2 nm), the dichroism of BN-HBP spectra is weaker compared to BN-HBP-2H, pointing to a more random orientation of BN-HBP. For the thickest film (4–5 nm), almost no angular dependence is observed in any of the three K edge spectra of BN-HBP and BN-HBP-2H, indicating an almost random orientation. We note that we cannot distinguish between a film of highly ordered molecules with large molecular tilt angles and an increase of disorder. For a completely disordered film, an average molecular tilt of 54.7° is calculated according to eq 1.

In summary, we observed that a flat-lying geometry (i.e., a parallel orientation between the BN core and the substrate surface) is favorable for all three molecules in the initial steps of the film growth. The initial orientation is maintained for the planar BN-HBC molecule. In contrast, an almost random orientation (or tilt angles close to 54.7°) is observed in thicker films of BN-HBP than for BN-HBP-2H. It seems that the nonplanarity reduces the ability of stronger molecule–molecule interactions, resulting in an almost random orientation in thin films.

This also affects the morphology of thin films visible in AFM micrographs of films grown on Au(111) (Figure 9). The average thickness is 4–5 nm for all three molecules. For BN-HBC, a pronounced island formation is visible, indicating a Volmer–Weber or Stranski–Krastanov growth mode. However, also significant differences can be detected: Only for BN-HBC, distinct grain boundaries are visible, which may indicate a high degree of crystallinity. The height difference in grain boundaries is up to 4–5 nm, (Figure 9a), resulting in a comparably high root-mean-square roughness (rms roughness) of typically 1.7 nm for the shown area ($1 \times 1 \mu\text{m}^2$). Grain boundaries are hardly visible for BN-HBP-2H and BN-HBP, and as a result, the typical corresponding rms roughness is less (about 0.52 nm in both cases) (Figure 9b,c). It seems that for the nonplanar molecules, rather an amorphous growth is preferred.

4. CONCLUSIONS

We investigated the influence of the degree of planarity on the electronic structure, orientation, and film growth of BN-HBC, BN-HBP-2H, and BN-HBP. The occupied electronic states probed by XPS and UPS reveal distinct differences. From different (relative) core-level binding energies, we conclude that the B–N bond has a higher polarity in BN-HBP compared to BN-HBP-2H and BN-HBC. Further, the degree of planarity significantly affects the unoccupied electronic structure probed by XAS. The calculation of individual C 1s excitation spectra allows the assignment of different transitions. As an example, the shoulder at the lowest photon energy arises from transitions localized at the three carbon atoms directly bonded to boron, whereas transitions from carbon atoms directly bonded to nitrogen appear at much higher photon energies. The similarity of the main features of the C–K XA spectra of BN-HBC and HBC indicates that the electronic structure of the outer carbon atoms is only weakly affected by the BN core. Similar to HBC, the splitting of the most intense feature A in the C–K edge of BN-HBC is mainly caused by a lower energy of transitions from outer C–H atoms.

The planarity has a considerable influence on growth mode and film morphology. Although for all three molecules a flat-lying adsorption geometry is preferred in the initial steps of deposition, tilt angles are not negligible for BN-HBP and BN-HBP-2H. Nevertheless, it could be shown that both BN-HBC and BN-HBP-2H form highly ordered monolayers of hexagonally arranged molecules. We suppose that the tilt angles result in weaker electronic interactions at the interface to Au(111) for BN-HBP and BN-HBP-2H, compared to BN-HBC.

Only for BN-HBC, the preferred initial molecular orientation is retained in films of 4–5 nm thickness. Almost no preferred molecular orientation was observed in 4 nm thick films of BN-HBP and BN-HBP-2H. In addition, the crystallinity of 4–5 nm thick BN-HBC films appears distinctly

higher compared to BN-HBP-2H and BN-HBP. This indicates that the planarity of BN-HBC significantly affects the molecule–molecule interactions and thus the ability of ordered film growth.

■ ASSOCIATED CONTENT

SI Supporting Information

The Supporting Information is available free of charge at <https://pubs.acs.org/doi/10.1021/acsaelm.0c00967>.

Gaussian widths of the XPS peak fits of BN-HBC, BN-HBP-2H, and BN-HBP; NPA charges of BN-HBC, BN-HBP-2H, and BN-HBP; UV–vis spectrum of BN-HBP; B3LYP/def2-TZVP molecular orbitals of BN-HBC and BN-HBP; calculated B-K and N-K XA spectra of the individual atoms in BN-HBP-2H; B-K edges of BN-HBC, BN-HBP-2H, and BN-HBP calculated by StoBe; difference densities for prominent transitions of the BN-HBC and BN-HBP N-K and B-K edges; and LEED images of annealed BN-HBC and BN-HBP monolayers on Au(111) (PDF)

■ AUTHOR INFORMATION

Corresponding Author

Heiko Peisert – Institute of Physical and Theoretical Chemistry, University of Tübingen, 72076 Tübingen, Germany; orcid.org/0000-0002-9742-5800; Phone: (+49) 07071/29-76931; Email: heiko.peisert@uni-tuebingen.de; Fax: (+49) 07071/29-5490

Authors

Katharina Greulich – Institute of Physical and Theoretical Chemistry, University of Tübingen, 72076 Tübingen, Germany

Axel Belser – Institute of Physical and Theoretical Chemistry, University of Tübingen, 72076 Tübingen, Germany

Daniel Bischof – Molekulare Festkörperphysik, Philipps-Universität Marburg, 35032 Marburg, Germany

Felix Widdascheck – Molekulare Festkörperphysik, Philipps-Universität Marburg, 35032 Marburg, Germany

Marie S. Sättele – Institute of Physical and Theoretical Chemistry, University of Tübingen, 72076 Tübingen, Germany; Institute of Organic Chemistry, University of Tübingen, 72076 Tübingen, Germany

Peter Grüninger – Institute of Physical and Theoretical Chemistry, University of Tübingen, 72076 Tübingen, Germany; Institute of Organic Chemistry, University of Tübingen, 72076 Tübingen, Germany

Holger F. Bettinger – Institute of Organic Chemistry, University of Tübingen, 72076 Tübingen, Germany; Center for Light-Matter Interaction, Sensors & Analytics (LISA⁺) at the University of Tübingen, 72076 Tübingen, Germany; orcid.org/0000-0001-5223-662X

Gregor Witte – Molekulare Festkörperphysik, Philipps-Universität Marburg, 35032 Marburg, Germany; orcid.org/0000-0003-2237-0953

Thomas Chassé – Institute of Physical and Theoretical Chemistry, University of Tübingen, 72076 Tübingen, Germany; Center for Light-Matter Interaction, Sensors & Analytics (LISA⁺) at the University of Tübingen, 72076 Tübingen, Germany; orcid.org/0000-0001-6442-8944

Complete contact information is available at: <https://pubs.acs.org/doi/10.1021/acsaelm.0c00967>

Author Contributions

[†]K.G. and A.B. contributed equally.

Notes

The authors declare no competing financial interest.

■ ACKNOWLEDGMENTS

The authors acknowledge support by the state of Baden-Württemberg through bwHPC and the German Research Foundation (DFG) through grant no. INST 40/467-1 FUGG (JUSTUS 2 cluster). They thank Reinhold Fink and Stefan Behnle (Tübingen) for valuable discussions related to the ORCA program package, Sven Bölke for fruitful discussions, and Ivana Mršić (Tübingen) for the help with AFM measurements. They also thank the Helmholtz-Zentrum Berlin (electron storage ring BESSY II) for provision of synchrotron radiation at the beamline HE-SGM. The Center for Light-Matter Interaction, Sensors & Analytics (LISA⁺) at the University of Tübingen is acknowledged for technical support. The research was supported in part by the Vector Foundation.

■ REFERENCES

- (1) Wu, J.; Pisula, W.; Müllen, K. Graphenes as Potential Material for Electronics. *Chem. Rev.* **2007**, *107*, 718–747.
- (2) Grimsdale, A. C.; Wu, J.; Müllen, K. New Carbon-Rich Materials for Electronics, Lithium Battery, and Hydrogen Storage Applications. *Chem. Commun.* **2005**, 2197–2204.
- (3) Schmidt-Mende, L.; Fechtenkötter, A.; Müllen, K.; Moons, E.; Friend, R. H.; MacKenzie, J. D. Self-Organized Discotic Liquid Crystals for High-Efficiency Organic Photovoltaics. *Science* **2001**, *293*, 1119.
- (4) Watson, M. D.; Fechtenkötter, A.; Müllen, K. Big Is Beautiful—“Aromaticity” Revisited from the Viewpoint of Macromolecular and Supramolecular Benzene Chemistry. *Chem. Rev.* **2001**, *101*, 1267–1300.
- (5) Clar, E.; Ironside, C. Hexabenzocoronene. *Proc. Chem. Soc.* **1958**, 150.
- (6) Goddard, R.; Haenel, M. W.; Herndon, W. C.; Krueger, C.; Zander, M. Crystallization of Large Planar Polycyclic Aromatic Hydrocarbons: The Molecular and Crystal Structures of Hexabenzobenzene [bc,ef,hi,kl,no,qr]coronene and Benzo[1,2,3-bc:4,5,6-b'c']diconene. *J. Am. Chem. Soc.* **1995**, *117*, 30–41.
- (7) Stabel, A.; Herwig, P.; Müllen, K.; Rabe, J. P. Diodelike Current–Voltage Curves for a Single Molecule–Tunneling Spectroscopy with Submolecular Resolution of an Alkylated, Peri-Condensed Hexabenzocoronene. *Angew. Chem., Int. Ed.* **1995**, *34*, 1609–1611.
- (8) Halleux, A.; Martin, R. H.; King, G. S. D. Synthèses dans la Série des Dérivés Polycycliques Aromatiques Hautement Condensés. L'hexabenzobenzène, 1,12; 2,3; 4,5; 6,7; 8,9; 10,11-coronène, le Tétrabenzobenzène, 4,5; 6,7; 11,12; 13,14-péropyrène et le Tétrabenzobenzène, 1,2; 3,4; 8,9; 10,11-bisanthène. *Helv. Chim. Acta* **1958**, *41*, 1177–1183.
- (9) Chen, L.; Hernandez, Y.; Feng, X. L.; Müllen, K. From Nanographene and Graphene Nanoribbons to Graphene Sheets: Chemical Synthesis. *Angew. Chem., Int. Ed.* **2012**, *51*, 7640–7654.
- (10) Angelova, P.; Vieker, H.; Weber, N.-E.; Matei, D.; Reimer, O.; Meier, I.; Kurasch, S.; Biskupek, J.; Lorbach, D.; Wunderlich, K.; Chen, L.; Terfort, A.; Klapper, M.; Müllen, K.; Kaiser, U.; Götzhäuser, A.; Turchanin, A. A Universal Scheme to Convert Aromatic Molecular Monolayers into Functional Carbon Nanomembranes. *ACS Nano* **2013**, *7*, 6489–6497.
- (11) Müller, M.; Kübel, C.; Müllen, K. Giant Polycyclic Aromatic Hydrocarbons. *Chem. – Eur. J.* **1998**, *4*, 2099–2109.
- (12) Ruffieux, P.; Wang, S.; Yang, B.; Sánchez-Sánchez, C.; Liu, J.; Dienel, T.; Talirz, L.; Shinde, P.; Pignedoli, C. A.; Passerone, D.; Dumslaff, T.; Feng, X.; Müllen, K.; Fasel, R. On-Surface Synthesis of Graphene Nanoribbons with Zigzag Edge Topology. *Nature* **2016**, *531*, 489–492.

- (13) Lin, Y.-M.; Dimitrakopoulos, C.; Jenkins, K. A.; Farmer, D. B.; Chiu, H.-Y.; Grill, A.; Avouris, P. 100-GHz Transistors from Wafer-Scale Epitaxial Graphene. *Science* **2010**, *327*, 662.
- (14) Wang, Y.; Shao, Y. Y.; Matson, D. W.; Li, J. H.; Lin, Y. H. Nitrogen-Doped Graphene and Its Application in Electrochemical Biosensing. *ACS Nano* **2010**, *4*, 1790–1798.
- (15) Lv, R. T.; Terrones, M. Towards New Graphene Materials: Doped Graphene Sheets and Nanoribbons. *Mater. Lett.* **2012**, *78*, 209–218.
- (16) Liu, H. T.; Liu, Y. Q.; Zhu, D. B. Chemical Doping of Graphene. *J. Mater. Chem.* **2011**, *21*, 3335–3345.
- (17) Bosdet, M. J. D.; Piers, W. E. B-N as a C-C Substitute in Aromatic Systems. *Can. J. Chem.* **2009**, *87*, 8–29.
- (18) Campbell, P. G.; Marwitz, A. J. V.; Liu, S.-Y. Recent Advances in Azaborine Chemistry. *Angew. Chem., Int. Ed.* **2012**, *51*, 6074–6092.
- (19) Giustra, Z. X.; Liu, S.-Y. The State of the Art in Azaborine Chemistry: New Synthetic Methods and Applications. *J. Am. Chem. Soc.* **2018**, *140*, 1184–1194.
- (20) Helten, H. B=N Units as Part of Extended π -Conjugated Oligomers and Polymers. *Chem. – Eur. J.* **2016**, *22*, 12972–12982.
- (21) Morgan, M. M.; Piers, W. E. Efficient Synthetic Methods for the Installation of Boron–Nitrogen Bonds in Conjugated Organic Molecules. *Dalton Trans.* **2016**, *45*, 5920–5924.
- (22) Wang, X.-Y.; Wang, J.-Y.; Pei, J. BN Heterosuperbenzenes: Synthesis and Properties. *Chem. – Eur. J.* **2015**, *21*, 3528–3539.
- (23) Helten, H. Doping the Backbone of π -Conjugated Polymers with Tricoordinate Boron: Synthetic Strategies and Emerging Applications. *Chem. Asian J.* **2019**, *14*, 919–935.
- (24) Sánchez-Sánchez, C.; Brüller, S.; Sachdev, H.; Müllen, K.; Krieg, M.; Bettinger, H. F.; Nicolai, A.; Meunier, V.; Talirz, L.; Fasel, R.; Ruffieux, P. On-Surface Synthesis of BN-Substituted Heteroaromatic Networks. *ACS Nano* **2015**, *9*, 9228–9235.
- (25) Beernink, G.; Gunia, M.; Dötz, F.; Öström, H.; Weiss, K.; Müllen, K.; Wöll, C. Synthesis of Polycyclic Aromatic Hydrocarbons and Graphite Islands Via Surface-Induced Reaction of Small Molecules. *ChemPhysChem* **2001**, *2*, 317–320.
- (26) Weiss, K.; Beernink, G.; Dötz, F.; Birkner, A.; Müllen, K.; Wöll, C. H. Template-Mediated Synthesis of Polycyclic Aromatic Hydrocarbons: Cyclodehydrogenation and Planarization of a Hexaphenylbenzene Derivative at a Copper Surface. *Angew. Chem., Int. Ed.* **1999**, *38*, 3748–3752.
- (27) Helten, H. B = N Units as Part of Extended π -Conjugated Oligomers and Polymers. *Chem. – Eur. J.* **2016**, *22*, 12972–12982.
- (28) Beaujuge, P. M.; Frechet, J. M. J. Molecular Design and Ordering Effects in π -Functional Materials for Transistor and Solar Cell Applications. *J. Am. Chem. Soc.* **2011**, *133*, 20009–20029.
- (29) Rand, B. P.; Cheyns, D.; Vasseur, K.; Giebink, N. C.; Mothy, S.; Yi, Y. P.; Coropceanu, V.; Beljonne, D.; Cornil, J.; Bredas, J. L.; Genoe, J. The Impact of Molecular Orientation on the Photovoltaic Properties of a Phthalocyanine/Fullerene Heterojunction. *Adv. Funct. Mater.* **2012**, *22*, 2987–2995.
- (30) Sellam, F.; Schmitz-Hübsch, T.; Toerker, M.; Mannfeld, S.; Proehl, H.; Fritz, T.; Leo, K.; Simpson, C.; Müllen, K. LEED and STM Investigations of Organic–Organic Heterostructures Grown by Molecular Beam Epitaxy. *Surf. Sci.* **2001**, *478*, 113–121.
- (31) Keil, M.; Samori, P.; dos Santos, D. A.; Kugler, T.; Stafström, S.; Brand, J. D.; Müllen, K.; Brédas, J. L.; Rabe, J. P.; Salaneck, W. R. Influence of the Morphology on the Electronic Structure of Hexa-peri-hexabenzocoronene Thin Films. *J. Phys. Chem. B* **2000**, *104*, 3967–3975.
- (32) Ruffieux, P.; Gröning, O.; Biemann, M.; Simpson, C.; Müllen, K.; Schlapbach, L.; Gröning, P. Supramolecular Columns of Hexabenzocoronenes on Copper and Gold (111) Surfaces. *Phys. Rev. B* **2002**, *66*, No. 073409.
- (33) Ciccullo, F.; Calzolari, A.; Piš, I.; Savu, S. A.; Krieg, M.; Bettinger, H. F.; Magnano, E.; Chassé, T.; Casu, M. B. A Quasi-Free-Standing Single Layer of a B₃N₃-Doped Nanographene Molecule Deposited on Au(111) Single Crystals. *J. Phys. Chem. C* **2016**, *120*, 17645–17651.
- (34) Belsler, A.; Greulich, K.; Grüninger, P.; Bettinger, H. F.; Peisert, H.; Chassé, T. Visualization of the Borazine Core of B₃N₃-Doped Nanographene by STM. *ACS Appl. Mater. Interfaces* **2020**, *12*, 19218–19225.
- (35) Luo, Y.; Ågren, H.; Keil, M.; Friedlein, R.; Salaneck, W. R. A Theoretical Investigation of the near-Edge X-Ray Absorption Spectrum of Hexa-Peri-Hexabenzocoronene. *Chem. Phys. Lett.* **2001**, *337*, 176–180.
- (36) Fajer, J.; Barkigia, K.; Smith, K.; Goff, D. *Consequences of Electron Transfer in Chlorophylls, Chlorins, and Porphyrins: Structural and Theoretical Considerations*; ACS Publications, 1986.
- (37) Geno, M. K.; Halpern, J. Why Does Nature Not Use the Porphyrin Ligand in Vitamin B12? *J. Am. Chem. Soc.* **1987**, *109*, 1238–1240.
- (38) Loew, G. H.; Harris, D. L. Role of the Heme Active Site and Protein Environment in Structure, Spectra, and Function of the Cytochrome P450s. *Chem. Rev.* **2000**, *100*, 407–420.
- (39) Alden, R. G.; Crawford, B. A.; Doolen, R.; Ondrias, M. R.; Shelnutt, J. A. Ruffling of Nickel(II) Octaethylporphyrin in Solution. *J. Am. Chem. Soc.* **1989**, *111*, 2070–2072.
- (40) Gottfried, J. M. Surface Chemistry of Porphyrins and Phthalocyanines. *Surf. Sci. Rep.* **2015**, *70*, 259–379.
- (41) Zhang, Q.; Zheng, X.; Kuang, G.; Wang, W.; Zhu, L.; Pang, R.; Shi, X.; Shang, X.; Huang, X.; Liu, P. N.; Lin, N. Single-Molecule Investigations of Conformation Adaptation of Porphyrins on Surfaces. *J. Phys. Chem. Lett.* **2017**, *8*, 1241–1247.
- (42) Köster, R.; Iwasaki, K.; Hattori, S.; Morita, Y. Borverbindungen, XIX1) Cyclisierungen von Bor-Stickstoff-Verbindungen in der Hitze. *Justus Liebigs Ann. Chem.* **1968**, *720*, 23–31.
- (43) Biswas, S.; Müller, M.; Tönshoff, C.; Eichele, K.; Maichle-Mössmer, C.; Ruff, A.; Speiser, B.; Bettinger, H. F. The Overcrowded Borazine Derivative of Hexabenzotriphenylene Obtained through Dehydrohalogenation. *Eur. J. Org. Chem.* **2012**, *2012*, 4634–4639.
- (44) Müller, M.; Maichle-Mössmer, C.; Sirsch, P.; Bettinger, H. F. Is There B–N Bond-Length Alternation in 1,2:3,4:5,6-Tris-(Biphenylene)Borazines? *ChemPlusChem* **2013**, *78*, 988–994.
- (45) Müller, M.; Behnle, S.; Maichle-Mössmer, C.; Bettinger, H. F. Boron–Nitrogen Substituted Perylene Obtained through Photocyclization. *Chem. Commun.* **2014**, *50*, 7821–7823.
- (46) Krieg, M.; Reicherter, F.; Haiss, P.; Ströbele, M.; Eichele, K.; Treanor, M.-J.; Schaub, R.; Bettinger, H. F. Construction of an Internally B₃N₃-Doped Nanographene Molecule. *Angew. Chem., Int. Ed.* **2015**, *54*, 8284–8286.
- (47) Breuer, T.; Klues, M.; Witte, G. Characterization of Orientational Order in π -Conjugated Molecular Thin Films by NEXAFS. *J. Electron. Spectrosc. Relat. Phenom.* **2015**, *204*, 102–115.
- (48) Hesse, R.; Chasse, T.; Streubel, P.; Szargan, R. Error Estimation in Peak-Shape Analysis of XPS Core-Level Spectra Using Unifit 2003: How Significant Are the Results of Peak Fits? *Surf. Interface Anal.* **2004**, *36*, 1373–1383.
- (49) Schöll, A.; Zou, Y.; Jung, M.; Schmidt, T.; Fink, R.; Umbach, E. Line Shapes and Satellites in High-Resolution X-Ray Photoelectron Spectra of Large π -Conjugated Organic Molecules. *J. Chem. Phys.* **2004**, *121*, 10260–10267.
- (50) Savu, S.-A.; Biswas, I.; Sorace, L.; Mannini, M.; Rovai, D.; Caneschi, A.; Chassé, T.; Casu, M. B. Nanoscale Assembly of Paramagnetic Organic Radicals on Au(111) Single Crystals. *Chem. – Eur. J.* **2013**, *19*, 3445–3450.
- (51) Thomas, T. D.; Püttner, R.; Fukuzawa, H.; Prümper, G.; Ueda, K.; Kuk, E.; Sankari, R.; Harries, J.; Tamenori, Y.; Tanaka, T.; Hoshino, M.; Tanaka, H. Boron 1s Photoelectron Spectrum of ¹¹BF₃: Vibrational Structure and Linewidth. *J. Chem. Phys.* **2007**, *127*, No. 244309.
- (52) Fernandez, H.; Gomez-Rodriguez Jm Colchero, J. M.; Colchero, J.; Gomez-Herrero, J.; Baro, A. M. *Rev. Sci. Instrum.* **2007**, *78*, No. 013705.
- (53) Nečas, D.; Klapetek, P. Gwyddion: An Open-Source Software for Spm Data Analysis. *Open Phys.* **2012**, *10*, 181–188.

- (54) Neese, F. The Orca Program System. *Wiley Interdiscip. Rev.: Comput. Mol. Sci.* **2012**, *2*, 73–78.
- (55) Becke, A. D. Density-Functional Exchange-Energy Approximation with Correct Asymptotic-Behavior. *Phys. Rev. A* **1988**, *38*, 3098–3100.
- (56) Becke, A. D. Density-Functional Thermochemistry. 3. The Role of Exact Exchange. *J. Chem. Phys.* **1993**, *98*, 5648–5652.
- (57) Weigend, F.; Ahlrichs, R. Balanced Basis Sets of Split Valence, Triple Zeta Valence and Quadruple Zeta Valence Quality for H to Rn: Design and Assessment of Accuracy. *Phys. Chem. Chem. Phys.* **2005**, *7*, 3297–3305.
- (58) Neese, F.; Wennmohs, F.; Hansen, A.; Becker, U. Efficient, Approximate and Parallel Hartree–Fock and Hybrid Dft Calculations. A ‘Chain-of-Spheres’ Algorithm for the Hartree–Fock Exchange. *Chem. Phys.* **2009**, *356*, 98–109.
- (59) Weigend, F. Accurate Coulomb-Fitting Basis Sets for H to Rn. *Phys. Chem. Chem. Phys.* **2006**, *8*, 1057–1065.
- (60) Glendening, E.; Badenhoop, J.; Reed, A.; Carpenter, J.; Bohmann, J.; Morales, C. Nbo 6.0, 2013, University of Wisconsin: Madison Search Pubmed;(B) Ed Glendening, Cr Landis and F. Weinhold. *J. Comput. Chem* **2013**, *34*, 1429.
- (61) Romaner, L.; Heimel, G.; Brédas, J.-L.; Gerlach, A.; Schreiber, F.; Johnson, R. L.; Zegenhagen, J.; Duhm, S.; Koch, N.; Zojer, E. Impact of Bidirectional Charge Transfer and Molecular Distortions on the Electronic Structure of a Metal–Organic Interface. *Phys. Rev. Lett.* **2007**, *99*, No. 256801.
- (62) Hwang, J.; Kim, E.-G.; Liu, J.; Brédas, J.-L.; Duggal, A.; Kahn, A. Photoelectron Spectroscopic Study of the Electronic Band Structure of Polyfluorene and Fluorene-Arylamine Copolymers at Interfaces. *J. Phys. Chem. C* **2007**, *111*, 1378–1384.
- (63) Cornil, J.; Vanderdonckt, S.; Lazzaroni, R.; dos Santos, D. A.; Thys, G.; Geise, H. J.; Yu, L. M.; Szablewski, M.; Bloor, D.; Lögdlund, M.; Salaneck, W. R.; Gruhn, N. E.; Lichtenberger, D. L.; Lee, P. A.; Armstrong, N. R.; Brédas, J. L. Valence Electronic Structure of π -Conjugated Materials: Simulation of the Ultraviolet Photoelectron Spectra with Semiempirical Hartree–Fock Approaches. *Chem. Mater.* **1999**, *11*, 2436–2443.
- (64) DeBeer George, S.; Petrenko, T.; Neese, F. Time-Dependent Density Functional Calculations of Ligand K-Edge X-Ray Absorption Spectra. *Inorg. Chim. Acta* **2008**, *361*, 965–972.
- (65) Pipek, J.; Mezey, P. G. A Fast Intrinsic Localization Procedure Applicable for Ab Initio and Semiempirical Linear Combination of Atomic Orbital Wave Functions. *J. Chem. Phys.* **1989**, *90*, 4916–4926.
- (66) Diller, K.; Maurer, R. J.; Müller, M.; Reuter, K. Interpretation of X-Ray Absorption Spectroscopy in the Presence of Surface Hybridization. *J. Chem. Phys.* **2017**, *146*, No. 214701.
- (67) Stöhr, J. *NEXAFS Spectroscopy*; Springer, 1992.
- (68) Hermann, K.; Petterson, L. G. M.; Casida, M. E.; Daul, C.; Goursoot, A.; Koester, A.; Proynov, E.; St-Amant, A.; Salahub, D. R.; Carravetta, V.; Duarte, H.; Friedrich, C.; Godbout, N.; Gruber, M.; Guan, J.; Jamorski, C.; Leboeuf, M.; Leetmaa, M.; Nyberg, M.; Patchkovskii, S.; Pedocchi, L.; Sim, F.; Triguero, L.; Vela, A. StoBeMon Version 3.3 (2014). <http://www.fhi-berlin.mpg.de/KHsoftware/StoBe>.
- (69) Klues, M.; Hermann, K.; Witte, G. Analysis of the near-Edge X-Ray-Absorption Fine-Structure of Anthracene: A Combined Theoretical and Experimental Study. *J. Chem. Phys.* **2014**, *140*, No. 014302.
- (70) Alagia, M.; Baldacchini, C.; Betti, M. G.; Bussolotti, F.; Carravetta, V.; Ekstrom, U.; Mariani, C.; Stranges, S. Core-Shell Photoabsorption and Photoelectron Spectra of Gas-Phase Pentacene: Experiment and Theory. *J. Chem. Phys.* **2005**, *122*, No. 124305.
- (71) Grüninger, P.; Polek, M.; Ivanovic, M.; Balle, D.; Karstens, R.; Nagel, P.; Merz, M.; Schuppler, S.; Ovsyannikov, R.; Bettinger, H. F.; Peisert, H.; Chasse, T. Electronic Structure of Hexacene and Interface Properties on Au(110). *J. Phys. Chem. C* **2018**, *122*, 19491–19498.
- (72) Simonov, K. A.; Vinogradov, N. A.; Vinogradov, A. S.; Generalov, A. V.; Zagrebina, E. M.; Martensson, N.; Cafolla, A. A.; Carpy, T.; Cunniffe, J. P.; Preobrajenski, A. B. Effect of Substrate Chemistry on the Bottom-up Fabrication of Graphene Nanoribbons: Combined Core-Level Spectroscopy and STM Study. *J. Phys. Chem. C* **2014**, *118*, 12532–12540.
- (73) Peisert, H.; Knupfer, M.; Schwieger, T.; Fuentes, G. G.; Olligs, D.; Fink, J.; Schmidt, T. Fluorination of Copper Phthalocyanines: Electronic Structure and Interface Properties. *J. Appl. Phys.* **2003**, *93*, 9683–9692.
- (74) Rocco, M. L. M.; Haeming, M.; Batchelor, D. R.; Fink, R.; Schöll, A.; Umbach, E. Electronic Relaxation Effects in Condensed Polyacenes: A High-Resolution Photoemission Study. *J. Chem. Phys.* **2008**, *129*, No. 074702.
- (75) Peisert, H.; Biswas, I.; Knupfer, M.; Chasse, T. Orientation and Electronic Properties of Phthalocyanines on Polycrystalline Substrates. *Phys. Status Solidi B* **2009**, *246*, 1529–1545.
- (76) Rocco, M. L. M.; Frank, K. H.; Yannoulis, P.; Koch, E. E. Unoccupied Electronic Structure of Phthalocyanine Films. *J. Chem. Phys.* **1990**, *93*, 6859–6864.
- (77) Floreano, L.; Cossaro, A.; Gotter, R.; Verdini, A.; Bavdek, G.; Evangelista, F.; Ruocco, A.; Morgante, A.; Cvetko, D. Periodic Arrays of Cu-Phthalocyanine Chains on Au(110). *J. Phys. Chem. C* **2008**, *112*, 10794–10802.
- (78) Shimoyama, I.; Baba, Y.; Sekiguchi, T.; Nath, K. G. NEXAFS Spectra of an Epitaxial Boron Nitride Film on Ni(1 1 1). *J. Electron. Spectrosc. Relat. Phenom.* **2004**, *137-140*, 573–578.
- (79) Pomerantz, A. E.; Crace, E.; Weng, T.-C.; Sokaras, D.; Nordlund, D. Carbon Core Electron Spectra of Polycyclic Aromatic Hydrocarbons. *J. Phys. Chem. A* **2018**, *122*, 5730–5734.
- (80) Oji, H.; Mitsumoto, R.; Ito, E.; Ishii, H.; Ouchi, Y.; Seki, K.; Yokoyama, T.; Ohta, T.; Kosugi, N. Core Hole Effect in NEXAFS Spectroscopy of Polycyclic Aromatic Hydrocarbons: Benzene, Chrysene, Perylene, and Coronene. *J. Chem. Phys.* **1998**, *109*, 10409–10418.
- (81) Stöhr, J.; Outka, D. A. Determination of Molecular Orientations on Surfaces from the Angular Dependence of Near-Edge X-Ray Absorption Fine-Structure Spectra. *Phys. Rev. B* **1987**, *36*, 7891–7905.
- (82) Belsler, A.; Karstens, R.; Nagel, P.; Merz, M.; Schuppler, S.; Chassé, T.; Peisert, H. Interaction Channels between Perfluorinated Iron Phthalocyanine and Cu(111). *Phys. Status Solidi B* **2019**, *256*, No. 1800292.
- (83) Balle, D.; Adler, H.; Grüninger, P.; Karstens, R.; Ovsyannikov, R.; Giangrisostomi, E.; Chassé, T.; Peisert, H. Influence of the Fluorination of CoPc on the Interfacial Electronic Structure of the Coordinated Metal Ion. *J. Phys. Chem. C* **2017**, *121*, 18564–18574.
- (84) Greulich, K.; Belsler, A.; Bölke, S.; Grüninger, P.; Karstens, R.; Sättele, M. S.; Ovsyannikov, R.; Giangrisostomi, E.; Basova, T. V.; Klyamer, D.; Chassé, T.; Peisert, H. Charge Transfer from Organic Molecules to Molybdenum Disulfide: Influence of the Fluorination of Iron Phthalocyanine. *J. Phys. Chem. C* **2020**, *124*, 16990–16999.
- (85) Seah, M. P.; Dench, W. A. Quantitative Electron Spectroscopy of Surfaces: A Standard Data Base for Electron Inelastic Mean Free Paths in Solids. *Surf. Interface Anal.* **1979**, *1*, 2–11.
- (86) Breuer, T.; Klues, M.; Liesfeld, P.; Viertel, A.; Conrad, M.; Hecht, S.; Witte, G. Self-Assembly of Partially Fluorinated Hexabenzocoronene Derivatives in the Solid State. *Phys. Chem. Chem. Phys.* **2016**, *18*, 33344–33350.

Perfluorinated Phthalocyanines on Cu(110) and Cu(110)-(2 × 1)O: The Special Role of the Central Cobalt Atom

Axel Belser, Katharina Greulich, Peter Grüninger, Reimer Karstens, Ruslan Ovsyannikov, Erika Giangrisostomi, Peter Nagel, Michael Merz, Stefan Schuppler, Thomas Chassé, and Heiko Peisert*

Cite This: *J. Phys. Chem. C* 2021, 125, 8803–8814

Read Online

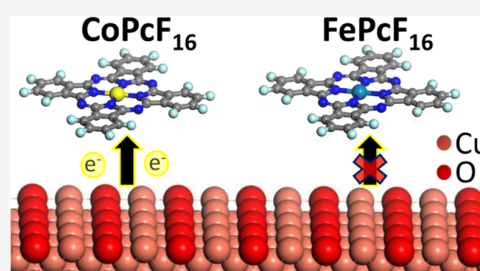
ACCESS |

Metrics & More

Article Recommendations

Supporting Information

ABSTRACT: Interface properties of CoPcF₁₆ on Cu(110) and Cu(110)-(2 × 1)O were investigated by X-ray photoemission spectroscopy (XPS), ultraviolet photoemission spectroscopy (UPS), X-ray absorption spectroscopy (XAS), and scanning tunneling microscopy (STM). The results are compared to FePcF₁₆ on Cu(110)-(2 × 1)O. A charge transfer from both substrates to the central Co ion of CoPcF₁₆ is observed. Unlike to FePcF₁₆ and related molecules, the strong interaction between CoPcF₁₆ molecules of the first layer and the Cu(110) substrate is only partially suppressed by oxygen termination. The special nature of the electronic structure of the Co ion in Co phthalocyanines is discussed. The analysis of the fluorine Auger parameter enables the discussion of initial and final state effects of core level binding energy shifts in photoemission. A bidirectional charge transfer also involving the macrocycle of CoPcF₁₆ molecules is concluded.



1. INTRODUCTION

The tuning of electronic interface properties between organic molecules and metallic substrates is of enormous importance for a broad variety of applications.^{1–3} Strong interactions including chemical reactions may especially alter the molecular electronic structure of the frontier orbitals, which are important for charge carrier transport and injection. Routes to avoid chemical interactions at interfaces include, among others, the optimization of the surface preparation or the introduction of intermediate layers.^{4–9} Copper surfaces are among the more reactive substrates, where a strong chemisorption is observed for many organic molecules.^{9–17} For some systems, such interactions can be avoided by an oxygen termination of the copper surface.^{16,18}

The interface properties of cobalt phthalocyanine (CoPc) seem to be different compared to other transition metal phthalocyanines: In many cases, interaction at the interfaces between CoPcF_X (X = 0, 16) and noble metals is governed by a local interaction between the Co 3d_{z²} orbital and states of the metal substrate,^{19,20} and a charge donation was observed for many interfaces (e.g., refs 19–22). In this study, we compare interface properties of CoPcF₁₆ on Cu(110) and Cu(110)-(2 × 1)O. To assess the special role of the central Co ion, the results are compared to FePcF₁₆ on Cu(110)-(2 × 1)O.

2. EXPERIMENTAL SECTION

The Cu(110) single crystal was cleaned by several cycles of Ar⁺-ion sputtering and subsequent annealing. The sputtering was performed at a voltage of 1.0 kV for typically 30 min at an argon partial pressure of 5 × 10⁻⁵ mbar, and the annealing was

performed for 30 min at a temperature of 750 K. The crystal cleanliness and orientation were checked by X-ray photoemission spectroscopy (XPS), low-energy electron diffraction (LEED), and scanning tunneling microscopy (STM). The Cu(110)-(2 × 1)O surface was prepared by exposing the clean surface to 20 langmuirs of oxygen at room temperature, followed by heating to 570 K for 4 min.

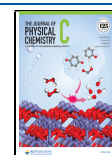
CoPcF₁₆ (Sigma-Aldrich) and FePcF₁₆ (SYNTHON Chemicals GmbH & Co. KG) powders were evaporated at rates of 0.2–0.4 nm/min and a temperature of 650–670 K from a temperature-controlled crucible. The evaporation rates were estimated from a quartz microbalance. The nominal film thickness was estimated from XPS intensity ratios by using sensitivity factors from Yeh and Lindau²³ assuming layer-by-layer growth for each deposition step.

The photoemission measurements (XPS and ultraviolet photoemission spectroscopy (UPS)) were performed in the home lab by using a multichamber UHV system (base pressure of 2 × 10⁻¹⁰ mbar) equipped with a Phoibos 150 hemispherical energy analyzer (SPECS), an X-ray source with monochromator (XR 50 M, SPECS), and a helium discharge lamp (SPECS). The energy resolution for XPS (excitation energy hν = 1486.7 eV) and UPS (hν = 21.22 eV) was 400 and

Received: February 9, 2021

Revised: April 7, 2021

Published: April 20, 2021



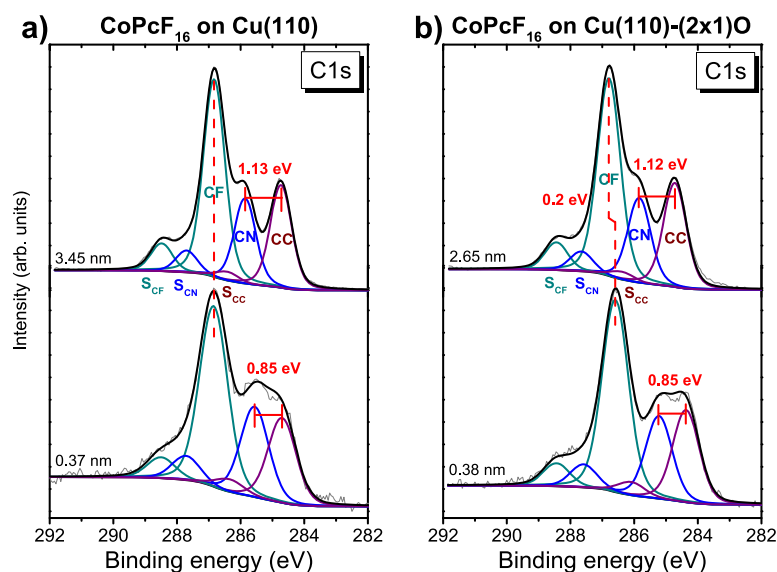


Figure 1. Thickness-dependent C 1s core level spectra for CoPcF₁₆ on (a) Cu(110) and (b) Cu(110)-(2 × 1)O. Except for minor differences in the relative energy position of the components, the same model can be applied for the description of all spectra.

Table 1. CoPcF₁₆ on Cu(110) and Cu(110)-(2 × 1)O: Thickness-Dependent C 1s Binding Energies as Obtained from Peak Fits in eV

| substrate | thickness (nm) | CF | SCF | CN | SCN | CC | SCC |
|------------------|----------------|--------|--------|--------|--------|--------|--------|
| Cu(110) | 3.45 | 286.83 | 288.48 | 285.86 | 287.70 | 284.73 | 286.42 |
| | 0.37 | 286.85 | 288.50 | 285.55 | 287.72 | 284.70 | 286.35 |
| Cu(110)-(2 × 1)O | 2.65 | 286.79 | 288.44 | 285.84 | 287.66 | 284.72 | 286.38 |
| | 0.38 | 286.59 | 288.44 | 285.22 | 287.59 | 284.37 | 286.09 |

150 meV, respectively. The binding energy was calibrated with respect to the Au 4f_{7/2} (84.0 eV) and the Cu 2p_{3/2} (932.6 eV) peak positions. The peak fitting of XP spectra was performed by using the program Unifit.²⁴ A Voigt profile peak shape (convolution of Gaussian and Lorentzian peaks) and a Shirley model background were used.

The corresponding X-ray absorption spectroscopy (XAS) measurements of the N-K and Co-L edges have been performed at the PM4 beamline (LowDose PES endstation) at BESSY II (Helmholtz-Zentrum Berlin, Germany) and the measurements of the Fe-L edge at the WERA beamline at the Karlsruhe Research Accelerator (KARA, Karlsruhe, Germany). The energy resolution at the PM4 beamline was set at 100 meV at a photon energy of 400 eV and at the WERA beamline at 220 and 340 meV at photon energies of 400 and 710 eV. The XA spectra at both beamlines were monitored indirectly by measuring the total electron yield (sample current).

The STM measurements were performed in a two-chamber UHV system equipped with a low-energy electron diffraction (LEED) system from OCI Vacuum Microengineering Inc. and a variable temperature (VT)-STM from Omicrometer GmbH. For the STM measurements, mechanically cut Pt/Ir tips were used. All given tunneling voltages are referenced to the sample. The WSxM program was used to tune the image contrast.²⁵

3. RESULTS AND DISCUSSION

3.1. Interaction between the CoPcF₁₆ Macrocycle and the Substrates. Different interaction channels are observed between phthalocyanines and a variety of substrates, involving both the macrocycle and the central metal atom; often the

charge transfer is bidirectional.^{15,26–28} First, we will discuss interactions between the CoPcF₁₆ macrocycle (i.e., the C and N atoms) and the copper substrates.

In Figure 1, we show C 1s core level spectra for CoPcF₁₆ on Cu(110) and Cu(110)-(2 × 1)O at about one monolayer coverage (0.37 nm) compared to bulklike thin films. 0.32 nm corresponds to one monolayer of flat-lying perfluorinated phthalocyanines, as can be inferred from the crystal structure.²⁹ Data for additional thicknesses are provided as Supporting Information (Figure S1). As for related perfluorinated phthalocyanines,^{15,30} the C 1s core level spectra for the bulklike, thickest films can be fitted by using three main components in sequential order from high to low binding energy: carbon bonded to fluorine (CF), bonded to nitrogen (CN), and bonded to other carbon (CC). All main peaks are accompanied by their respective satellites, denoted S_{CF}, S_{CN}, and S_{CC} in Figure 1. The intensity ratio estimated from the peak areas CF:CN:CC (including related satellites) of 4:1.9:2 is in reasonable agreement with the stoichiometric composition (4:2:2). Energetic positions obtained from the peak fits shown in Figure 1 are summarized in Table 1.

Essentially the same model can be applied for the description of the spectra for low coverages of about 0.37 nm. The intensity ratio CF:CN:CC agrees well with the expectation according to stoichiometry: 4:2.3:1.9 and 4:2:2 for Cu(110) and Cu(110)-(2 × 1)O, respectively. The energetic position of satellites with respect to the main lines as well as the Lorentzian widths (0.2 eV) were kept constant. Generally higher Gaussian widths were obtained for the low coverages (about 0.9 eV; thicker films: about 0.7 eV), which might be

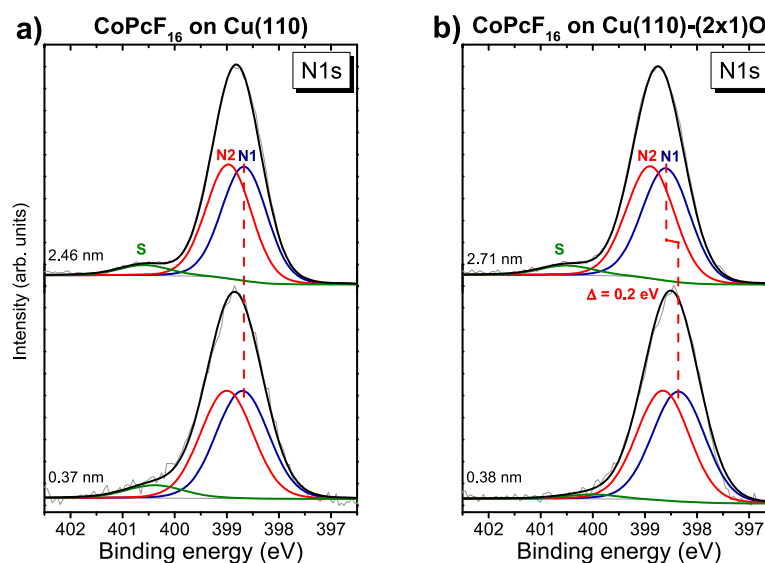


Figure 2. Thickness-dependent N 1s core level spectra for CoPcF₁₆ on (a) Cu(110) and (b) Cu(110)-(2 × 1)O.

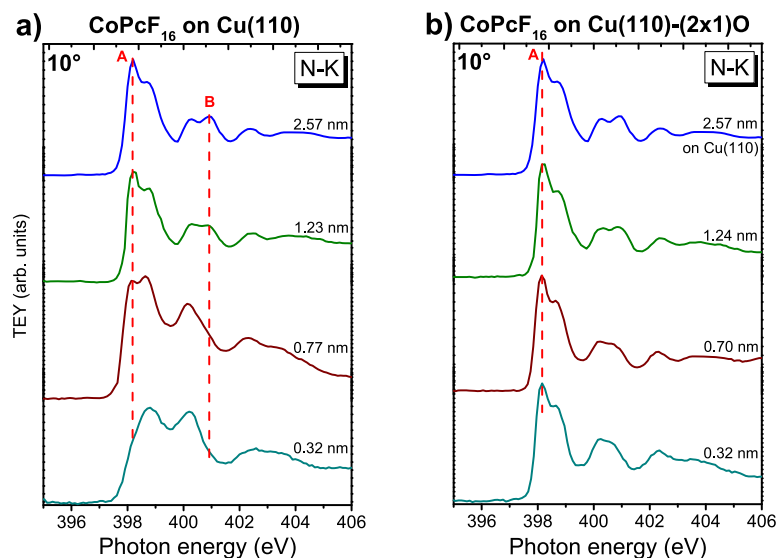


Figure 3. Thickness-dependent N 1s excitation spectra at grazing incidence (10°) for CoPcF₁₆ on (a) Cu(110) and (b) Cu(110)-(2 × 1)O. The reference for the bulklike spectrum of the thickest film in (b) is taken from (a). Because of a complex background treatment, the exact determination of the step height is complicated.

ascribed to adsorption at inequivalent adsorption sites or another kind of disorder, which may cause a statistical distribution of orbital energies.³¹

However, the detailed analysis of energetic positions of the C 1s components in Figure 1 (cf. Table 1) reveals distinct differences between monolayer coverages and thicker films. Generally, in close proximity to metallic substrates, a shift of core level binding energies to lower values is expected due to final state screening effects of the photohole as the additional mirror charge screening. Such energetic shifts are often in the range 0.3–0.6 eV.^{32–35} For the investigated samples these effects may affect the observed binding energies. However, additional effects must influence the observed energetic positions because the peak components are not shifted by equal amounts. Most visible in Figure 1, the distance between CC and CN is decreased by more than 0.25 eV for molecules

directly at the interface (monolayer coverage), compared to thicker films, similar to FePcF₁₆ on Cu(111).¹⁵ A possible reason might be a site-dependent screening or a redistribution of electrons for molecules of the first layer on both substrates.³⁶ The stronger shift of CN to lower binding energies compared to CC at the interface would imply a relative increase of electron density at the CN atoms of the interface layer.

Also, N 1s spectra, shown in Figure 2, exhibit almost no thickness-dependent changes of the peak shape (complete series shown in Figure S2). The main line consists of two signals of the same intensity for the pyrrole and the bridging nitrogen atoms, denoted N1 and N2 in Figure 2. Because their energy separation is small for related phthalocyanines (0.3–0.5 eV),^{37–42} they cannot be clearly resolved by XPS. Peak fit parameters are given as Supporting Information (Table

S1). Similar to C 1s (cf. Figure 1), all N 1s spectra can be fitted by using the same model, independent of the layer thickness. Only the Gaussian width is slightly increased for low coverages (by about 0.1 eV), most likely due to adsorption at inequivalent sites of the substrate surface (cf. discussion of the C 1s peak shape). Similar to C 1s, peak shifts to lower binding energy are observed for low coverages CoPcF₁₆ on Cu(110)-(2 × 1)O, most likely due to screening effects.

The corresponding N 1s XA spectra taken at grazing incidence are shown in Figure 3. The CoPcF₁₆ molecules grow in a preferred flat-lying adsorption geometry, as concluded from the angular (polarization) dependence of N-K XA spectra at higher film thicknesses (see Figure S3). Thus, at the chosen measurement geometry, features below 404 eV arise predominantly from transitions into π^* molecular orbitals. For phthalocyanines, most intense π^* resonances (denoted A) are assigned to transitions from N 1s to LUMO e_g orbitals.^{43,44} The complex structure of feature A arises from an involvement of the ligand LUMO in the hybridization with the central metal atom of the Pc.^{42,43,45–49}

It was shown that π^* resonances in N-K edge absorption spectra are very sensitive on involvement of nitrogen in the interfacial interactions.^{20,45,50,51} Indeed, for CoPcF₁₆ on Cu(110) distinct changes of the peak shape as a function of the film thickness are visible in Figure 3a. The ratio between the intensities of features A and B at photon energies of 398.2 and 400.9 eV decreases for lower coverages, reminiscent of FePcF₁₆ on Cu(111) or FePc on Ag(111).^{15,50} This may indicate (partial) charge transfer from the Cu(110) substrate to the (ligand) LUMO of CoPcF₁₆. Because the corresponding N 1s core level photoemission spectra are almost unaffected by the interface interaction, the charge transfer may occur into the (delocalized) LUMO; in other words, the electron density is not (only) localized at the nitrogen atoms. In contrast to the Cu(110) substrate, for CoPcF₁₆ on Cu(110)-(2 × 1)O (Figure 4b), the peak shape is almost the same for all thicknesses, indicating that nitrogen is not involved in the interaction at the interface.

A localized, strong interaction between nitrogen and the Cu(110) substrate may result in the breaking of chemical

bonds within the macrocycle of CoPcF₁₆. To further investigate the interface interaction in more detail, we performed STM measurements for the apparently most reactive interface CoPcF₁₆/Cu(110). In Figure 4, an STM image of a CoPcF₁₆ submonolayer is shown. Clearly, the typical 4-fold symmetry of the phthalocyanine molecules can be identified. Similar to CoPcF₁₆ on Ag(110),⁵² the molecules are aligned along the $[1\bar{1}0]$ direction of the substrate. Thus, we conclude that the CoPcF₁₆ molecules appear intact upon adsorption on the Cu(110) surface.

3.2. Interactions between the Central Metal Atom of the Phthalocyanines and the Substrates. For transition metal phthalocyanines, the study of both 2p photoemission and X-ray absorption spectroscopy yields valuable information about the electronic structure of the central metal atom at interfaces. In Figure 5, we show Co 2p_{3/2} core level photoemission for CoPcF₁₆ on Cu(110) (Figure 5a) and on Cu(110)-(2 × 1)O (Figure 5b) as a function of thickness. On both substrates the spectrum of the thickest layer shows the typical multiplet structure, as known for Co phthalocyanines.^{26,40,53,54} Clearly visible, with decreasing layer thickness an additional (interface) peak at lower binding energy develops, located at 778.4 and 778.1 eV for CoPcF₁₆ on Cu(110) and Cu(110)-(2 × 1)O, respectively. The lower binding energy compared to the main component implies a higher electron density or, in other words, a reduction of the Co²⁺ ion at the interface. The different binding energy on both substrates is most likely caused by a different energy level alignment of the first layer. Thus, a charge transfer from the substrate to the central metal atom of the phthalocyanine occurs on both substrates, similar to CoPcF₁₆ on other metals.^{5,26,53}

Also visible in Figure 5, the intensity of the interface component is clearly different for the about monolayer coverages (0.37 and 0.38 nm) on the two substrates. On the Cu(110) substrate (Figure 5a), the shape of the spectrum is typical for reduced Co at reactive metal substrates,^{26,27,53,55} the intensity at binding energies >780 eV can be assigned to satellite (i.e., multiplet) structures.⁴⁰ In contrast, for the same CoPcF₁₆ coverage on Cu(110)-(2 × 1)O (Figure 5b), the relative intensity at binding energies >780 eV is distinctly increased, indicating remaining intensity from the Co²⁺ multiplet, which is similar to CoPcF₁₆ at a copper intercalated graphene/Ni(111) interface.⁵ Thus, it seems that not all molecules of the first monolayer on Cu(110)-(2 × 1)O undergo a charge transfer; apparently the interaction strength depends crucially on the adsorption site. The importance of different adsorption sites has been shown in detail for other large organic molecules as, for example, 4'-(4-tolyl)-2,2':6',2''-terpyridine on Au(111).⁵⁶

Additional information about the (unoccupied) electronic structure of the central metal atom can be gained from the corresponding Co 2p excitation spectra. Thickness-dependent Co L₃-edge XA spectra of CoPcF₁₆ on both substrates are shown in Figure 6 for grazing (10°) and normal (90°) incidence of the incoming linearly polarized synchrotron light. The angular dependence can be understood by polarization rules for transitions into different orbitals. For the almost flat-lying molecules (cf. discussion of the angular dependence of N-K XA spectra, Figure S3), transitions into orbitals with out-of-plane components (e.g., d_{z²}) are strongest at grazing incidence, while at normal incidence transitions into orbitals with in-plane components (d_{x²-y²} and d_{xy}) are most intense. For a detailed

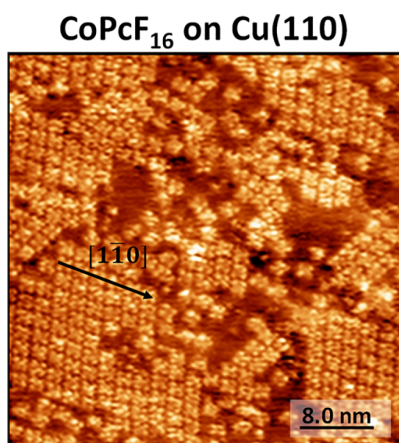


Figure 4. STM image of a submonolayer coverage of CoPcF₁₆ on Cu(110) (about 0.7 ML). The 4-fold symmetry of the molecules is typical for phthalocyanines, indicating that the molecules remain intact upon adsorption on Cu(110). Measurement parameters: $I = 300$ pA and $U = 0.7$ V.

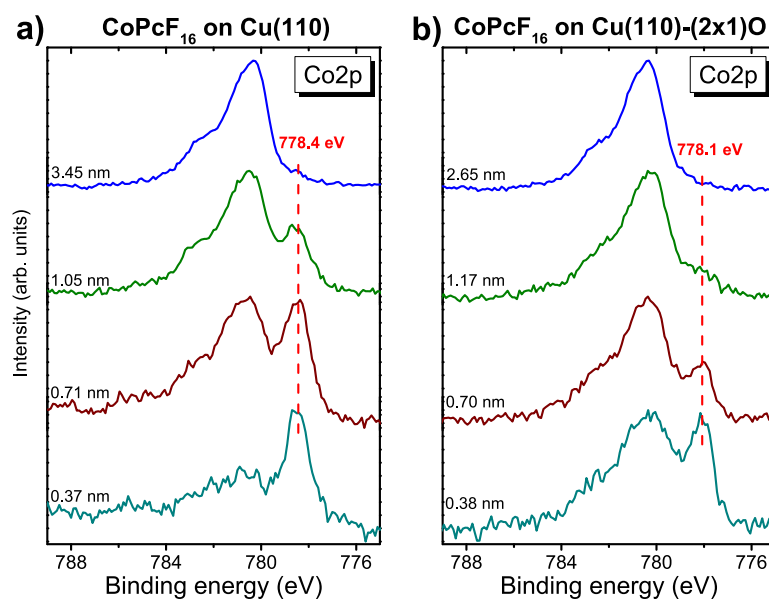


Figure 5. Thickness-dependent Co $2p_{3/2}$ core level spectra for CoPcF₁₆ on (a) Cu(110) and (b) Cu(110)-(2 × 1)O.

discussion of the spectral shape, see refs 5, 57, and 58. Out-of-plane transitions are labeled with “A”, while in-plane transitions are labeled with “B” in Figure 6. The spectra for the thickest, bulklike film of 2.57 nm are typical for flat-lying CoPc or CoPcF₁₆ molecules on different substrates.^{5,20,57} However, for lower coverages the peak shape of Co 2p excitation spectra changes distinctly. While the feature A dominates the bulklike spectra at grazing incidence, a new feature, denoted A0, appears for lower coverages in Figure 6a,b. Such a feature A0 was observed for CoPc on other reactive substrates, such as Ag or Ni, and can be understood by a hybridization of the Co d_{z^2} orbital with substrate-related orbitals.^{20,59} At the same time, at normal incidence feature B2 disappears for low coverages (Figure 6c,d), indicating that the charge transfer is accompanied by a redistribution of the d-electrons at the central metal atom of the phthalocyanine at the interface.²⁰

Comparing the Co $L_{3\text{-edge}}$ XA spectra for monolayer coverages in Figure 6, it becomes evident that the shape distinctly depends on the substrate. Feature A0 completely dominates the spectrum at grazing incidence on Cu(110), whereas A is still the most intense feature on Cu(110)-(2 × 1)O. At normal incidence, feature B2 disappears on Cu(110), while it is still visible on Cu(110)-(2 × 1)O. The behavior indicates that for a portion of the molecules of the first layer on Cu(110)-(2 × 1)O no charge transfer occurs at the interface.

Thus, both 2p photoemission and excitation spectra reveal that the oxygen termination of the Cu(110)-(2 × 1)O substrate prevents the interfacial charge transfer to the Co²⁺ ion only partly. This is somewhat surprising, since for even smaller molecules like hexacene,¹⁸ an almost complete electronic decoupling by the oxygen rows is observed. The one-dimensional Cu–O rows, aligned along the [001] direction of the Cu(110) surface, have a distance of about 0.51 nm, i.e., distinctly smaller than the size of CoPc or CoPcF₁₆ molecules. For details of the Cu(110)-(2 × 1)O reconstruction, see Figures S7 and S8 and refs 60–62. Thus, one might conclude that the charge transfer occurs between atoms of the Cu–O rows and the Co ion of the phthalocyanine.

The different behavior of CoPcF₁₆ compared to other molecules might be the special nature of the half-filled d_{z^2} orbital of the Co ion of Co phthalocyanines, which is oriented toward the substrate for flat-lying molecules. Recent experimental and theoretical works demonstrate that charge transfer occurs from the formation of a molecule–metal hybrid state, which is most likely due to a local bond between the Co $3d_{z^2}$ orbital and metal states.^{19,53,55,63,64} In addition, the observation of similar interface interactions for cobalt octaethylporphyrin and cobalt tetraphenylporphyrin on different substrates suggests they are almost independent of the ligand or macrocycle.^{65–67}

To study the particular role of the central Co ion in CoPcF₁₆ for interface interactions, we compare our results to FePcF₁₆ on Cu(110)-(2 × 1)O. Fe 2p XP spectra and Fe $L_{3\text{-edge}}$ XA spectra for FePcF₁₆ on Cu(110)-(2 × 1)O as a function of the film thicknesses are shown in Figure 7. For a detailed discussion of the peak shape, we refer to the literature on FePc and FePcF₁₆.^{20,43,47,51,68,69} Although most literature confirms for Fe²⁺ in FePc a 3E_g ground state with a configuration $(b_{2g})^2(e_g)^3(a_{1g})^1$, the electronic configuration is much more flexible compared to Co²⁺ in Co phthalocyanines.^{70–72}

The Fe 2p XP spectrum of a multilayer (0.83 nm) in Figure 7a exhibits a broad multiplet structure; similar spectra were reported for both FePc and FePcF₁₆.^{50,51,68} Most important, no interface component can be detected in the related monolayer spectrum, which might be expected at about 707 eV (compare, e.g., FePc on Ag(111)⁵⁰ and FePcF₁₆ on Cu(111)¹⁵). Also, the peak shape of the corresponding XA spectra is almost independent of the film thickness; differences may also arise from artifacts due to the complex background subtraction procedure. For example, a feature similar to “A0” observed on Cu(110) (Figure 6a) and related reactive interfaces^{15,50} at grazing incidence of the incoming p-polarized synchrotron light is not detectable.

Therefore, we conclude that the first monolayer of FePcF₁₆ is widely decoupled from the Cu(110)-(2 × 1)O substrate surface. There is no evidence for a substantial charge transfer

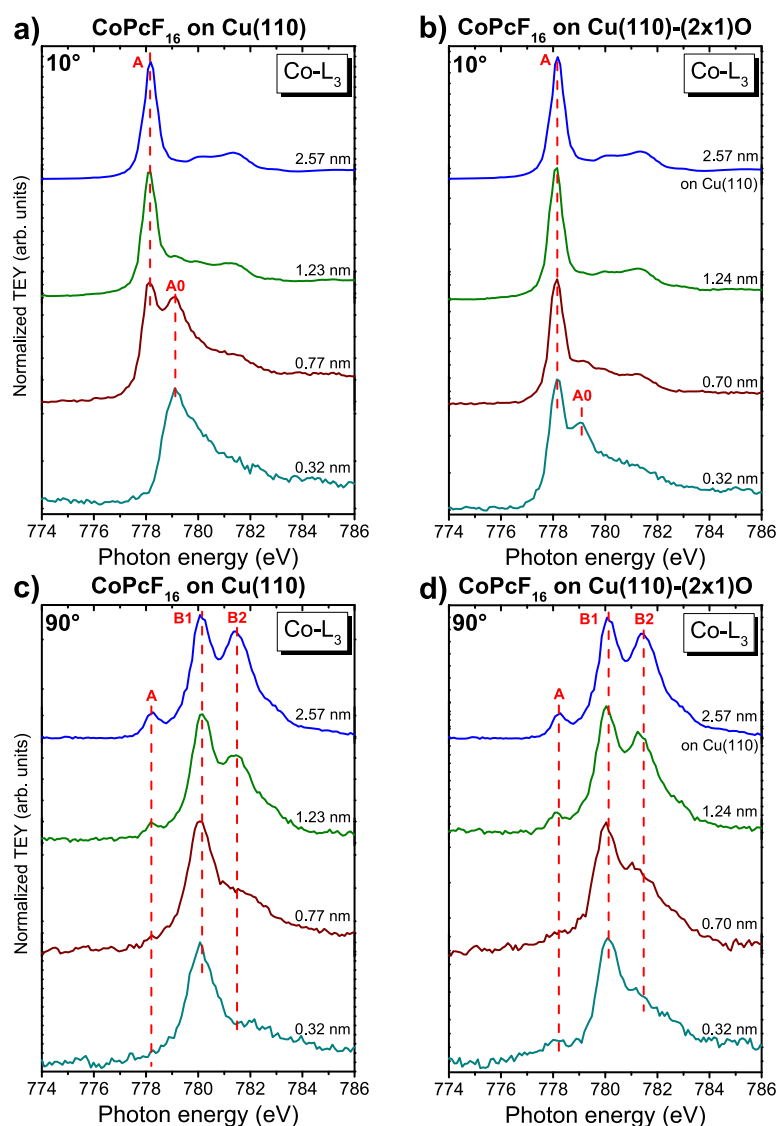


Figure 6. Thickness-dependent Co 2p excitation spectra at grazing incidence (10°) for CoPcF₁₆ on (a) Cu(110) and (b) Cu(110)-(2 × 1)O and normal incidence (90°) for CoPcF₁₆ on (c) Cu(110) and (d) Cu(110)-(2 × 1)O.

to the Fe²⁺ ion. The result is in good agreement with studies of FePc on Cu(110) and Cu(110)-(2 × 1)O, where a switching of the spin state of the central Fe ion was observed on the strongly interacting Cu(110) substrate, while such spin switching is absent on the oxygen-terminated Cu(110)-(2 × 1)O with weak or negligible interactions.¹⁶ As a consequence, we are left with the conclusion that the special electronic configuration of the Co ion in CoPcF₁₆ triggers the charge transfer at some adsorption sites on Cu(110)-(2 × 1)O.

3.3. Total Interfacial Charge Transfer and Valence Electronic Structure. So far, evidence for a rather local charge transfer from both substrates to the Co ion of CoPcF₁₆ was provided. In addition, for the Cu(110) substrate, also a charge transfer to the LUMO of CoPcF₁₆ was discussed. As a consequence of such charge transfer, dipoles at the interface are formed, which can be quantitatively determined by UPS (for details, see Figure S4).

In Figure 8, the energy level alignment for CoPcF₁₆ on Cu(110) and Cu(110)-(2 × 1)O is summarized. In first

approximation, the ionization potential (IP) can be regarded as a property of the material, although it was shown that presence of an intrinsic surface dipole may result in distinctly different values of the IP in highly ordered assemblies with differently oriented molecules.^{73,74} The measured ionization potentials of CoPcF₁₆ in thin films (6.19 and 6.12 eV in Figure 8) are typical for fluorinated phthalocyanines and in good agreement with the literature.⁵ The high IP supports charge transfer to the molecule on substrates with comparably low work function.⁵ Indeed, large interface dipoles are observed on both substrates in Figure 8, indicating a total charge transfer from the substrate to the molecule. We note that not only interfacial charge transfer causes the formation of interface dipoles, an important effect is the modification of the substrate work function upon adsorption of molecules (push-back effect).^{32,75,76} However, for many systems values for a push-back effect in the order of 0.3–0.6 eV were found,^{32,34,77} which is distinctly lower than dipoles determined in Figure 8.

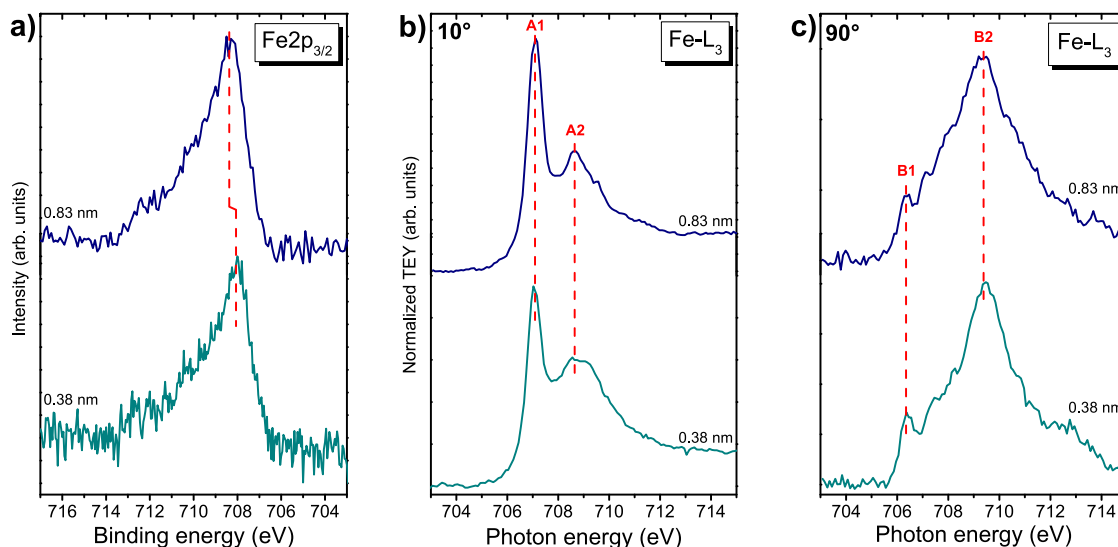
FePcF₁₆ on Cu(110)-(2x1)O

Figure 7. Thickness-dependent FePcF₁₆ on Cu(110)-(2 × 1)O. (a) Fe 2p_{3/2} core level spectra, (b) X-ray absorption spectra at grazing incidence (10°), and (c) X-ray absorption spectra at normal incidence (90°).

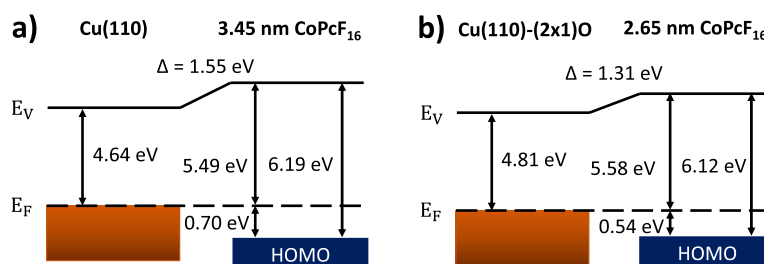


Figure 8. Energy level alignment of CoPcF₁₆ on (a) Cu(110) and (b) Cu(110)-(2 × 1)O. In both cases, the large dipoles indicate a total charge transfer from the substrate to the molecule.

The question may arise whether the charge transfer occurs unidirectionally from the substrate to the molecule or whether the interaction is bidirectional, as observed for related interfaces.^{15,26–28} To discuss a possible charge transfer from the macrocycle to the substrate in more detail, we come back to the core level shifts, observed in section 3.1. Generally, such shifts can be caused by initial state effects (i.e., a different local electron density) or final state effects as a response to the formation of the photohole (screening).^{36,78–80} Whereas the screening causes a lowering of the binding energy, an opposite effect is expected by an electron transfer from the molecule to the substrate (oxidation).

To distinguish between initial and final state effects, combined photoemission and X-ray excited Auger electron spectroscopy (XAES) can be applied.^{36,78,80–83} The basic idea is that different final states in XPS (one hole) and XAES (two holes) cause different shifts in binding energy (E_B). For the analysis of these shifts often the change of the modified Auger parameter α' is monitored according to $\Delta\alpha' = \Delta E_B(\text{XPS}) + \Delta E_{\text{kin}}(\text{XAES})$ (E_{kin} corresponds to the kinetic energy), which is correlated to the dynamical or one-hole relaxation energy R_D ($\Delta\alpha' \approx 2\Delta R_D$).^{79,80,84} ΔR_D can be correlated to the change of the polarization energy induced by the redistribution of environmental charges. The extra-atomic relaxation energy R_D^{ea} is determined in macroscopic dielectric models by the

polarization charge $(1 - 1/\epsilon)e$, where ϵ is the optical dielectric constant of the environment.

For fluorinated Pcs the absence of a local charge transfer process at the fluorine atom allows the estimation of the polarization screening via the corresponding Auger parameter.³⁶ In addition, in contrast to C KVV and N KVV Auger spectra, F KLL Auger spectra include deeper valence levels (shallow core levels), resulting in comparably well-resolved spectra. This allows a determination of the modified fluorine Auger parameter with an accuracy of about ± 0.15 eV. For a discussion of the shape of F KLL Auger spectra we refer to the literature.^{85,86}

We note that fluorinated phthalocyanines might be bended upon adsorption on metal surfaces. For submonolayers of CuPcF₁₆ on Cu(111) it was reported that fluorine atoms reside 0.027 nm above the benzene rings, which would result in an underestimation of the relaxation energy for carbon and nitrogen atoms. However, the effect is in the range of about 0.1 eV (cf. ref 36) and does not influence not the discussion below.

In Figure 9, we compare the development of the modified Auger parameter α' during the film growth of CoPcF₁₆ on Cu(110) and Cu(110)-(2 × 1)O. The corresponding F 1s and F KLL spectra are shown in Figures S5 and S6. Because of the mirror charge screening effect of the metallic substrate, the

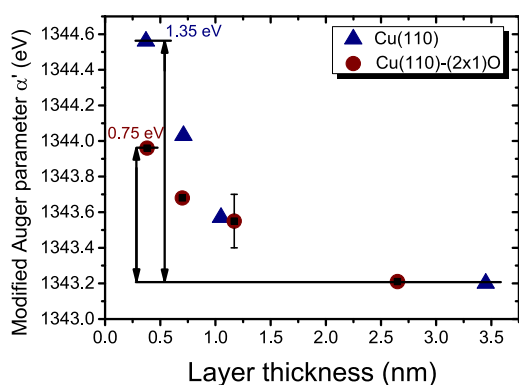


Figure 9. Modified Auger parameter α' for fluorine in CoPcF₁₆ as a function of film thickness of CoPcF₁₆ on Cu(110) and Cu(110)-(2 × 1)O. The modified Auger parameter α' is calculated from the binding energy of the F 1s core level and the kinetic energy of the related F KLL. An accuracy of ± 0.15 eV is estimated.

highest value of α' in Figure 9 is found at monolayer coverages, that is, for molecules directly at the interface, where the screening ability is highest. Comparing the thickest films with monolayer coverages, changes of α' are 1.35 and 0.75 eV for CoPcF₁₆/Cu(110) and CoPcF₁₆/Cu(110)-(2 × 1)O, respectively. The higher value for $\Delta\alpha'$ on Cu(110) can be well understood by the closer distance of CoPcF₁₆ molecules to the metallic mirror plane compared to the oxygen-terminated surface.^{81,87} We mention that rather similar (higher or lower) values $\Delta\alpha'$ of 1.5 and 0.7 eV were obtained on the interfaces CoPcF₁₆/graphene/Ni(111) and CoPcF₁₆/Au(111),^{26,88} respectively, which were attributed to either stronger or weaker interacting interfaces. This similarity even extends to the Co 2p spectra and the apparent contributions of the interface peaks as discussed above.

Values for the relaxation energy contribution ΔR_D estimated from $\Delta\alpha'$ (Figure 9) are 0.7 and 0.4 eV for CoPcF₁₆ on Cu(110) and Cu(110)-(2 × 1)O, respectively. This implies that shifts of photoemission core level spectra to lower binding

energies in the same order of magnitude might be expected as a function of the film thickness. Whereas shifts of C 1s and N 1s spectra of 0.2–0.3 eV are visible for CoPcF₁₆ on Cu(110)-(2 × 1)O, on Cu(110) thickness-dependent shifts are almost negligible (cf. Figures 1 and 2). Thus, we are left with the scenario that screening-related shifts to lower binding energies, at least on Cu(110), are compensated to a large extent by another effect: a charge transfer from the macrocycle to the substrate at the very interface.

The complex charge transfer at both interfaces affects the valence band spectra, shown in Figure 10 as a function of the thickness. At about 3 nm CoPcF₁₆ film thickness, a single HOMO feature is visible in the spectra recorded from both surfaces; the energetic position (energy level alignment) is slightly different by 0.12 eV for the two surfaces (cf. Figure 8). This might be caused by the different interaction strength or energy level alignment of the first CoPcF₁₆ layer on both substrates. Clearly visible in the spectra is the formation of interface states (or a splitting of the HOMO) for low coverages. Such interface states may arise from a partial filling of the LUMO of the molecule as a consequence of the charge transfer,⁸⁹ or stronger changes of the electronic structure, such as the formation of new states due to hybridization between Co d orbitals and substrate-related states, as proposed for other CoPcF₁₆/metal interfaces.^{19,53} From the XA spectra (cf. Figure 6), we conclude that a hybridization occurs at both investigated interfaces. On the other hand, the shapes of monolayer valence band spectra are somewhat different for the two substrates (features A, B, and C). We ascribe these variations to the different electronic interactions involved at the respective interfaces, rather likely related to different contributions of interacting molecules of the first layer on both substrates as well as to different involvement of the macrocycle in the interaction. Feature B, only visible for CoPcF₁₆ on Cu(110), might be related to the interaction between the macrocycle and the substrate.

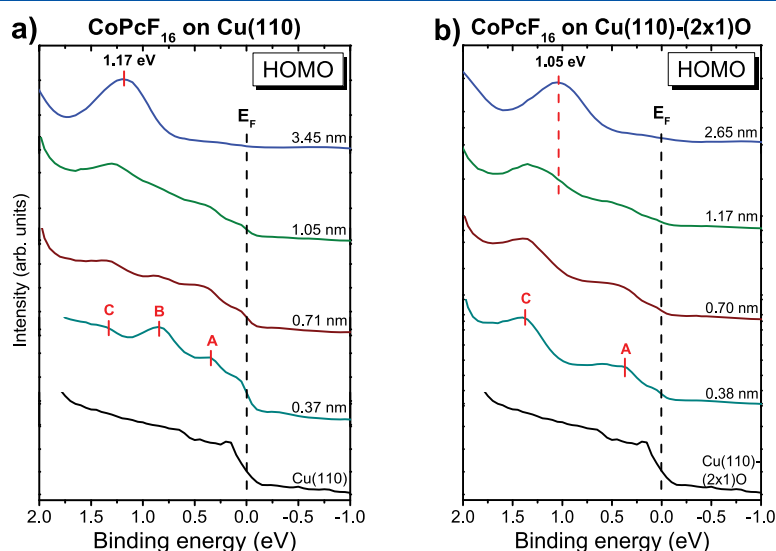


Figure 10. Thickness-dependent valence band spectra (zoom into the HOMO region) of CoPcF₁₆ on (a) Cu(110) and (b) Cu(110)-(2 × 1)O. Measured with an excitation energy of $h\nu = 21.22$ eV.

4. CONCLUSIONS

We studied interface properties of CoPcF₁₆ on Cu(110) and Cu(110)-(2 × 1)O. In both cases, a charge transfer from the substrate to the central Co ion of CoPcF₁₆ is observed, even if the oxygen termination suppresses such a strong interaction for a part of the molecules of the first monolayer. The absence of such an interaction for FePcF₁₆ on Cu(110)-(2 × 1)O indicates that the interfacial interaction in the case of CoPcF₁₆ is governed by a local interaction between the Co 3d_{z²} orbital and states of the substrate, similar to many CoPc and CoPcF₁₆ interfaces to noble metals.^{5,19,20} Considering the geometry of the Cu(110)-(2 × 1)O surface, the interaction occurs most likely between the Co ion of CoPcF₁₆ and atoms of Cu–O rows of the added row reconstruction. Thus, this study demonstrates the special nature of the Co ion in Co phthalocyanines and related compounds.

Analyzing the energetic shifts of all core levels, distinguishing between screening of the photohole and initial state effects, we propose that the charge transfer between CoPcF₁₆ and Cu(110) is bidirectional, involving also the macrocycle of CoPcF₁₆. The conclusion is supported by analysis of the shape of N–K XA spectra as a function of the thickness. It is demonstrated that the application of the Auger parameter concept is a very useful tool for the estimation of polarization screening contributions in binding energy shifts of core level photoemission spectra.

■ ASSOCIATED CONTENT

SI Supporting Information

The Supporting Information is available free of charge at <https://pubs.acs.org/doi/10.1021/acs.jpcc.1c01215>.

Thickness-dependent C 1s, N 1s, F 1s, and F–KLL core level spectra with $h\nu = 1486.7$ eV; table with energetic positions of the different N 1s peakfit components; N–K absorption spectra of 2.57 nm layer CoPcF₁₆ on Cu(110) and of the 1.24 nm layer CoPcF₁₆ on Cu(110)-(2 × 1)O at grazing (10°) and normal (90°) incidence; secondary electron cutoff and zoom into the HOMO region of CoPcF₁₆ on Cu(110) and Cu(110)-(2 × 1)O; LEED patterns of the bare Cu(110) and Cu(100)-(2 × 1)O surface at $h\nu = 134$ eV; STM images of the Cu(110)-(2 × 1)O surface (PDF)

■ AUTHOR INFORMATION

Corresponding Author

Heiko Peisert – Institute of Physical and Theoretical Chemistry, University of Tübingen, 72076 Tübingen, Germany; orcid.org/0000-0002-9742-5800; Phone: (+49) 07071/29-76931; Email: heiko.peisert@uni-tuebingen.de; Fax: (+49) 07071/29-5490

Authors

Axel Belser – Institute of Physical and Theoretical Chemistry, University of Tübingen, 72076 Tübingen, Germany
Katharina Greulich – Institute of Physical and Theoretical Chemistry, University of Tübingen, 72076 Tübingen, Germany
Peter Grüninger – Institute of Physical and Theoretical Chemistry, University of Tübingen, 72076 Tübingen, Germany

Reimer Karstens – Institute of Physical and Theoretical Chemistry, University of Tübingen, 72076 Tübingen, Germany

Ruslan Ovsyannikov – Institute for Methods and Instrumentation in Synchrotron Radiation Research, Helmholtz-Zentrum Berlin für Materialien und Energie GmbH, 12489 Berlin, Germany

Erika Giangrisostomi – Institute for Methods and Instrumentation in Synchrotron Radiation Research, Helmholtz-Zentrum Berlin für Materialien und Energie GmbH, 12489 Berlin, Germany

Peter Nagel – Institute for Quantum Materials and Technologies (IQMT), Karlsruher Institut für Technologie, 76021 Karlsruhe, Germany

Michael Merz – Institute for Quantum Materials and Technologies (IQMT), Karlsruher Institut für Technologie, 76021 Karlsruhe, Germany

Stefan Schuppler – Institute for Quantum Materials and Technologies (IQMT), Karlsruher Institut für Technologie, 76021 Karlsruhe, Germany

Thomas Chassé – Institute of Physical and Theoretical Chemistry, University of Tübingen, 72076 Tübingen, Germany; Center for Light–Matter Interaction, Sensors & Analytics (LISA+) at the University of Tübingen, 72076 Tübingen, Germany; orcid.org/0000-0001-6442-8944

Complete contact information is available at: <https://pubs.acs.org/10.1021/acs.jpcc.1c01215>

Notes

The authors declare no competing financial interest.

■ ACKNOWLEDGMENTS

The authors thank the Helmholtz-Zentrum Berlin (electron storage ring BESSY II) for provision of synchrotron radiation at the beamline PM4. Financial travel support by HZB is thankfully acknowledged. The authors are grateful to the synchrotron light source KARA and to KNMF, both Karlsruhe, Germany, for the provision of beamtime. The Center for Light–Matter Interaction, Sensors & Analytics (LISA+) at the University of Tübingen is acknowledged for technical support.

■ REFERENCES

- (1) Koch, N. Organic Electronic Devices and Their Functional Interfaces. *ChemPhysChem* **2007**, *8*, 1438–1455.
- (2) Ma, H.; Yip, H. L.; Huang, F.; Jen, A. K. Y. Interface Engineering for Organic Electronics. *Adv. Funct. Mater.* **2010**, *20*, 1371–1388.
- (3) Sanvito, S. Molecular Spintronics. *Chem. Soc. Rev.* **2011**, *40*, 3336–3355.
- (4) Uihlein, J.; Polek, M.; Glaser, M.; Adler, H.; Ovsyannikov, R.; Bauer, M.; Ivanovic, M.; Preobrajenski, A. B.; Generalov, A. V.; Chassé, T.; et al. Influence of Graphene on Charge Transfer between CoPc and Metals: The Role of Graphene–Substrate Coupling. *J. Phys. Chem. C* **2015**, *119*, 15240–15247.
- (5) Balle, D.; Adler, H.; Grüninger, P.; Karstens, R.; Ovsyannikov, R.; Giangrisostomi, E.; Chassé, T.; Peisert, H. Influence of the Fluorination of CoPc on the Interfacial Electronic Structure of the Coordinated Metal Ion. *J. Phys. Chem. C* **2017**, *121*, 18564–18574.
- (6) Ameri, T.; Li, N.; Brabec, C. J. Highly Efficient Organic Tandem Solar Cells: A Follow up Review. *Energy Environ. Sci.* **2013**, *6*, 2390–2413.
- (7) Chung, K.; Lee, C.-H.; Yi, G.-C. Transferable Gan Layers Grown on ZnO-Coated Graphene Layers for Optoelectronic Devices. *Science* **2010**, *330*, 655–657.

- (8) Kawasaki, T.; Ichimura, T.; Kishimoto, H.; Akbar, A. A.; Ogawa, T.; Oshima, C. Double Atomic Layers of Graphene/Monolayer H-BN on Ni(111) Studied by Scanning Tunneling Microscopy and Scanning Tunneling Spectroscopy. *Surf. Rev. Lett.* **2002**, *09*, 1459–1464.
- (9) Scarfato, A.; Chang, S. H.; Kuck, S.; Brede, J.; Hoffmann, G.; Wiesendanger, R. Scanning Tunneling Microscope Study of Iron(II) Phthalocyanine Growth on Metals and Insulating Surfaces. *Surf. Sci.* **2008**, *602*, 677–683.
- (10) Ferretti, A.; Baldacchini, C.; Calzolari, A.; Di Felice, R.; Ruini, A.; Molinari, E.; Betti, M. G. Mixing of Electronic States in Pentacene Adsorption on Copper. *Phys. Rev. Lett.* **2007**, *99*, 046802.
- (11) Baldacchini, C.; Allegretti, F.; Gunnella, R.; Betti, M. G. Molecule-Metal Interaction of Pentacene on Copper Vicinal Surfaces. *Surf. Sci.* **2007**, *601*, 2603–2606.
- (12) Koch, N.; Gerlach, A.; Duhm, S.; Glowatzki, H.; Heimel, G.; Vollmer, A.; Sakamoto, Y.; Suzuki, T.; Zegenhagen, J.; Rabe, J. P.; et al. Adsorption-Induced Intramolecular Dipole: Correlating Molecular Conformation and Interface Electronic Structure. *J. Am. Chem. Soc.* **2008**, *130*, 7300–7304.
- (13) Müller, K.; Seitsonen, A. P.; Brugger, T.; Westover, J.; Greber, T.; Jung, T.; Kara, A. Electronic Structure of an Organic/Metal Interface: Pentacene/Cu(110). *J. Phys. Chem. C* **2012**, *116*, 23465–23471.
- (14) Ules, T.; Lüftner, D.; Reinisch, E. M.; Koller, G.; Puschnig, P.; Ramsey, M. G. Orbital Tomography of Hybridized and Dispersing Molecular Overlayers. *Phys. Rev. B: Condens. Matter Mater. Phys.* **2014**, *90*, 8.
- (15) Belsler, A.; Karstens, R.; Nagel, P.; Merz, M.; Schuppler, S.; Chassé, T.; Peisert, H. Interaction Channels between Perfluorinated Iron Phthalocyanine and Cu(111). *Phys. Status Solidi B* **2019**, *256*, 1800292.
- (16) Tsukahara, N.; Noto, K. I.; Ohara, M.; Shiraki, S.; Takagi, N.; Takata, Y.; Miyawaki, J.; Taguchi, M.; Chainani, A.; Shin, S.; et al. Adsorption-Induced Switching of Magnetic Anisotropy in a Single Iron(II) Phthalocyanine Molecule on an Oxidized Cu(110) Surface. *Phys. Rev. Lett.* **2009**, *102*, 167203.
- (17) Shen, K. C.; Narsu, B.; Ji, G. W.; Sun, H. L.; Hu, J. B.; Liang, Z. F.; Gao, X. Y.; Li, H. Y.; Li, Z. S.; Song, B.; et al. On-Surface Manipulation of Atom Substitution between Cobalt Phthalocyanine and the Cu(111) Substrate. *RSC Adv.* **2017**, *7*, 13827–13835.
- (18) Grüninger, P.; Greulich, K.; Karstens, R.; Belsler, A.; Ovsyannikov, R.; Giangrisostomi, E.; Bettinger, H. F.; Batchelor, D.; Peisert, H.; Chassé, T. Highly Oriented Hexacene Molecules Grown in Thin Films on Cu(110)-(2 × 1)O. *J. Phys. Chem. C* **2019**, *123*, 27672–27680.
- (19) Ruckerl, F.; Waas, D.; Buchner, B.; Knupfer, M. Particular Electronic Properties of F₁₆CoPc: A Decent Electron Acceptor Material. *J. Electron Spectrosc. Relat. Phenom.* **2017**, *215*, 1–7.
- (20) Peisert, H.; Uihlein, J.; Petraki, F.; Chassé, T. Charge Transfer between Transition Metal Phthalocyanines and Metal Substrates: The Role of the Transition Metal. *J. Electron Spectrosc. Relat. Phenom.* **2015**, *204*, 49–60.
- (21) Guo, J.; Li, H.; He, H.; Chu, D.; Chen, R. CoPc- and CoPcF16-Modified Ag Nanoparticles as Novel Catalysts with Tunable Oxygen Reduction Activity in Alkaline Media. *J. Phys. Chem. C* **2011**, *115*, 8494–8502.
- (22) Baran, J. D.; Larsson, J. A.; Woolley, R. A. J.; Cong, Y.; Moriarty, P. J.; Cafolla, A. A.; Schulte, K.; Dhanak, V. R. Theoretical and Experimental Comparison of Snpc, Pbpc, and CoPc Adsorption on Ag(111). *Phys. Rev. B: Condens. Matter Mater. Phys.* **2010**, *81*, 075413.
- (23) Yeh, J. J.; Lindau, I. Atomic Subshell Photoionization Cross Sections and Asymmetry Parameters: 1 ≤ Z ≤ 103. *At. Data Nucl. Data Tables* **1985**, *32*, 1–155.
- (24) Hesse, R.; Chassé, T.; Streubel, P.; Szargan, R. Error Estimation in Peak-Shape Analysis of XPS Core-Level Spectra Using Unifit 2003: How Significant Are the Results of Peak Fits? *Surf. Interface Anal.* **2004**, *36*, 1373–1383.
- (25) Horcas, I.; Fernández, R.; Gómez-Rodríguez, J. M.; Colchero, J.; Gómez-Herrero, J.; Baro, A. M. WSXM: A software for scanning probe microscopy and a tool for nanotechnology. *Rev. Sci. Instrum.* **2007**, *78*, 013705.
- (26) Petraki, F.; Peisert, H.; Uihlein, J.; Aygül, U.; Chassé, T. CoPc and CoPcF₁₆ on Gold: Site-Specific Charge-Transfer Processes. *Beilstein J. Nanotechnol.* **2014**, *5*, S24–S31.
- (27) Lindner, S.; Treske, U.; Knupfer, M. The Complex Nature of Phthalocyanine/Gold Interfaces. *Appl. Surf. Sci.* **2013**, *267*, 62–65.
- (28) Huang, Y.; Wruss, E.; Egger, D.; Kera, S.; Ueno, N.; Saidi, W.; Bucko, T.; Wee, A.; Zojer, E. Understanding the Adsorption of CuPc and ZnPc on Noble Metal Surfaces by Combining Quantum-Mechanical Modelling and Photoelectron Spectroscopy. *Molecules* **2014**, *19*, 2969–2992.
- (29) Jiang, H.; Ye, J.; Hu, P.; Wei, F.; Du, K.; Wang, N.; Ba, T.; Feng, S.; Kloc, C. Fluorination of Metal Phthalocyanines: Single-Crystal Growth, Efficient N-Channel Organic Field-Effect Transistors, and Structure-Property Relationships. *Sci. Rep.* **2015**, *4*, 7573.
- (30) Peisert, H.; Knupfer, M.; Schwieger, T.; Fuentes, G. G.; Olligs, D.; Fink, J.; Schmidt, T. Fluorination of Copper Phthalocyanines: Electronic Structure and Interface Properties. *J. Appl. Phys.* **2003**, *93*, 9683–9692.
- (31) Wang, J.; Wang, J.; Dougherty, D. B. Direct Molecular Quantification of Electronic Disorder in N,N'-Di-[(1-Naphthyl)-N,N'-Diphenyl]-1,1'-Biphenyl)-4,4'-Diamine on Au(111). *J. Vac. Sci. Technol., B: Nanotechnol. Microelectron.: Mater., Process., Meas., Phenom.* **2020**, *38*, 053401.
- (32) Peisert, H.; Knupfer, M.; Fink, J. Energy Level Alignment at Organic/Metal Interfaces: Dipole and Ionization Potential. *Appl. Phys. Lett.* **2002**, *81*, 2400–2402.
- (33) Vazquez, H.; Dappe, Y. J.; Ortega, J.; Flores, F. Energy Level Alignment at Metal/Organic Semiconductor Interfaces: “Pillow” Effect, Induced Density of Interface States, and Charge Neutrality Level. *J. Chem. Phys.* **2007**, *126*, 144703.
- (34) Betti, M. G.; Kanjilal, A.; Mariani, C.; Vázquez, H.; Dappe, Y. J.; Ortega, J.; Flores, F. Barrier Formation at Organic Interfaces in a Cu(100)-Benzenethiolate-Pentacene Heterostructure. *Phys. Rev. Lett.* **2008**, *100*, 027601.
- (35) Yamane, H.; Yoshimura, D.; Kawabe, E.; Sumii, R.; Kanai, K.; Ouchi, Y.; Ueno, N.; Seki, K. Electronic Structure at Highly Ordered Organic/Metal Interfaces: Pentacene on Cu(110). *Phys. Rev. B: Condens. Matter Mater. Phys.* **2007**, *76*, 165436.
- (36) Peisert, H.; Kolacyk, D.; Chassé, T. Site-Specific Charge-Transfer Screening at Organic/Metal Interfaces. *J. Phys. Chem. C* **2009**, *113*, 19244–19250.
- (37) Evangelista, F.; Ruocco, A.; Gotter, R.; Cossaro, A.; Floreano, L.; Morgante, A.; Crispoldi, F.; Betti, M. G.; Mariani, C. Electronic States of CuPc Chains on the Au(110) Surface. *J. Chem. Phys.* **2009**, *131*, 174710.
- (38) Papageorgiou, N.; Ferro, Y.; Salomon, E.; Allouche, A.; Layet, J. M.; Giovanelli, L.; Le Lay, G. Geometry and Electronic Structure of Lead Phthalocyanine: Quantum Calculations Via Density-Functional Theory and Photoemission Measurements. *Phys. Rev. B: Condens. Matter Mater. Phys.* **2003**, *68*, 235105.
- (39) Papageorgiou, N.; Salomon, E.; Angot, T.; Layet, J.-M.; Giovanelli, L.; Lay, G. L. Physics of Ultra-Thin Phthalocyanine Films on Semiconductors. *Prog. Surf. Sci.* **2004**, *77*, 139–170.
- (40) Schmid, M.; Kaftan, A.; Steinrück, H. P.; Gottfried, J. M. The Electronic Structure of Cobalt(II) Phthalocyanine Adsorbed on Ag(111). *Surf. Sci.* **2012**, *606*, 945–949.
- (41) Maslyuk, V. V.; Aristov, V. Y.; Molodtsova, O. V.; Vyalikh, D. V.; Zhilin, V. M.; Ossipyan, Y. A.; Bredow, T.; Mertig, I.; Knupfer, M. The Electronic Structure of Cobalt Phthalocyanine. *Appl. Phys. A: Mater. Sci. Process.* **2009**, *94*, 485–489.
- (42) Åhlund, J.; Nilson, K.; Schiessling, J.; Kjeldgaard, L.; Berner, S.; Mårtensson, N.; Puglia, C.; Brena, B.; Nyberg, M.; Luo, Y. The Electronic Structure of Iron Phthalocyanine Probed by Photoelectron and X-Ray Absorption Spectroscopies and Density Functional Theory Calculations. *J. Chem. Phys.* **2006**, *125*, 034709.

- (43) Willey, T. M.; Bagge-Hansen, M.; Lee, J. R.; Call, R.; Landt, L.; van Buuren, T.; Colesniuc, C.; Monton, C.; Valmianski, I.; Schuller, I. K. Electronic Structure Differences between H_2 , Fe-, Co-, and Cu-Phthalocyanine Highly Oriented Thin Films Observed Using NEXAFS Spectroscopy. *J. Chem. Phys.* **2013**, *139*, 034701.
- (44) Holland, B. N.; Peltekis, N.; Farrelly, T.; Wilks, R. G.; Gavrila, G.; Zahn, D. R. T.; McGuinness, C.; McGovern, I. T. NEXAFS Studies of Copper Phthalocyanine on Ge(001)- 2×1 and Ge(111)- $c(2 \times 8)$ Surfaces. *Phys. Status Solidi B* **2009**, *246*, 1546–1551.
- (45) Petraki, F.; Peisert, H.; Hoffmann, P.; Uihlein, J.; Knupfer, M.; Chassé, T. Modification of the 3d-Electronic Configuration of Manganese Phthalocyanine at the Interface to Gold. *J. Phys. Chem. C* **2012**, *116*, 5121–5127.
- (46) Kuz'min, M. D.; Hayn, R.; Oison, V. Ab Initio Calculated XANES and XMCD Spectra of Fe(II) Phthalocyanine. *Phys. Rev. B: Condens. Matter Mater. Phys.* **2009**, *79*, 024413.
- (47) Betti, M. G.; Gargiani, P.; Frisenda, R.; Biagi, R.; Cossaro, A.; Verdini, A.; Floreano, L.; Mariani, C. Localized and Dispersive Electronic States at Ordered FePc and CoPc Chains on Au(110). *J. Phys. Chem. C* **2010**, *114*, 21638–21644.
- (48) Bartolomé, J.; Bartolomé, F.; Garcia, L. M.; Filoti, G.; Gredig, T.; Colesniuc, C. N.; Schuller, I. K.; Cezar, J. C. Highly Unquenched Orbital Moment in Textured Fe-Phthalocyanine Thin Films. *Phys. Rev. B: Condens. Matter Mater. Phys.* **2010**, *81*, 195405.
- (49) Javaid, S.; Bowen, M.; Boukari, S.; Joly, L.; Beaufrand, J. B.; Chen, X.; Dappe, Y. J.; Scheurer, F.; Kappler, J. P.; Arabski, J.; et al. Impact on Interface Spin Polarization of Molecular Bonding to Metallic Surfaces. *Phys. Rev. Lett.* **2010**, *105*, 077201.
- (50) Petraki, F.; Peisert, H.; Aygul, U.; Latteyer, F.; Uihlein, J.; Vollmer, A.; Chassé, T. Electronic Structure of FePc and Interface Properties on Ag(111) and Au(100). *J. Phys. Chem. C* **2012**, *116*, 11110–11116.
- (51) Karstens, R.; Glaser, M.; Belser, A.; Balle, D.; Polek, M.; Ovsyannikov, R.; Giangrisostomi, E.; Chassé, T.; Peisert, H. FePc and FePcF₁₆ on Rutile TiO₂(110) and (100): Influence of the Substrate Preparation on the Interaction Strength. *Molecules* **2019**, *24*, 4579.
- (52) Toader, M.; Gopakumar, T. G.; Shukryna, P.; Hietschold, M. Exploring the F₁₆CoPc/Ag(110) Interface Using Scanning Tunneling Microscopy and Spectroscopy. 2. Adsorption-Induced Charge Transfer Effect. *J. Phys. Chem. C* **2010**, *114*, 21548–21554.
- (53) Lindner, S.; Treske, U.; Grobosch, M.; Knupfer, M. Charge Transfer at F₁₆CoPc and CoPc Interfaces to Au. *Appl. Phys. A: Mater. Sci. Process.* **2011**, *105*, 921–925.
- (54) Petraki, F.; Peisert, H.; Biswas, I.; Chassé, T. Electronic Structure of Co-Phthalocyanine on Gold Investigated by Photoexcited Electron Spectroscopies: Indication of Co Ion-Metal Interaction. *J. Phys. Chem. C* **2010**, *114*, 17638–17643.
- (55) Toader, M.; Knupfer, M.; Zahn, D. R. T.; Hietschold, M. Initial Growth at the F₁₆CoPc/Ag(111) Interface. *Surf. Sci.* **2011**, *605*, 1510–1515.
- (56) Pawlak, R.; Meier, T.; Renaud, N.; Kisiel, M.; Hinaut, A.; Glatzel, T.; Sordes, D.; Durand, C.; Soe, W.-H.; Baratoﬀ, A.; et al. Design and Characterization of an Electrically Powered Single Molecule on Gold. *ACS Nano* **2017**, *11*, 9930–9940.
- (57) Lindner, S.; Mahns, B.; Treske, U.; Vilkov, O.; Haidu, F.; Fronk, M.; Zahn, D. R. T.; Knupfer, M. Epitaxial Growth and Electronic Properties of Well Ordered Phthalocyanine Heterojunctions MnPc/F₁₆CoPc. *J. Chem. Phys.* **2014**, *141*, 094706.
- (58) Fernández-Rodríguez, J.; Toby, B.; van Veenendaal, M. Mixed Configuration Ground State in Iron(II) Phthalocyanine. *Phys. Rev. B: Condens. Matter Mater. Phys.* **2015**, *91*, 214427.
- (59) Uihlein, J.; Peisert, H.; Glaser, M.; Polek, M.; Adler, H.; Petraki, F.; Ovsyannikov, R.; Bauer, M.; Chassé, T. Communication: Influence of Graphene Interlayers on the Interaction between Cobalt Phthalocyanine and Ni(111). *J. Chem. Phys.* **2013**, *138*, 081101.
- (60) Coulman, D. J.; Wintterlin, J.; Behm, R. J.; Ertl, G. Novel Mechanism for the Formation of Chemisorption Phases: The (2 × 1)O-Cu(110) “Added Row” Reconstruction. *Phys. Rev. Lett.* **1990**, *64*, 1761–1764.
- (61) Jensen, F.; Besenbacher, F.; Laegsgaard, E.; Stensgaard, I. Surface Reconstruction of Cu(110) Induced by Oxygen Chemisorption. *Phys. Rev. B: Condens. Matter Mater. Phys.* **1990**, *41*, 10233–10236.
- (62) Duan, X.; Warschkow, O.; Soon, A.; Delley, B.; Stampfl, C. Density Functional Study of Oxygen on Cu(100) and Cu(110) Surfaces. *Phys. Rev. B: Condens. Matter Mater. Phys.* **2010**, *81*, 15.
- (63) Stepanow, S.; Miedema, P. S.; Mugarza, A.; Ceballos, G.; Moras, P.; Cezar, J. C.; Carbone, C.; de Groot, F. M. F.; Gambardella, P. Mixed-Valence Behavior and Strong Correlation Effects of Metal Phthalocyanines Adsorbed on Metals. *Phys. Rev. B: Condens. Matter Mater. Phys.* **2011**, *83*, 220401.
- (64) Li, Z.; Li, B.; Yang, J.; Hou, J. G. Single-Molecule Chemistry of Metal Phthalocyanine on Noble Metal Surfaces. *Acc. Chem. Res.* **2010**, *43*, 954–962.
- (65) Bai, Y.; Sekita, M.; Schmid, M.; Bischof, T.; Steinrueck, H. P.; Gottfried, J. M. Interfacial Coordination Interactions Studied on Cobalt Octaethylporphyrin and Cobalt Tetraphenylporphyrin Monolayers on Au(111). *Phys. Chem. Chem. Phys.* **2010**, *12*, 4336–4344.
- (66) Lukaszczuk, T.; Flechtner, K.; Merte, L. R.; Jux, N.; Maier, F.; Gottfried, J. M.; Steinrueck, H. P. Interaction of Cobalt(II) Tetraarylporphyrins with a Ag(111) Surface Studied with Photoelectron Spectroscopy. *J. Phys. Chem. C* **2007**, *111*, 3090–3098.
- (67) Hieringer, W.; Flechtner, K.; Kretschmann, A.; Seufert, K.; Auwärter, W.; Barth, J. V.; Görling, A.; Steinrueck, H.-P.; Gottfried, J. M. The Surface Trans Effect: Influence of Axial Ligands on the Surface Chemical Bonds of Adsorbed Metalloporphyrins. *J. Am. Chem. Soc.* **2011**, *133*, 6206–6222.
- (68) Greulich, K.; Belser, A.; Bölke, S.; Grüninger, P.; Karstens, R.; Sättele, M. S.; Ovsyannikov, R.; Giangrisostomi, E.; Basova, T. V.; Klyamer, D.; et al. Charge Transfer from Organic Molecules to Molybdenum Disulfide: Influence of the Fluorination of Iron Phthalocyanine. *J. Phys. Chem. C* **2020**, *124*, 16990–16999.
- (69) Kroll, T.; Kraus, R.; Schonfelder, R.; Aristov, V. Y.; Molodtsova, O. V.; Hoffmann, P.; Knupfer, M. Transition Metal Phthalocyanines: Insight into the Electronic Structure from Soft X-Ray Spectroscopy. *J. Chem. Phys.* **2012**, *137*, 054306.
- (70) Nakamura, K.; Kitaoka, Y.; Akiyama, T.; Ito, T.; Weinert, M.; Freeman, A. J. Constraint Density Functional Calculations for Multiplets in a Ligand-Field Applied to Fe-Phthalocyanine. *Phys. Rev. B: Condens. Matter Mater. Phys.* **2012**, *85*, 235129.
- (71) Dale, B. W.; Williams, R. J. P.; Johnson, C. E.; Thorp, T. L. S = 1 Spin State of Divalent Iron. I. Magnetic Properties of Phthalocyanine Iron (II). *J. Chem. Phys.* **1968**, *49*, 3441–3444.
- (72) Natoli, C. R.; Kruger, P.; Bartolome, J.; Bartolome, F. Determination of the Ground State of an Au-Supported FePc Film Based on the Interpretation of Fe K- and L-Edge X-Ray Magnetic Circular Dichroism Measurements. *Phys. Rev. B: Condens. Matter Mater. Phys.* **2018**, *97*, 16.
- (73) Ivanco, J.; Haber, T.; Krenn, J. R.; Netzer, F. P.; Resel, R.; Ramsey, M. G. Sexithiophene Films on Ordered and Disordered TiO₂ Surfaces: Electronic, Structural and Morphological Properties. *Surf. Sci.* **2007**, *601*, 178–187.
- (74) Duhm, S.; Heimel, G.; Salzmänn, I.; Glowatzki, H.; Johnson, R. L.; Vollmer, A.; Rabe, J. P.; Koch, N. Orientation-Dependent Ionization Energies and Interface Dipoles in Ordered Molecular Assemblies. *Nat. Mater.* **2008**, *7*, 326–332.
- (75) Ishii, H.; Sugiyama, K.; Ito, E.; Seki, K. Energy Level Alignment and Interfacial Electronic Structures at Organic/Metal and Organic/Organic Interfaces. *Adv. Mater.* **1999**, *11*, 605–625.
- (76) Hwang, J.; Wan, A.; Kahn, A. Energetics of Metal-Organic Interfaces: New Experiments and Assessment of the Field. *Mater. Sci. Eng., R* **2009**, *64*, 1–31.
- (77) Crispin, X.; Geskin, V.; Crispin, A.; Cornil, J.; Lazzaroni, R.; Salaneck, W. R.; Brédas, J.-L. Characterization of the Interface Dipole at Organic/ Metal Interfaces. *J. Am. Chem. Soc.* **2002**, *124*, 8131–8141.

- (78) Kaindl, G.; Chiang, T. C.; Eastman, D. E.; Himpsel, F. J. Distance-Dependent Relaxation Shifts of Photoemission and Auger Energies for Xe on Pd(001). *Phys. Rev. Lett.* **1980**, *45*, 1808–1811.
- (79) Peisert, H.; Chassé, T.; Streubel, P.; Meisel, A.; Szargan, R. Relaxation Energies in XPS and XAES of Solid Sulfur-Compounds. *J. Electron Spectrosc. Relat. Phenom.* **1994**, *68*, 321–328.
- (80) Moretti, G. The Wagner Plot and the Auger Parameter as Tools to Separate Initial- and Final-State Contributions in X-Ray Photoemission Spectroscopy. *Surf. Sci.* **2013**, *618*, 3–11.
- (81) Kolacyak, D.; Peisert, H.; Chassé, T. Charge Transfer and Polarization Screening in Organic Thin Films: Phthalocyanines on Au(100). *Appl. Phys. A: Mater. Sci. Process.* **2009**, *95*, 173–178.
- (82) Chiang, T. C.; Kaindl, G.; Mandel, T. Layer-Resolved Shifts of Photoemission and Auger-Spectra from Physisorbed Rare-Gas Multilayers. *Phys. Rev. B: Condens. Matter Mater. Phys.* **1986**, *33*, 695–711.
- (83) Peisert, H.; Petershans, A.; Chassé, T. Charge Transfer and Polarization Screening at Organic/Metal Interfaces: Distinguishing between the First Layer and Thin Films. *J. Phys. Chem. C* **2008**, *112*, 5703–5706.
- (84) Moretti, G. The Auger Parameter and the Polarization Energy - a Simple Electrostatic Model. *Surf. Interface Anal.* **1990**, *16*, 159–162.
- (85) Albridge, R. G.; Hamrin, K.; Johansson, G.; Fahlman, A. The KLL Auger Spectrum of Fluorine. *Z. Phys. A: Hadrons Nucl.* **1968**, *209*, 419–427.
- (86) Vékey, K. Multiply Charged Ions. *Mass Spectrom. Rev.* **1995**, *14*, 195–225.
- (87) Helander, M. G.; Greiner, M. T.; Wang, Z. B.; Lu, Z. H. Effect of Electrostatic Screening on Apparent Shifts in Photoemission Spectra near Metal/Organic Interfaces. *Phys. Rev. B: Condens. Matter Mater. Phys.* **2010**, *81*, 153308.
- (88) Balle, D.; Schedel, C.; Chassé, T.; Peisert, H. Interface Properties of CoPc and CoPcF₁₆ on Graphene/Nickel: Influence of Germanium Intercalation. *J. Phys.: Condens. Matter* **2019**, *31*, 174004.
- (89) Schwieger, T.; Peisert, H.; Knupfer, M. Direct Observation of Interfacial Charge Transfer from Silver to Organic Semiconductors. *Chem. Phys. Lett.* **2004**, *384*, 197–202.

c) Noch nicht eingereichte Manuskripte

- Comparison of Interface Properties of Perfluorinated FePc on Au(111) and Ag(111)
- Influence of BN-doping of Nanographene Molecules on the Interaction at Different Metal Interfaces
- Molecular exchange of Hexabenzocoronene and Cobalt Phthalocyanine on Au(111)

Comparison of Interface Properties of Perfluorinated FePc on Au(111) and Ag(111)

*Axel Belser,[†] Katharina Greulich,[†] Peter Nagel,[§] Michael Merz,[§] Stefan Schuppler,[§] Thomas Chassé,^{† ‡}
and Heiko Peisert^{†*}*

[†]Institute of Physical and Theoretical Chemistry, University of Tübingen, Auf der Morgenstelle 18, 72076 Tübingen, Germany

[‡]Center for Light-Matter Interaction, Sensors & Analytics (LISA⁺) at the University of Tübingen, Auf der Morgenstelle 18, 72076 Tübingen, Germany

[§]Karlsruher Institut für Technologie, Institut für Festkörperphysik, 76021 Karlsruhe, Germany

* Corresponding author, heiko.peisert@uni-tuebingen.de, Tel.: (+49) 07071 / 29-76931, Fax: (+49) 07071 / 29-5490

Abstract

The electronic structure of Fe(II) hexadecafluoro-phthalocyanine (FePcF₁₆) and interface properties on Au(111) and Ag(111) were investigated by photoexcited electron spectroscopies (X-ray Photoemission spectroscopy (XPS) and X-ray absorption spectroscopy (XAS)). On Au(111) just a weak interaction is observed, while on Ag(111) the electronic structure of FePcF₁₆ is distinctly altered at the interface. The macrocycle as well as the central metal atom are involved in this strong interaction on Ag(111). Valence band measurements show the existence of an interface peak at 0.4 nm coverage. Resonant Photoemission indicates the interface state has Fe character. However, possible scenarios for the different interaction on the Au and Ag surfaces are discussed.

Keywords Fluorinated Phthalocyanine, polarization screening, charge transfer, interaction, photoemission spectroscopy, X-ray absorption spectroscopy

1. Introduction

Molecules from the family of metal phthalocyanines have been already extensively applied in numerous molecular devices, recently opto-electronic devices such as light-emitting diodes, field-effect transistors, solar cells and spintronic devices are in the focus of research.¹⁻⁴ For several transition metal phthalocyanine (TMPc) layers on noble metal surfaces (e.g. Au and Ag), a charge transfer towards the central metal atom has been previously reported, affecting the electronic and magnetic properties of the organic/metal interface, thus, the performance of the molecular device. Furthermore, phthalocyanines are highly ordered in organic thin films, which is advantageous for many properties of organic devices. The fluorination of phthalocyanines represents an ideal route for the tuning of the ionization potential (IP), a basic electronic parameter which can affect the interface dipole significantly and therefore, the energy level alignment.⁵⁻⁶ In the context of applications, perfluorinated counterparts of Pcs have demonstrated high performance and stability in air and they are used as n-type channels in electronic devices.⁷⁻⁸ Knowledge of the electronic structure and the transport of charge carriers in the organic devices is important for the understanding of the properties of the device components.

We study electronic properties and the molecular orientation of FePcF₁₆ in thin films on two metal substrates (Ag and Au) with different work function. Generally low work function metals (Ag) are more chemically reactive than metals with a high work function (Au). The electronic structure was investigated by XPS, XAS and ResPES (resonant photoemission spectroscopy), and the orientation by XAS.

2. Experimental

Au(111) and Ag(111) single crystals were cleaned by cycles of argon ion sputtering and annealing. The sputtering was carried out at a voltage of 0.8 – 1.0 kV for typically 30 min with a pressure of $1 \cdot 10^{-6}$ mbar, subsequently the annealing was performed for 30 min at a temperature of 770 K (Au(111)) and 800 K (Ag(111)). FePcF₁₆ purchased from SYNTHON Chemicals GmbH & Co.KG, was resublimed and thoroughly degassed *in vacuo*. The molecules were evaporated at rates of about 1-2 Å/min determined by a quartz microbalance. All values of the film thicknesses were obtained by the comparison of photoemission intensities of substrate and overlayer related peaks assuming layer-by-layer growth. Atomic cross sections were taken from Ref. ⁹.

The X-ray absorption spectroscopy (XAS) and photoemission (PES) measurements have been performed at the WERA beamline at the Karlsruhe Research Accelerator (KARA, Karlsruhe, Germany). The energy resolution for XAS and PES was set to about 220 meV at a photon energy of 400 eV. For the calibration of the photon energy the binding energies (BE) of the Au 4f_{7/2} and Ag 3d_{5/2} peaks of 84.0 and 368.2 eV were used for PES. The absorption was monitored indirectly by measuring the total electron yield (sample current). The x-ray absorption (XA) spectra have been normalized to the same step height well above the ionization threshold. For XAS the energy was calibrated to reproduce the Ni-L₃ absorption edge of NiO at 853.0 eV. For the peak-fitting procedure we assumed a Voigt profile (convolution of Gaussian and Lorentzian peaks) and a Shirley model background.

3. Results and Discussion

3.1. Molecular orientation in thin films

The growth of organic molecules is of enormous importance for intermolecular interactions and thus for the electronic structure in thin films. Moreover, the orientation at interfaces can significantly affect the strength of the interaction between the molecule and the substrate under consideration. Planar transition metal phthalocyanines (TMPcs) grow often in a flat lying geometry with respect to the substrate surface on single crystalline metal substrates.¹⁰⁻¹⁴ Nevertheless, for VOPc and VOPcF₁₆ it was obtained that the fluorination may affect the growth mode distinctly.¹⁵

We performed polarization dependent XAS measurements to study the molecular orientation in thin films. For planar π -conjugated carbon systems, the molecular orientation can be probed by monitoring the relative intensities of excitations from occupied C1s core levels into unoccupied molecular levels (π^* or σ^*).¹⁶ For example, in a planar conjugated carbon system the excitation from C1s to a π^* orbital is allowed maximal for E vertical to the molecular plane (parallel to 2pz), whereas the transition to σ^* is allowed maximal for E parallel to the molecular plane and to the chemical bond. For phthalocyanines, besides C1s- π^* in a similar manner also N1s- π^* excitations can be used for the analysis of the molecular orientation,¹⁰ avoiding problems of the analysis of C1s- π^* spectra arising from common carbon contaminations of beamline components.

In **Figure 1**, we show N-K edge absorption spectra of thin films of FePcF₁₆ on Au(111) and Ag(111) as a function of the incidence angle θ of the p-polarized synchrotron radiation to investigate the orientation of the molecules on the different substrates (see inset). The region at photon energies below 402 eV belongs to transitions into the π^* -orbitals, the region above

to σ^* -transitions, although we note that weak in-plane polarized transitions appear below 402 eV.^{10, 17-18}

On both substrates the spectra show strong out-of-plane π^* -transitions for grazing incidence (10°). For normal incidence (90°), strong in-plane σ^* -transitions can be observed. This suggests mainly flat-lying molecules on both substrates. A quantitative analysis of the tilt angle is hindered by weak in-plane transitions appearing in the same region as the π^* resonances^{10, 17-18} because of hybridization of unoccupied nitrogen related states with d-orbitals of the transition metal atom.¹⁹⁻²² Additionally, in the case of FePcF_{16} on $\text{Ag}(111)$ the background strongly affects the spectra.

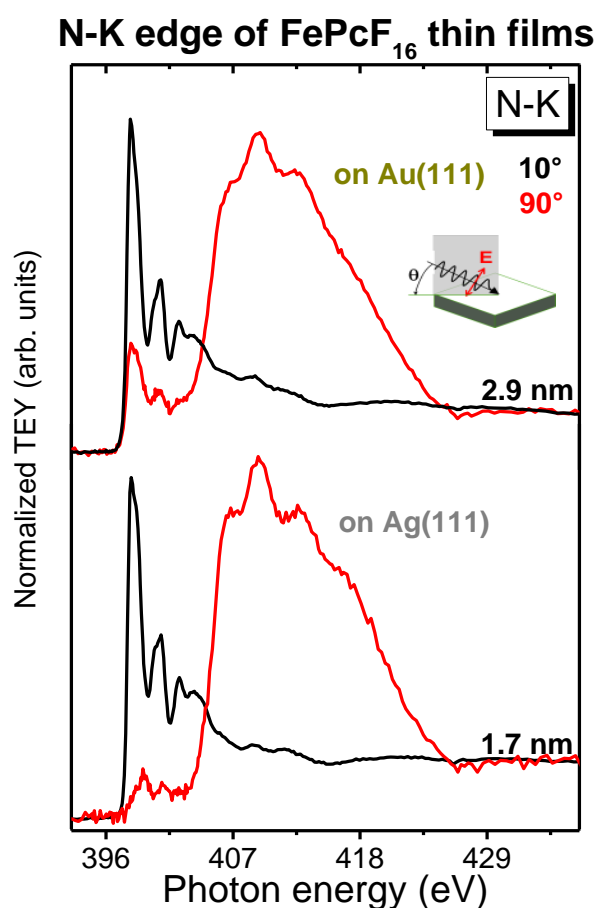


Figure 1. *N1s* X-ray absorption spectra of thin films of FePcF_{16} on $\text{Au}(111)$ (upper panel) and $\text{Ag}(111)$ (lower panel) as a function of the incidence angle θ of the incoming synchrotron light.

3.2. Interface properties of the macrocycle of FePcF₁₆ on Au(111) and Ag(111)

First we focus on the different electronic behavior of the macrocycle, comparing the less reactive Au(111) and the more reactive Ag(111) substrate. Between phthalocyanines and a multitude of substrates different interaction channels were observed, involving both the macrocycle and the central metal atom. In many cases the charge transfer is even bidirectional.²³⁻²⁶

In **Figure 2** we show thickness dependent C1s core level spectra including detailed peak fits for the bulk-like thin films and ultrathin films of 1-2 monolayers (ML) coverage. One monolayer corresponds to 0.32 nm of flat lying perfluorinated phthalocyanines.²⁷ The spectra were recorded at a surface sensitive excitation energy of 385 eV, which corresponds to a surface sensitive kinetic energy of about 95 eV in case of C1s.

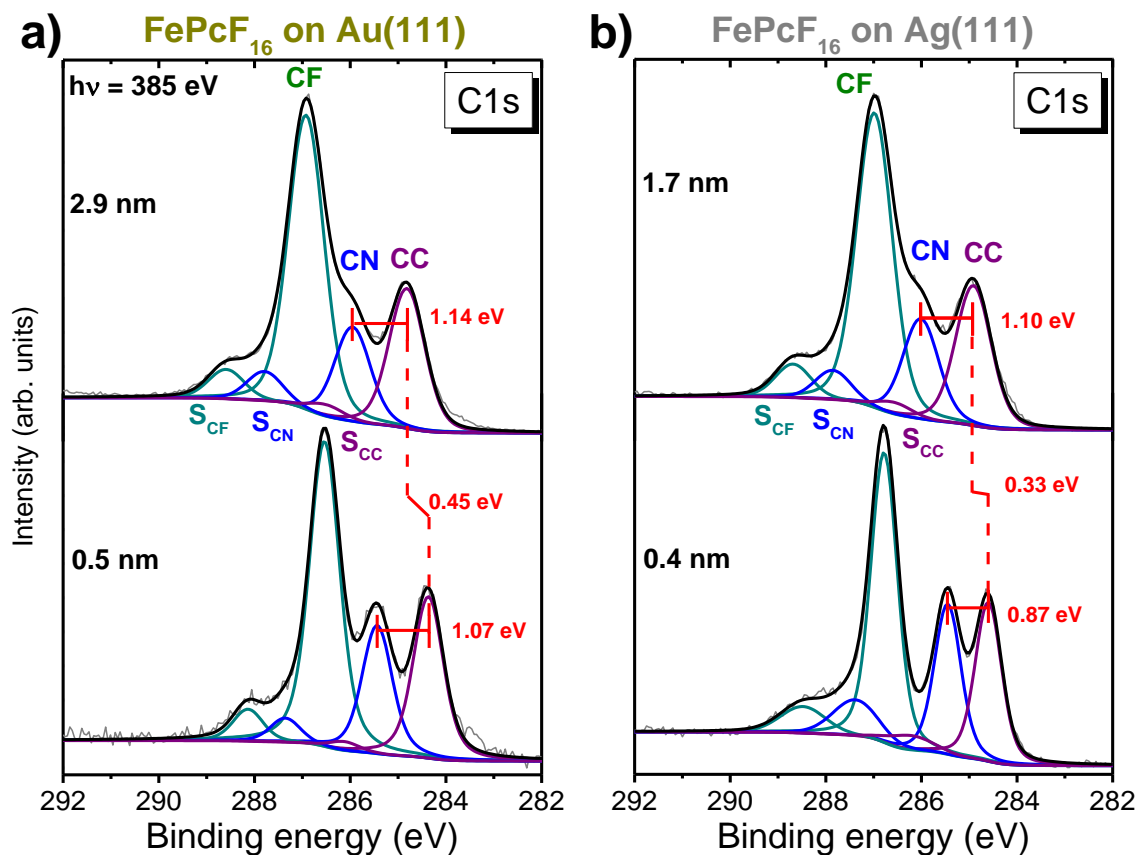


Figure 2. Thickness dependent C1s core level spectra of FePcF₁₆ on a) Au(111) and b) Ag(111). Measured with an excitation energy of $h\nu = 385$ eV.

The spectra recorded at the higher thicknesses of 2.9 nm and 1.7 nm on Au(111) and Ag(111), respectively, are very similar in their peak shapes. Three main peak components can be observed in the C1s spectrum, which may be assigned to carbon bonded to fluorine (CF), bonded to nitrogen (CN) and bonded to other carbon (CC) atoms and the respective satellites (S_{CF} , S_{CN} , S_{CC}) from high to low binding energy. The CN-related components in the center of the peak appear more separated in energy from the CF peak for both of the interface-related spectra. The energetic position of all components is summarized in **Table 1**. Additional peak fit data is shown in **Tables S1+2**.

Table 1. FePcF₁₆ on Au(111) and Ag(111): Thickness dependent C1s binding energies as obtained from peak fits in eV.

| substrate | thickness (nm) | CF | S_{CF} | CN | S_{CN} | CC | S_{CC} |
|----------------|----------------|--------|----------|--------|----------|--------|----------|
| Au(111) | 2.9 | 286.92 | 288.59 | 285.95 | 287.79 | 284.82 | 286.51 |
| | 0.5 | 286.54 | 288.14 | 285.44 | 287.36 | 284.37 | 286.13 |
| Ag(111) | 1.7 | 286.98 | 288.68 | 286.01 | 287.85 | 284.91 | 286.57 |
| | 0.4 | 286.79 | 288.48 | 286.45 | 287.38 | 284.58 | 286.23 |

For the thin films the intensity ratios $CF+S_{CF}:CN+S_{CN}:CC+S_{CC}$ of 4.3:1.6:2 and 4.3:1.7:2 for Au(111) and Ag(111) respectively, are in reasonable agreement with the stoichiometry of differently bound carbon atoms in FePcF₁₆ (4:2:2). The small deviations may be explained by the high surface sensitivity at the chosen excitation energy and the tilt angle of the molecules. Note that for almost standing or edge on phthalocyanines the relative intensity related to the outermost carbon (CF) would be significantly larger than that of the carbon near the macrocycle center (CN) under these surface sensitive measurement conditions.²⁸ Further, some uncertainties will also derive from the assignment of the satellite intensity contributions.

The stoichiometry of the C1s core level of the 0.5 nm layer on Au(111) fits rather well to the expected stoichiometry (4:1.8:2). However, this is different for the monolayer on Ag(111). The CF+S_{CF} part is of lower intensity than expected. The intensity ratio of CF+S_{CF} to CN+S_{CN} is 1.6:1. A possible reason is a substrate induced decomposition, similar to Perfluoro-Pentacene.²⁹ It was shown that Perfluoro-Pentacene decomposes on Cu(111) after annealing the exposed sample. So, the CF bonds possibly break at the interface and the carbon atoms are not anymore bonded to fluorine atoms. Aggravating to come along, the situation at the interface is more complex, what makes the detailed peak fit much more complicated. For more information we will discuss the F1s core level spectra below.

Nevertheless, detailed analysis of energetic positions of the C1s components reveals distinct differences between the thin films and the 1-2 ML coverages. By means of the CC component, the C1s shifts about 0.45 and 0.33 eV on Au(111) and Ag(111), respectively, to lower binding energies from high to low coverage. Such energetic shifts of the core level binding energies are caused by final state screening effects of the photohole as for example the additional mirror charge screening. These energetic shifts are often in the range of 0.3 – 0.6 eV.³⁰⁻³³ The smaller shift on Ag(111) may indicate a different effect, which is opposite to final state screening effects. For further investigation we take a closer look on the relative shifts of the different C1s components (**Table 2**). The relative binding energies of the CC component show negligible shifts on the Au(111) substrate, while on Ag(111) the shifts are distinctly more by 0.16 – 0.19 eV for CN and CF to CC respectively. This indicates a different electronic redistribution on the interface. Besides the different shifts from high to low coverage this may also indicate a different interaction of the molecules at the interface to Au(111) and Ag(111). Shifts in the range of 0.23 eV of the CN component in respect to the CC component are often

observed for strong interacting phthalocyanine-substrate systems as for example FePcF₁₆ on Cu(111) or CoPcF₁₆ on Cu(110).^{26, 34}

Table 2: Relative binding energy shifts of C1s components from high to low coverage in eV.

| | CF to CC | CN to CC |
|----------------|----------|----------|
| Au(111) | 0.00 | -0.07 |
| Ag(111) | -0.19 | -0.23 |

To get more evidence about the participation of the macrocycle atoms on the interaction at the interface to both metal substrates, we take a closer look into the F1s and N1s core level spectra (**Figures 3+4**). Absolute binding energies and line widths of each component of the F1s and N1s core levels are summarized in **Table S3-5**. While for the F1s core level a peak fit with only one main component can be made, the main line of the N1s consists of two signals of the same intensity due to two chemically different nitrogen atoms in the molecule: The pyrrole and the bridging nitrogen atoms, denoted N1 and N2. They cannot be clearly resolved by XPS, since their energy separation is small, as shown for related phthalocyanines (0.3 - 0.5 eV).³⁵⁻⁴⁰

As for the C1s, the shift of the binding energy of the F1s and N1s core levels, going from high to low coverage, is stronger on Au(111) than on Ag(111). However, the shift of the F1s is 0.6 eV on Au(111) and just 0.12 eV on Ag(111), but the N1s shifts nearly by about the same amount (0.36 and 0.30 eV on Au(111) and Ag(111), respectively, indicated by the pyrrole component N1 in the N1s peak fit).

This also indicates a different participation of the atoms of the macrocycle on the redistribution of charge at the interface, not only on the different substrates, but also between the different atoms on both of the substrates. Besides the shifts, the F1s spectrum of the 0.4 nm coverage on Ag(111) reveals further information: On the low binding energy side occurs

an additional component at 683.88 eV with a relative ratio of 2.5 % of the whole peak. However, such an additional component at lower binding energy was also detected for FePcF₁₆ on TiO₂, interpreted as a formation of new bonds between the F-atoms and the substrate.⁴¹ As a consequence, a direct bonding between the phthalocyanine and the substrate or a new C-H bond might be formed, also explaining the lower CF ratio in the C1s peakfit (cf. **Figure 2b**). Another possible reason is a substrate induced decomposition, similar to perfluoro-pentacene on Ag and Cu substrates.⁴² As indicated by the striking differences in the C1s peak fits mentioned above, we fortify that CF bonds break at the interface. It seems that fluorine atoms partly bind to the Ag(111) surface, but may also trail off in the vacuum. This tentative claim is due to the variational number of fluorine atoms, which are bonded to Ag and which are absent in the CF component of the C1s.

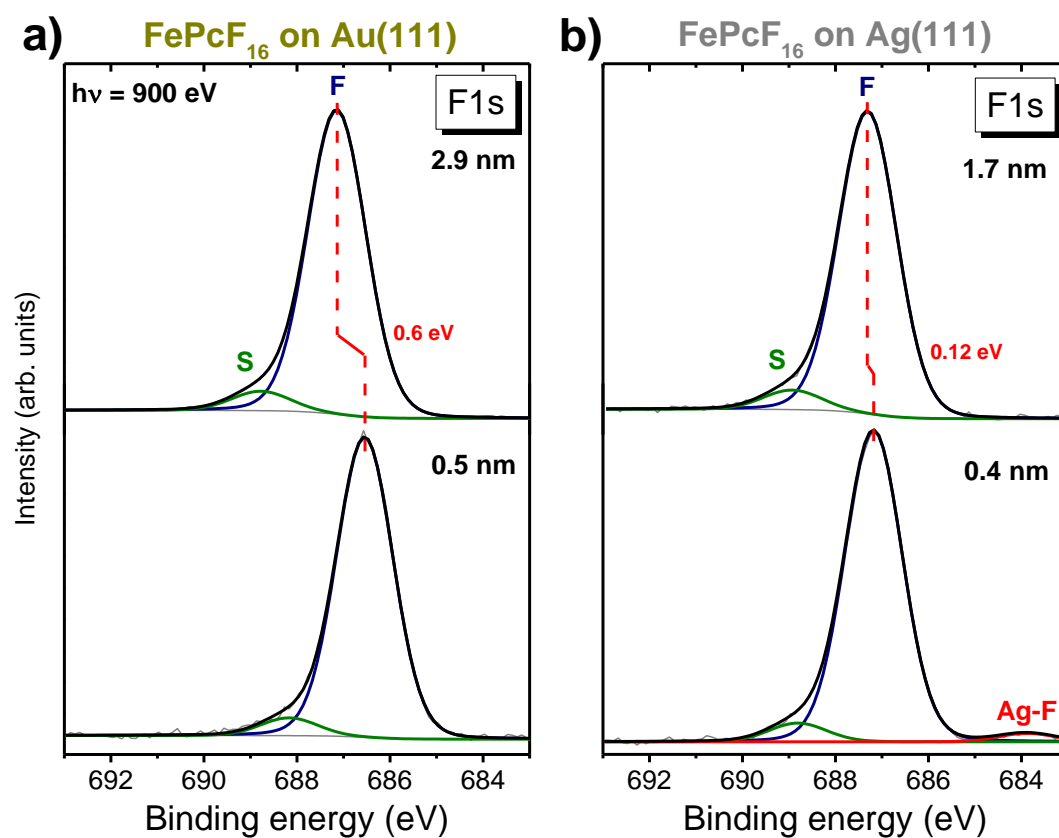


Figure 3. Thickness dependent $F1s$ core level spectra of $FePcF_{16}$ on a) $Au(111)$ and b) $Ag(111)$. Measured with an excitation energy of $h\nu = 900$ eV. The satellite feature is located at 1.63 eV higher binding energy than the main component F and can be explained by HOMO-LUMO transitions.⁶

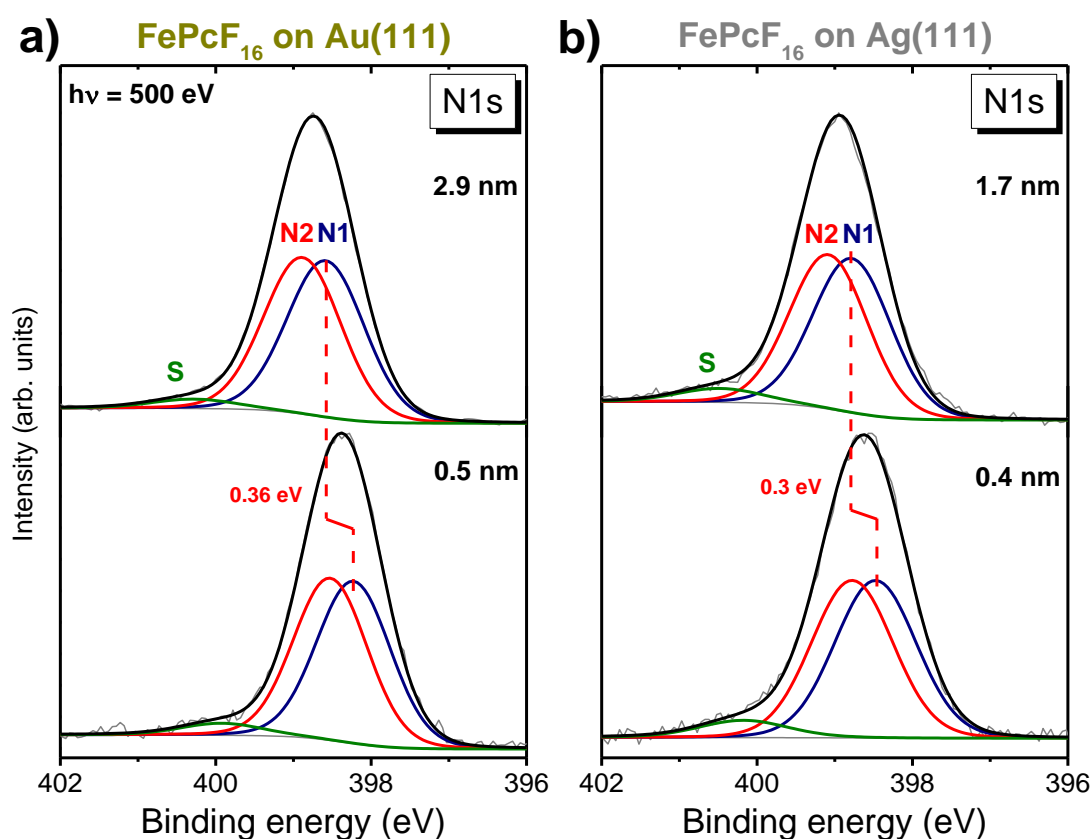


Figure 4. Thickness dependent $N1s$ core level spectra of $FePcF_{16}$ on a) $Au(111)$ and b) $Ag(111)$. Measured with an excitation energy of $h\nu = 500$ eV. The main line of the $N1s$ consists of two signals of the same intensity due to two chemically different nitrogen atoms in the molecule: The pyrrole and the bridging nitrogen atoms, denoted $N1$ and $N2$ and one additional satellite feature. Analogously to the $F1s$, this satellite feature is due to HOMO-LUMO transitions.⁶

There are no clear hints for interaction in the $N1s$ core level spectra (**Figure 4b**), and therefore, we also performed XAS measurements of the $N-K$ edge in dependence of the thickness at grazing incidence (**Figure 5**). As concluded from the angular (polarization) dependence of $N-K$

XA spectra at higher film thicknesses, the FePcF₁₆ molecules grow in a preferred flat lying adsorption geometry (see **Figure 1**). The features below 404 eV arise predominantly from transitions into π^* molecular orbitals. For phthalocyanines, most intense π^* resonances (denoted A) are assigned to transitions from N1s to LUMO e_g orbitals.¹⁹⁻²⁰ The more complex structure of feature A arises from an involvement of the ligand LUMO in the hybridization with the central metal atom of the Pc.^{19, 21-22, 26, 40, 43-45}

It was shown that π^* resonances in N-K edge absorption spectra are very sensitive to the involvement of nitrogen in the interfacial interactions.^{14, 41, 43, 46} Indeed, there is an obvious difference between the spectra recorded from the different substrate interfaces. While on Au(111) the π^* resonances exhibit very similar spectra for the thin film and 1 - 2 monolayer coverage (**Figure 5a**), they look distinctly different on Ag(111) (**Figure 5b**). The thin film spectrum on Ag(111) is very similar to the thin film on Au(111) and other thin films of related phthalocyanines.⁴⁶ However, the spectra from the 0.4 nm ultrathin film (monolayer range) exhibits striking differences to the former ones. Features A and B decrease drastically. A possible reason could be a partial filling of the corresponding orbitals at the interface in connection with the hybridization as a result of hybridization between wave functions of the nitrogen p-orbitals and d-orbitals of the central Fe atom of the phthalocyanine.^{21-22, 26, 40, 43, 45} This behavior indicates a strong involvement of the nitrogen atoms in the interaction at the interface.

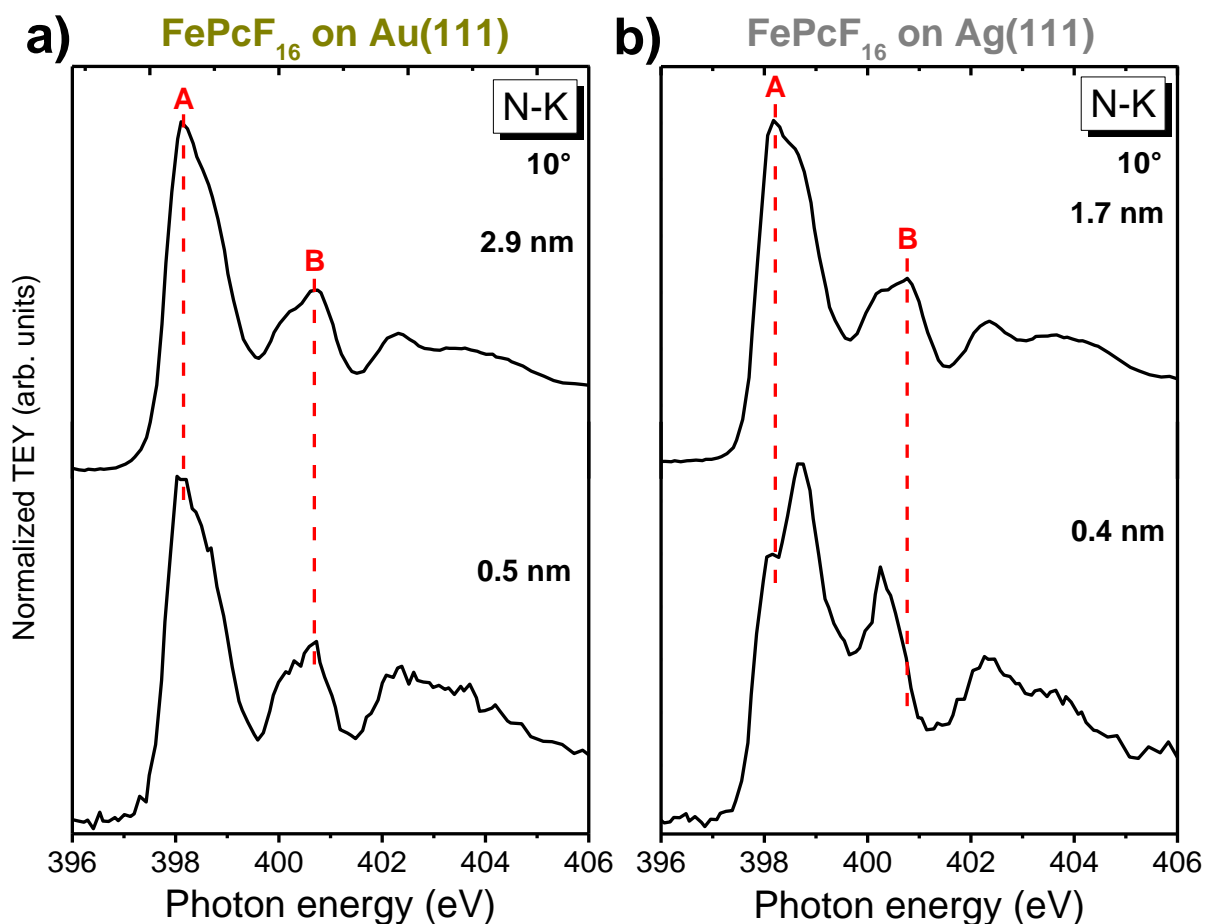


Figure 5. Closer look into the π^* resonances of the N-K edge of FePcF₁₆ on a) Au(111) and b) Ag(111) as a function of the thickness at grazing incidence (10°).

3.3. Involvement of the central iron atom at the interaction at the interface

Besides the macrocycle, also the central metal atom may interact with the substrate. In the case of transition metal phthalocyanines evidence for interaction with the substrate is delivered by the appearance of additional low binding energy peaks in the metal 2p core levels, which likely arise from charge transfer processes towards the central metal atom sites.^{26, 46-47} In order to obtain evidence about a possible charge transfer we examine the Fe2p spectra (**Figure 6**). On Au(111), the metal spectrum recorded from the thin film is dominated by a feature at 708.5 eV with a complex structure to higher binding energies. This structure arises from the complex multiplet structure of the Fe²⁺ ion. Additionally, a broad loss peak

related to the F1s appears at a binding energy of about 711 eV, which makes the background treatment even more difficult. The dominant feature at 0.5 nm coverage appears shifted by 0.5 eV to lower binding energy, which is in the range of the shifts of the core levels of the macrocycle and can be interpreted by final state screening effects of the photohole. At lower binding energies a shoulder is hardly visible. This could be due to interactions between the Au(111) substrate and the central metal atom as indicated for FePc.⁴⁸ We note that different adsorption sites are available on Au(111), where interactions with the organic molecules may vary in strength.⁴⁹

However, the Fe2p interface spectrum on Ag(111) looks different: A new feature at 706.8 eV dominates the spectrum. This feature is located at about 2 eV lower binding energy than for the thin film and can be assigned to reduced iron, as also detected for FePc on Ag(111).¹⁴ Thus, we also assume a charge transfer from the substrate to the central metal atom of the phthalocyanine.

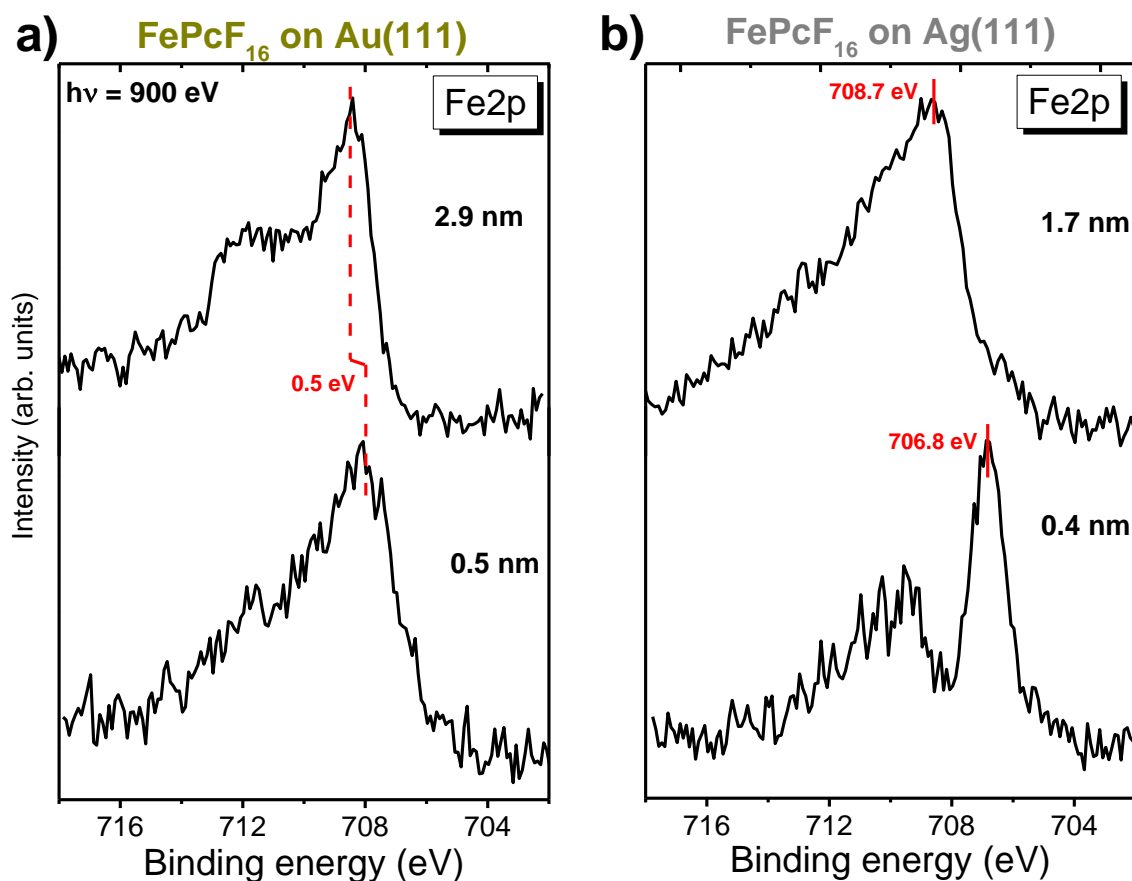


Figure 6. Thickness dependent Fe2p core level spectra of FePcF₁₆ on a) Au(111) and b) Ag(111). Measured with an excitation energy of $h\nu = 900$ eV.

XAS measurements of the Fe edge provide a great tool to obtain further information about the electronic structure of unoccupied states of the Fe ion. Fe-L₃ edge spectra at grazing and normal incidence as a function of the film thickness are shown in **Figure 7**. The angular dependence can be explained by the polarization influence on the intensities for transitions into different orbitals.⁵⁰ For the almost flat lying molecules (cf. discussion of the angular dependence of N-K XA spectra, **Figure 1**), transitions into orbitals with in-plane components ($d_{x^2-y^2}$ and d_{xy}) are strongest at normal incidence, while at grazing incidence transitions into orbitals with out-of-plane components (d_{xz} , d_{yz} , d_{z^2}) are most intense. For a detailed discussion of the spectral shape, see Refs.⁵⁰⁻⁵². The prominent features in the spectra recorded at grazing incidence are labeled "A" and represent out-of-plane transitions into a_{1g} and e_g orbitals, while the distinctly different features labeled "B" observed at normal incidence conditions represent

in-plane transitions, which are dominated by excitations into b_{1g} and b_{2g} orbitals, but also carry some weaker contributions related to other symmetries (**Figure 7**). Both multilayer film Fe- L_3 edge spectra measured on Ag(111) (**Figure 7b+d**) appear as expected for flat lying iron phthalocyanines, as for example FePcF₁₆ on MoS₂ or the related FePc on Ag(111).^{14, 53} Features A1 (grazing incidence) and B2 (normal incidence) clearly dominate the corresponding spectra. However, the Fe- L_3 edge spectra of the thin film on Au(111) exhibit notable differences. At grazing incidence, besides feature A1 a feature at higher photon energy becomes also prominent, which is assigned to B2 superimposed on A3 contributions. Further, the relative A1 intensity with respect to the edge jump is lower than for the thin film on Ag(111). This is apparently caused by the higher tilt angle of the FePcF₁₆ molecules in the investigated multilayer film on Au(111) compared to Ag(111) (cf. discussion of the tilt angle, **Figure 1**). In this case also features arising from in-plane transitions are enhanced at grazing incidence. However, the Fe- L_3 spectra representing 0.5 nm coverage of FePcF₁₆ on Au(111) are comparable to the FePcF₁₆ thin film spectra on Ag(111), which are due to flat lying molecules in these ultrathin films at the interface (cf. angle dependent N-K edge spectra, **Figure S1**). Comparing the Fe- L_3 edge absorption spectra for the interface sensitive 1-2 monolayer coverages in **Figure 7**, it becomes evident that the corresponding spectral shape depends distinctly on the substrate. On Ag(111) a new feature A0 dominates the spectrum at grazing incidence, while A1 disappears completely. Analogously to related systems,^{26, 46} feature A0 can be understood by an hybridization of Fe related and substrate related orbitals as a result of the chemisorption of FePcF₁₆ on the substrate surface. At normal incidence features B1 and B2 also disappear and two different features at 708.4 and 709.8 eV dominate the spectrum. To sum up, the data presented in **Figure 7b+d** clearly demonstrate that the d-orbitals related to feature A1 at grazing incidence and features B1 and B2 at normal incidence are involved in

the interaction between the central metal Fe atom of FePcF₁₆ and Ag(111). These features result from transitions into all 3d-orbitals, except the 3d_{xy}-orbital. For more information about the assignment of the orbitals we refer to the literature.²¹⁻²²

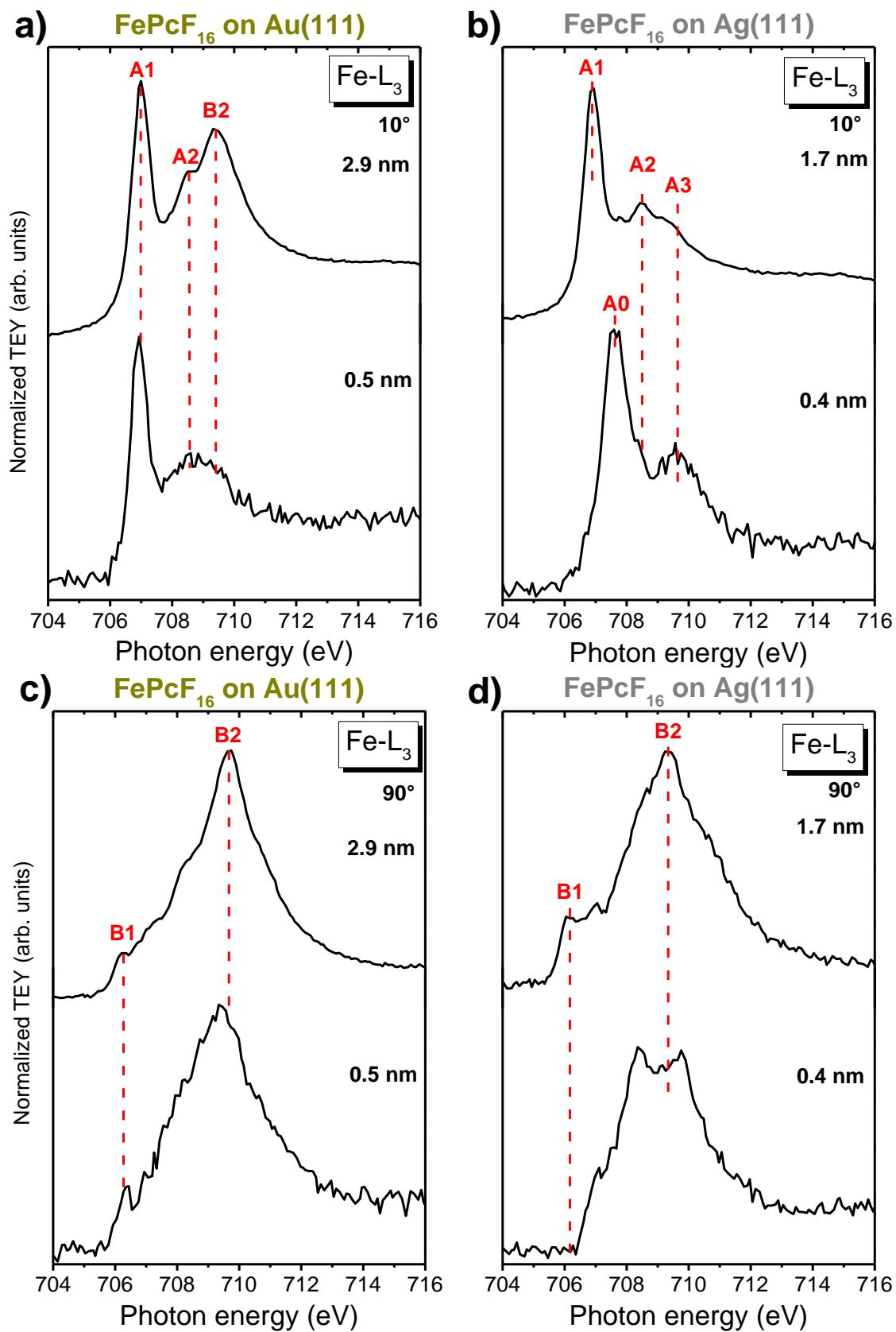


Figure 7. $\text{Fe } L_3$ edge spectra of FePcF_{16} on Au(111) (a+c) and Ag(111) (b+d) as a function of the thickness at grazing and normal incidence. The feature A0 at grazing incidence of FePcF_{16} on

Ag(111) (b) can be understood by a hybridization of Fe and substrate related orbitals at the interface.

In order to shed more light on the different interaction of FePcF₁₆ on both substrates, we performed valence band measurements at an excitation energy of 140 eV (**Figure 8**). At this photon energy, states with metal character are enhanced according to the corresponding photoelectron cross sections.⁹ For interpretation of the 1-2 ML coverage spectra it is important to compare the spectra to those of the clean substrate. Both substrates, Au(111) and Ag(111), show no features in the HOMO region (**Figure 8c+d**) at this energy. Thus, features in the 1-2 ML spectra can be assigned to FePcF₁₆.

In the spectra representing 1-2 ML coverage (**Figure 8a+b**) one dominant feature can be observed on each substrate (green and red arrow on Au(111) and Ag(111), respectively). On Au(111) this broad feature can be assigned to the interface HOMO of FePcF₁₆ with a typical binding energy of about 1 eV.⁵³ However, on Ag(111) a distinct feature appears at a binding energy of 0.4 eV. This feature can be assigned to the formation of an interface state, for example caused by a partial filling of the LUMO of the molecules as a consequence of the charge transfer,^{34, 54} or a formation of new states caused by hybridization between Fe d-orbitals and substrate related states, as proposed for related CoPcF₁₆/metal interfaces.^{34, 47, 55} Such an interface state is often observed for strongly interacting metal phthalocyanine/ metal systems, as for example FePc on Ag(111).¹⁴

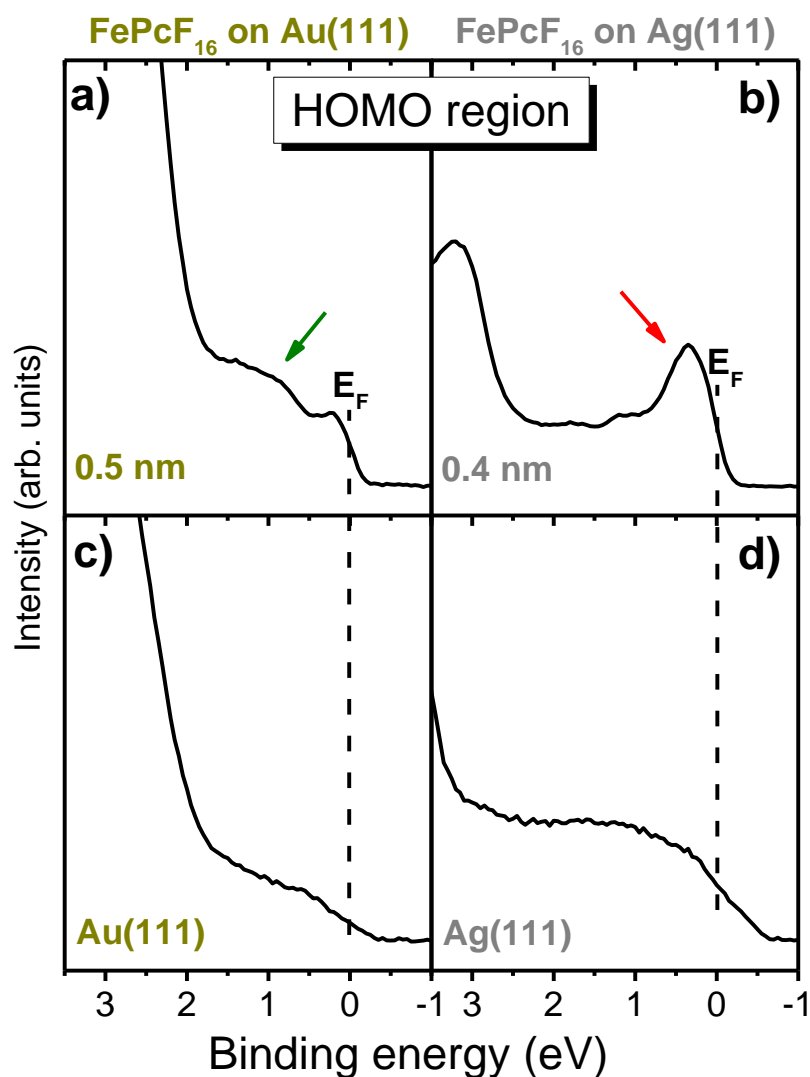


Figure 8. Zoom into the HOMO region of a) 0.5 nm FePcF₁₆ on Au(111) and b) 0.4 nm on Ag(111). For comparison the clean substrate is also shown: c) Au(111) and d) Ag(111). Measured with an excitation energy of $h\nu = 140$ eV at normal emission.

Resonant photoemission can show the contributions of different atomic species to electronic states in the valence band. We performed ResPES measurements with an excitation energy close the absorption threshold of the Fe 2p core level on a sample of 0.4 nm FePcF₁₆ on Ag(111) (**Figure 9**). Because of final state interference between direct photoemission from the 3d states and autoionization processes following the 2p \rightarrow 3d core excitation,⁵⁶ this experiment can show contributions of Fe-related states to the interface state. The y-axis

represents the excitation energy, while the x-axis represents the binding energy. On the color scale, blue represents the highest and brown the lowest intensity.

The fermi-edge at a binding energy of 0 eV is clearly visible. From XAS (**Figure 7**) excitation energies for Fe related resonant transitions are known and can be used for resonant excitation of the fermi region.

With an excitation energy between 707 and 709 eV, additional intensity is detected between binding energies of 0 and 2 eV. Additional intensity most notably right above the Fermi edge around 0.4 eV, is caused by resonant excitation and indicates Fe related states. The data clearly shows that the gap states (interface states) at the fermi edge possess distinct iron character and thus, these findings provide an additional hint for a strong interaction of the central metal atom on the interface to Ag(111). The relationship between gap states and the central iron atom was also determined for FePc on Ag(111).¹⁴

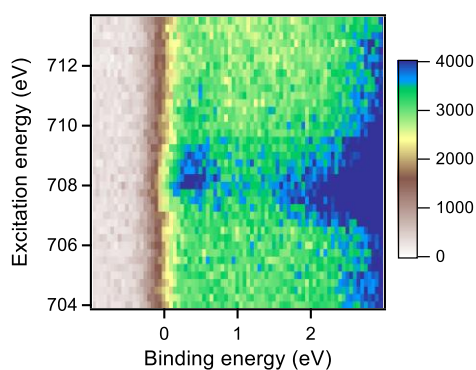


Figure 9. Resonant photoemission spectroscopy (ResPES) of a 0.4 nm layer FePcF₁₆ on Ag(111). It is possible to identify Fe related states by the right choice of the excitation energy known from XAS. The intensity of Fe related states can be indicated by the blue color. For excitation linearly polarized light with an angle of incidence of $\theta = 40^\circ$ was used.

Conclusions

We studied the electronic structure and orientation of thin films and 1-2 ML coverage of FePcF₁₆ on Au(111) and Ag(111). On both studied substrates, FePcF₁₆ grows in a preferred flat lying adsorption geometry. The interaction strengths at the FePcF₁₆/Au(111) and FePcF₁₆/Ag(111) interfaces however, are distinctly different. While the interaction between FePcF₁₆ and Au(111) is comparably weak, we report a strong interaction between FePcF₁₆ and Ag(111). At the interface to Ag(111), the electronic structure of both the FePcF₁₆ macrocycle and the central Fe atom is drastically changed. The alteration of the macrocycle electronic structure is shown by XPS core level shifts and changes in the N-K edge absorption spectra indicating charge transfer from the substrate to the macrocycle. From interface peaks in the Fe 2p core level and the L_{3,2} edge absorption spectra, we conclude that the electronic structure of the central Fe atom is changed at the interface to Ag(111) as well. The strong interaction is accompanied by the formation of gap states near the Fermi edge. ResPES studies reveal that these gap states are of partial Fe character. Our study shows that the choice of substrate has major effect on the electronic structure of the adsorbed FePcF₁₆ atoms.

Acknowledgements

We are grateful to the synchrotron light source KARA and to KNMF, both Karlsruhe, Germany, for the provision of beamtime.

ASSOCIATED CONTENT

Supporting Information

Absolute binding energies of the F1s and N1s peak fit components, Gaussian and Lorentzian widths of the C1s, F1s and N1s components, N1s X-ray absorption spectra of 0.5 nm FePcF₁₆ on Au(111) as a function of the incidence angle θ of the incoming synchrotron light.

References

1. Walzer, K.; Maennig, B.; Pfeiffer, M.; Leo, K., Highly Efficient Organic Devices Based on Electrically Doped Transport Layers. *Chem. Rev.* **2007**, *107*, 1233-1271.
2. Martinez-Diaz, M. V.; de la Torrea, G.; Torres, T., Lighting Porphyrins and Phthalocyanines for Molecular Photovoltaics. *Chem. Commun.* **2010**, *46*, 7090-7108.
3. Cinchetti, M.; Heimer, K.; Wustenberg, J. P.; Andreyev, O.; Bauer, M.; Lach, S.; Ziegler, C.; Gao, Y. L.; Aeschlimann, M., Determination of Spin Injection and Transport in a Ferromagnet/Organic Semiconductor Heterojunction by Two-Photon Photoemission. *Nat. Mater.* **2009**, *8*, 115-119.
4. Bogani, L.; Wernsdorfer, W., Molecular Spintronics Using Single-Molecule Magnets. *Nat. Mater.* **2008**, *7*, 179-186.
5. Peisert, H.; Knupfer, M.; Fink, J., Electronic Structure of Partially Fluorinated Copper Phthalocyanine (CuPcF₄) and Its Interface to Au(100). *Surf. Sci.* **2002**, *515*, 491-498.
6. Peisert, H.; Knupfer, M.; Schwieger, T.; Fuentes, G. G.; Olligs, D.; Fink, J.; Schmidt, T., Fluorination of Copper Phthalocyanines: Electronic Structure and Interface Properties. *J. Appl. Phys.* **2003**, *93*, 9683-9692.
7. Brinkmann, H.; Kelting, C.; Makarov, S.; Tsaryova, O.; Schnurpfeil, G.; Wohrle, D.; Schlettwein, D., Fluorinated Phthalocyanines as Molecular Semiconductor Thin Films. *Phys. Status Solidi A* **2008**, *205*, 409-420.
8. Ling, M. M.; Bao, Z. N., Copper Hexafluorophthalocyanine Field-Effect Transistors with Enhanced Mobility by Soft Contact Lamination. *Org. Electron.* **2006**, *7*, 568-575.
9. Yeh, J. J.; Lindau, I., Atomic Subshell Photoionization Cross Sections and Asymmetry Parameters: $1 \leq Z \leq 103$. *At. Data Nucl. Data Tables* **1985**, *32*, 1-155.
10. Peisert, H.; Biswas, I.; Knupfer, M.; Chassé, T., Orientation and Electronic Properties of Phthalocyanines on Polycrystalline Substrates. *Phys. Status Solidi B* **2009**, *246*, 1529-1545.
11. Kera, S.; Casu, M. B.; Bauchspiess, K. R.; Batchelor, D.; Schmidt, T.; Umbach, E., Growth Mode and Molecular Orientation of Phthalocyanine Molecules on Metal Single Crystal Substrates: A NEXAFS and XPS Study. *Surf. Sci.* **2006**, *600*, 1077-1084.
12. Okudaira, K. K.; Setoyama, H.; Yagi, H.; Mase, K.; Kera, S.; Kahn, A.; Ueno, N., Study of Excited States of Fluorinated Copper Phthalocyanine by Inner Shell Excitation. *J. Electron. Spectrosc. Relat. Phenom.* **2004**, *137*, 137-140.
13. Forrest, S. R., Ultrathin Organic Films Grown by Organic Molecular Beam Deposition and Related Techniques. *Chem. Rev.* **1997**, *97*, 1793-1896.
14. Petraki, F.; Peisert, H.; Aygul, U.; Latteyer, F.; Uihlein, J.; Vollmer, A.; Chassé, T., Electronic Structure of FePc and Interface Properties on Ag(111) and Au(100). *J. Phys. Chem. C* **2012**, *116*, 11110-11116.
15. Basova, T. V.; Kiselev, V. G.; Dubkov, I. S.; Latteyer, F.; Gromilov, S. A.; Peisert, H.; Chassé, T., Optical Spectroscopy and XRD Study of Molecular Orientation, Polymorphism, and Phase Transitions in Fluorinated Vanadyl Phthalocyanine Thin Films. *J. Phys. Chem. C* **2013**, *117*, 7097-7106.
16. Stöhr, J., *NEXAFS Spectroscopy*; Springer, 1992.

17. Rocco, M. L. M.; Frank, K. H.; Yannoulis, P.; Koch, E. E., Unoccupied Electronic Structure of Phthalocyanine Films. *J. Chem. Phys.* **1990**, *93*, 6859-6864.
18. Floreano, L.; Cossaro, A.; Gotter, R.; Verdini, A.; Bavdek, G.; Evangelista, F.; Ruocco, A.; Morgante, A.; Cvetko, D., Periodic Arrays of Cu-Phthalocyanine Chains on Au(110). *J. Phys. Chem. C* **2008**, *112*, 10794-10802.
19. Willey, T. M.; Bagge-Hansen, M.; Lee, J. R.; Call, R.; Landt, L.; van Buuren, T.; Colesniuc, C.; Monton, C.; Valmianski, I.; Schuller, I. K., Electronic Structure Differences between H₂, Fe-, Co-, and Cu-Phthalocyanine Highly Oriented Thin Films Observed Using NEXAFS Spectroscopy. *J. Chem. Phys.* **2013**, *139*, 034701.
20. Holland, B. N.; Peltekis, N.; Farrelly, T.; Wilks, R. G.; Gavrilu, G.; Zahn, D. R. T.; McGuinness, C.; McGovern, I. T., NEXAFS Studies of Copper Phthalocyanine on Ge(001)-2 × 1 and Ge(111)-(2 × 8) Surfaces. *Phys. Status Solidi A* **2009**, *246*, 1546-1551.
21. Betti, M. G.; Gargiani, P.; Frisenda, R.; Biagi, R.; Cossaro, A.; Verdini, A.; Floreano, L.; Mariani, C., Localized and Dispersive Electronic States at Ordered FePc and CoPc Chains on Au(110). *J. Phys. Chem. C* **2010**, *114*, 21638-21644.
22. Bartolomé, J.; Bartolomé, F.; Garcia, L. M.; Filoti, G.; Gredig, T.; Colesniuc, C. N.; Schuller, I. K.; Cezar, J. C., Highly Unquenched Orbital Moment in Textured Fe-Phthalocyanine Thin Films. *Phys. Rev. B* **2010**, *81*.
23. Petraki, F.; Peisert, H.; Uihlein, J.; Aygül, U.; Chassé, T., CoPc and CoPcF₁₆ on Gold: Site-Specific Charge-Transfer Processes. *Beilstein J. Nanotechnol.* **2014**, *5*, 524-531.
24. Lindner, S.; Treske, U.; Knupfer, M., The Complex Nature of Phthalocyanine/Gold Interfaces. *Appl. Surf. Sci.* **2013**, *267*, 62-65.
25. Huang, Y.; Wruss, E.; Egger, D.; Kera, S.; Ueno, N.; Saidi, W.; Bucko, T.; Wee, A.; Zojer, E., Understanding the Adsorption of CuPc and ZnPc on Noble Metal Surfaces by Combining Quantum-Mechanical Modelling and Photoelectron Spectroscopy. *Molecules* **2014**, *19*, 2969-2992.
26. Belser, A.; Karstens, R.; Nagel, P.; Merz, M.; Schuppler, S.; Chassé, T.; Peisert, H., Interaction Channels between Perfluorinated Iron Phthalocyanine and Cu(111). *Phys. Status Solidi B* **2019**, *256*, 1800292.
27. Jiang, H.; Ye, J.; Hu, P.; Wei, F.; Du, K.; Wang, N.; Ba, T.; Feng, S.; Kloc, C., Fluorination of Metal Phthalocyanines: Single-Crystal Growth, Efficient N-Channel Organic Field-Effect Transistors and Structure-Property Relationships. *Sci. Rep.* **2014**, *4*, 7573.
28. Biswas, I.; Peisert, H.; Zhang, L.; Chassé, T.; Knupfer, M.; Hanack, M.; Dini, D.; Schmidt, T.; Batchelor, D., Orientation of Differently Substituted Phthalocyanines: First Layers and Thin Films. *Mol. Cryst. Liq. Cryst.* **2006**, *455*, 241-249.
29. Glowatzki, H.; Heimel, G.; Vollmer, A.; Wong, S.; Huang, H.; Chen, W.; Wee, A.; Rabe, J.; Koch, N., Impact of Fluorination on Initial Growth and Stability of Pentacene on Cu (111). *J. Phys. Chem. C* **2012**, *116*, 7726-7734.
30. Peisert, H.; Knupfer, M.; Fink, J., Energy Level Alignment at Organic/Metal Interfaces: Dipole and Ionization Potential. *Appl. Phys. Lett.* **2002**, *81*, 2400-2402.
31. Vazquez, H.; Dappe, Y. J.; Ortega, J.; Flores, F., Energy Level Alignment at Metal/Organic Semiconductor Interfaces: "Pillow" Effect, Induced Density of Interface States, and Charge Neutrality Level. *J. Chem. Phys.* **2007**, *126*, 144703.
32. Betti, M. G.; Kanjilal, A.; Mariani, C.; Vázquez, H.; Dappe, Y. J.; Ortega, J.; Flores, F., Barrier Formation at Organic Interfaces in a Cu(100)-Benzenethiolate-Pentacene Heterostructure. *Phys. Rev. Lett.* **2008**, *100*, 027601.
33. Yamane, H.; Yoshimura, D.; Kawabe, E.; Sumii, R.; Kanai, K.; Ouchi, Y.; Ueno, N.; Seki, K., Electronic Structure at Highly Ordered Organic/Metal Interfaces: Pentacene on Cu(110). *Phys. Rev. B* **2007**, *76*, 165436.
34. Belser, A., et al., Perfluorinated Phthalocyanines on Cu(110) and Cu(110)-(2 × 1)O: The Special Role of the Central Cobalt Atom. *J. Phys. Chem. C* **2021**.

35. Evangelista, F.; Ruocco, A.; Gotter, R.; Cossaro, A.; Floreano, L.; Morgante, A.; Crispoldi, F.; Betti, M. G.; Mariani, C., Electronic States of CuPc Chains on the Au(110) Surface. *J. Chem. Phys.* **2009**, *131*, 174710.
36. Papageorgiou, N.; Ferro, Y.; Salomon, E.; Allouche, A.; Layet, J. M.; Giovanelli, L.; Le Lay, G., Geometry and Electronic Structure of Lead Phthalocyanine: Quantum Calculations Via Density-Functional Theory and Photoemission Measurements. *Phys. Rev. B* **2003**, *68*, 235105.
37. Papageorgiou, N.; Salomon, E.; Angot, T.; Layet, J.-M.; Giovanelli, L.; Lay, G. L., Physics of Ultra-Thin Phthalocyanine Films on Semiconductors. *Prog. Surf. Sci.* **2004**, *77*, 139-170.
38. Schmid, M.; Kaftan, A.; Steinrueck, H. P.; Gottfried, J. M., The Electronic Structure of Cobalt(II) Phthalocyanine Adsorbed on Ag(111). *Surf. Sci.* **2012**, *606*, 945-949.
39. Maslyuk, V. V.; Aristov, V. Y.; Molodtsova, O. V.; Vyalykh, D. V.; Zhilin, V. M.; Ossipyan, Y. A.; Bredow, T.; Mertig, I.; Knupfer, M., The Electronic Structure of Cobalt Phthalocyanine. *Appl. Phys. A* **2009**, *94*, 485-489.
40. Åhlund, J.; Nilson, K.; Schiessling, J.; Kjeldgaard, L.; Berner, S.; Mårtensson, N.; Puglia, C.; Brena, B.; Nyberg, M.; Luo, Y., The Electronic Structure of Iron Phthalocyanine Probed by Photoelectron and X-Ray Absorption Spectroscopies and Density Functional Theory Calculations. *J. Chem. Phys.* **2006**, *125*, 034709.
41. Karstens, R.; Glaser, M.; Belser, A.; Balle, D.; Polek, M.; Ovsyannikov, R.; Giangrisostomi, E.; Chassé, T.; Peisert, H., FePc and FePcF₁₆ on Rutile TiO₂(110) and (100): Influence of the Substrate Preparation on the Interaction Strength. *Molecules* **2019**, *24*, 4579.
42. Schmidt, C.; Breuer, T.; Wippermann, S.; Schmidt, W. G.; Witte, G., Substrate Induced Thermal Decomposition of Perfluoro-Pentacene Thin Films on the Coinage Metals. *J. Phys. Chem. C* **2012**, *116*, 24098-24106.
43. Petraki, F.; Peisert, H.; Hoffmann, P.; Uihlein, J.; Knupfer, M.; Chassé, T., Modification of the 3d-Electronic Configuration of Manganese Phthalocyanine at the Interface to Gold. *J. Phys. Chem. C* **2012**, *116*, 5121-5127.
44. Kuz'min, M. D.; Hayn, R.; Oison, V., Ab Initio Calculated XANES and XMCD Spectra of Fe(II) Phthalocyanine. *Phys. Rev. B* **2009**, *79*, 024413.
45. Javaid, S., et al., Impact on Interface Spin Polarization of Molecular Bonding to Metallic Surfaces. *Phys. Rev. Lett.* **2010**, *105*, 077201.
46. Peisert, H.; Uihlein, J.; Petraki, F.; Chassé, T., Charge Transfer between Transition Metal Phthalocyanines and Metal Substrates: The Role of the Transition Metal. *J. Electron. Spectrosc. Relat. Phenom.* **2015**, *204*, 49-60.
47. Lindner, S.; Treske, U.; Grobosch, M.; Knupfer, M., Charge Transfer at F16CoPc and CoPc Interfaces to Au. *Appl. Phys. A* **2011**, *105*, 921-925.
48. Schmid, M.; Zirlmeier, J.; Steinrück, H.-P.; Gottfried, J. M., Interfacial Interactions of Iron(II) Tetrapyrrole Complexes on Au(111). *J. Phys. Chem. C* **2011**, *115*, 17028-17035.
49. Pawlak, R., et al., Design and Characterization of an Electrically Powered Single Molecule on Gold. *ACS Nano* **2017**, *11*, 9930-9940.
50. Fernández-Rodríguez, J.; Toby, B.; van Veenendaal, M., Mixed Configuration Ground State in Iron(II) Phthalocyanine. *Phys. Rev. B* **2015**, *91*, 214427.
51. Balle, D.; Adler, H.; Grüninger, P.; Karstens, R.; Ovsyannikov, R.; Giangrisostomi, E.; Chassé, T.; Peisert, H., Influence of the Fluorination of CoPc on the Interfacial Electronic Structure of the Coordinated Metal Ion. *J. Phys. Chem. C* **2017**, *121*, 18564-18574.
52. Lindner, S.; Mahns, B.; Treske, U.; Vilkov, O.; Haidu, F.; Fronk, M.; Zahn, D. R. T.; Knupfer, M., Epitaxial Growth and Electronic Properties of Well Ordered Phthalocyanine Heterojunctions MnPc/F16CoPc. *J. Chem. Phys.* **2014**, *141*, 4.
53. Greulich, K., et al., Charge Transfer from Organic Molecules to Molybdenum Disulfide: Influence of the Fluorination of Iron Phthalocyanine. *J. Phys. Chem. C* **2020**, *124*, 16990-16999.
54. Schwieger, T.; Peisert, H.; Knupfer, M., Direct Observation of Interfacial Charge Transfer from Silver to Organic Semiconductors. *Chem. Phys. Lett.* **2004**, *384*, 197-202.

55. Ruckerl, F.; Waas, D.; Buchner, B.; Knupfer, M., Particular Electronic Properties of F16CoPc: A Decent Electron Acceptor Material. *J. Electron. Spectrosc. Relat. Phenom.* **2017**, *215*, 1-7.
56. Magnan, H.; Le Fèvre, P.; Chandesris, D.; Krüger, P.; Bourgeois, S.; Domenichini, B.; Verdini, A.; Floreano, L.; Morgante, A., Resonant Photoelectron and Photoelectron Diffraction across the Fe L₃ Edge of Fe₃O₄. *Phys. Rev. B* **2010**, *81*, 085121.

Influence of BN-doping of Nanographene Molecules on the Interaction at Different Metal Interfaces

Axel Belser,[†] Katharina Greulich,[†] Peter Grüninger,^{†#} Marie Sophie Sättele,^{†#} Michael Fingerle,[#] Holger F. Bettinger,^{#‡} Thomas Chassé,^{†‡} and Heiko Peisert^{†}*

[†]Institute of Physical and Theoretical Chemistry, University of Tübingen, Auf der Morgenstelle 18, 72076 Tübingen, Germany

[#] Institute of Organic Chemistry, University of Tübingen, Auf der Morgenstelle 18, 72076 Tübingen, Germany

[‡] Center for Light-Matter Interaction, Sensors & Analytics (LISA⁺) at the University of Tübingen, Auf der Morgenstelle 18, 72076 Tübingen, Germany

* Corresponding author, heiko.peisert@uni-tuebingen.de, Tel.: (+49) 07071 / 29-76931, Fax: (+49) 07071 / 29-5490

Abstract

BN-substituted nanographene molecules are currently in focus of interest because the substitution of C-C units by isoelectronic and isosteric BN-units is a straightforward way of changing electronic properties of nanographenes. The substitution strongly influences the usage of the molecules in electronic devices. Interactions at the interface between the organic molecules and possible metal electrode materials influence the possible use for applications. Thus, we investigated interface properties of the prominent nanographene Hexa-*peri*-hexabenzocoronene (HBC) and the parent BN doped B₃N₃-hexa-*peri*-hexabenzocoronene (BN-HBC) and B₃N₃-hexabenzotriphenylen (BN-HBP) mainly by means of photoelectron spectroscopy (PES). The substitution of the inner benzene ring of HBC by a borazine core (resulting in BN-HBC) changes the nature of interaction strongly, but also the loss of planarity (resulting in BN-HBP) reveals distinct changes of the interface properties.

Keywords

Hexa-*peri*-hexabenzocoronene, BN doped hexa-*peri*-hexabenzocoronene, BN doped hexabenzotriphenylene, interaction, photoemission, scanning tunneling microscopy, planarity, π -conjugated systems, reactive surfaces

Introduction

In the last decade, the research interest in polycyclic aromatic hydrocarbons (PAHs) grows very fast, supported mainly by the experimental accessibility of graphene.¹ PAHs are also called “nanographenes” and can be regarded as the starting point for a bottom-up approach for the graphene synthesis.²⁻⁵ The bottom-up synthesis allows access to monodisperse nanographenes with defined structures and properties, whereas top-down approaches cannot control the resulting structure or size distribution of the nanographenes.⁶⁻⁷ One prominent representative of the class of nanographenes is hexa-*peri*-hexabenzocoronene (HBC, **Figure 1**), a planar molecule that exhibits magnificent electronic properties, such as a very high charge carrier mobility.⁸⁻⁹ Because of the magnificent electronic properties, HBC has been studied intensely for possible applications in electronic devices.^{8, 10-16} A well-known path to modify the electronic characteristics of nanographenes is the substitution of C-C units by isosteric and isoelectronic B-N units.¹⁷⁻²² Actually it was possible to incorporate a borazine core (B₃N₃) in the center of HBC (BN-HBC, **Figure 1**) in an atom-precise manner.²³ Borazine doping results in a tuning of the band gap in the same energy range as of carbon-doped hexagonal boron nitride (h-BN).²⁴ This agrees with the increasing HOMO-LUMO gap of borazine substituted aromatic rings in nanographenes.²⁵⁻²⁶ For BN-HBC and his parent molecule HBC, the substitution specifically changes the nature of the lowest unoccupied molecular orbital (LUMO).²⁷⁻²⁸ In the last four years, the first experiments to identify the electronic structure, the adsorption geometry, film morphology and interaction of BN-HBC at Au(111) surfaces were realised successfully.^{24, 28-29}

Besides the substitution of benzene by a borazine unit, it is also possible to modify the surrounding π -conjugated carbon system. B_3N_3 -hexabenzotriphenylene (BN-HBP, **Figure 1**) has got three CC-bonds less compared to BN-HBC, what results in a propeller-like structure and the loss of the planar structure. With the loss of the planarity, the molecules are not anymore flat lying on the Au(111) surface.²⁹ This observation results in a different adsorption geometry, film morphology and electronic structure.

In our research we investigate if the substitution of benzene by a borazine ring results in a different interaction strength at the interface to metal substrates. For this we choose metal substrates with different reactivities ($Au(111) < Cu(111) < Ni(111)$). Furthermore, we investigate if there is a change in reactivity when modifying the number of CC-bonds in the π -conjugated carbon system (BN-HBC vs. BN-HBP).

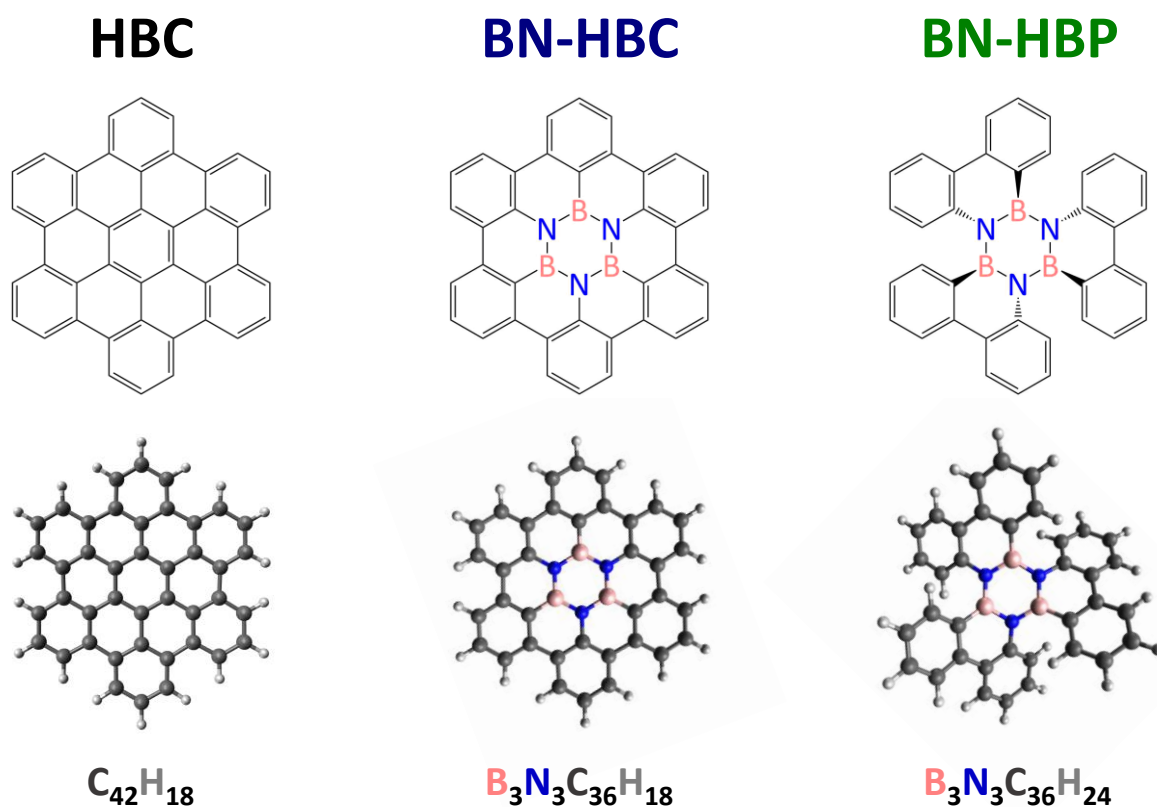


Figure 1. Chemical structure (top) and geometric structure as obtained from DFT (bottom) of hexa-peri-hexabenzocoronene (HBC), B_3N_3 -doped hexa-peri-hexabenzocoronene (BN-HBC) and the propeller-like B_3N_3 -hexabenzotriphenylene (BN-HBP) (carbon atoms are dark grey, hydrogen light grey, nitrogen blue and boron red). HBC and BN-HBC are planar molecules, while BN-HBP is nonplanar due to steric hindrance.

Methods and Experimental

The Au(111) single crystal was cleaned by several cycles of Ar^+ -ion sputtering with 0.8 kV for 30 min at an argon partial pressure of $5 \cdot 10^{-5}$ mbar and subsequent annealing for 30 min at a temperature of 770 K. The orientation and cleanliness were checked by LEED, XPS, UPS and STM.

The molecules were evaporated at rates of about 0.2 – 0.4 nm/min by a Knudsen-cell with a temperature-controlled crucible. The rates were estimated by a quartz microbalance. During evaporation, the crystal was held at room temperature. Film thickness was determined by the XPS intensity ratios assuming layer-by-layer growth and using sensitivity factors from Yeh and Lindau.³⁰ HBC, BN-HBC and BN-HBP were synthesized in the organic chemistry labs of Tübingen university. Photoemission (PES) measurements were performed in our home laboratory in a multi-chamber UHV system equipped with a Phoibos 150 Hemispherical Energy Analyzer (SPECS) and an X-ray source with monochromator (XR 50 M, SPECS). The base-pressure was $2 \cdot 10^{-10}$ mbar and the excitation energies were 1486.6 eV and 40.8 eV for XPS and UPS, respectively. The binding energy was calibrated with respect to the Au4f_{7/2} (84.00 eV) and the Cu2p_{3/2} (932.56 eV) peak positions. Peak fitting of XPS spectra was performed using the program Unifit.³¹ A Shirley model background and a Voigt profiles (convolution of Gaussian and Lorentzian peaks) were used for the peak fitting procedure of the core levels. The error of absolute binding energies is estimated to be less than ± 0.05 eV.

The STM measurements were performed in a two-chamber system equipped with a variable temperature (VT)-STM from Omicron GmbH and a LEED/AES spectrometer from OCI Vacuum Microengineering Inc. Mechanically cut Pt/Ir tips were used for the STM measurements. Sample and tip were held at room temperature and all given tunneling voltages are given with respect to the sample. For the shown STM images, the WSxM program was used to improve the image contrast and apply light filtering.³²

Results and Discussion

Electronic structure of thin films

For a detailed study of the interfaces of the investigated molecules (**Figure 1**) to metallic substrates, a look into the bulk electronic structure is indispensable. In thin films, influence of the substrate on the peak shape can be neglected. XP core level spectra of thin films of HBC, BN-HBC and BN-HBP are shown in **Figure 2**. Binding energies of the core levels and the different peak fit components are summarized in **Table 1**, additional data (Gaussian + Lorentzian widths) can be found in **Table S1+2** (supporting information).

HBC consists of two different kinds of carbon atoms: carbon in the inside, which is bonded just to other carbon (CC) and the carbons at the outside, which are bonded also to hydrogen (CH) (**Figure 1a**). This kind of separation results in a stoichiometric ratio of 24:18 (CC:CH), which was adopted for the peak fit. The respective C1s peak fit matches very well to the experimental data (**Figure 2a**). The two components are separated by 0.27 eV. In agreement with the literature on graphene nanoribbons³³ and related acenes³⁴⁻³⁵ the CH component appears at a lower binding energy compared to CC.

Through the exchange of the inner benzene (C₆) with a borazine ring (B₃N₃) (BN-HBC), two additional carbon components have to be considered: carbon bonded to nitrogen (CN) and carbon bonded to boron (CB). Further, calculations showed that the binding energy of CC carbons in proximity to nitrogen (CCN) is somewhat lower compared to CC carbons in proximity to boron (CCB).²⁹ Consequently, for BN-HBC the stoichiometric ratio of the involved carbon components results in 18:6:6:3:3 (CH:CCN:CCB:CN:CB). Besides the exchange of the inner core, a breaking of

three C-C bonds in the outer carbon systems results in the propeller-like BN-HBP with a stoichiometric ratio of 24:3:3:3:3 (CH:CCN:CCB:CN:CB). The CC-CH separation in both BN molecules is larger compared to the parent HBC. Thus, the exchange of the inner benzene by a borazine ring causes a different electronic structure for all carbon atoms. The N1s and B1s spectra (**Figure 2b+c**) can be described by a single component for both BN-HBC and BN-HBP molecules. The similarity of the spectra may be related to the rather similar chemical environments of the N and B atoms in both molecules. For more detailed analysis of thin films of BN-HBC and BN-HBP we refer to reference ²⁹.

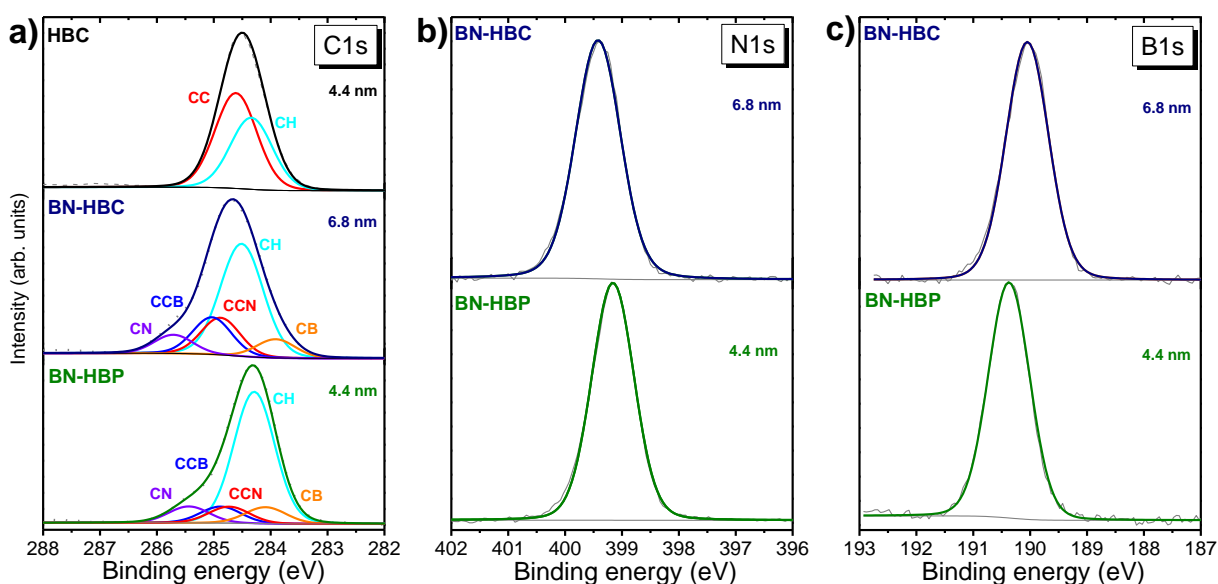


Figure 2. Core level spectra of thin films of HBC, BN-HBC and BN-HBP on Au(111): a) C1s, b) N1s and c) B1s. Peak fit data of the different components and sum curves have been added to the experimental data.

Table 1. Absolute core level binding energies of the thin films of HBC, BN-HBC and BN-HBP shown in Figure 2 in eV.

| | | C1s | | | | | |
|--------|--------|--------|--------|--------|--------|--------|--------|
| | | CC | CH | | | | |
| HBC | | 284.61 | 284.34 | | | | |
| | CN | CCB | CCN | CH | CB | N1s | B1s |
| BN-HBC | 285.71 | 285.03 | 284.88 | 284.51 | 283.91 | 398.92 | 189.60 |
| BN-HBP | 285.44 | 284.88 | 284.73 | 284.29 | 284.09 | 398.75 | 190.00 |

Electronic structure of HBC on various reactive metal interfaces

For the possible application of HBC in electronic devices, the interface characteristics of possible electrode materials are of enormous importance. If physisorption is the main adsorption process on the interface of the substrate and the organic molecules, no or just weak changes in the peak shape between the thin film and the monolayer (ML) can be expected.^{28, 36-39} However, if chemisorption processes dominate the interface, the peak shape of the core levels may change drastically, indicated by additional components and/or strong binding energy shifts of individual components.⁴⁰⁻⁴⁶ Therefore, we investigated 1-2 monolayer (ML) coverage of HBC on Au(111), Cu(111) and Ni(111) using C1s core level photoemission (**Figure 3**). For a detailed study, exemplary peak fits were performed. Additional information is summarized in **Figure S1** (C1s series of different film thicknesses on all three metal substrates) and **Table S3-S5** (binding energies of each peak fit component + Gaussian and Lorentzian widths) in the supporting information. The observed energetic shifts of the monolayer peaks to lower binding energies with respect to the thin films for HBC on all three substrates can be ascribed to additional screening of the photohole at the interface to the metal, mostly due to mirror charges (**Figure S1 + Table**

S3). For many organic-metal interfaces effects of the same magnitude were observed.⁴⁷⁻⁵⁰ Nevertheless, the shifts in binding energy are of different amount on the different substrates, which may be caused by different kinds of interaction at the interfaces. In principle, the 1-2 ML films on Au(111) and Cu(111) can be described similarly as the related thin films, only two components are required to fit the experimental data. On Au(111) Gaussian widths are somewhat lower (0.1 eV) than in the thin film, while on Cu(111) Gaussian widths are slightly higher (0.02 eV). This may be caused by slightly different strength of interaction comparing both substrates and a resultant slight redistribution of charge at the interfaces, but nevertheless, the interaction of HBC on both substrates is apparently weak.

Compared to Au(111) and Cu(111), the 1-2 ML C1s spectrum on Ni(111) looks distinctly different to the related thin film spectrum. The peak shape changes drastically. At the low binding energy side, additional intensity arises. Two new interface features (IF1 and IF2) located at 284.26 and 283.51 eV must be introduced compared to the thin film to match the experimental data. These two features can be ascribed to smaller fragments of HBC and Nickel carbide (NiC) formed at the interface.⁵¹ In addition, the ratio of CC/CH changes also distinctly: In the thin film it is 24 - 18 (stoichiometric), but at the interface 24 - 13.9. From the additional interface components and the distinct change of the CC/CH ratio, we conclude a very strong interaction, that implicates a breaking of the bonds in the HBC molecules to form smaller fragments and NiC-species on the surface. It was reported that organic molecules can underlie a fragmentation at strongly reactive interfaces.^{45, 52-53} In addition, the peak shape is asymmetric to the higher binding energy side, which reminds of graphene on Ni(111).^{45, 54} Thus, we used an additional asymmetry parameter of 0.14 for the C1s components, which is in good agreement to graphene on Ni(111).⁵⁵⁻⁵⁶

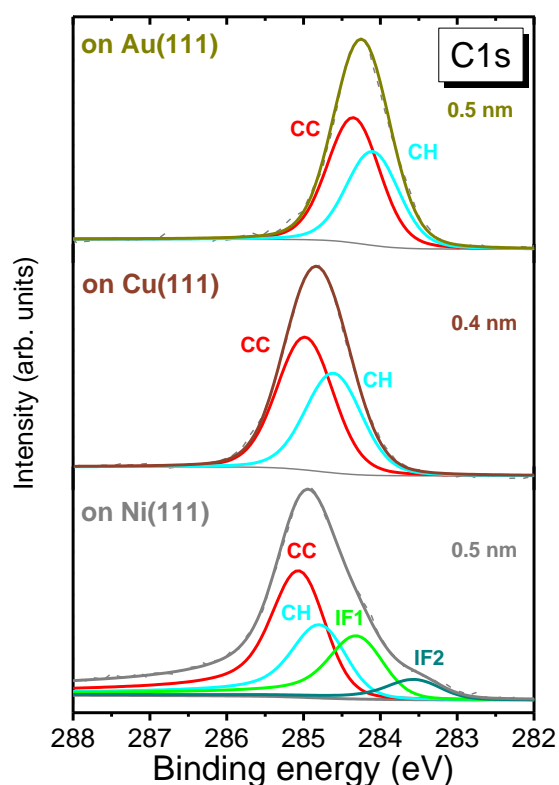


Figure 3. Core level spectra of 1-2 monolayer coverage HBC on Au(111) (top panel), Cu(111) (middle panel) and Ni(111) (bottom panel). HBC consists of two different kinds of carbon atoms: carbon in the inside, which is bonded just to other carbon (CC) and the carbons at the outside, which are bonded also to hydrogen (CH). In addition two interface components were added for the ML on Ni(111), which are described in the text.

For further investigation, a submonolayer of HBC on Ni(111) was prepared and investigated using STM (**Figure 4**). Most of the HBC molecules are clearly separated and can be made out as single molecules (**Figure 4a**). Adsorbed molecules with less neighbours and thus more free space around them are much larger (2.15 nm) than the expected value of about 1.46 ± 0.01 nm (**Figure 4b**), that was reported on Au(111) for monolayer coverage.^{28, 57-58} The apparent height of the molecules in respect to the Ni(111) surface is determined as 0.2 nm. That indicates a short

bond distance and a strong interaction between the molecules and the Ni(111)⁵⁹ and is a comparable value to graphene on Ni(111).⁶⁰ We note, STM measurements include a complex interplay between the STM tip, the substrate and the electronic structure of the molecule. Molecular levels can get mixed, broadened or shifted because of the interaction with the substrate.⁶¹ Ni(111) is a very strongly reactive surface and thus the electron densities of the HBC molecules and the substrate may overlap and the molecules appear broader. We may also recognize several molecules on the surface, which apparently show no clear separation to direct neighbour molecules, which show no separation between each other (**Figure 4c**). Hence, the electron densities are also overlapping, perhaps due to the fragmentation of the HBC molecules and new formed bonds, according to the C1s core level. Previously it was shown that nanographene molecules like pentacene can form graphene sheets on Ni(111) after annealing. However, this did not happen without annealing at room temperature deposition conditions.⁶²

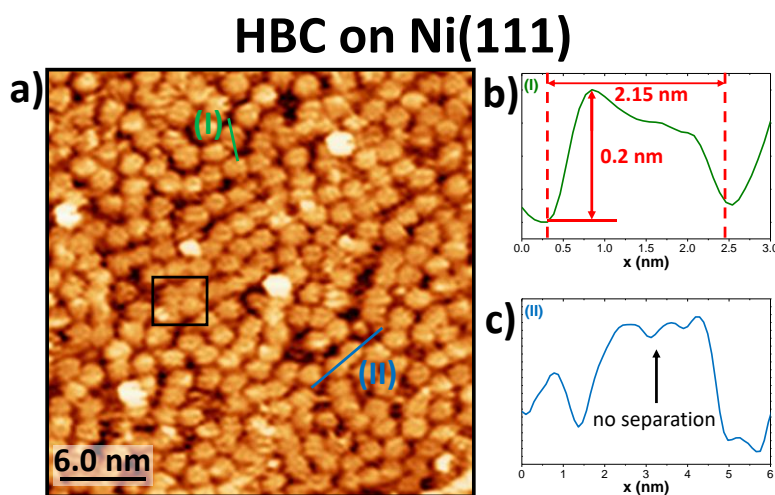


Figure 4. a) STM image of HBC on Ni(111) in submonolayer coverage (0.8 ML) ($U = -1.0$ V, $I = 500$ pA). b) Line profile of a single molecule (I). c) Line profile of two molecules with no separation in between (II).

Electronic structure of BN-HBC on various reactive metal interfaces

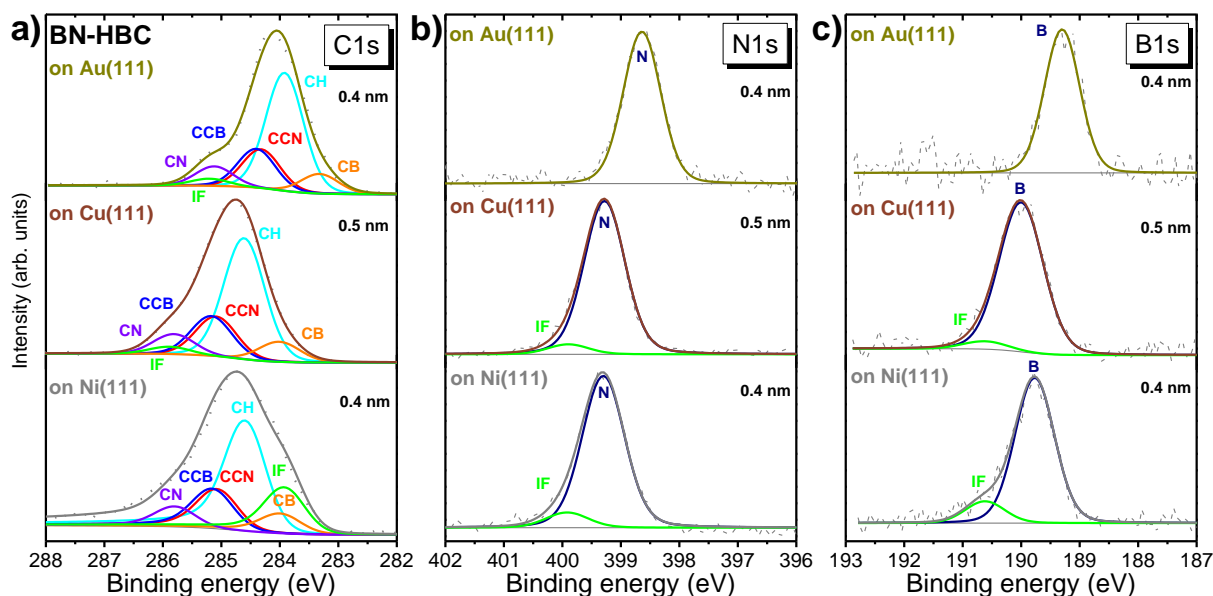


Figure 5. Core level spectra of 1-2 monolayer coverage BN-HBC on Au(111) (top panel), Cu(111) (middle panel) and Ni(111) (bottom panel): a) C1s, b) N1s and c) B1s. BN-HBC consists of five different kinds of carbon atoms: carbon bonded to hydrogen (CH), bonded to boron (CB), bonded to nitrogen (CN) and carbon bonded to carbon in proximity to nitrogen (CCN) and to boron (CCB). All N and B atoms are in the same chemical environment. In addition, interface components were added, which are described in the text.

To investigate the interface characteristics of the B_3N_3 doped nanographene molecule BN-HBC, we performed XPS measurements of ultrathin films of 1-2 ML coverage on various reactive metal substrates (**Figure 5**). Additional data can be reviewed in **Figure S2-S4** (thickness dependent core level series) and **Table S6-S8** (absolute binding energies, Gaussian and Lorentzian widths). From the thickness dependent core level series of C1s (indicated by CH), N1s and B1s (**Figure S2-S4**) a shift to lower binding energy from high to low coverage can be extracted and illustrated (**Figure**

6). Analogously to HBC, the shifts can be essentially ascribed to a screening of the photohole at the interface to the metal due to mirror charges. Obviously, the core level shifts are of different amount on substrates exhibiting different reactivities (**Figure 6**). Except the B1s core level shift on Ni(111), the shifts on the more reactive substrates Cu(111) and Ni(111) are smaller compared to Au(111). This is evidence for differences in the interaction at the interface between BN-HBC and the metal substrates comparing the less reactive substrate Au(111) with the more reactive substrates Cu(111) and Ni(111).

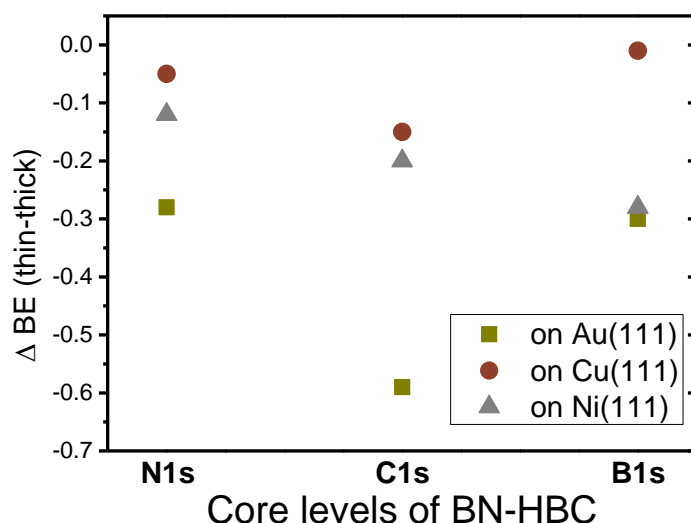


Figure 6. Difference in binding energies between the thin films and the ultrathin films of 1-2 ML coverage for BN-HBC on Au, Cu and Ni(111) in eV. The shift of the C1s is indicated by the CH component.

For a more detailed analysis of the interaction at the interface between BN-HBC and the different metal substrates we performed a detailed peak fit analysis of the ultrathin films of 1-2 ML coverage (**Figure 5**). Analogously to the thin film on Au(111), the N1s and B1s core levels can be fitted by one component (**Figure 5b+c**). For the C1s core level a small additional component to

the higher binding energy side must be used to fit the experimental data (**Figure 5a**). However, on Cu(111) we had to take into account an additional component at the higher binding energy side to fit the experimental data for each core level appropriately (middle panel in **Figure 5a-c**). On Ni(111) a distinctly stronger change in the peak shape of the ultrathin film of 1-2 ML coverage, compared to the thin film, (**Figure S2-S4**) can be made out. For the N1s and B1s core level one additional component at the higher binding energy side is enough to fit the experimental data. However, to model the experimental data of the C1s core level an additional component to the lower binding energy side (283.89 eV) and an asymmetry parameter of 0.1 was used for all components.

The small additional components at the higher binding energy side at different metal substrates may be interpreted by molecules adsorbed at more reactive sites, like vacancies or steps as observed for other organic-metal systems.⁶³ The additional component to the lower binding energy side on Ni(111) can be related to partial fragmentation and the asymmetric peak shape also reminds on graphene like peak shapes as discussed for HBC. All in all it is obvious that the strength of interaction of BN-HBC at the interface increases in the row Au(111) < Cu(111) < Ni(111). This is consistent with previous investigations of organic molecules on different metal substrates as for example PTCDA on Au(111) and Cu(111), where physisorption is suggested for PTCDA on Au(111) and chemisorption on Cu(111).⁶⁴ Ni(111) is often used for on-surface syntheses because of its catalytical properties.^{62, 65-67} Comparing Ni(111) with Cu(111) it was shown that pentacene can be transformed to graphene at much lower temperatures on Ni(111), indicating amongst others a stronger reactivity of the surface.⁶⁵

Electronic structure of BN-HBP on various reactive metal interfaces

In a next step we investigate the interaction of the nonplanar BN-HBP on Au(111) and Ni(111) surfaces. At first glance BN-HBP and BN-HBC look very similar, but while BN-HBC is completely planar, three CC-bonds of the outer π -conjugated carbon systems of BN-HBC are broken to form the nonplanar propeller-like BN-HBP (see **Figure 1**). Similar to BN-HBC, BN-HBP consists of 36 C, 3 B and 3 N atoms, but a different amount of H atoms (24 instead of 18) due to the breaking of the three CC bonds in the π -conjugated carbon system. These structural differences lead to different growth modes and electronic properties, as shown in a previous study about thin films of BN-HBC and BN-HBP.²⁹ To understand the thin film properties we also performed thickness dependent XPS measurements of ultrathin films of 1-2 ML coverage up to thin films of BN-HBP on the less reactive Au(111) and more reactive Ni(111) surface (**Figure S5-S7**). As before, we performed detailed peak fits (**Figure 7**). Additional peak fit data can be reviewed in **Tables S9-S13** (supporting information).

A comparison of the core level binding energies of the thin film and the monolayer of BN-HBP on these two metal substrates reveal a typical shift of 0.19 – 0.29 eV to lower binding energies due to screening of the photohole at the interface. For the two core levels of the borazine core, the same shift of 0.20 ± 0.05 eV can be observed. For the peak fit of the spectra representing 1-2 ML coverage just one component was used, as expected from the chemical environment of the molecule. Hence, we see no evidence for interaction of the borazine core at the interface to Au(111). On the other hand, additional intensity in the C1s spectrum of the monolayer is obvious and may be described by an additional peak at a binding energy of 284.80 eV. For the interpretation of the C1s core level spectrum on Au(111), one must have in mind that BN-HBP is

not planar like BN-HBC, whereby not all atoms have the same distance to the substrate surface. In a recent study, it was shown, that a monolayer of BN-HBP is not flat lying on Au(111) and that the interaction at the interface of BN-HBC on Au(111) is much stronger than for BN-HBP.²⁹ No evidence for interactions involving significant charge transfer of BN-HBP on Au(111) was found. We suggest that this additional intensity is caused by the random orientation of BN-HBP on Au(111) we mentioned above. Because of the twisted shape of the molecule, not all the atoms with the same nominal bonding environment in the molecule (CH, CCB, CCN, CN, CB) have the same distance to the Au(111) surface. Thus, the geometrical and electronic environment of the equivalent carbon atoms within one component of the molecule becomes different at the interface to the metal substrates is different. This is supported by slightly higher Gaussian widths of the C1s components at the interface (**Table S10**).

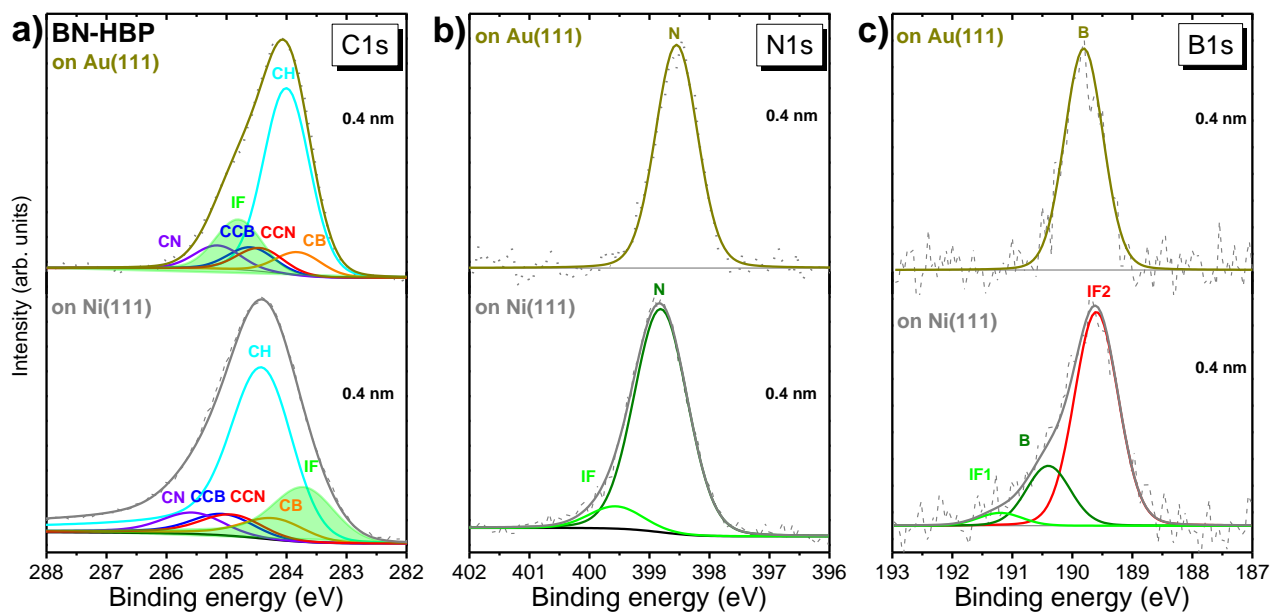


Figure 7. Core level spectra of 1-2 monolayer coverage BN-HBP on Au(111) (top panel) and Ni(111) (bottom panel): a) C1s, b) N1s and c) B1s. BN-HBP consists of five different kinds of carbon atoms:

carbon bonded to hydrogen (CH), bonded to boron (CB), bonded to nitrogen (CN) and carbon bonded to carbon in proximity to nitrogen (CCN) and to boron (CCB). All N and B atoms are in the same chemical environment. In addition, interface components were added, which are described in the text.

On the strongly reactive Ni(111) substrate, a totally different situation occurs (**Figure 7**, bottom panel). While the peak fits of the thin films are very similar to BN-HBP on Au(111), the interaction at the interface to Ni(111) is much more complex and consequently, the spectral shape is more difficult to explain. Besides the strong shifts to lower binding energies, significant differences in the peak shape of the ultrathin film of 1-2 ML coverage compared to the thin film are obvious, indicated by a tail to higher binding energies (C1s), additional interface components and a broadening of the peaks (C1s, N1s, B1s). The C1s and N1s core levels (**Figure 7a+b**, bottom panel) recorded from the ultrathin film of BN-HBP on Ni(111) can be described in a similar manner compared to BN-HBC (**Figure 4a+b**), by adding another component and an asymmetric peak shape (asymmetry parameter 0.1) in the case of the C1s. However a distinct broadening of the Gaussian width occurs (**Table S10**), which can be interpreted by molecules interacting differently strong with the Ni(111) substrate and thus, exhibit different energetic positions. In contrast, distinct differences to BN-HBC can be observed in the B1s core level of BN-HBP (**Figure 7c**). In the spectra measured from the ultrathin film of 1-2 ML coverage a very intensive new peak arises at lower binding energy (IF2). This peak decreases for higher coverages and in parallel increases the component labeled B, and it finally develops towards the bulk signal (**Figure 8+S7, Table S13**). Thus, the two components can be clearly assigned to a bulk-like component (B) and an interface related component (IF2). The small IF1 component, which was more intense for BN-HBC on

Ni(111) plays just an underpart for the interpretation of the interaction of BN-HBP on Ni(111). Because of these drastic changes in the peak shapes of the core levels at the interface, a partial fragmentation of BN-HBP on Ni(111) cannot be ruled out. Compared to the planar BN-HBC, the nonplanar BN-HBP seems to interact stronger with the Ni(111) surface. We suggest this is due to the more stabilizing effect of the larger π -conjugated carbon system of BN-HBC.

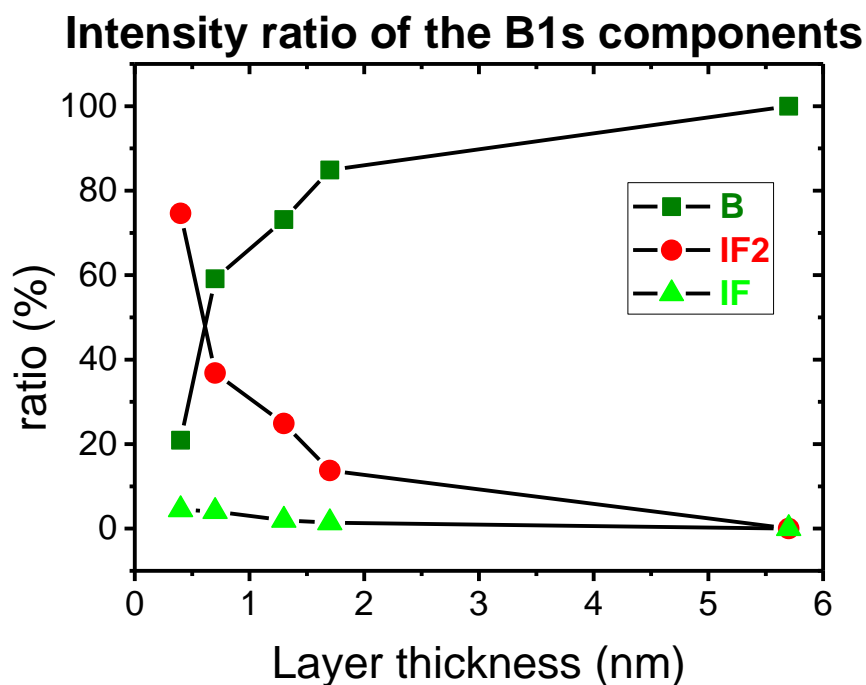


Figure 8. Intensity ratios (relative areas) of the peak fit components of the B1s core level series of BN-HBP on Ni(111). Assignments refer to the components shown in **Figure S7b**.

Conclusions

We investigated the interface properties of the molecules HBC, BN-HBC and BN-HBP on different possible metal electrode materials. The nature of interaction at the interface is strongly

influenced by the exchange of the inner benzene ring of HBC by a borazine core, resulting in BN-HBC, but also by the loss of planarity, resulting in BN-HBP.

It is apparent that the interaction strength of the investigated nanographene molecules at the interface is strongly dependent on the underlying substrate. Only weak interactions are observed at the interface to Au(111) for all of the three investigated molecules. Essentially, the monolayer core level peaks can be described by the same peak fit model than the thin films of the respective molecule. For HBC no interface component is needed for the peak fits, while for BN-HBC a small additional component is added in the C1s. The relatively large interface component for BN-HBP might arise from the fact that the carbon atoms can have different distances to the Au(111) surface due to the twisted shape of the molecule. The adsorption process can mainly be described by physisorption and the electronic structure of the molecules at the interface is not significantly altered.

On Cu(111) we can clearly see the influence of the BN-doping. Although, Cu(111) is more reactive than Au(111), we cannot see drastic changes in the C1s core level of HBC (besides a larger Gaussian width). However, for BN-HBC one additional component for each core level is needed to fit the experimental data. This indicates a stronger interaction at the interface through BN-doping.

The situation at the interface is completely different when Ni(111) is used as a substrate. Compared to the thin film, the 1-2 ML C1s spectra of HBC, BN-HBC and BN-HBP on Ni(111) have very different peak shapes and interface features or asymmetries have to be introduced for an adequate description of the core levels. The different peak shapes might be caused by a very

strong chemisorption or even fragmentation of the molecules: For the C1s core level of HBC, the two interface peaks might arise from smaller HBC fragments or NiC species. The STM image however still shows dedicated molecules. For the BN-HBC and BN-HBP core levels on Ni(111), interface peaks and asymmetries need to be introduced as well. The peak shape changes and energetic shifts are even more drastic for BN-HBP than for BN-HBC - the nonplanarity, the smaller π -system and the more random orientation of BN-HBP seem to be further destabilizing factors leading to a fragmentation of the molecules.

Associated Content

Supporting Information

Additional peakfitparameters, core level series of each experiment.

Acknowledgements

The Center for Light-Matter Interaction, Sensors & Analytics (LISA+) at the University of Tübingen is acknowledged for technical support.

References

1. Narita, A.; Wang, X.-Y.; Feng, X.; Müllen, K., New Advances in Nanographene Chemistry. *Chem. Soc. Rev.* **2015**, *44*, 6616-6643.
2. Chen, L.; Hernandez, Y.; Feng, X. L.; Müllen, K., From Nanographene and Graphene Nanoribbons to Graphene Sheets: Chemical Synthesis. *Angew. Chem. Int. Ed.* **2012**, *51*, 7640-7654.
3. Müller, M.; Kübel, C.; Müllen, K., Giant Polycyclic Aromatic Hydrocarbons. *Chem. Eur. J.* **1998**, *4*, 2099-2109.
4. Ruffieux, P., et al., On-Surface Synthesis of Graphene Nanoribbons with Zigzag Edge Topology. *Nature* **2016**, *531*, 489-492.
5. Angelova, P., et al., A Universal Scheme to Convert Aromatic Molecular Monolayers into Functional Carbon Nanomembranes. *ACS Nano* **2013**, *7*, 6489-6497.
6. Müllen, K., Evolution of Graphene Molecules: Structural and Functional Complexity as Driving Forces Behind Nanoscience. *ACS Nano* **2014**, *8*, 6531-6541.

7. Bacon, M.; Bradley, S. J.; Nann, T., Graphene Quantum Dots. *Part. Part. Syst. Char.* **2014**, *31*, 415-428.
8. Grimsdale, A. C.; Wu, J.; Müllen, K., New Carbon-Rich Materials for Electronics, Lithium Battery, and Hydrogen Storage Applications. *Chem. Commun.* **2005**, 2197-2204.
9. Seyler, H.; Purushothaman, B.; Jones David, J.; Holmes Andrew, B.; Wong Wallace, W. H., Hexa-peri-hexabenzocoronene in Organic Electronics. In *Pure Appl. Chem.*, 2012; Vol. 84, p 1047.
10. Watson, M. D.; Fechtenkötter, A.; Müllen, K., Big Is Beautiful—"Aromaticity" Revisited from the Viewpoint of Macromolecular and Supramolecular Benzene Chemistry. *Chem. Rev.* **2001**, *101*, 1267-1300.
11. Schmidt-Mende, L.; Fechtenkötter, A.; Müllen, K.; Moons, E.; Friend, R. H.; MacKenzie, J. D., Self-Organized Discotic Liquid Crystals for High-Efficiency Organic Photovoltaics. *Science* **2001**, *293*, 1119.
12. Wu, J.; Pisula, W.; Müllen, K., Graphenes as Potential Material for Electronics. *Chem. Rev.* **2007**, *107*, 718-747.
13. Yan, X.; Li, L.-s., Solution-Chemistry Approach to Graphene Nanostructures. *Journal of Materials Chemistry* **2011**, *21*, 3295-3300.
14. Baldridge, K. K.; Siegel, J. S., Of Graphs and Graphenes: Molecular Design and Chemical Studies of Aromatic Compounds. *Angew. Chem. Int. Ed.* **2013**, *52*, 5436-5438.
15. Morita, Y.; Suzuki, S.; Sato, K.; Takui, T., Synthetic Organic Spin Chemistry for Structurally Well-Defined Open-Shell Graphene Fragments. *Nat. Chem.* **2011**, *3*, 197-204.
16. Sun, Z.; Zeng, Z.; Wu, J., Benzenoid Polycyclic Hydrocarbons with an Open-Shell Biradical Ground State. *Chem. Asian J.* **2013**, *8*, 2894-2904.
17. Wang, X.-Y.; Wang, J.-Y.; Pei, J., BN Heterosuperbenzenes: Synthesis and Properties. *Chem. Eur. J.* **2015**, *21*, 3528-3539.
18. Morgan, M. M.; Piers, W. E., Efficient Synthetic Methods for the Installation of Boron-Nitrogen Bonds in Conjugated Organic Molecules. *Dalton Trans.* **2016**, *45*, 5920-5924.
19. Helten, H., B=N Units as Part of Extended π -Conjugated Oligomers and Polymers. *Chem. Eur. J.* **2016**, *22*, 12972-12982.
20. Giustra, Z. X.; Liu, S.-Y., The State of the Art in Azaborine Chemistry: New Synthetic Methods and Applications. *J. Am. Chem. Soc.* **2018**, *140*, 1184-1194.
21. Campbell, P. G.; Marwitz, A. J. V.; Liu, S.-Y., Recent Advances in Azaborine Chemistry. *Angew. Chem. Int. Ed.* **2012**, *51*, 6074-6092.
22. Bosdet, M. J. D.; Piers, W. E., B-N as a C-C Substitute in Aromatic Systems. *Can. J. Chem.* **2009**, *87*, 8-29.
23. Krieg, M.; Reicherter, F.; Haiss, P.; Ströbele, M.; Eichele, K.; Treanor, M.-J.; Schaub, R.; Bettinger, H. F., Construction of an Internally B₃N₃-Doped Nanographene Molecule. *Angew. Chem. Int. Ed.* **2015**, *54*, 8284-8286.
24. Ciccullo, F.; Calzolari, A.; Piš, I.; Savu, S. A.; Krieg, M.; Bettinger, H. F.; Magnano, E.; Chassé, T.; Casu, M. B., A Quasi-Free-Standing Single Layer of a B₃N₃-Doped Nanographene Molecule Deposited on Au(111) Single Crystals. *J. Phys. Chem. C* **2016**, *120*, 17645-17651.
25. Otero, N.; Karamanis, P.; El-Kelany, K. E.; Rérat, M.; Maschio, L.; Civalieri, B.; Kirtman, B., Exploring the Linear Optical Properties of Borazine (B₃N₃) Doped Graphenes. 0D Flakes vs 2D Sheets. *J. Phys. Chem. C* **2017**, *121*, 709-722.
26. Otero, N.; El-Kelany, K. E.; Pouchan, C.; Rérat, M.; Karamanis, P., Establishing the Pivotal Role of Local Aromaticity in the Electronic Properties of Boron-Nitride Graphene Lateral Hybrids. *Phys. Chem. Chem. Phys.* **2016**, *18*, 25315-25328.
27. Tönshoff, C.; Müller, M.; Kar, T.; Latteyer, F.; Chassé, T.; Eichele, K.; Bettinger, H. F., B₃N₃ Borazine Substitution in Hexa-peri-Hexabenzocoronene: Computational Analysis and Scholl Reaction of Hexaphenylborazine. *ChemPhysChem* **2012**, *13*, 1173-1181.

28. Belser, A.; Greulich, K.; Grüninger, P.; Bettinger, H. F.; Peisert, H.; Chassé, T., Visualization of the Borazine Core of B₃N₃-Doped Nanographene by STM. *ACS Appl. Mater. Interfaces* **2020**, *12*, 19218-19225.
29. Greulich, K.; Belser, A.; Bischof, D.; Widdascheck, F.; Sättele, M. S.; Grüninger, P.; Bettinger, H. F.; Witte, G.; Chassé, T.; Peisert, H., B₃N₃-Substituted Nanographene Molecules: Influence of Planarity on the Electronic Structure and Molecular Orientation in Thin Films. *ACS Applied Electronic Materials* **2021**.
30. Yeh, J. J.; Lindau, I., Atomic Subshell Photoionization Cross-Sections and Asymmetry Parameters - 1 Less-Than-or-Equal-to Z Less-Than-or-Equal-to 103. *At. Data Nucl. Data Tables* **1985**, *32*, 1-155.
31. Hesse, R.; Chassé, T.; Streubel, P.; Szargan, R., Error Estimation in Peak-Shape Analysis of XPS Core-Level Spectra Using Unifit 2003: How Significant Are the Results of Peak Fits? *Surf. Interface Anal.* **2004**, *36*, 1373-1383.
32. Horcas, I.; Fernández, R., WSXM: A Software for Scanning Probe Microscopy and a Tool for Nanotechnology. *Rev. Sci. Instrum* **2007**, *78*, 013705.
33. Simonov, K. A.; Vinogradov, N. A.; Vinogradov, A. S.; Generalov, A. V.; Zagrebina, E. M.; Mårtensson, N.; Cafolla, A. A.; Carpy, T.; Cunniffe, J. P.; Preobrajenski, A. B., Correction to "Effect of Substrate Chemistry on the Bottom-up Fabrication of Graphene Nanoribbons: Combined Core-Level Spectroscopy and STM Study". *J. Phys. Chem. C* **2015**, *119*, 880-881.
34. Grüninger, P., et al., Electronic Structure of Hexacene and Interface Properties on Au(110). *J. Phys. Chem. C* **2018**, *122*, 19491-19498.
35. Alagia, M.; Baldacchini, C.; Betti, M. G.; Bussolotti, F.; Carravetta, V.; Ekstrom, U.; Mariani, C.; Stranges, S., Core-Shell Photoabsorption and Photoelectron Spectra of Gas-Phase Pentacene: Experiment and Theory. *J. Chem. Phys.* **2005**, *122*.
36. Kang, S. J.; Yi, Y.; Kim, C. Y.; Cho, S. W.; Noh, M.; Jeong, K.; Whang, C. N., Energy Level Diagrams of C60/Pentacene/Au and Pentacene/C60/Au. *Synth. Met.* **2006**, *156*, 32-37.
37. Grüninger, P.; Greulich, K.; Karstens, R.; Belser, A.; Ovsyannikov, R.; Giangrisostomi, E.; Bettinger, H. F.; Batchelor, D.; Peisert, H.; Chassé, T., Highly Oriented Hexacene Molecules Grown in Thin Films on Cu(110)-(2 × 1)O. *J. Phys. Chem. C* **2019**, *123*, 27672-27680.
38. Peisert, H.; Knupfer, M.; Fink, J., Electronic Structure of Partially Fluorinated Copper Phthalocyanine (CuPcF₄) and Its Interface to Au(100). *Surf. Sci.* **2002**, *515*, 491-498.
39. Peisert, H.; Knupfer, M.; Schwieger, T.; Auerhammer, J. M.; Golden, M. S.; Fink, J., Full Characterization of the Interface between the Organic Semiconductor Copper Phthalocyanine and Gold. *J. Appl. Phys.* **2002**, *91*, 4872-4878.
40. Belser, A.; Karstens, R.; Nagel, P.; Merz, M.; Schuppler, S.; Chassé, T.; Peisert, H., Interaction Channels between Perfluorinated Iron Phthalocyanine and Cu(111). *Phys. Status Solidi B* **2019**, *256*, 1800292.
41. Baldacchini, C.; Allegretti, F.; Gunnella, R.; Betti, M. G., Molecule-Metal Interaction of Pentacene on Copper Vicinal Surfaces. *Surf. Sci.* **2007**, *601*, 2603-2606.
42. Petraki, F.; Peisert, H.; Biswas, I.; Chassé, T., Electronic Structure of Co-Phthalocyanine on Gold Investigated by Photoexcited Electron Spectroscopies: Indication of Co Ion-Metal Interaction. *J. Phys. Chem. C* **2010**, *114*, 17638-17643.
43. Ruckerl, F.; Waas, D.; Buchner, B.; Knupfer, M., Particular Electronic Properties of F16CoPc: A Decent Electron Acceptor Material. *J. Electron. Spectrosc. Relat. Phenom.* **2017**, *215*, 1-7.
44. Bournel, F.; Laffon, C.; Parent, P.; Tourillon, G., Adsorption of Some Substituted Ethylene Molecules on Pt(111) at 95 K Part 1: NEXAFS, XPS and UPS Studies. *Surf. Sci.* **1996**, *350*, 60-78.
45. Uihlein, J.; Peisert, H.; Adler, H.; Glaser, M.; Polek, M.; Ovsyannikov, R.; Bauer, M.; Chassé, T., Strong Interaction of MnPc on Ni(111): Influence of Graphene Buffer Layer. *J. Phys. Chem. C* **2014**, *118*, 28671-28678.

46. Uihlein, J.; Peisert, H.; Glaser, M.; Polek, M.; Adler, H.; Petraki, F.; Ovsyannikov, R.; Bauer, M.; Chassé, T., Communication: Influence of Graphene Interlayers on the Interaction between Cobalt Phthalocyanine and Ni(111). *J. Chem. Phys.* **2013**, *138*, 081101.
47. Helander, M. G.; Greiner, M. T.; Wang, Z. B.; Lu, Z. H., Effect of Electrostatic Screening on Apparent Shifts in Photoemission Spectra near Metal/Organic Interfaces. *Phys. Rev. B* **2010**, *81*, 153308.
48. Browning, R.; Sobolewski, M. A.; Helms, C. R., Effect of Electrostatic Screening on Energy Positions of Electron Spectra near SiO₂/Si Interfaces. *Phys. Rev. B* **1988**, *38*, 13407-13410.
49. Kaindl, G.; Chiang, T. C.; Eastman, D. E.; Himpsel, F. J., Distance-Dependent Relaxation Shifts of Photoemission and Auger Energies for Xe on Pd(001). *Phys. Rev. Lett.* **1980**, *45*, 1808-1811.
50. Belser, A., et al., Perfluorinated Phthalocyanines on Cu(110) and Cu(110)-(2 × 1)O: The Special Role of the Central Cobalt Atom. *J. Phys. Chem. C* **2021**.
51. Kovacs, G. J.; Bertóti, I.; Radnóczy, G., X-Ray Photoelectron Spectroscopic Study of Magnetron Sputtered Carbon–Nickel Composite Films. *Thin Solid Films* **2008**, *516*, 7942-7946.
52. Bébin, P.; Prud'homme, R. E., Comparative XPS Study of Copper, Nickel, and Aluminum Coatings on Polymer Surfaces. *Chem. Mater.* **2003**, *15*, 965-973.
53. Chen, J. J.; Winograd, N., The Adsorption and Decomposition of Methylamine on Pd{111}. *Surf. Sci.* **1995**, *326*, 285-300.
54. Uihlein, J., et al., Influence of Graphene on Charge Transfer between CoPc and Metals: The Role of Graphene–Substrate Coupling. *J. Phys. Chem. C* **2015**, *119*, 15240-15247.
55. Grüneis, A.; Kummer, K.; Vyalikh, D. V., Dynamics of Graphene Growth on a Metal Surface: A Time-Dependent Photoemission Study. *New J. Phys.* **2009**, *11*, 073050.
56. Preobrajenski, A. B.; Ng, M. L.; Vinogradov, A. S.; Martensson, N., Controlling Graphene Corrugation on Lattice-Mismatched Substrates. *Phys. Rev. B* **2008**, *78*, 073401.
57. Proehl, H.; Toerker, M.; Sellam, F.; Fritz, T.; Leo, K.; Simpson, C.; Müllen, K., Comparison of Ultraviolet Photoelectron Spectroscopy and Scanning Tunneling Spectroscopy Measurements on Highly Ordered Ultrathin Films of Hexa-Peri-Hexabenzocoronene on Au (111). *Phys. Rev. B* **2001**, *63*, 205409.
58. Sellam, F.; Schmitz-Hübsch, T.; Toerker, M.; Mannsfeld, S.; Proehl, H.; Fritz, T.; Leo, K.; Simpson, C.; Müllen, K., LEED and STM Investigations of Organic–Organic Heterostructures Grown by Molecular Beam Epitaxy. *Surf. Sci.* **2001**, *478*, 113-121.
59. Liu, W.; Tkatchenko, A.; Scheffler, M., Modeling Adsorption and Reactions of Organic Molecules at Metal Surfaces. *Acc. Chem. Res.* **2014**, *47*, 3369-3377.
60. Dahal, A.; Bätzill, M., Graphene–Nickel Interfaces: A Review. *Nanoscale* **2014**, *6*, 2548-2562.
61. Villagomez, C. J.; Zambelli, T.; Gauthier, S.; Gourdon, A.; Stojkovic, S.; Joachim, C., STM Images of a Large Organic Molecule Adsorbed on a Bare Metal Substrate or on a Thin Insulating Layer: Visualization of HOMO and LUMO. *Surf. Sci.* **2009**, *603*, 1526-1532.
62. Dinca, L. E.; Fu, C.; MacLeod, J. M.; Lipton-Duffin, J.; Brusso, J. L.; Szakacs, C. E.; Ma, D.; Perepichka, D. F.; Rosei, F., Unprecedented Transformation of Tetrathienoanthracene into Pentacene on Ni (111). *ACS Nano* **2013**, *7*, 1652-1657.
63. Balle, D.; Adler, H.; Grüninger, P.; Karstens, R.; Ovsyannikov, R.; Giangrisostomi, E.; Chassé, T.; Peisert, H., Influence of the Fluorination of CoPc on the Interfacial Electronic Structure of the Coordinated Metal Ion. *J. Phys. Chem. C* **2017**, *121*, 18564-18574.
64. Duhm, S.; Gerlach, A.; Salzmann, I.; Bröker, B.; Johnson, R. L.; Schreiber, F.; Koch, N., PTCDA on Au(111), Ag(111) and Cu(111): Correlation of Interface Charge Transfer to Bonding Distance. *Org. Electron.* **2008**, *9*, 111-118.
65. Dinca, L. E.; De Marchi, F.; MacLeod, J. M.; Lipton-Duffin, J.; Gatti, R.; Ma, D.; Perepichka, D. F.; Rosei, F., Pentacene on Ni(111): Room-Temperature Molecular Packing and Temperature-Activated Conversion to Graphene. *Nanoscale* **2015**, *7*, 3263-3269.

66. Auwärter, W.; Suter, H. U.; Sachdev, H.; Greber, T., Synthesis of One Monolayer of Hexagonal Boron Nitride on Ni (111) from B-Trichloroborazine (ClBNH)₃. *Chem. Mater.* **2004**, *16*, 343-345.
67. Song, S.; Su, J.; Telychko, M.; Li, J.; Li, G.; Li, Y.; Su, C.; Wu, J.; Lu, J., On-Surface Synthesis of Graphene Nanostructures with π -Magnetism. *Chem. Soc. Rev.* **2021**.

Molecular exchange of Hexabenzocoronene and Cobalt Phthalocyanine on Au(111)

*Axel Belser,[†] Katharina Greulich,[†] Marie Sophie Sättele,^{†#} Michael Fingerle,[#] Ruslan Ovsyannikov,[§]
Erika Giangrisostomi,[§] Holger F. Bettinger,[#] Thomas Chassé,[‡] and Heiko Peisert^{†*}*

[†] Institute of Physical and Theoretical Chemistry, University of Tübingen, Auf der Morgenstelle 18, 72076 Tübingen, Germany

[#] Institute of Organic Chemistry, University of Tübingen, Auf der Morgenstelle 18, 72076 Tübingen, Germany

[§] Institute for Methods and Instrumentation in Synchrotron Radiation Research, Helmholtz-Zentrum Berlin für Materialien und Energie GmbH, Albert-Einstein-Straße 15, 12489 Berlin, Germany

[‡] Center for Light-Matter Interaction, Sensors & Analytics (LISA⁺) at the University of Tübingen, Auf der Morgenstelle 18, 72076 Tübingen, Germany

* Corresponding author, heiko.peisert@uni-tuebingen.de, Tel.: (+49) 07071 / 29-76931, Fax: (+49) 07071 / 29-5490

Abstract

Organic bilayer systems and heterostructures are of enormous importance for optoelectronic devices. We study interface properties and the structural ordering of cobalt phthalocyanine (CoPc) on a highly ordered monolayer (ML) hexa-*peri*-hexabenzocoronene (HBC), grown on Au(111), using photoemission X-ray absorption (XAS), scanning tunneling microscopy (STM) and low-energy electron diffraction (LEED). A charge transfer between CoPc and the gold substrate is almost completely prevented by the HBC intermediate layer. We show that HBC acts as a template for the initial growth of CoPc molecules. After annealing to 630 K, a molecular exchange takes place, both CoPc and HBC molecules are present at the interface.

Keywords hexa-*peri*-hexabenzocoronene, cobalt phthalocyanine, transition metal phthalocyanines, bilayers, intermediate layer, valence band, π -conjugated systems, orientation, interaction, photoemission, x-ray absorption spectroscopy, near edge x-ray absorption fine structure, scanning tunneling microscopy, low-energy electron diffraction

1. Introduction

The tuning of electronic interface properties between organic molecules and metallic substrates is of enormous importance for a broad variety of applications.¹⁻⁷ Strong interactions including chemical reactions may alter the molecular electronic structure in particular of the frontier orbitals, which are important for charge carrier transport and injection. Routes to avoid chemical interactions at interfaces include, among others, the optimization of the surface preparation or the introduction of intermediate layers.⁸⁻¹³ Such intermediate layers can be of different nature, a well-known representative is the 2D material graphene. However, the number of substrates for the growth of well-defined graphene layers is limited, best growth conditions are achieved for perfect (111) single crystal surfaces with reasonable lattice matching.¹⁴⁻¹⁵ Although even on Au(111) a direct growth of graphene can be reached at comparably high temperatures, the formation of islands cannot be excluded.¹⁶⁻¹⁷

An alternative route to establish an intermediate carbon layer on Au(111) under smooth conditions could be the preparation of a well-ordered monolayer of nanographene molecules. The possibly best-known representative of nanographene molecules is hexa-*peri*-hexabenzocoronene (HBC), a planar polycyclic aromatic hydrocarbon (PAH) with noble electronic properties.¹⁸⁻¹⁹ Well-ordered HBC monolayers with large domains can be easily prepared by deposition of several layers and subsequent annealing.²⁰⁻²³ The stability of molecular intermediate layers will essentially depend on the strength of the molecule-substrate interaction. If the molecule-substrate interaction of molecules deposited subsequently on the intermediate layer is significantly stronger than for molecules of the first (intermediate) layer, a molecular

exchange can take place.²⁴⁻²⁸ For the PTCDA/CuPc/Ag(111) such effects were already observed at very low temperatures (1.1 K).²⁸ In contrast, pentacene/para-sexiphenyl/Cu(111) is stable against molecular exchange at 15 K and only after annealing to 300 K an irreversible reversed bilayer is formed.²⁶ Thus, molecular exchange depends crucial on the combination of the materials, which has been investigated for several bilayer model systems.^{21, 26-32}

In the present study we address the question if an HBC intermediate layer on Au(111) is stable against molecular exchange with phthalocyanine molecules. Cobalt phthalocyanine (CoPc) was chosen as a representative for the family of phthalocyanines, because of its known strong interaction with the gold substrate (interfacial charge transfer).³³ The stability was monitored up to temperatures of 630 K, which may simulate a long-term stability. The experimental procedure is illustrated in **Figure 1**.

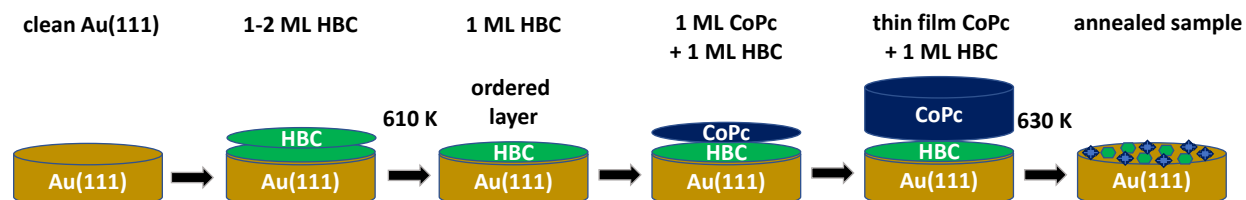


Figure 1. *Experimental procedure. First, 2-3 monolayers of HBC were deposited on a well-defined Au(111) surface and subsequently annealed to 610 K to form a homogeneous monolayer. On top, CoPc was deposited in a stepwise manner. Finally, the sample was annealed to 630 K.*

2. Experimental Section

The Au(111) single crystal was cleaned by repeated cycles of each 30 min Ar⁺-ion sputtering at a voltage of 0.8 kV and a partial pressure of $5 \cdot 10^{-5}$ mbar and subsequent annealing to 770 K. The purity and orientation of the crystal was checked by x-ray photoelectron spectroscopy (XPS), ultraviolet photoelectron spectroscopy (UPS), scanning tunneling microscopy (STM) and low-energy electron diffraction (LEED). HBC was synthesized as described previously.³⁴ CoPc was purchased from Sigma-Aldrich. The molecules were evaporated from a Knudsen cell at rates of 0.2 - 0.5 nm/min, controlled by a quartz crystal microbalance (QCM). The nominal layer thickness was estimated from substrate and adsorbate related XPS intensity ratios using photoemission cross sections from Yeh and Lindau;³⁵ the mean free path of photoelectrons was estimated according to Seah and Dench.³⁶ To produce a closed, highly ordered monolayer, 2-3 layers of HBC were evaporated on the Au(111) single crystal, followed by an annealing of the sample to 610 K for about 15 min. During all deposition steps the crystal was held at room temperature at a pressure of $< 3 \cdot 10^{-8}$ mbar.

All experiments were performed in UHV systems with a base pressure of $2 \cdot 10^{-10}$ mbar. The STM and LEED measurements were carried out in a two-chamber system equipped with a variable temperature (VT)-STM from Omicron GmbH and a LEED optics from OCI Vacuum Microengineering Inc. For the STM measurements, mechanically cut Pt/Ir tips were used. Tip and sample were held at room temperature. Given tunneling voltages refer to the tip with respect to the sample. The program WSxM was used to improve the contrast of the shown STM images.³⁷

The photoelectron spectroscopy (PES) measurements of the core-levels were performed using a multi-chamber UHV system equipped with a Phoibos 150 hemispherical energy analyzer (SPECS), and an X-ray source (Al-K α radiation, $h\nu = 1486.7$ eV) with monochromator (XR 50 M, SPECS). The energy scale was calibrated reproducing the binding energies (BE) of Cu 2p $_{3/2}$ and Au 4f $_{7/2}$ at 932.56 eV and 84.00 eV, respectively. The peak fitting of core level spectra was performed using Unifit version 2018.³⁸ A Voigt profile (convolution of Lorentzian and Gaussian profiles) and a Shirley model background was used. The error of absolute binding energies is estimated to be less than ± 0.05 eV.

The X-ray absorption spectroscopy (XAS) and PES measurements of the valence band have been performed using synchrotron radiation at the LowDose PES endstation of the PM4 beamline at BESSY II (Helmholtz-Zentrum, Berlin, Germany).³⁹⁻⁴⁰ The endstation is equipped with an angle-resolved time-of-flight (ArTOF) analyzer, which was used for PES measurements by integrating over an angle range of $\pm 15^\circ$. The improved detection efficiency by a factor of 2-3 orders of magnitude with respect to conventional hemispherical analyzers,³⁹ allows the study of sensitive organic molecules with limited photon flux. For valence band spectra the energy resolution was about 40 meV ($h\nu = 40.8$ eV), 55 meV ($h\nu = 75$ eV) and 120 meV ($h\nu = 110$ eV). The energy resolution of XAS set to 100 meV and 250 meV at a photon energy ($h\nu$) of 400 and 780 eV, respectively. The absorption was monitored indirectly in total electron yield (TEY) mode by measuring the sample current.

3. Results and Discussion

3.1. CoPc Growth on HBC/Au(111) from Monolayer to Thin Films

The structural ordering of the first monolayer may affect the structure and ordering of subsequent layers in many cases (e.g. refs. ⁴¹⁻⁴³). Therefore, we will first discuss the arrangement of HBC molecules forming the intermediate (mono-)layer on Au(111).

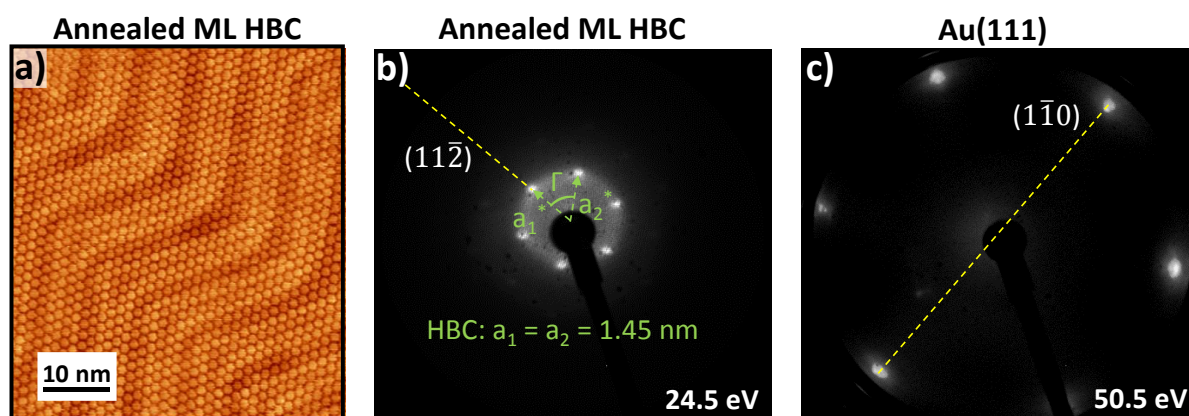


Figure 2. a) STM image of the intermediate HBC ML (Parameter), b) LEED pattern of the intermediate HBC ML at 24.5 eV, c) LEED pattern of the Au(111) substrate at 50.5 eV for comparison.

In **Figure 2** STM and LEED images of the HBC monolayer (ML) are shown, prepared by deposition of a multilayer and subsequent annealing to 610 K for 15 minutes. The formation of a highly ordered layer is clearly visible in the STM image of **Figure 2a**; the HBC molecules are aligned along the herringbone structure ($(11\bar{2})$ -direction) of the substrate. The corresponding LEED pattern at 24.5 eV shows very bright spots in the Au- $(11\bar{2})$ direction (**Figure 2b**). The comparison to

reference pattern from the bare Au(111) substrate taken at 50.5 eV (**Figure 2c**) allows the construction of the HBC unit cell. Since substrate related spots are visible in the $(1\bar{1}0)$ direction, the HBC lattice is rotated by 30° with respect to the unreconstructed Au(111) surface, as reported in other studies.^{20-21, 44} The determined lattice parameters obtained from STM and LEED ($a_1 = a_2 = 1.45$ nm, angle between the lattice vectors of $\Gamma = 60^\circ$) are in good agreement to the literature.^{20, 44} Thus, a commensurate (5x5)-superstructure for HBC on Au(111) can be inferred from the LEED data.

In order to prove the stability of the highly ordered HBC monolayer on Au(111), about 0.8 - 0.9 ML of CoPc were subsequently deposited on top. New structures are clearly visible in the STM images of **Figure 3**. Some CoPc molecules agglomerate in islands, visible as bright areas in **Figure 3a**, resulting in an apparently lower quality of the image. But nevertheless, three directions of CoPc growth, which are rotated by 60° to each other can be identified, indicated by blue arrows in **Figure 3a**. A zoom into one of the domains (**Figure 3b**) reveals more details: The rows are formed mostly by sections of three CoPc molecules arranged side by side. These rows show the same direction as the HBC molecules and the herringbone of the Au(111) substrate. In between these broader rows, rows of single molecules can be identified. A line profile was generated along the blue line in **Figure 3b**, depicted in **Figure 3d**. The apparent height difference of about 0.15 – 0.2 nm between the single and the threefold rows can be attributed to single, flat lying CoPc molecules; it perfectly matches reported heights of CoPc on Si(100)2x1 and Si(100)2x1:H surfaces.⁴⁵

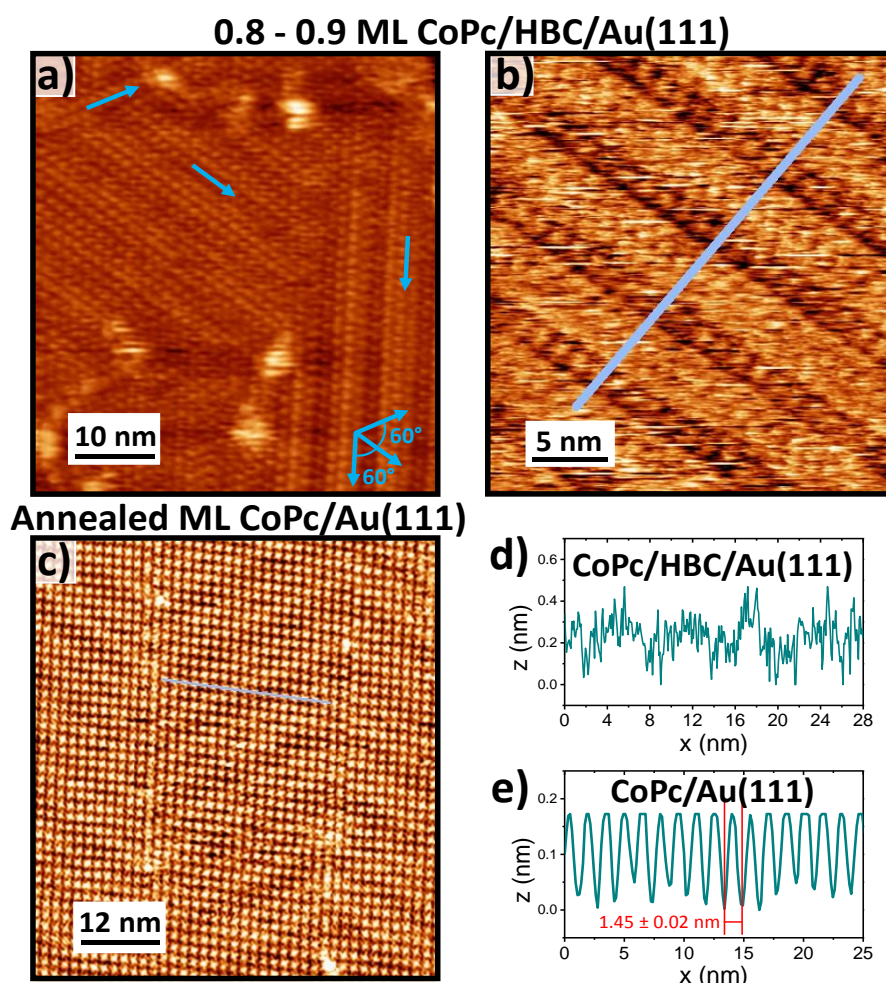


Figure 3. STM images of 0.8 - 0.9 ML of CoPc deposited on HBC/Au(111) and directly on Au(111) and the respective line profiles: a) About a ML of CoPc on HBC/Au(111) on the domain boundaries, b) closer look into one domain of CoPc on HBC/Au(111), c) annealed ML of CoPc on Au(111), d) respective line profile of CoPc on HBC/Au(111), e) respective line profile of CoPc on Au(111).

We note that similar rows were also observed for sub-monolayer coverages of CoPc on Au(111),⁴⁶ and other metal-phthalocyanines on HOPG and Ag(111).⁴⁷⁻⁴⁸ However, the CoPc rows on HBC/Au(111) appear more uniform compared to the rows formed on other substrates. The

threefold symmetry suggests a templating effect of the substrate and/or the well-ordered HBC monolayer. Thus, a reason for the ordered growth might be an optimization of the CoPc-substrate and CoPc-CoPc interaction strength, i.e. the mobility of the CoPc molecules is high enough for the diffusion to energetically favored adsorption places (due to comparably weak CoPc-substrate interactions), whereas at the same time the templating effect by the substrate is still present. A further origin for the ordered growth might be the exact coverage in the sub-monolayer range, stabilizing the ordering of the molecules.⁴⁶

For comparison, 1-2 monolayers of CoPc were deposited directly on Au(111) and heated subsequently to 610 K to form a ML without defects. In contrast to CoPc on HBC/Au(111), the STM image of **Figure 3c** reveals a long-range square ordering of the CoPc molecules. A square adsorption geometry of CoPc and other TMPcs was reported on various substrate surfaces including Au(111).⁴⁹⁻⁵⁵ From **Figure 3c** a line profile (blue line) was generated, shown in **Figure 3e**. The line profile illustrates the high regularity of the formed CoPc ML and allows an accurate determination of the lattice parameters: $a_1 = a_2 = 1.45 \pm 0.02$ nm. This value is in good agreement with recently published lattice parameters of quadratic ordered monolayers of CoPc and other transition metal phthalocyanines (TMPcs).^{49, 52, 56-57} Three different domains aligned to the direction of the herringbone reconstruction of the Au(111) substrate can be observed (see below). The presence of such different domains of CoPc and CuPc on Au(111) was investigated in detail in previous studies.^{46, 57-59}

In order to average over larger sample areas, we show in **Figure 4** LEED patterns corresponding to **Figure 3**. In the LEED image of the 0.8 - 0.9 ML CoPc layer on HBC/Au(111) taken at 18.5 eV (**Figure 4a**), patterns of both the CoPc overlayer and the HBC/Au(111) substrate can be identified,

marked by red and green arrows, respectively. The CoPc spots form a hexagonal pattern inside the hexagonal pattern of the HBC molecules and thus the lattice parameters obtained from LEED are larger, we obtain $a_1 = a_2 = 1.78 \pm 0.02$ nm. The angle between the lattice vectors is the same as for the annealed HBC monolayer ($\Gamma = 60^\circ$).

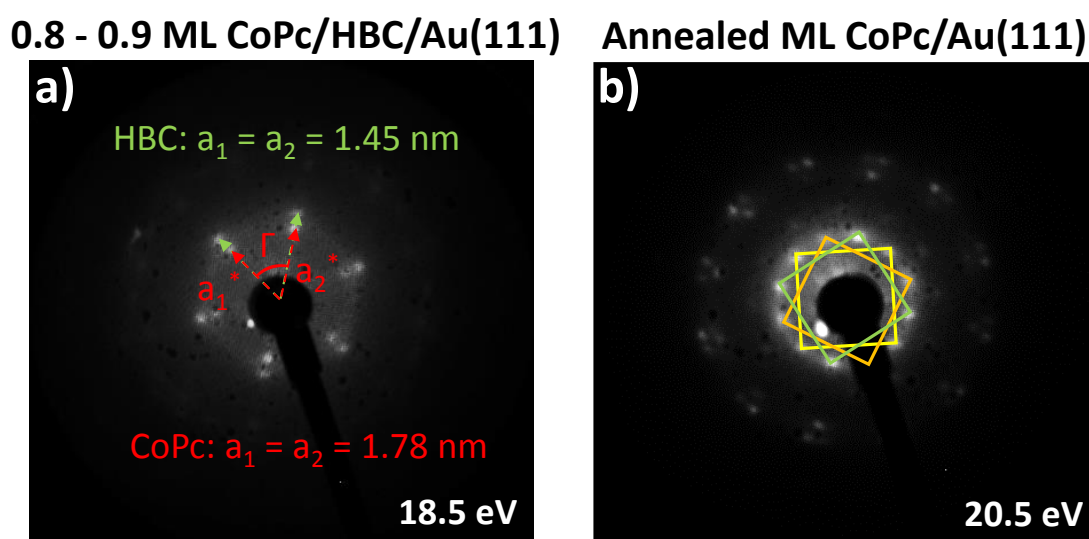


Figure 4. LEED pattern of CoPc monolayers: a) about a ML CoPc on HBC/Au(111) at 18.5 eV, b) an annealed ML CoPc on Au(111) at 20.5 eV.

The determination of the lattice parameters for CoPc deposited directly on Au(111) from LEED (**Figure 4b**) is more imprecise compared to STM due to the missing substrate-related spots at this energy. However, the LEED pattern in **Figure 4b** confirms the presence of three different domains, observed already in several STM images. The pattern can be interpreted as a superposition of three square patterns rotated by 120° (green, orange and yellow squares in **Figure 4b**), as previously reported and discussed in detail for CuPc on Au(111) and MoS₂.⁵⁹⁻⁶⁰ LEED

spots corresponding to different domains do not exhibit the same intensity in **Figure 4b**, which indicates that the three domains are not equally distributed in the considered area.

Remarkably, the lattice parameters of the hexagonal unit cell for CoPc/HBC/Au(111) are distinctly larger compared to the square unit cell (CoPc/Au(111)), i.e. the CoPc molecules are more densely packed on Au(111). The area per molecule is 4.75 nm² and 4.2 nm² for CoPc on HBC/Au(111) and Au(111), respectively. The different geometry of the unit cell and the different packing density illustrates nicely the templating effect of the Au(111) substrate, which can be tuned by the introduction of intermediate layers.

To gain further information about molecular orientation of CoPc on HBC/Au(111) as a function of film thickness, polarization dependent XA spectra at the N-K edge were taken for CoPc/HBC/Au(111). N1s π^* -excitations can be used in a similar manner as C1s π^* -excitations for the analysis of the molecular orientation of TMPcs.^{42, 61-64} For CoPc on HBC, C1s π^* -excitations are in superposition with HBC related transitions and cannot be used for the determination of the orientation. In **Figure 5**, polarization dependent N-K edge spectra for a 0.3 nm CoPc layer (about 1 ML) and a thin film of 1.5 nm thickness are shown for the two prominent angles grazing ($\theta = 10^\circ$) and normal ($\theta = 90^\circ$) incidence of the incoming p-polarized synchrotron light. The measurement geometry is shown as an inset in **Figure 5**. We can distinguish between two regions: Features at photon energies < 402 eV arise predominantly from transitions into π^* -orbitals, while feature at higher energies are attributed to transitions into σ^* -orbitals. Both XA spectra for the 0.3 and the 1.5 nm thick layers show essentially the same dichroism: The maximal intensity for π^* -transitions is visible grazing incidence, while for normal incidence maximal intensity is obtained from σ^* -transitions. This indicates a flat lying adsorption geometry in both

cases. Remaining intensity in the π^* -region of normal incidence spectra is hardly detectable, indicating very small tilt angles ($< 10^\circ$). The result is in good agreement to CoPc multilayer films on related substrates, such as graphene/Au/Ni(111) and CoPc/Au(111).^{8, 55}

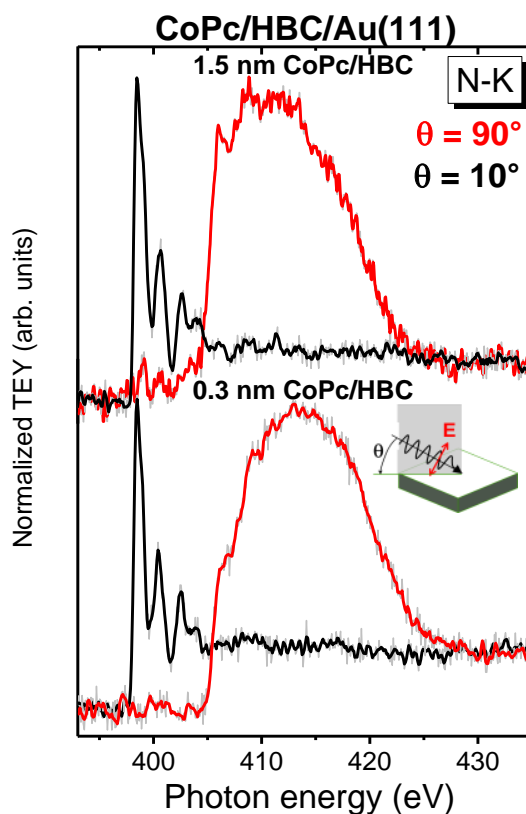


Figure 5. *N-K XA spectra of CoPc on a ML of HBC on Au(111) for two different CoPc thicknesses. The red curves correspond to an angle of incidence of 90° (normal incidence) and the black curves to 10° (grazing incidence). The measurement geometry is shown as an inset. The preferred flat lying adsorption geometry is maintained in thicker films of 1.5 nm.*

3.2. Electronic Interface Properties of CoPc on HBC/Au(111)

For CoPc on Au strong interactions were observed, including a charge transfer to the central Co ion (e.g. Refs.^{33, 65}). Charge transfer cannot always be completely prevented by an intermediate layer, as reported for CoPc on graphene/Ni(111).³³ Therefore the question arises whether the HBC intermediate layer on Au(111) provoke an electronic decoupling of CoPc molecules from the Au(111) substrate.

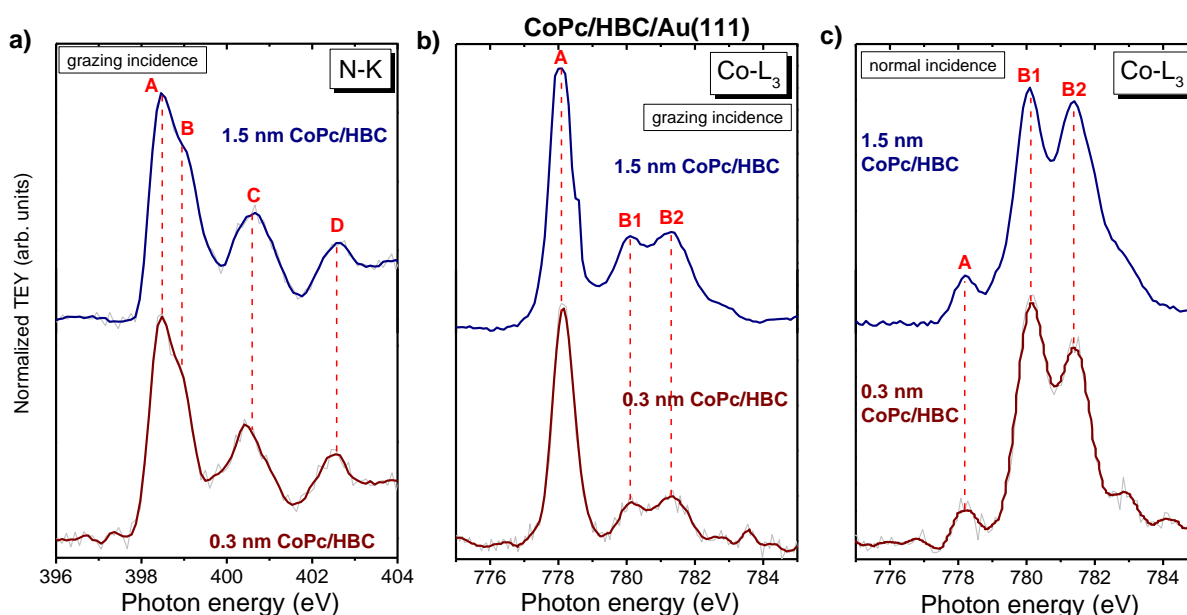


Figure 6. Thickness dependent N-K and Co-L₃ XA spectra of CoPc on a ML of HBC on Au(111): a) N-K at grazing incidence (10°), b) Co-L₃ at grazing incidence (10°), c) Co-L₃ at normal incidence (90°).

In addition to information about the molecular orientation in thin films, XAS provides also valuable information about the electronic structure, in particular at interfaces. We will discuss changes of XAS peak shapes qualitatively, for a detailed discussion of the origin of features, we

refer to the literature (e.g. Refs. ⁶⁶⁻⁶⁹). In **Figure 6** we compare N-K edge and Co-L₃ edge spectra for two different CoPc thicknesses on HBC/Au(111). Since the 0.3 nm layer corresponds to a coverage of about 1 ML, it represents information from the interface, whereas bulk-like spectra are obtained for the 1.5 nm thin film. The N-K edge spectra in **Figure 6a** are shown for grazing incidence of the incoming synchrotron light, exhibiting the maximal intensity of π^* resonances. Four different features denoted A-D can be distinguished, discussed in more detail in Refs. ^{33, 70}. Most important, there are only minuscule changes of peak shape with thickness, indicating that the nitrogen atoms are not strongly involved interfacial interactions.

The Co-L₃ XA spectra in **Figures 6b** and **6c** show a complex fine structure, resulting from multiplet effects due to the strong overlap of the core wave function with the valence wave functions.⁷¹ As a consequence, 16 transitions are possible for the absorption process $3d^7 \rightarrow 2p^5 3d^8$.⁷¹ The different shape of Co-L₃ XA spectra at grazing and normal incidence in **Figures 6b** and **6c** arises from transitions into different d-orbitals (A: transitions into orbitals with out-of-plane components, B: transitions into orbitals with in-plane components). For both measurement geometries, changes of the shape of Co-L₃ XA spectra as a function of film thickness are minor, indicating the absence of charge transfer to the central Co ion, as observed, e.g. for CoPc on gold-intercalated graphene/Ni(111).⁸ In contrast, for CoPc deposited directly on different gold surfaces, distinct thickness-dependent changes of both photoemission and XA spectra were observed, revealing an interfacial charge transfer.^{33, 68, 72-73} Thus, we conclude that the HBC intermediate layer can prevent charge transfer from gold to CoPc.

This conclusion is confirmed by the corresponding Co2p_{3/2}, N1s and C1s XPS core level spectra, shown in **Figure 7** for two different thicknesses. Peak fit parameters for N1s and C1s spectra are

summarized in **Tables S1-S4** (supporting information). All spectra of the bulk-like 2.7 nm CoPc thin film show the typical shape known from the literature.^{8, 64, 74} The N1s signal is described by two components with same intensity ascribed to pyrrole (N1) and bridging nitrogen (N2) atoms. Because of their small energy separation (typically 0.3 - 0.5 eV for phthalocyanines^{67, 75-79}), they cannot be clearly resolved by XPS. Two main components contribute to the C1s spectrum of the 2.7 nm thin film: Carbon bonded to nitrogen (C2) and carbon bonded to other carbon and hydrogen (C1). The main peaks are accompanied by their respective satellites, denoted S_{C1} , and S_{C2} in **Figure 7c**. The intensity ratio estimated from the peak areas $C1+S_{C1}:C2+S_{C2}$ of 3:1 matches perfectly to the stoichiometric composition (3:1).

Comparing the two film thicknesses, all core-level spectra for the lower coverages (0.3 nm) in **Figure 7** are shifted to 0.05 - 0.2 eV lower binding energies, which can be explained by screening effects of the photohole close to substrates with higher dielectric constants.^{61, 80-84} However, most important, the shape of Co2p_{3/2} and N1s core-level spectra in **Figure 7** almost independent of film thickness. The small shoulder at the low binding energy side of the Co2p_{3/2} spectrum of the 0.3 nm CoPc film in **Figure 7a** at about 778 eV, might arise from molecules at defect sites of the HBC layer, which may also explain the small changes in the shape of the corresponding XA spectra. Furthermore, the peak fit analysis reveals that the apparent change of the shape of the C1s core-level spectra in **Figure 7c** is caused by a superposition of HBC and CoPc related features. Thus, the analysis of the thickness-dependent core level spectra confirms the absence of strong interactions like charge transfer at the interface to HBC/Au(111).

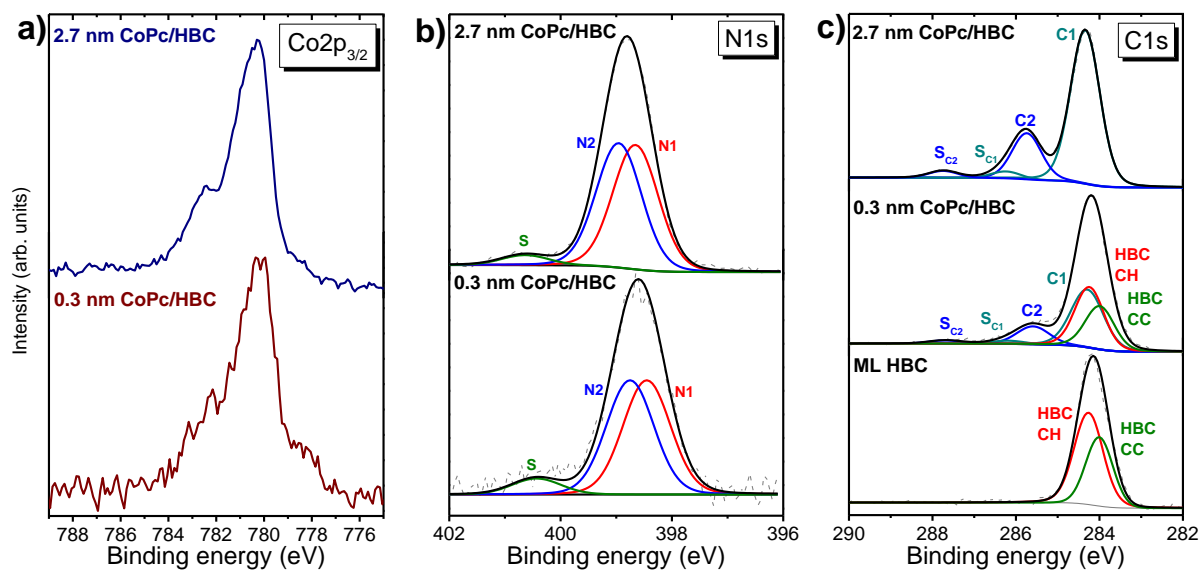


Figure 7. Thickness dependent core level spectra of CoPc on a ML of HBC on Au(111) with $h\nu = 1486.7$ eV: a) Co2p, b) N1s, c) C1s.

Finally, the development of valence structures at the interface between CoPc and HBC/Au(111) was monitored as a function of CoPc film thickness. In **Figure 8**, we show the region of the highest occupied molecular orbital (HOMO) for HBC/Au(111), and two different CoPc thicknesses on HBC/Au(111) at different excitation energies. The spectrum of the clean Au (111) substrate is shown as a reference. The spectra were taken at an emission angle of 18.5° with respect to normal emission, which was chosen to achieve higher intensity compared to normal emission. No features within the first 2 eV relative to the Fermi-edge are visible in reference spectrum of the Au(111) substrate in **Figure 8**. After the preparation of the HBC ML two features at 1.4 eV and 1.8 eV appear; the structure at 1.4 eV can be assigned to the HOMO of HBC.²⁰ After depositing 0.3 nm of CoPc on top, the intensity of the HBC-related feature at 1.4 eV becomes attenuated by the overlayer and a new peak at 1.0 eV appears. The binding energy of 1 eV is typical for the HOMO of CoPc for monolayer coverages on less reactive substrates.^{68, 85} The

HOMO of the 1.5 nm thin film shifts slightly by about 0.2 eV to 1.2 eV and thus, about the same amount as the core-levels, explained by screening effects of the photohole (see above). Interestingly, the HOMO of the bulk-like 1.5 nm film in **Figure 8** is clearly split into two features with maxima at 1.1 and 1.3 eV, which is not always observed in the literature. Since the mean free path of electrons at a kinetic energy of 40 eV is estimated to about 0.5 nm,³⁶ a strong attenuation of the HBC related features by the 1.5 nm CoPc overlayer is expected. In most experimental and theoretical studies the nature of the CoPc HOMO is attributed to the ligand states, built from C2p orbitals.^{66, 74, 85-89} Generally, a splitting of the HOMO can be understood by different reasons, among others by electron-phonon coupling^{74, 90-91} or a contribution of mixed domains.⁹² Moreover, a dispersion of the HOMO feature might be observed as a consequence of molecule-molecule interaction.⁵⁵ However, also the molecular electronic structure might be the origin of the splitting of the HOMO level. It was reported that the feature at 1.1 eV mostly has contribution from π -orbitals, while the feature at 1.3 eV originates from σ -orbitals.⁶⁷ The contribution of Co-related d-levels was discussed, the lowest lying state in CoPc might be attributed to a 3d orbital, which by symmetry cannot mix with ligand π states.⁸⁹ In all cases, the splitting and intensity crucially depends on the chosen excitation energy and measurement geometry. Thus, we ascribe the fact that a split feature is not always observed in the literature to differently chosen experimental parameters and the angular resolution of the spectrometer.

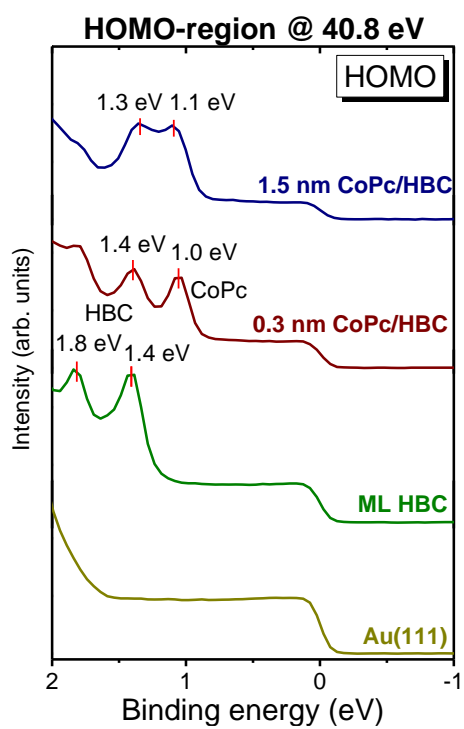


Figure 8. HOMO-region of each deposition step and the clean Au(111) substrate at 40.8 eV and an emission angle of 18.5° with respect to normal emission,

3.3. Temperature-induced molecular exchange

So far, we have demonstrated that the HBC intermediate layer can prevent interactions between CoPc and gold. In order to study whether this layer structure is (thermodynamically) stable, we annealed CoPc/HBC/Au(111) samples to 630 K and performed PES, XAS and STM measurements.

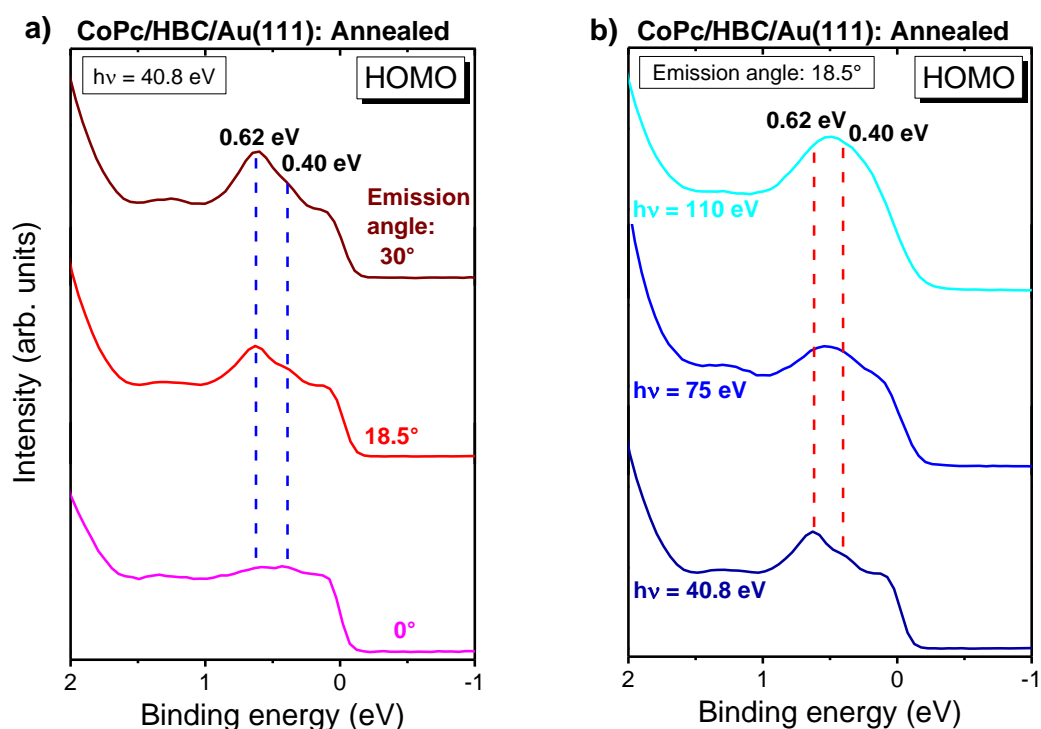


Figure 9. Valence band spectra with zoom into the HOMO-region after annealing: a) Variation of the angle with respect to normal emission, b) Variation of the excitation energy (angle 18.5° with respect to normal emission).

First, we will discuss photoemission valence band spectra (**Figure 9**) of an annealed CoPc(1.5 nm)/HBC/Au(111) sample. In contrast to the sample before annealing (cf. **Figure 8**), two new well-defined and intense states at 0.62 and 0.40 eV appear in the HOMO-region, while the former features at 1.3 and 1.1 eV are almost vanished. Generally, the intensity of valence

band features depends crucially on both the emission angle and the excitation energy (see, e.g. Refs. ^{74, 93-98}). Unfortunately, for both HBC-derivatives and phthaloyanines, the maximal intensity of the lowest lying valence band features is expected around $1.5-1.7 \text{ \AA}^{-1}$,^{74, 95-98} and thus it is difficult to distinguish between both molecules.

The intensity of features at binding energies of 0.40 and 0.62 eV in **Figure 9a** increases with higher polar angle; they are most intense at 30° , which corresponds to $k_{\parallel} \sim 1.5 \text{ \AA}^{-1}$. Since such a behavior is expected for valence band features of CoPc and HBC, we conclude that the interface states can be assigned to molecular orbitals, most likely to the HOMO of CoPc and/or HBC. The fact that they are observed at distinctly lower binding energy compared to the HOMO before annealing (cf. **Figure 8**) may point to a strong coupling to the substrate. Further information about the nature of these states might be obtained from energy dependent valence band spectra, because the (relative) intensity varies for different orbitals. In particular, the relative intensity of Co related 3d states will increase at the highest excitation energy (110 eV), compared to lower energies due to the higher relative cross section (the ratio of Co 3d/C 2p is 4.6 and 38.0 at $h\nu = 40.8 \text{ eV}$ and 110.0 , respectively).³⁵ Indeed, a higher spectral weight at the position of the lower energy feature at 0.4 eV might be visible in **Figure 9b** for $h\nu = 110 \text{ eV}$, even if the decreased energy resolution (40 meV @40.8 eV and 120 meV @110 eV) does not allow the separation of both features at higher excitation energies. Valence band features at lowest binding energy with (partial) Co character were observed for CoPc in thin films and at interfaces,^{89, 99} and thus these features might be partially assigned to CoPc.

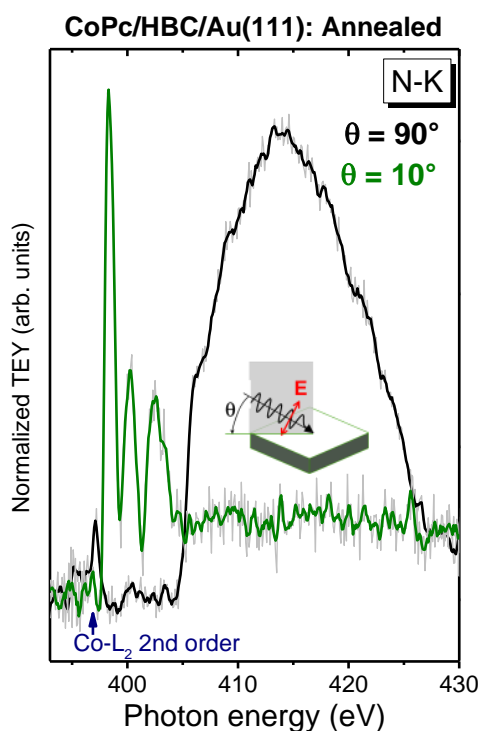


Figure 10. Angle-dependent N-K XA spectra of CoPc/HBC/Au(111) after annealing to 630 K.

As already mentioned, distinct changes of the XAS peak shape are expected for CoPc molecules in direct contact to gold surfaces. In **Figure 10**, we show angle-dependent N-K edge XA spectra of the CoPc/HBC/Au(111) sample after annealing. The angular dependence indicates that CoPc molecules remain flat lying after annealing. Very low intensity in the π^* -region at grazing incidence points to an almost perfect orientation parallel to the substrate surface. However, the N-K peak shape is very similar to the sample before annealing (cf. **Figure 5**), indicating that nitrogen atoms of CoPc are not involved in an interaction at the interface to Au(111), which might be expected even for CoPc molecules in direct contact to Au.⁶⁸

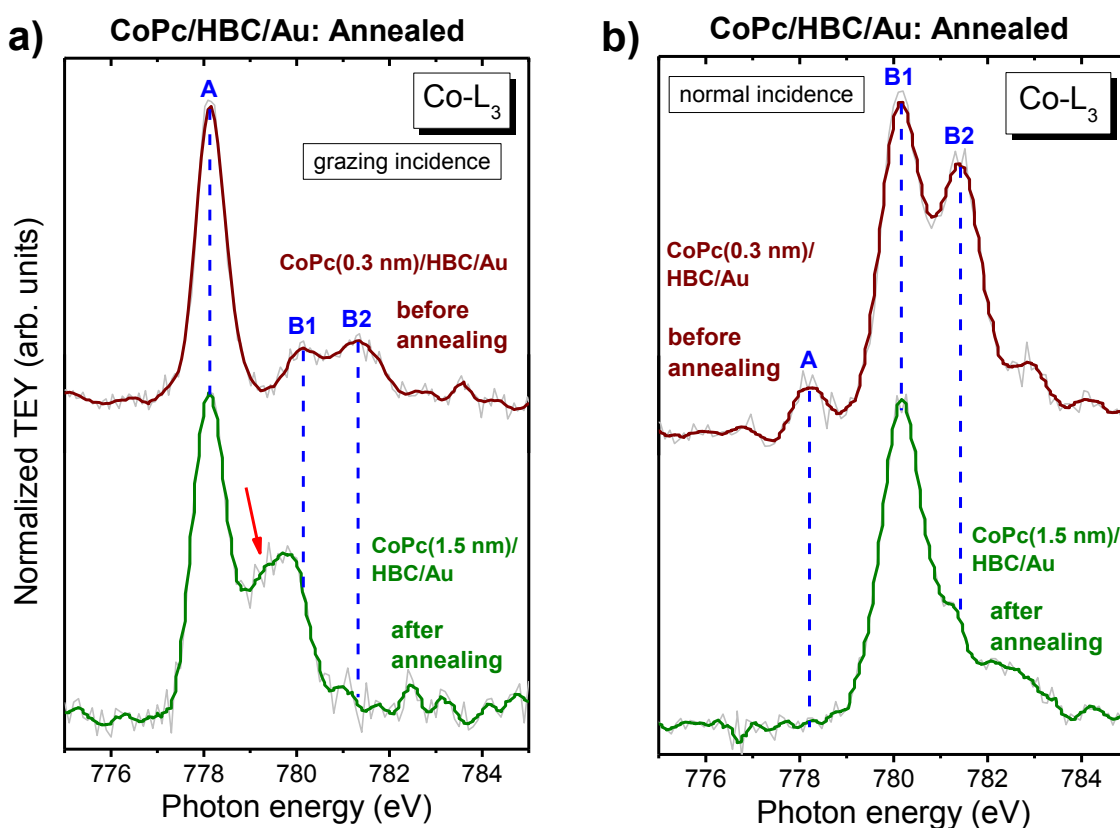


Figure 11. Angle-dependent Co-L₃ XA spectra of CoPc(1.5 nm)/HBC/Au(111) after annealing to 630 K (green curves) compared to CoPc(0.3 nm)/HBC/Au(111) before annealing (brown curves) taken at grazing (10°) and normal incidence (90°) of the incoming p-polarized synchrotron light.

In contrast, the shape of Co-L₃ XA spectra is clearly different comparing a 0.3 nm CoPc layer on HBC/Au(111) without annealing and CoPc(1.5 nm)/HBC/Au(111) after annealing to 630 K (**Figure 11**). Most visible, the prominent feature B2 disappears after annealing in the spectra taken at grazing and normal incidence. Also, the shape of feature A changes slightly and additional intensity is observed at higher photon energies (red arrow in **Figure 11a**). The changes of the peak shape indicate a charge transfer from the substrate to the Co ion of CoPc, accompanied by

a redistribution of the d-electrons. Such a behavior is typical for CoPc in direct contact to Au.^{68, 72} Thus, we conclude from Co-L₃ XA spectra that the interaction between CoPc and Au is no longer prevented by an HBC intermediate layer, the CoPc molecules are most likely diffused to the Au(111) interface upon annealing.

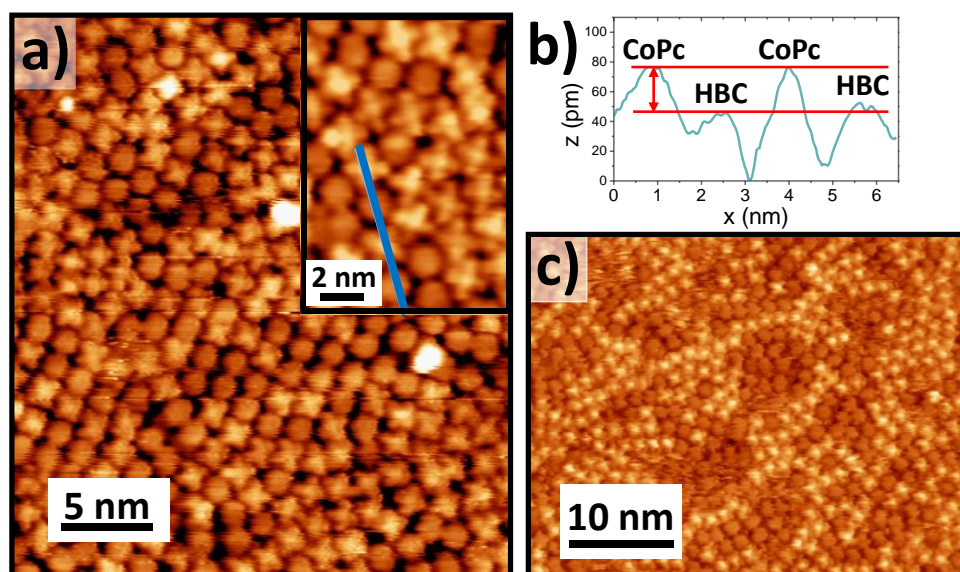


Figure 12. STM images of CoPc/HBC/Au(111), annealed to 630 K. a) 25 · 25 nm² image ($U = 1.5$ V, $I = 950$ pA). The inset shows a close-up measured with the same parameters, used for the line profile shown in b). c) 45 · 35 nm² image ($U = 1.0$ V and $I = 800$ pA). CoPc molecules are visible as bright spots.

The question may arise, whether CoPc molecules replace the HBC molecules after annealing completely. Therefore, we performed STM measurements of the annealed CoPc/HBC/Au(111) sample. Two different molecular structures can be identified in the STM images of **Figure 12**. The four-leaved pattern, typical for phthalocyanines, is best visible for some molecules in **Figure 12a**,

for other molecules a hexagonal structure typical for HBC might be supposed. The CoPc molecules appear somewhat brighter than the HBC molecules in **Figure 12a** (bias voltage of + 1.5 V). This effect is more pronounced in **Figure 12c**, at a bias voltage of + 1.0 V. This effect is caused by the increased brightness of the central Co-atom due to enhanced tunneling via the half-filled d_{z^2} orbitals at this tunneling voltage.¹⁰⁰ Due to the local density of molecular states of the d -orbitals, the central metal atoms of TMPcs appear at increased apparent heights compared to the macrocycle.¹⁰⁰⁻¹⁰¹ Therefore, depending on the tunneling voltage, we can distinguish between CoPc and HBC molecules from their apparent height. A line profile is generated from the close-up of **Figure 12a** (inset), illustrated in **Figure 12b**. The line profile reveals a height difference between the CoPc and HBC molecules of about 30 pm. From the slight differences in the apparent height we conclude, that the CoPc and HBC molecules are present in the same layer, i.e. they form a mixed monolayer on Au(111).

Often bimolecular layers form ordered structures due to molecule – molecule interaction by H-bonds, dipole-dipole interaction or metal coordination.¹⁰²⁻¹⁰⁶ In **Figure 12**, it seems that molecules of the same type (CoPc or HBC) tend to form domains, but also a large number of single molecules and irregular spaces between the molecules (dark areas) are visible. Consequently, we could not identify a preferred orientation as discussed for CoPc and HBC monolayers (cf. **Figure 2-4**). This is confirmed by the absence of a LEED pattern, shown in **Figure S1**.

Thus, our results verify that a molecular exchange takes place after annealing of CoPc(1.5 nm)/HBC/Au(111). However, not all of the CoPc molecules are able to replace HBC molecules at the interface to Au(111). Obviously, the interactions between CoPc molecules are

weak enough to enable the desorption of CoPc at the chosen temperature of 630 K. Thus, it seems that the detailed composition of the remaining, mixed HBC-CoPc monolayer strongly depends on both the desorption kinetics of CoPc and the kinetics of the diffusion/exchange. Therefore, we suggest that especially the variation of the temperature regime enables the tuning of the arrangement of molecules and their composition in the mixed layer.

Summary

We studied interface properties and the structural ordering of cobalt phthalocyanine (CoPc) on a highly ordered monolayer (ML) hexa-*peri*-hexabenzocoronene (HBC), grown on Au(111). LEED and STM measurements reveal that well-ordered CoPc layers are formed on HBC/Au(111). The HBC layer acts as a template for the initial growth of CoPc molecules. An hexagonal arrangement is observed for CoPc on HBC/Au(111); the angle between the lattice vectors is the same as for the annealed HBC monolayer ($\Gamma = 60^\circ$). A charge transfer between CoPc and the gold substrate is almost completely prevented by the HBC intermediate layer. After annealing to 630 K, a molecular exchange takes place and a mixed monolayer of CoPc and HBC is formed on the Au(111) substrate. We conclude that the interaction strength between CoPc and Au(111) is not significantly stronger compared to HBC/Au(111).

Acknowledgements

The authors thank the Helmholtz-Zentrum Berlin (HZB) for the allocation of synchrotron radiation. Financial travel support by HZB is thankfully acknowledged. The Center for Light-Matter Interaction, Sensors & Analytics (LISA⁺) at the University of Tübingen is acknowledged for technical support.

ASSOCIATED CONTENT

Supporting Information

XPS peakfit data of C1s and N1s spectra of CoPc on HBC/Au(111) and HBC/Au(111), *LEED pattern of CoPc/HBC/Au(111) after annealing to 630 K.*

References

1. Koch, N., Organic Electronic Devices and Their Functional Interfaces. *ChemPhysChem* **2007**, *8*, 1438-1455.
2. Ma, H.; Yip, H. L.; Huang, F.; Jen, A. K. Y., Interface Engineering for Organic Electronics. *Adv. Funct. Mater.* **2010**, *20*, 1371-1388.
3. Sanvito, S., Molecular Spintronics. *Chemical Society Reviews* **2011**, *40*, 3336-3355.
4. Forrest, S. R., The Path to Ubiquitous and Low-Cost Organic Electronic Appliances on Plastic. *Nature* **2004**, *428*, 911-918.
5. Dodabalapur, A.; Katz, H. E.; Torsi, L.; Haddon, R. C., Organic Heterostructure Field-Effect Transistors. *Science* **1995**, *269*, 1560.
6. Tang, C. W., Two-Layer Organic Photovoltaic Cell. *Applied Physics Letters* **1986**, *48*, 183-185.
7. Katz, H. E.; Lovinger, A. J.; Johnson, J.; Kloc, C.; Siegrist, T.; Li, W.; Lin, Y. Y.; Dodabalapur, A., A Soluble and Air-Stable Organic Semiconductor with High Electron Mobility. *Nature* **2000**, *404*, 478-481.
8. Uihlein, J., et al., Influence of Graphene on Charge Transfer between Copc and Metals: The Role of Graphene-Substrate Coupling. *J. Phys. Chem. C* **2015**, *119*, 15240-15247.
9. Balle, D.; Adler, H.; Grüninger, P.; Karstens, R.; Ovsyannikov, R.; Giangrisostomi, E.; Chassé, T.; Peisert, H., Influence of the Fluorination of Copc on the Interfacial Electronic Structure of the Coordinated Metal Ion. *J. Phys. Chem. C* **2017**, *121*, 18564-18574.
10. Ameri, T.; Li, N.; Brabec, C. J., Highly Efficient Organic Tandem Solar Cells: A Follow up Review. *Energy & Environmental Science* **2013**, *6*, 2390-2413.

11. Chung, K.; Lee, C.-H.; Yi, G.-C., Transferable Gan Layers Grown on Zno-Coated Graphene Layers for Optoelectronic Devices. *Science* **2010**, *330*, 655.
12. Kawasaki, T.; Ichimura, T.; Kishimoto, H.; Akbar, A. A.; Ogawa, T.; Oshima, C., Double Atomic Layers of Graphene/Monolayer H-Bn on Ni(111) Studied by Scanning Tunneling Microscopy and Scanning Tunneling Spectroscopy. *Surface Review and Letters* **2002**, *09*, 1459-1464.
13. Scarfato, A.; Chang, S.-H.; Kuck, S.; Brede, J.; Hoffmann, G.; Wiesendanger, R., Scanning Tunneling Microscope Study of Iron(II) Phthalocyanine Growth on Metals and Insulating Surfaces. *Surface Science* **2008**, *602*, 677-683.
14. Dahal, A.; Batzill, M., Graphene–Nickel Interfaces: A Review. *Nanoscale* **2014**, *6*, 2548-2562.
15. Wintterlin, J.; Bocquet, M. L., Graphene on Metal Surfaces. *Surface Science* **2009**, *603*, 1841-1852.
16. Nie, S.; Bartelt, N. C.; Wofford, J. M.; Dubon, O. D.; McCarty, K. F.; Thürmer, K., Scanning Tunneling Microscopy Study of Graphene on Au(111): Growth Mechanisms and Substrate Interactions. *Physical Review B* **2012**, *85*, 205406.
17. Oznuluer, T.; Pince, E.; Polat, E. O.; Balci, O.; Salihoglu, O.; Kocabas, C., Synthesis of Graphene on Gold. *Applied Physics Letters* **2011**, *98*, 183101.
18. Grimsdale, A. C.; Wu, J.; Mullen, K., New Carbon-Rich Materials for Electronics, Lithium Battery, and Hydrogen Storage Applications. *Chem. Commun.* **2005**, 2197-2204.
19. Helga, S.; Balaji, P.; David, J. J.; Andrew, B. H.; Wallace, W. H. W., Hexa-Peri-Hexabenzocoronene in Organic Electronics. *Pure and Applied Chemistry* **2012**, *84*, 1047-1067.
20. Proehl, H.; Toerker, M.; Sellam, F.; Fritz, T.; Leo, K.; Simpson, C.; Müllen, K., Comparison of Ultraviolet Photoelectron Spectroscopy and Scanning Tunneling Spectroscopy Measurements on Highly Ordered Ultrathin Films of Hexa-Peri-Hexabenzocoronene on Au(111). *Physical Review B* **2001**, *63*, 205409.
21. Sellam, F.; Schmitz-Hübsch, T.; Toerker, M.; Mannsfeld, S.; Proehl, H.; Fritz, T.; Leo, K.; Simpson, C.; Müllen, K., Leed and Stm Investigations of Organic–Organic Heterostructures Grown by Molecular Beam Epitaxy. *Surf. Sci.* **2001**, *478*, 113-121.
22. Ruffieux, P.; Gröning, O.; Biemann, M.; Simpson, C.; Müllen, K.; Schlapbach, L.; Gröning, P., Supramolecular Columns of Hexabenzocoronenes on Copper and Gold (111) Surfaces. *Phys. Rev. B* **2002**, *66*, 073409.
23. Belser, A.; Greulich, K.; Grüninger, P.; Bettinger, H. F.; Peisert, H.; Chassé, T., Visualization of the Borazine Core of B₃N₃-Doped Nanographene by Stm. *ACS Appl. Mater. Interfaces* **2020**, *12*, 19218-19225.
24. Amsalem, P.; Wilke, A.; Frisch, J.; Niederhausen, J.; Vollmer, A.; Rieger, R.; Müllen, K.; Rabe, J. P.; Koch, N., Interlayer Molecular Diffusion and Thermodynamic Equilibrium in Organic Heterostructures on a Metal Electrode. *Journal of Applied Physics* **2011**, *110*, 113709.
25. Duhm, S.; Salzmann, I.; Bröker, B.; Glowatzki, H.; Johnson, R. L.; Koch, N., Interdiffusion of Molecular Acceptors through Organic Layers to Metal Substrates Mimics Doping-Related Energy Level Shifts. *Applied Physics Letters* **2009**, *95*, 093305.
26. Sun, L.; Liu, C.; Queteschiner, D.; Weidinger, G.; Zeppenfeld, P., Layer Inversion in Organic Heterostructures. *Phys. Chem. Chem. Phys.* **2011**, *13*, 13382-13386.
27. Gallego, J. M.; Ecija, D.; Martín, N.; Otero, R.; Miranda, R., An Stm Study of Molecular Exchange Processes in Organic Thin Film Growth. *Chemical Communications* **2014**, *50*, 9954-9957.
28. Stadtmüller, B.; Gruenewald, M.; Peuker, J.; Forker, R.; Fritz, T.; Kumpf, C., Molecular Exchange in a Heteromolecular Ptcda/Cupc Bilayer Film on Ag(111). *The Journal of Physical Chemistry C* **2014**, *118*, 28592-28602.
29. Gruenewald, M.; Sauer, C.; Peuker, J.; Meissner, M.; Sojka, F.; Schöll, A.; Reinert, F.; Forker, R.; Fritz, T., Commensurism at Electronically Weakly Interacting Phthalocyanine/Ptcda Heterointerfaces. *Phys. Rev. B* **2015**, *91*, 155432.

30. Kleimann, C.; Stadtmüller, B.; Schröder, S.; Kumpf, C., Electrostatic Interaction and Commensurate Registry at the Heteromolecular F16cupc–Cupc Interface. *J. Phys. Chem. C* **2014**, *118*, 1652-1660.
31. Häming, M.; Greif, M.; Sauer, C.; Schöll, A.; Reinert, F., Electronic Structure of Ultrathin Heteromolecular Organic-Metal Interfaces: Snpc/Ptcda/Ag(111) and Snpc/Ag(111). *Physical Review B* **2010**, *82*, 235432.
32. Borghetti, P.; de Oteyza, D. G.; Rogero, C.; Goiri, E.; Verdini, A.; Cossaro, A.; Floreano, L.; Ortega, J. E., Molecular-Level Realignment in Donor–Acceptor Bilayer Blends on Metals. *The Journal of Physical Chemistry C* **2016**, *120*, 5997-6005.
33. Peisert, H.; Uihlein, J.; Petraki, F.; Chassé, T., Charge Transfer between Transition Metal Phthalocyanines and Metal Substrates: The Role of the Transition Metal. *J. Electron Spectros. Relat. Phenomena* **2015**, *204*, 49-60.
34. Liu, R.; Wu, D.; Feng, X.; Müllen, K., Bottom-up Fabrication of Photoluminescent Graphene Quantum Dots with Uniform Morphology. *J. Am. Chem. Soc.* **2011**, *133*, 15221-15223.
35. Yeh, J. J.; Lindau, I., Atomic Subshell Photoionization Cross-Sections and Asymmetry Parameters - 1 Less-Than-or-Equal-to Z Less-Than-or-Equal-to 103. *Atom. Data Nucl. Data Tables* **1985**, *32*, 1-155.
36. Seah, M. P.; Dench, W. A., Quantitative Electron Spectroscopy of Surfaces: A Standard Data Base for Electron Inelastic Mean Free Paths in Solids. *Surf. Interface Anal.* **1979**, *1*, 2-11.
37. Horcas, I.; Fernández, R.; Gómez-Rodríguez, J. M.; Colchero, J.; Gómez-Herrero, J.; Baro, A. M., Wsxn: A Software for Scanning Probe Microscopy and a Tool for Nanotechnology. *Review of Scientific Instruments* **2007**, *78*, 013705.
38. Hesse, R.; Chasse, T.; Streubel, P.; Szargan, R., Error Estimation in Peak-Shape Analysis of Xps Core-Level Spectra Using Unifit 2003: How Significant Are the Results of Peak Fits? *Surf. Interface Anal.* **2004**, *36*, 1373-1383.
39. Giangrisostomi, E., et al., Low Dose Photoelectron Spectroscopy at Bessy II: Electronic Structure of Matter in Its Native State. *J. Electron Spectros. Relat. Phenomena* **2018**, *224*, 68-78.
40. Vollmer, A., et al., Two Dimensional Band Structure Mapping of Organic Single Crystals Using the New Generation Electron Energy Analyzer Artof. *J. Electron Spectros. Relat. Phenomena* **2012**, *185*, 55-60.
41. Schreiber, F., Organic Molecular Beam Deposition: Growth Studies Beyond the First Monolayer. *Phys Status Solidi A* **2004**, *201*, 1037-1054.
42. Peisert, H.; Biswas, I.; Knupfer, M.; Chasse, T., Orientation and Electronic Properties of Phthalocyanines on Polycrystalline Substrates. *Phys Status Solidi B* **2009**, *246*, 1529-1545.
43. Novák, J.; Oehzelt, M.; Berkebile, S.; Koini, M.; Ules, T.; Koller, G.; Haber, T.; Resel, R.; Ramsey, M. G., Crystal Growth of Para-Sexiphenyl on Clean and Oxygen Reconstructed Cu (110) Surfaces. *Phys. Chem. Chem. Phys.* **2011**, *13*, 14675-14684.
44. Wagner, C.; Kasemann, D.; Golnik, C.; Forker, R.; Esslinger, M.; Müllen, K.; Fritz, T., Repulsion between Molecules on a Metal: Monolayers and Submonolayers of Hexa-Peri-Hexabenzocoronene on Au(111). *Phys. Rev. B* **2010**, *81*, 035423.
45. Liu, L.; Yu, J.; Viernes, N. O. L.; Moore, J. S.; Lyding, J. W., Adsorption of Cobalt Phthalocyanine on Si(100)2×1 and Si(100)2×1:H Surfaces Studied by Scanning Tunneling Microscopy and Spectroscopy. *Surface Science* **2002**, *516*, 118-126.
46. Barlow, D. E.; Scudiero, L.; Hipps, K. W., Scanning Tunneling Microscopy Study of the Structure and Orbital-Mediated Tunneling Spectra of Cobalt(II) Phthalocyanine and Cobalt(II) Tetraphenylporphyrin on Au(111): Mixed Composition Films. *Langmuir* **2004**, *20*, 4413-4421.
47. Walzer, K.; Hietschold, M., Stm and Sts Investigation of Ultrathin Tin Phthalocyanine Layers Adsorbed on Hcp(0001) and Au(111). *Surface Science* **2001**, *471*, 1-10.
48. Lackinger, M.; Hietschold, M., Determining Adsorption Geometry of Individual Tin–Phthalocyanine Molecules on Ag(111)—a Stm Study at Submonolayer Coverage. *Surface Science* **2002**, *520*, L619-L624.

49. Gopakumar, T. G.; Lackinger, M.; Hackert, M.; Müller, F.; Hietschold, M., Adsorption of Palladium Phthalocyanine on Graphite: Stm and Leed Study. *The Journal of Physical Chemistry B* **2004**, *108*, 7839-7843.
50. Buchholz, J. C.; Somorjai, G. A., The Surface Structures of Phthalocyanine Monolayers and Vapor-Grown Films: A Low-Energy Electron Diffraction Study. *The Journal of Chemical Physics* **1977**, *66*, 573-580.
51. England, C.; Collins, G.; Schuerlein, T.; Armstrong, N. R., Epitaxial Thin Films of Large Organic Molecules: Characterization of Phthalocyanine and Coronene Overlayers on the Layered Semiconductors Mos2 and Sns2. *Langmuir* **1994**, *10*, 2748-2756.
52. Hämäläinen, S. K.; Stepanova, M.; Drost, R.; Liljeroth, P.; Lahtinen, J.; Sainio, J., Self-Assembly of Cobalt-Phthalocyanine Molecules on Epitaxial Graphene on Ir(111). *The Journal of Physical Chemistry C* **2012**, *116*, 20433-20437.
53. Jarvinen, P.; Hamalainen, S. K.; Ijas, M.; Harju, A.; Liljeroth, P., Self-Assembly and Orbital Imaging of Metal Phthalocyanines on a Graphene Model Surface. *J. Phys. Chem. C* **2014**, *118*, 13320-13325.
54. Barlow, D. E.; Hips, K. W., A Scanning Tunneling Microscopy and Spectroscopy Study of Vanadyl Phthalocyanine on Au(111): The Effect of Oxygen Binding and Orbital Mediated Tunneling on the Apparent Corrugation. *The Journal of Physical Chemistry B* **2000**, *104*, 5993-6000.
55. Yamane, H.; Kosugi, N., Site-Specific Intermolecular Valence-Band Dispersion in A-Phase Crystalline Films of Cobalt Phthalocyanine Studied by Angle-Resolved Photoemission Spectroscopy. *J. Chem. Phys.* **2014**, *141*, 224701.
56. Cheng, Z. H.; Gao, L.; Deng, Z. T.; Jiang, N.; Liu, Q.; Shi, D. X.; Du, S. X.; Guo, H. M.; Gao, H. J., Adsorption Behavior of Iron Phthalocyanine on Au(111) Surface at Submonolayer Coverage. *J. Phys. Chem. C* **2007**, *111*, 9240-9244.
57. Yoshimoto, S.; Tada, A.; Suto, K.; Itaya, K., Adlayer Structures and Electrocatalytic Activity for O₂ of Metallophthalocyanines on Au(111): In Situ Scanning Tunneling Microscopy Study. *The Journal of Physical Chemistry B* **2003**, *107*, 5836-5843.
58. Yoshimoto, S.; Higa, N.; Itaya, K., Two-Dimensional Supramolecular Organization of Copper Octaethylporphyrin and Cobalt Phthalocyanine on Au(111): Molecular Assembly Control at an Electrochemical Interface. *Journal of the American Chemical Society* **2004**, *126*, 8540-8545.
59. Chizhov, I.; Scoles, G.; Kahn, A., The Influence of Steps on the Orientation of Copper Phthalocyanine Monolayers on Au(111). *Langmuir* **2000**, *16*, 4358-4361.
60. England, C.; Collins, G.; Schuerlein, T.; Armstrong, N., Epitaxial Thin Films of Large Organic Molecules: Characterization of Phthalocyanine and Coronene Overlayers on the Layered Semiconductors Mos2 and Sns2. *Langmuir* **1994**, *10*, 2748-2756.
61. Belser, A.; Karstens, R.; Nagel, P.; Merz, M.; Schuppler, S.; Chassé, T.; Peisert, H., Interaction Channels between Perfluorinated Iron Phthalocyanine and Cu(111). *physica status solidi (b)* **2019**, *256*, 1800292.
62. Greulich, K., et al., Charge Transfer from Organic Molecules to Molybdenum Disulfide: Influence of the Fluorination of Iron Phthalocyanine. *The Journal of Physical Chemistry C* **2020**.
63. Karstens, R.; Glaser, M.; Belser, A.; Balle, D.; Polek, M.; Ovsyannikov, R.; Giangrisostomi, E.; Chasse, T.; Peisert, H., Fepc and Fepcf16 on Rutile TiO₂(110) and (100): Influence of the Substrate Preparation on the Interaction Strength. *Molecules* **2019**, *24*, 20.
64. Scardamaglia, M.; Struzzi, C.; Lizzit, S.; Dalmiglio, M.; Lacovig, P.; Baraldi, A.; Mariani, C.; Betti, M. G., Energetics and Hierarchical Interactions of Metal Phthalocyanines Adsorbed on Graphene/Ir(111). *Langmuir* **2013**, *29*, 10440-10447.
65. Lindner, S.; Treske, U.; Knupfer, M., The Complex Nature of Phthalocyanine/Gold Interfaces. *Appl. Surf. Sci.* **2013**, *267*, 62-65.

66. Zhang, T., et al., Conclusively Addressing the Copc Electronic Structure: A Joint Gas-Phase and Solid-State Photoemission and Absorption Spectroscopy Study. *J. Phys. Chem. C* **2017**, *121*, 26372-26378.
67. Maslyuk, V. V.; Aristov, V. Y.; Molodtsova, O. V.; Vyalikh, D. V.; Zhilin, V. M.; Ossipyan, Y. A.; Bredow, T.; Mertig, I.; Knupfer, M., The Electronic Structure of Cobalt Phthalocyanine. *Appl Phys a-Mater* **2009**, *94*, 485-489.
68. Betti, M. G.; Gargiani, P.; Frisenda, R.; Biagi, R.; Cossaro, A.; Verdini, A.; Floreano, L.; Mariani, C., Localized and Dispersive Electronic States at Ordered Fepc and Copc Chains on Au(110). *J. Phys. Chem. C* **2010**, *114*, 21638-21644.
69. Kroll, T.; Aristov, V. Y.; Molodtsova, O. V.; Ossipyan, Y. A.; Vyalikh, D. V.; Buchner, B.; Knupfer, M., Spin and Orbital Ground State of Co in Cobalt Phthalocyanine. *J. Phys. Chem. A* **2009**, *113*, 8917-8922.
70. Willey, T. M.; Bagge-Hansen, M.; Lee, J. R. I.; Call, R.; Landt, L.; van Buuren, T.; Colesniuc, C.; Monton, C.; Valmianski, I.; Schuller, I. K., Electronic Structure Differences between H-2-, Fe-, Co-, and Cu-Phthalocyanine Highly Oriented Thin Films Observed Using Nexafs Spectroscopy. *J. Chem. Phys.* **2013**, *139*.
71. de Groot, F., Multiplet Effects in X-Ray Spectroscopy. *Coord. Chem. Rev.* **2005**, *249*, 31-63.
72. Petraki, F.; Peisert, H.; Biswas, I.; Aygul, U.; Latteyer, F.; Vollmer, A.; Chasse, T., Interaction between Cobalt Phthalocyanine and Gold Studied by X-Ray Absorption and Resonant Photoemission Spectroscopy. *J Phys Chem Lett* **2010**, *1*, 3380-3384.
73. Gargiani, P., et al., Spin and Orbital Configuration of Metal Phthalocyanine Chains Assembled on the Au(110) Surface. *Phys Rev B* **2013**, *87*, 165407.
74. Yamane, H.; Kosugi, N., Site-Specific Organic/Metal Interaction Revealed from Shockley-Type Interface State. *J. Phys. Chem. C* **2016**, *120*, 24307-24313.
75. Evangelista, F.; Ruocco, A.; Gotter, R.; Cossaro, A.; Floreano, L.; Morgante, A.; Crispoldi, F.; Betti, M. G.; Mariani, C., Electronic States of Cupc Chains on the Au(110) Surface. *J. Chem. Phys.* **2009**, *131*, 174710.
76. Papageorgiou, N.; Ferro, Y.; Salomon, E.; Allouche, A.; Layet, J. M.; Giovanelli, L.; Le Lay, G., Geometry and Electronic Structure of Lead Phthalocyanine: Quantum Calculations Via Density-Functional Theory and Photoemission Measurements. *Phys. Rev. B* **2003**, *68*, 235105.
77. Papageorgiou, N.; Salomon, E.; Angot, T.; Layet, J.-M.; Giovanelli, L.; Lay, G. L., Physics of Ultra-Thin Phthalocyanine Films on Semiconductors. *Prog. Surf. Sci.* **2004**, *77*, 139-170.
78. Schmid, M.; Kaftan, A.; Steinruck, H. P.; Gottfried, J. M., The Electronic Structure of Cobalt(II) Phthalocyanine Adsorbed on Ag(111). *Surf. Sci.* **2012**, *606*, 945-949.
79. Åhlund, J.; Nilson, K.; Schiessling, J.; Kjeldgaard, L.; Berner, S.; Mårtensson, N.; Puglia, C.; Brena, B.; Nyberg, M.; Luo, Y., The Electronic Structure of Iron Phthalocyanine Probed by Photoelectron and X-Ray Absorption Spectroscopies and Density Functional Theory Calculations. *J. Chem. Phys.* **2006**, *125*, 034709.
80. Petraki, F.; Peisert, H.; Biswas, I.; Chasse, T., Electronic Structure of Co-Phthalocyanine on Gold Investigated by Photoexcited Electron Spectroscopies: Indication of Co Ion-Metal Interaction. *J. Phys. Chem. C* **2010**, *114*, 17638-17643.
81. Adler, H.; Paszkiewicz, M.; Uihlein, J.; Polek, M.; Ovsyannikov, R.; Basova, T. V.; Chasse, T.; Peisert, H., Interface Properties of Vopc on Ni(111) and Graphene/Ni(111): Orientation-Dependent Charge Transfer. *J. Phys. Chem. C* **2015**, *119*, 8755-8762.
82. Ruocco, A.; Evangelista, F.; Attili, A.; Donzello, M. P.; Betti, M. G.; Giovanelli, L.; Gotter, R., Copper-Phthalocyanine Ultra Thin Films Grown onto Al(1 0 0) Surface Investigated by Synchrotron Radiation. *Journal of Electron Spectroscopy and Related Phenomena* **2004**, *137-140*, 165-169.
83. Peisert, H.; Knupfer, M.; Schwieger, T.; Auerhammer, J. M.; Golden, M. S.; Fink, J., Full Characterization of the Interface between the Organic Semiconductor Copper Phthalocyanine and Gold. *J. Appl. Phys.* **2002**, *91*, 4872-4878.

84. Peisert, H.; Knupfer, M.; Fink, J., Electronic Structure of Partially Fluorinated Copper Phthalocyanine (Cupcf4) and Its Interface to Au(100). *Surf. Sci.* **2002**, *515*, 491-498.
85. Gargiani, P.; Angelucci, M.; Mariani, C.; Betti, M. G., Metal-Phthalocyanine Chains on the Au(110) Surface: Interaction States Versus D-Metal States Occupancy. *Phys Rev B* **2010**, *81*.
86. Brumboiu, I. E.; Prokopiou, G.; Kronik, L.; Brena, B., Valence Electronic Structure of Cobalt Phthalocyanine from an Optimally Tuned Range-Separated Hybrid Functional. *J. Chem. Phys.* **2017**, *147*, 11.
87. Brumboiu, I. E.; Haldar, S.; Lüder, J.; Eriksson, O.; Herper, H. C.; Brena, B.; Sanyal, B., Influence of Electron Correlation on the Electronic Structure and Magnetism of Transition-Metal Phthalocyanines. *Journal of Chemical Theory and Computation* **2016**, *12*, 1772-1785.
88. Ellis, T. S.; Park, K. T.; Ulrich, M. D.; Hulbert, S. L.; Rowe, J. E., Interaction of Metallophthalocyanines (Mpc,M=Co,Ni) on Au(001): Ultraviolet Photoemission Spectroscopy and Low Energy Electron Diffraction Study. *Journal of Applied Physics* **2006**, *100*, 093515.
89. Grobosch, M.; Aristov, V. Y.; Molodtsova, O. V.; Schmidt, C.; Doyle, B. P.; Nannarone, S.; Knupfer, M., Engineering of the Energy Level Alignment at Organic Semiconductor Interfaces by Intramolecular Degrees of Freedom: Transition Metal Phthalocyanines. *J. Phys. Chem. C* **2009**, *113*, 13219-13222.
90. Ueno, N.; Kera, S.; Sakamoto, K.; Okudaira, K. K., Energy Band and Electron-Vibration Coupling in Organic Thin Films: Photoelectron Spectroscopy as a Powerful Tool For studying The charge Transport. *Applied Physics A* **2008**, *92*, 495-504.
91. Kera, S.; Yamane, H.; Ueno, N., First-Principles Measurements of Charge Mobility in Organic Semiconductors: Valence Hole-Vibration Coupling in Organic Ultrathin Films. *Progress in Surface Science* **2009**, *84*, 135-154.
92. Wang, J.; Wang, J.; Dougherty, D. B., Direct Molecular Quantification of Electronic Disorder in N, N'-Di-[(1-Naphthyl)-N, N'-Diphenyl]-1, 1'-Biphenyl)-4, 4'-Diamine on Au (111). *Journal of Vacuum Science & Technology B, Nanotechnology and Microelectronics: Materials, Processing, Measurement, and Phenomena* **2020**, *38*, 053401.
93. Koller, G.; Berkebile, S.; Oehzelt, M.; Puschnig, P.; Ambrosch-Draxl, C.; Netzer, F. P.; Ramsey, M. G., Intra- and Intermolecular Band Dispersion in an Organic Crystal. *Science* **2007**, *317*, 351-355.
94. Sättele, M. S., et al., Going Beyond Pentacene: Photoemission Tomography of a Heptacene Monolayer on Ag(110). *J. Phys. Chem. C* **2021**, *125*, 2918-2925.
95. Friedlein, R., et al., Electronic Structure of Highly Ordered Films of Self-Assembled Graphitic Nanocolumns. *Phys Rev B* **2003**, *68*.
96. Ueno, N.; Kera, S., Electron Spectroscopy of Functional Organic Thin Films: Deep Insights into Valence Electronic Structure in Relation to Charge Transport Property. *Progress in Surface Science* **2008**, *83*, 490-557.
97. Shang, M.-H.; Nagaosa, M.; Nagamatsu, S.-i.; Hosoumi, S.; Kera, S.; Fujikawa, T.; Ueno, N., Photoemission from Valence Bands of Transition Metal-Phthalocyanines. *J. Electron Spectros. Relat. Phenomena* **2011**, *184*, 261-264.
98. Schönauer, K., et al., Charge Transfer and Symmetry Reduction at the Cupc/Ag(110) Interface Studied by Photoemission Tomography. *Phys. Rev. B: Condens. Matter* **2016**, *94*, 205144.
99. Lindner, S.; Treske, U.; Grobosch, M.; Knupfer, M., Charge Transfer at F16copc and Copc Interfaces to Au. *Appl Phys a-Mater* **2011**, *105*, 921-925.
100. Lu, X.; Hipps, K. W.; Wang, X. D.; Mazur, U., Scanning Tunneling Microscopy of Metal Phthalocyanines: D7 and D9 Cases. *Journal of the American Chemical Society* **1996**, *118*, 7197-7202.
101. Lu, X.; Hipps, K. W., Scanning Tunneling Microscopy of Metal Phthalocyanines: D6 and D8 Cases. *The Journal of Physical Chemistry B* **1997**, *101*, 5391-5396.
102. Goiri, E.; Borghetti, P.; El-Sayed, A.; Ortega, J. E.; de Oteyza, D. G., Multi-Component Organic Layers on Metal Substrates. *Advanced Materials* **2016**, *28*, 1340-1368.

103. Bouju, X.; Mattioli, C.; Franc, G.; Pujol, A.; Gourdon, A., Bicomponent Supramolecular Architectures at the Vacuum–Solid Interface. *Chem. Rev.* **2017**, *117*, 1407-1444.
104. El-Sayed, A., et al., Understanding Energy-Level Alignment in Donor-Acceptor/Metal Interfaces from Core-Level Shifts. *Acs Nano* **2013**, *7*, 6914-6920.
105. Wakayama, Y., On-Surface Molecular Nanoarchitectonics: From Self-Assembly to Directed Assembly. *Jpn. J. Appl. Phys.* **2016**, *55*, 1102AA.
106. Henneke, C.; Felter, J.; Schwarz, D.; Stefan Tautz, F.; Kumpf, C., Controlling the Growth of Multiple Ordered Heteromolecular Phases by Utilizing Intermolecular Repulsion. *Nature Materials* **2017**, *16*, 628-633.

Danksagung

Während dieser Arbeit haben mich viele Menschen begleitet, ohne deren Unterstützung diese Arbeit eine andere wäre. Ich möchte die Gelegenheit nutzen, mich bei all jenen dafür zu bedanken.

Insbesondere bei **Prof. Dr. Thomas Chassé** für die Möglichkeit diese Promotion anzufertigen, das interessante Thema, die vielen hilfreichen Diskussionen und das in mich gesetzte Vertrauen.

Ebenfalls möchte ich mich ganz herzlich bei **Prof. Dr. Heiko Peisert** für die vielen wissenschaftlichen Diskussionen, Ratschläge und die allgemeine Unterstützung bedanken.

Den **Mitarbeitern der Synchrotron Speicherringe BESSY II und KARA** möchte ich für die ausführliche Einweisung, Unterstützung und viele wissenschaftliche Diskussionen danken.

Dem kompletten **Arbeitskreis Chassé** danke ich für eine schöne Zeit, unzählbar viele interessante, (wissenschaftliche) Diskussionen, Kameradschaft, Hilfsbereitschaft und Beistand bei verschiedenen mehr oder weniger wissenschaftlichen Problemen, sowie den schönen gemeinschaftlichen Aktivitäten, wie Ausflüge in Berlin, während das Synchrotron stillstand, oder auf das Adlersche Weingut. Insbesondere bei **Reimer Karstens** und **Katharina Greulich** für die Hilfe an den Geräten und bei der Lösung vieler mehr oder weniger wissenschaftlicher Fragestellungen, sowie **Sven Bölke** für die unzähligen Tage der gemeinsamen Prüfungsvorbereitung.

Bei **Prof. Dr. Bettinger** und seinen Mitarbeitern für die Synthese der nanographenartigen Moleküle.

Bei meinen Eltern **Marina** und **Jörg** bedanke ich mich für die bedingungslose Unterstützung, Geduld und ihren Glauben an mich.

Zu guter Letzt und ganz besonders möchte ich meiner starken Freundin **Jennifer** danken, die in schwierigen Zeiten meine schlechte Laune ertragen musste und mir immer zur Seite stand. Du bist ein großes Vorbild für mich.